Technische Universität München
TUM School of Engineering and Design

Comprehensive and consistent models for the linear analysis of thermoacoustic phenomena

Moritz Josua Merk

Vollständiger Abdruck der von der TUM School of Engineering and Design der Technischen Universität München zur Erlangung des akademischen Grades eines

DOKTORS DER INGENIEURWISSENSCHAFTEN (DR.-ING.)

genehmigten Dissertation.

Vorsitz:
Prof. Dr.-Ing. Hans-Jakob Kaltenbach
Prüfende der Dissertation:
1. Prof. Wolfgang Polifke, Ph.D.
2. Prof. Dong Yang, Ph.D.

Die Dissertation wurde am 30.09.2024 bei der Technischen Universität München eingereicht und durch die TUM School of Engineering and Design am 29.01.2025 angenommen.

Abstract

Modern low-emission gas turbines operate close to the lean blowout limit, a regime in which the combustor is susceptible to thermoacoustic instabilities. Understanding the various thermoacoustic feedback loops and reliably, accurately, and efficiently predicting their stability properties is an essential prerequisite to mitigate these undesired instabilities. Linearized thermoacoustic models are an established class of approaches to analyze thermoacoustic instabilities during their onset.

Linearized thermoacoustic models are commonly derived based on application-specific assumptions, and their transferability to other applications is, thus, limited. In contrast, this thesis focuses on comprehensibility and consistency, such that the developed models apply to a wide range of application cases. Furthermore, the models are adaptable to application-specific efficiency requirements by introducing assumptions *a posteriori*. The linearized thermoacoustic models developed in the context of this thesis include:

- *a framework for the consistent analysis of thermoacoustic sources in motion.* Isolating analytical source terms in differential equations for a moving source region, e.g. the exothermic reaction zone of a flame, requires tracking its motion. An Arbitrary Lagrangian-Eulerian reference frame is utilized to consistently track perturbation sources. This approach provides an analytical framework for consistently analyzing acoustic, entropic, vortical and compositional perturbation sources, offering insight into the underlying source mechanisms. The framework has been exemplified for the source terms of entropic inhomogeneities. For models approximating the source movement, the framework gives an analytical insight into spurious disturbances generated due to modeling errors.

- *a framework to consistently infer global flame transfer functions from experimental pressure measurements.* Inferring the global flame transfer function from the acoustic transfer matrix of the whole combustor requires a model. In the context of this thesis, a generalized model-based inference method has been developed to consistently identify the global flame transfer function from experimental measurements. The developed method extends the state-of-the-art burner-flame transfer matrix approach to test rigs with complex features such as bypass annulus, effusion holes and combustion chamber end contractions. The capabilities of the new framework have been showcased for the Scaled Acoustic Rig for Low Emission Technology by Rolls-Royce.

- *a Jacobian-based framework for the derivation of comprehensive thermoacoustic jump conditions.* The proposed procedure provides highly accurate jump conditions, including acoustic, entropic and compositional perturbations. Assumptions during the derivation are

minimized and the resulting jump conditions are, thus, valid for a wide range of application cases. Application-specific efficiency requirements might be achieved by introducing assumptions *a posteriori* without a lengthy rederivation. As an example, the framework has been used to derive a comprehensive jump condition of a lean premixed flame, which was subsequently validated for a lean hydrogen-vitiated air autoignition flame.

Besides the developed frameworks mentioned above, the following detailed analysis contributes to this thesis:

- *Assessment of various solution strategies to solve the thermoacoustic eigenvalue problem.* This study focuses on evaluating and comparing contour integration methods with methods that approximate and reformulate the eigenvalue problem. Solving the thermoacoustic eigenvalue problem reliably, accurately and efficiently is essential for the meaningful linear stability analysis of a thermoacoustic system.

The models developed and the analysis performed within this thesis add to a basis of consistent and comprehensive thermoacoustic models. These models contribute to understanding and predicting thermoacoustic instabilities, accelerating future research and the development of gas turbine combustors.

Kurzfassung

Moderne schadstoffarme Gasturbinen operieren nahe der Magergrenze, einem Bereich, in dem die Brennkammer anfällig für thermoakustische Instabilitäten ist. Das Verständnis der verschiedenen thermoakustischen Rückkopplungsschleifen und die zuverlässige, genaue und effiziente Vorhersage ihrer Stabilitätseigenschaften ist eine wesentliche Voraussetzung für die Minderung dieser unerwünschten Instabilitäten. Linearisierte thermoakustische Modelle sind eine etablierte Klasse von Ansätzen, um thermoakustische Instabilitäten während ihres anfänglichen Wachstums zu analysieren.

Linearisierte thermoakustische Modelle werden in der Regel auf der Grundlage anwendungsspezifischer Annahmen abgeleitet und sind daher nur begrenzt auf andere Anwendungen übertragbar. Im Gegensatz dazu liegt der Schwerpunkt dieser Arbeit auf Allgemeingültigkeit und Konsistenz, so dass die entwickelten Modelle auf eine Vielzahl von Anwendungsfällen anwendbar sind. Darüber hinaus sind die Modelle durch die Einführung von nachgestellten Annahmen an anwendungsspezifische Effizienzanforderungen anpassbar. Die im Rahmen dieser Arbeit entwickelten linearisierten thermoakustischen Modelle umfassen:

- *einen mathematischen Rahmen für die konsistente Analyse von thermoakustischen Quellen in Bewegung.* Die Isolierung von analytischen Quelltermen in Differentialgleichungen für eine bewegte Quellregion, z. B. die exotherme Reaktionszone einer Flamme, erfordert die Verfolgung ihrer Bewegung. Ein Arbitrary Lagrangian-Eulerian Bezugssystem wird verwendet, um Quellregionen von Störungen konsistent zu verfolgen. Dieser Ansatz bietet einen analytischen Rahmen, um die Quellen akustischer, entropischer, wirbelartiger und kompositioneller Störungen konsistent zu analysieren und Einblicke in die zugrunde liegenden Quellenmechanismen zu gewinnen. Der mathematische Rahmen wurde für die Quellterme von entropischen Inhomogenitäten beispielhaft angewendet. Für Modelle, die eine Näherung der Quellenbewegung verwenden, bietet der mathematische Rahmen analytische Einblicke in fehlerhafte Störungen, die aufgrund von Modellierungsfehlern entstehen.
- *eine Methode zur konsistenten Bestimmung globaler Flammenübertragungsfunktionen aus experimentellen Druckmessungen.* Die Bestimmung der globalen Flammenübertragungsfunktion aus der akustischen Übertragungsmatrix der gesamten Brennkammer erfordert ein Modell. Im Rahmen dieser Arbeit wurde eine verallgemeinerte modellbasierte Methode entwickelt, um die globale Flammenübertragungsfunktion aus experimentellen Messungen konsistent zu bestimmen. Die entwickelte Methode erweitert den Standardansatz der Brenner-Flammen-Übertragungsmatrix auf Prüfstände mit komplexen Merkmalen wie Nebenstromringraum, Effusionslöcher und Querschnittsreduktion

am Brennkammerauslass. Die Leistungsfähigkeit der neuen Methode wurde am Scaled Acoustic Rig for Low Emission Technology von Rolls-Royce demonstriert.

- *einen auf Jacobi-Matrizen basierender mathematischer Rahmen für die Herleitung allgemeingültiger thermoakustischer Sprungbedingungen.* Das vorgeschlagene Verfahren liefert hochgenaue Sprungbedingungen, die akustische, entropische und kompositionelle Störungen einschließen. Die Annahmen während der Herleitung sind minimiert und die resultierenden Sprungbedingungen sind daher für eine große Anzahl von Anwendungsfällen gültig. Anwendungsspezifische Effizienzanforderungen können durch die Einführung von nachträglichen Annahmen ohne langwierige Herleitung erreicht werden. Als Beispiel wurde der mathemaische Rahmen verwendet, um eine allgemeine Sprungbedingung für eine magere Vormischflamme abzuleiten, die anschließend für eine magere Wasserstoff-Selbstzündflamme validiert wurde.

Neben den oben erwähnten entwickelten mathematischen Rahmenwerken trägt die folgende detaillierte Analyse zu dieser Arbeit bei:

- *Bewertung von verschiedenen Lösungsstrategien zur Lösung des thermoakustischen Eigenwertproblems.* In dieser Arbeit wurde der Schwerpunkt auf die Bewertung und den Vergleich von Konturintegrationsverfahren mit Verfahren zur Approximation und Reformulierung des Eigenwertproblems gelegt. Die zuverlässige, genaue und effiziente Lösung des thermoakustischen Eigenwertproblems ist für eine aussagekräftige lineare Stabilitätsanalyse eines thermoakustischen Systems unerlässlich.

Die entwickelten Modelle und die im Rahmen dieser Arbeit durchgeführten Analysen erweitern eine Basis konsistenter und umfassender thermoakustischer Modelle. Diese Modelle tragen zum Verständnis und zur Vorhersage thermoakustischer Instabilitäten bei und beschleunigen die zukünftige Erforschung und Entwicklung von Gasturbinenbrennkammern.

Vorwort

An dieser Stelle möchte ich mich bei all den Menschen bedanken, die auf unterschiedlichste Art und Weise zu der vorliegenden Arbeit beigetragen haben.

Zuvorderst gehört mein Dank meinem Doktorvater Wolfgang Polifke. Deine offene Art, dein tiefgreifendes Fachwissen sowie dein ehrliches Interesse an der Forschung haben meine Arbeit an der Professur positiv geprägt. Unsere fachlichen Diskussionen sowie deine Ratschläge haben mich viel gelehrt und waren stets bereichernd für meine Forschung. Deine Leitung der Professur ist maßgeblich für die kollegiale und konstruktive Arbeitsatmosphäre verantwortlich, welche mich positiv auf meine Zeit an der Professur zurückdenken lässt.

Weiter möchte ich mich bei all den weiteren Menschen bedanken, welche ich während meiner Zeit am Institut kennenlernen durfte und welche zu der kollegialen Atmosphäre am Institut beigetragen haben. Insbesondere möchte ich einige Personen hervorheben, welche meine Zeit am Lehrstuhl geprägt haben. Dir, Max, möchte ich für unsere wertvollen Diskussionen, deine Ratschläge, deine Unterstützung und deine Einsichten während unserer gemeinsamen Zeit am Lehrstuhl danken. Dir, Philip Buschmann, danke ich für deine tatkräftige Unterstützung bei unserem gemeinsamen Paper, durch welches ich vieles über die Erstellung wissenschaftlicher Veröffentlichungen gelernt habe. Dir, Alex, danke ich für die produktive Zusammenarbeit zum Ende unserer Zeit am Lehrstuhl, welche in zwei Publikationen gipfelte. Dir, Grégoire, danke für die Zeit und freundschaftliche Stimmung im gemeinsamen Büro. Dir, Matthias, sowie der gesamten Fußballer-Truppe, danke ich für den wöchentlichen Kick, dir, Julian, für unsere anstrengenden Squash Duelle und, euch, Simon, Flo und Jonathan, für intensive Spike-Ball Matches. Ihr und unsere sportlichen Auseinandersetzungen haben mich mit durch die Höhen und Tiefen meiner Promotion getragen. Mein zusätzlicher Dank an Axel und Philipp für entspannende Bootsfahrten auf der Isar und dir, Jonathan, für die Partynächte in- und außerhalb Münchens.

Meine Eltern haben mir das Studium ermöglicht und meinen Weg bis an diesen Punkt geprägt. Ihr seid für mich da, wenn ich euch brauche und dafür bin ich euch zutiefst dankbar.

Zu guter Letzt einen Dank an all meine Freunde, die ich durch Höhen und Tiefen immer an meiner Seite weiß.

Contents

1 Introduction **1**
- 1.1 Thermoacoustic instabilities in gas turbines . . . 2
- 1.2 The scope of this thesis . . . 4

2 Governing equations **7**
- 2.1 Reference frames . . . 7
- 2.2 The reactive flow equations . . . 8
- 2.3 The linearized reactive flow equations . . . 9
- 2.4 Characteristic flow decomposition . . . 11
- 2.5 Transformation to the Laplace Domain . . . 12

3 Hybrid linearized thermoacoustic models **13**
- 3.1 Spatially resolved three-dimensional hybrid models . . . 13
- 3.2 Thermoacoustic network models . . . 15
- 3.3 Flow-flame interactions . . . 17

4 The thermoacoustic eigenvalue problem **21**
- 4.1 Special structures of the thermoacousic eigenvalue problem . . . 22
- 4.2 Eigenpairs and their classification . . . 23
- 4.3 Spurious eigenpairs and incomplete spectra . . . 23

5 Contextualization and Discussion of Publications **25**
- 5.1 Consistent analysis of source terms in thermoacoustic systems . . . 25
- 5.2 Consistent inference of global flame transfer functions from experimental pressure measurements . . . 28
- 5.3 Comprehensive thermoacoustic jump conditions . . . 30
- 5.4 Coherent solution strategies for the thermoacoustic eigenvalue problems . . . 32

6 Outlook **37**

7 Summary of Papers **43**
- 7.1 An Arbitrary Lagrangian-Eulerian framework for the consistent analysis of entropy wave generation . . . 43
- 7.2 Model-based inference of flame transfer matrices from acoustic measurements in an aero-engine test rig . . . 45
- 7.3 A Jacobian-based framework for the derivation of comprehensive thermoacoustic jump conditions . . . 47

7.4 The Nonlinear Thermoacoustic Eigenvalue Problem and Its Rational Approximations: Assessment of Solution Strategies 48

Appendix A Modeling errors of $u'_{s,j}$: Spurious generation of disturbances in three-dimensional linearized flows 51
A.1 Convective characteristics 51
A.2 Acoustic perturbations 52

Appendix B On the derivation of comprehensive jump conditions of junctions 55
B.1 The flow split – a 1-N-junction 55
B.2 The flow merge – a N-1-junction 56

Appendix C Towards relaxing the assumption of compactness for jump conditions of premixed flames 59
C.1 A non-compact premixed flame with an infinitely thin flame front 59
C.2 A non-compact flame sheet 61

Appendix D Reproduction of peer-reviewed publications 63
D.1 PAPER-ALE 63
D.2 PAPER-MBI 74
D.3 PAPER-JUMP 85
D.4 PAPER-NLEVP 102

Nomenclature

Latin Characters

A	$[\mathrm{m}^2]$	cross-section
$\mathbf{A}$		operator matrix (NLEVP)
$\mathbf{B}$		burner transfer matrix
c	$[\frac{\mathrm{m}}{\mathrm{s}}]$	speed of sound
c_p	$[\frac{\mathrm{J}}{\mathrm{kg\,K}}]$	specific heat capacity at constent pressure
c_v	$[\frac{\mathrm{J}}{\mathrm{kg\,K}}]$	specific heat capacity at constent volume
$\mathfrak{c}$		compositional inhomogenity (characteristic)
$\mathbf{C}$		combustor transfer matrix
e	$[\frac{\mathrm{J}}{\mathrm{kg}}]$	sensible non-chemical internal energy
E	$[\frac{\mathrm{J}}{\mathrm{kg}}]$	total non-chemical internal energy
$\mathscr{E}$	$[\frac{\mathrm{J}}{\mathrm{m}^3}]$	perturbation energy
f	$[\mathrm{Hz}]$	frequency
$\mathscr{F}$	$[-]$	flame transfer function
$\mathbf{F}$		flame transfer matrix
g	$[\frac{\mathrm{J}}{\mathrm{kg}}]$	sensible non-chemical Gibbs' free enthalpy
h	$[\frac{\mathrm{J}}{\mathrm{kg}}]$	sensible non-chemical enthalpy
$\mathbf{H}$		filter matrix
He	$[-]$	Helmholtz number
Δh^0	$[\frac{\mathrm{J}}{\mathrm{kg}}]$	enthalpy of formation
I	$[\mathrm{cd}]$	chemiluminescence intensity
$\mathbf{J}$		Jacobian
$\mathbf{K}$		operator matrix (NLEVP)
$\mathscr{L}$		linear operator
M		Mach number
$\mathbf{M}$		operator matrix (NLEVP)
n	$[-]$	normal vector
$\mathscr{N}$		nonlinear operator (NLEVP)

N_a	$[-]$	algebraic multiplicity
N_g	$[-]$	geometric multiplicity
N_Y	$[-]$	number of species
p	$[\mathsf{Pa}]$	pressure
$\mathscr{Q}$	$[-]$	spatial distribution of distributed flame transfer function
$\mathbf{Q}$		operator matrix (source terms, NLEVP)
R	$[\frac{\mathsf{J}}{\mathsf{kg}\,\mathsf{K}}]$	specific gas constant
$\mathscr{R}$		rational operator (REVP)
s	$[\frac{\mathsf{J}}{\mathsf{kg}\,\mathsf{K}}]$	entropy
s	$[\frac{1}{\mathsf{s}}]$	Laplace-variable
$\mathfrak{s}$		entropic inhomogenity (characteristic)
$\mathbf{S}$		scattering matrix
St	$[-]$	Strouhal number
T	$[\mathsf{K}]$	temperature
$\mathbf{T}$		transfer matrix
u	$[\frac{\mathsf{m}}{\mathsf{s}}]$	material velocity
u_s	$[\frac{\mathsf{m}}{\mathsf{s}}]$	mesh velocity
$\mathbf{U}$		state vector
$\mathbf{v}$		eigenvector
$\mathfrak{v}$		vortical disturbance (characteristic)
V	$[\mathsf{m}^3]$	volume
V_D	$[\frac{\mathsf{m}}{\mathsf{s}}]$	diffusion velocity
$\mathbf{w}$		vector of characteristics
W		flux
x	$[\mathsf{m}]$	spatial coordinate (Eulerian reference frame)
X	$[\mathsf{m}]$	spatial coordinate (Lagrangian reference frame)
Y	$[-]$	species mass fraction
$\mathbf{Z}$		operator matrix (boundary conditions, NLEVP)

Greek Characters

ϵ		error
ζ		diffusive flux
λ	$[\frac{\mathsf{W}}{\mathsf{m}\,\mathsf{K}}]$	heat conductivity
τ	$[\frac{\mathsf{N}}{\mathsf{m}^2}]$	viscous stress tensor
Π		acoustic wave (characteristic)
ρ	$[\frac{\mathsf{kg}}{\mathsf{m}^3}]$	mass density
σ	$[\frac{1}{\mathsf{s}}]$	growth rate

χ	[m]	spatial coordinate (ALE reference frame)
ψ		arbitrary physical quantity
ω	$[\frac{1}{\mathrm{s}}]$	angular frequency
$\dot{\omega}$		source term
Ω	$[\frac{\mathrm{m}}{\mathrm{s}}]$	vorticity
$\dot{\Omega}$		integral source term

Operators

$\frac{\partial}{\partial t}\Big\|_{\mathrm{x}}$	time derivative at constant x
$\frac{\partial}{\partial t}\Big\|_{\mathrm{X}}$	time derivative at constant X
$\frac{\partial}{\partial t}\Big\|_{\chi}$	time derivative at constant χ
$\det(\cdot)$	determinant
$\int_{\Omega}$	integration over the domain Ω
$\mathcal{O}$	order of magnitude
!	factorial

Superscripts

$\overline{(\cdot)}$	steady mean
$(\cdot)'$	perturbation (time domain)
$\hat{(\cdot)}$	perturbation (frequency domain)
$\breve{(\cdot)}$	perturbation within the ALE framework
$\widetilde{(\cdot)}'$	approximation

Subscripts

$(\cdot)_{\mathrm{ac}}$	acoustic
$(\cdot)_{\mathrm{c}}$	compact
$(\cdot)_{\mathrm{ch}}$	corresponding to a characteristic
$(\cdot)_{\mathrm{conv}}$	convective
$(\cdot)_{\mathfrak{c}_k}$	corresponding to compositional inhomogeneities k
$(\cdot)_{\mathrm{d}}$	downstream
$(\cdot)_{\epsilon}$	spurious
$(\cdot)_{\mathrm{ene}}$	corresponding to the energy balance equation
$(\cdot)_{\mathscr{E}}$	corresponding to the perturbation energy
$(\cdot)_{\mathrm{nc}}$	non-compact
$(\cdot)_{\mathrm{mom}}$	corresponding to the momentum balance equation

$(\cdot)_\mathrm{p}$	products
$(\cdot)_\mathrm{r}$	reactants
$(\cdot)_\mathfrak{s}$	corresponding to entropic inhomogeneities
$(\cdot)_\mathrm{spec}$	corresponding to the species balance equation
$(\cdot)_\mathrm{u}$	upstream

Abbreviations

ALE	Arbitrary Lagrangian-Eulerian
APE	Acoustic Perturbation Equations
BFTM	Burner-Flame Transfer Matrix
CFD	Computational Fluid Dynamics
DTD	Distributed Time Delay
FTF	Flame Transfer Function
ITA	Intrinsic Thermoacoustic
LEE	Linearized Euler Equations
LEVP	Linear Eigenvalue Problem
LNSE	Linearized Navier-Stokes Equations
LRF	Linearized Reactive Flow
MBI	Model-Based Inference
NLEVP	Nonlinear Eigenvalue Problem
REVP	Rational Eigenvalue Problem
RQL	Rich-Quench-Lean
SCARLET	Scaled Acoustic Rig for Low Emission Technology

1 Introduction

The emission of greenhouse gases is the primary driver of anthropogenic climate change, causing, among other things, a rise in average global temperature (≈1.1 °C above 1850-1900 in 2011-2020, see Fig. 1.1), worldwide changes in many weather and climate extremes and negative impacts on food and water security as well as human health [120]. To limit these risks, 195 countries committed to joined efforts of limiting global warming to 1.5 °C but at least well below 2.0 °C above preindustrial levels [238]. In pursuit of this target, the committed countries aim for a reduction in greenhouse gas emissions, eventually reaching greenhouse gas neutrality (e.g. Germany by 2045 [97], European Union [233] and the United States of America [234] by 2050, China before 2060 [98] and India by 2070 [96]).

Today, the dominant contribution to worldwide greenhouse gas emissions results from fossil fuel combustion [120], accounting for almost 80 % of the worldwide total energy supply [183]. To reduce fossil fuel consumption, generating electricity from renewable sources (mainly wind and solar) combined with increased electrification[1] of end-users in industry and transportation is essential in the transition to a decarbonized future [183]. Until 2050, the global electricity demand is projected to increase by at least 80 % with an increasing share in the worldwide energy consumption from approximately 20 % today to 30 – 50 % [183]. However, a major challenge in deploying large shares of renewable energy sources in the overall power generation is their natural intermittency and uncertainty [8, 141].

Gas turbines, with their high operational flexibility [45, 78, 191] and comparably low green-

[1] Electrification may include direct electrification or the use of hydrogen using electrolyzers.

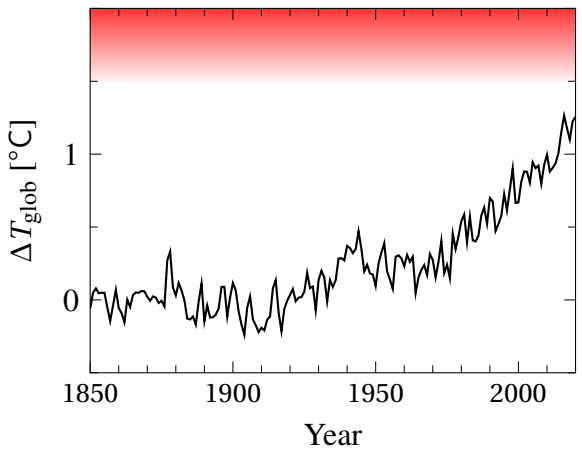

Figure 1.1: Change in global surface temperature T_{glob} relative to 1850-1900 (Dataset from [121, 128, 237]). The red shaded area indicates temperature levels above the 1.5 °C limit agreed on in the Paris agreement [238].

house gas emissions compared to coal-fired plants [61], are essential to counterbalance these issues during the transition to fully renewable power generation and maybe beyond that point if powered with synthetic fuels produced from renewable energies [78, 100]. Besides the application in power generation, gas turbines in aero engines are expected to remain the dominant propulsion system in short[2], medium[3] and long-haul[4] aircraft throughout the following decades, utilizing Sustainable Aviation Fuels or hydrogen (H_2) as a propellant [7]. Full electrification will most likely remain restricted to commuter[5] and regional[6] air transport due to the comparably low power densities of batteries (today) [7]. The continuous development of gas turbine technology to increase efficiency and fuel flexibility while simultaneously reducing emissions thus contributes to the transition to carbon-neutral power generation and air transportation.

Gas turbines burning hydrocarbon fuels emit greenhouse gases and pollutants such as carbondioxide (CO_2), carbonmonoxid (CO), nitrogen oxides (NO_x), unburned hydrocarbons, and soot, which may contribute to climate change and/or have other detrimental effects on the environment and human health [139, 151]. While the CO_2 emissions solely depend on the type and amount of burned fuel, the formation of CO, NO_x, unburned hydrocarbons, and soot are significantly impacted by the combustion process [139, 151]. Over the last decades, numerous industrialized countries implemented increasingly restrictive emission regulations of pollutants and greenhouse gases for stationary gas turbines [139] and aero engines [151]. Regulatory limits particularly focused on NO_x emissions [139, 151], which contribute to the formation/depletion of ozone in the troposphere/stratosphere and other detrimental environmental effects such as acid rain [151]. Lean premixed combustion has been established for stationary gas turbines to meet the strict NO_x emission limits by reducing overall gas temperatures [52]. Simultaneously, emissions of CO, unburned hydrocarbons and soot can be minimized while keeping NO_x emissions low by avoiding fuel-rich mixtures and enabling longer residence times in the combustor [151]. Future aero engines may also require moving away from RQL (Rich-Quench-Lean) systems towards lean premixed injection technologies to further decrease fuel consumption and NO_x emissions [151].

1.1 Thermoacoustic instabilities in gas turbines

A major issue - lean premixed combustion systems are designed to operate close to the lean blowout condition to decrease NO_x emissions, where the combustion process becomes more sensitive to perturbations and tends to become unstable [52, 148, 225, 250]. So-called self-excited thermoacoustic instabilities[7] may establish. Thermoacoustic instabilities result from a complex coupling between unsteady heat release fluctuations in the flame region and the acoustics of the system including possible additional contributions of unsteady vortical, entropic or mixture perturbations. This coupling may establish a positive feedback loop inducing large pressure oscillations, which can limit the gas turbine's operational range, degrade its performance,

[2] short haul: 100-150 seats, 45-120 min flights [7]
[3] medium haul: 150-250 seats, 60-150 min flights [7]
[4] long haul: > 250 seats, > 150 min flights [7]
[5] commuter: 9 – 19 seats, < 60 min flights [7]
[6] regional: 50 – 100 seats, 30 – 90 min flights [7]
[7] Also referred to as "combustion instabilities" or "combustion dynamics".

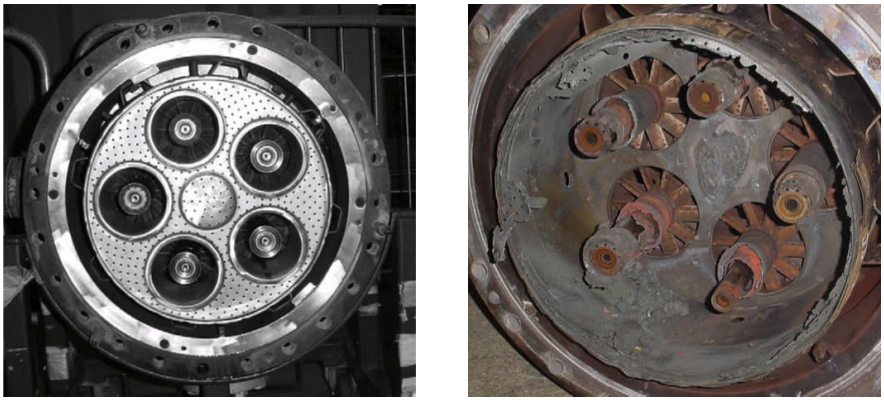

Figure 1.2: Burner assembly of a gas turbine combustor (left) new and (right) damaged by thermoacoustic instabilities. (Goy *et al.*. [99] (original, Copyright © 2005 by E.ON UK and republished in this work with permission) and Huang and Yang [118] (reproduction with improved quality))

increase emissions, promote mechanical fatigue and may even result in catastrophic failure of the combustor [147, 194]. Fig. 1.2 illustrates an example of the detrimental effects thermoacoustic instabilities may have on the gas turbine combustor. Thus, thermoacoustic instabilities must be avoided at all costs during the operation of a gas turbine and are an essential part of combustion research [194].

Note that switching fuel from hydrocarbons to carbon-free alternatives such as hydrogen to eliminate CO_2 emissions significantly impacts the combustion process within the combustor. However, the susceptibility to thermoacoustic instabilities remains and may even increase [3, 6, 47, 149].

The research on thermoacoustic instabilities may be subdivided in three fields:

1. *Understanding the various feedback loops and the contributing physical mechanisms.*

   Starting from the first description of thermoacoustic instabilities by Lord Rayleigh [202] in the 1870's, researchers investigate the underlying physical mechanisms that can contribute to various thermoacoustic feedback loops in different combustors or under different operating conditions. Examples are contributions of indirect sound sources emitted by accelerated vortical perturbations [116, 117, 137], hot spots[8] [41, 55, 57, 80, 155] and mixture inhomogeneities [119, 153, 154], e.g. in the area contraction downstream of a combustion chamber, intrinsic thermoacoustic feedback loops [29, 75, 110], clusters of eigenmodes in annular and can-annular combustors [84, 85, 241, 242], the dynamics and sensitivities of autoignition flames in reheat combustors [31, 86, 87, 220, 258], high-frequency dynamics of transverse modes [170, 259], or the effect of preferential diffusion in hydrogen-fuel blends [71]. Still today, not all effects are perfectly understood due to the complexity and variety of possible thermoacoustic feedback loops and the research on fundamental mechanisms continues.

[8] Also referred to as "entropy waves" or entropic inhomogeneities

2. *Modeling the various feedback loops to accurately and efficiently predict thermoacoustic instabilities.*

   Detecting thermoacoustic instabilities that require design chances late in the design process of gas turbine combustors, e.g. during full-scale engine testing, is very expensive and time-consuming. Therefore, analytical and numerical models of different complexity may be used to assist throughout all development stages of gas turbine combustors, increasing the likelihood of earlier detection of instabilities. Today, a variety of models and prediction tools for the different design stages exist, ranging from numerically inexpensive network models [28, 64, 70, 76, 131, 165, 186, 214, 218] to accurate but numerically expensive high-fidelity simulations [6, 31, 71, 247, 248]. Modeling assumptions to increase efficiency may be chosen based on the knowledge of essential physical mechanisms in the system at hand. Research continues to further increase the reliability, accuracy and efficiency of prediction tools.

3. *Techniques to mitigate thermoacoustic intabilities.*

   Mitigation techniques build on the experimental observation or the numerical/analytical prediction of thermoacoustic instabilities. Various active [12, 13, 157, 196, 214, 263] and passive control methods [56, 205, 245, 246, 249, 262] exist and are continuously developed. Passive control methods detune the combustor by introducing passive dampers such as Helmholtz resonators or by changing the geometry of the combustor. Active control methods actively detune the combustion system during operation, e.g. by changing the fuel mass flow or emitting additional sound via loudspeakers for active noise canceling.

1.2 The scope of this thesis

An accurate understanding, modeling and prediction of thermoacoustic instabilities during their onset is essential for their efficient mitigation and a crucial part of thermoacoustic research. During the onset of thermoacoustic instabilities, the amplitudes of perturbations in gas turbine combustors are typically small before growing exponentially and saturating at a finite amplitude. To predict this onset of instability, the assumption of small perturbation amplitudes can be used to significantly simplify the underlying balance equations for reactive flows, reducing the numerical effort of the resulting methods significantly compared to full-scale high-fidelity simulations. The approaches based on this small amplitude assumption are called *linearized thermoacoustic models*. These models are widely used for various tasks in all three pillars of thermoacoustic research. This thesis focuses on the development and analysis of linear models within the first two pillars - understanding and modeling/prediction.

In thermoacoustic research, models to analyze or predict thermoacoustic phenomena are typically developed focusing on a specific application case. Simplifications, such as the neglect of certain physical effects, simplified gas properties, or other approximations, are introduced to simplify the corresponding derivation or streamline the corresponding computations. While the derived models are suited for the specific application case at hand, their applicability to other applications is, in most cases, strongly limited by the introduction of simplification a priori or during the derivation. The models must be rederived for scenarios that deviate significantly from the original application case. The goal of this thesis is to develop linear methods and frameworks

that are *comprehensive* and *consistent*, making them applicable to a wide range of thermoacoustic systems. Rather than focusing on specific application cases, a priori assumptions are minimized. Application-specific optimizations to increase efficiency may be introduced a posteriori, rendering the derived models highly flexible. Overall, this thesis aims to add to a basis of consistent and comprehensive methodologies to accelerate future research and the development of gas turbine combustors.

This thesis is organized as follows. Chapter 2 recalls the fundamental governing equations for general three-dimensional reactive flows and their linearization in different reference frames. Chapter 3 revisits state-of-the-art hybrid linearized thermoacoustic models. Chapter 4 details the resulting thermoacoustic eigenvalue problem from which the stability of an thermoacoustic system may be assessed. Chapter 5 puts the papers that contributed to this thesis in perspective with literature. Finally, an outlook is given in Chapter 6.

2 Governing equations

This chapter reviews the differential balance equations of three-dimensional reactive flows and their simplification under the small amplitude assumption. The characteristic perturbations propagating in such flows are discussed. Additionally, mathematical tools for a change in reference system and the transformation from time to frequency domain are outlined.

2.1 Reference frames

The governing equations of reacting flows may be expressed using one of three distinct reference frames [62]. Depending on the application, each may offer some advantages:

- The *Lagrangian reference frame* X tracks individual material particles during motion. In the context of combustion, the Lagrangian perspective is predominantly used to model and track evaporating droplets in fuel sprays, e.g. [2, 92, 138, 142, 236].
- The *Eulerian reference frame* x describes the flow properties at a fixed point in space. The Eulerian perspective is the standard approach for the formulation and numerical computation of fluid flow problems and has been extensively used in the context of combustion, e.g., [31, 71, 138, 247, 248, 257].
- The *Arbitrary Lagrangian-Eulerian (ALE) reference frame* χ represents a moving reference frame that does not track the material particles but another user-defined quantity. It is well suited to track free surfaces and interfaces, e.g. between different materials or media [62]. The ALE method is, for example, used in the KIVA family [10, 11, 235] of computational fluid dynamic solvers for complex fuel and air flows, ignition, combustion, and pollution formation. Furthermore, the ALE framework has been used in the context of thermoacoustic instabilities to track the displacement of a perturbed flame front or another moving source region to understand and model the underlying physical mechanisms [105, 168, 259].

Mathematically, the coordinate transform between the different reference frames is represented by correcting the temporal derivatives when expressed in fixed spatial coordinates $\mathbf{x}$ [62],

$$\underbrace{\left.\frac{\partial \psi}{\partial t}\right|_{\mathrm{x}}}_{\text{Eulerian}} = \underbrace{\left.\frac{\partial \psi}{\partial t}\right|_{\chi} - u_{\mathrm{s},j}\frac{\partial \psi}{\partial x_j}}_{\text{ALE}} = \underbrace{\left.\frac{\partial \psi}{\partial t}\right|_{\mathrm{X}} - u_j\frac{\partial \psi}{\partial x_j}}_{\text{Lagrangian}}, \tag{2.1}$$

where

$$u_j = \left.\frac{\partial x_j}{\partial t}\right|_{\mathrm{X}} \quad \text{and} \quad u_{\mathrm{s},j} = \left.\frac{\partial x_j}{\partial t}\right|_{\chi} \tag{2.2}$$

are the material velocity (temporal derivative at constant X) and the mesh velocity (temporal derivative at constant χ) of the ALE framework, with respect to a spatially fixed observer, respectively.

2.2 The reactive flow equations

The balance equations of mass, momentum, energy and species provide the basis for the mathematical description of three-dimensional reactive flows. Utilizing the Eulerian framework and Einstein's summation convention[1], the reactive flow equations read [195]

$$\frac{\partial}{\partial t}\begin{bmatrix}\rho\\ \rho u_i\\ \rho E\\ \rho Y_k\end{bmatrix}_{\mathrm{x}} + \frac{\partial}{\partial x_j}\begin{bmatrix}\rho u_j\\ \rho u_j u_i\\ \rho u_j E\\ \rho u_j Y_k\end{bmatrix} = -\frac{\partial}{\partial x_j}\begin{bmatrix}0\\ p\\ p u_i\\ 0\end{bmatrix}\delta_{ij} + \frac{\partial}{\partial x_j}\begin{bmatrix}0\\ \zeta_{\mathrm{mom},ij}\\ \zeta_{\mathrm{ene},j}\\ \zeta_{\mathrm{spec},j}\end{bmatrix} + \begin{bmatrix}0\\ 0\\ \dot{\omega}_{\mathrm{T}}\\ \dot{\omega}_k\end{bmatrix} \tag{2.3}$$

with density ρ, pressure p, the species mass fraction Y_k of species k, the heat release rate $\dot{\omega}_{\mathrm{T}}$ and the species reaction rates $\dot{\omega}_k$. $E = e + \frac{1}{2}u_l u_l$ and e are the total and sensible non-chemical internal energy, respectively. Due to mass conservation,

$$\sum_{k=1}^{N_{\mathrm{Y}}} Y_k = 1\,, \tag{2.4}$$

only $N_{\mathrm{Y}} - 1$ species need to be balanced. The diffusive terms

$$\begin{bmatrix}0\\ \zeta_{\mathrm{mom},ij}\\ \zeta_{\mathrm{ene},j}\\ \zeta_{\mathrm{spec},j}\end{bmatrix} = \begin{bmatrix}0\\ \tau_{ij}\\ \tau_{ij}u_i\\ 0\end{bmatrix} + \begin{bmatrix}0\\ 0\\ \lambda\frac{\partial T}{\partial x_j}\\ 0\end{bmatrix} - \begin{bmatrix}0\\ 0\\ \rho V_{\mathrm{D}_k,j} Y_k h_k\\ \rho V_{\mathrm{D}_k,j} Y_k\end{bmatrix} \tag{2.5}$$

may be separated into viscous effects related to the viscous stress tensor τ_{ij}, thermal diffusion effects formulated in terms of Fourier's law with the isotropic thermal conductivity λ and the effects of species diffusion with an effective diffusion velocity $V_{\mathrm{D}_k,j}$ of species k. T is the temperature and h is the sensible non-chemical enthalpy. In the context of combustion, the stress tensor is typically used assuming a Newtonian fluid combined with Stoke's hypothesis [20],

$$\tau_{ij} = \mu\left(\frac{\partial u_i}{\partial x_j} + \frac{\partial u_j}{\partial x_i}\right) - 2/3\mu\frac{\partial u_l}{\partial x_l}\delta_{ij}\,. \tag{2.6}$$

μ is the dynamic viscosity. The determination of the diffusion velocity $V_{k,j}$ depends on the diffusion model used, e.g. Fick's law [81] or the Hirschfelder and Curtiss approximation [109]. The species' reaction rates $\dot{\omega}_k$ are typically expressed in terms of the thermal state variables (p,T,ρ) and the gas composition [195]. The heat release rate of chemical reactions

$$\dot{\omega}_{\mathrm{T}} = \Delta h_k^0 \dot{\omega}_k \tag{2.7}$$

[1] In Einstein's summation convention, a product with two repeated indices is summed over,

$$a_i b_i = \sum_i a_i b_i\,.$$

is governed by the species' reaction rates. Δh_k^0 is the enthalpy of formation of species k.

To close Eq. (2.3), a thermal equation of state relating the thermal state variables p, ρ and T as well as a caloric equation of state relating the thermal energy with the sensible internal energy e_s is required. This thesis uses the assumption of a perfect gas mixture with the thermal equation of state

$$p = \rho R T \quad \text{with} \quad R = R_k Y_k \tag{2.8}$$

and the caloric equation of state

$$\mathrm{d}e = c_\mathrm{v}\,\mathrm{d}T + e_k\,\mathrm{d}Y_k\,. \tag{2.9}$$

Instead of Eqs. (2.8) and (2.9), the Gibbs equation for an ideal gas mixture (canonical equation of state)

$$\mathrm{d}e = T\,\mathrm{d}s + \frac{p}{\rho^2}\,\mathrm{d}\rho + g_k\,\mathrm{d}Y_k \tag{2.10}$$

is often used, e.g. [150, 153, 154, 168, 206]. R, s, c_v and g_k are the specific gas constant, entropy, specific heat capacity at constant volume and the sensible non-chemical Gibbs' free enthalpy of species k. Note that the material derivative $\partial/\partial t|_X$ (Lagragian framework) replaces the the total differentials d in Eqs. (2.9) and (2.10) for flow problems.

The equations stated in this section or approximations thereof are solved directly by high-fidelity simulations of reactive flows. Furthermore, the reactive flow equation in an ALE or Lagrangian reference frame can easily derived from the Eulerian framework (Eq. (2.3)) by utilizing Eq. (2.1).

2.3 The linearized reactive flow equations

To isolate unsteady processes in the reactive flow, which may contribute to thermoacoustic instabilities, a Reynolds decomposition [2] [204]

$$\psi(\mathbf{x}, t) = \overline{\psi}(\mathbf{x}) + \psi'(\mathbf{x}, t) \tag{2.11}$$

is typically applied for any physical quantity ψ. Additionally, the unsteady perturbations ψ' are assumed to be much smaller than the underlying steady base variables $\overline{\psi}$ ($\psi'(\mathbf{x}, t) \ll \overline{\psi}(\mathbf{x})$) during the onset of thermoacoustic instabilities. Then, Eq. (2.3) can be separated into two sets of equations, which are solved subsequently. The first set of equations describes the steady base flow fields $\overline{\psi}(\mathbf{x})$ unaffected by small perturbation. This set of equations is analogous to Eq. (2.3) with vanishing time derivatives and is therefore not explicitly stated here. The second set of equations expresses the generation and propagation of small perturbations in the steady base flow fields. Neglecting non-linear perturbation terms ($\mathcal{O}(\psi'\psi') \approx 0$) reveals the Linearized

[2] For many applications, it might be reasonable to further decompose the flow perturbations, e.g. to distinguish between random fluctuations of fine-scale turbulence and coherent flow structures [150]. However, this is beyond the scope of this work.

Reactive Flow (LRF) equations [17],

$$\begin{aligned}\frac{\partial}{\partial t}\begin{bmatrix}\rho'\\ \rho'\overline{u}_i+\overline{\rho}u_i'\\ \rho'\overline{E}+\overline{\rho}E'\\ \rho'\overline{Y}_k+\overline{\rho}\overline{Y}_k\end{bmatrix}_{\mathrm{x}}+\frac{\partial}{\partial x_j}\begin{bmatrix}\rho'\overline{u}_j+\overline{\rho}u_j'\\ \left(\rho'\overline{u}_j+\overline{\rho}u_j'\right)\overline{u}_i+\overline{\rho\,u}_j u_i'\\ \left(\rho'\overline{u}_j+\overline{\rho}u_j'\right)\overline{E}+\overline{\rho\,u}_j E'\\ \left(\rho'\overline{u}_j+\overline{\rho}u_j'\right)\overline{Y}_k+\overline{\rho\,u}_j Y_k'\end{bmatrix}\\ =-\frac{\partial}{\partial x_j}\begin{bmatrix}0\\ p'\\ p'\overline{u}_i+\overline{p}u_i'\\ 0\end{bmatrix}\delta_{ij}+\frac{\partial}{\partial x_j}\begin{bmatrix}0\\ \zeta'_{\mathrm{mom},ij}\\ \zeta'_{\mathrm{ene},j}\\ \zeta'_{\mathrm{spec},j}\end{bmatrix}+\begin{bmatrix}0\\ 0\\ \dot{\omega}'_{\mathrm{T}}\\ \dot{\omega}'_k\end{bmatrix}\end{aligned} \tag{2.12}$$

with the linearized diffusive fluxes

$$\begin{aligned}\begin{bmatrix}0\\ \zeta'_{\mathrm{mom},ij}\\ \zeta'_{\mathrm{ene},j}\\ \zeta'_{\mathrm{spec},j}\end{bmatrix}=\begin{bmatrix}0\\ \tau'_{ij}\\ \tau'_{ij}\overline{u}_i+\overline{\tau}_{ij}u_i'\\ 0\end{bmatrix}+\begin{bmatrix}0\\ 0\\ \lambda'\frac{\partial\overline{T}}{\partial x_j}+\overline{\lambda}\frac{\partial T'}{\partial x_j}\\ 0\end{bmatrix}\\ -\begin{bmatrix}0\\ 0\\ \left(\rho'\overline{V}_{\mathrm{D}_k,j}+\overline{\rho}\overline{V}_{\mathrm{D}_k,j}\right)\overline{Y}_k\overline{h}_k+\overline{\rho}\overline{V}_{\mathrm{D}_k,j}\left(Y_k'\overline{h}_k+\overline{Y}_k h_k'\right)\\ \left(\rho'\overline{V}_{\mathrm{D}_k,j}+\overline{\rho}\overline{V}_{\mathrm{D}_k,j}\right)\overline{Y}_k+\overline{\rho}\overline{V}_{\mathrm{D}_k,j}Y_k'\end{bmatrix}.\end{aligned} \tag{2.13}$$

The linearized thermal (Eq. (2.8)), caloric (Eq, (2.9)) and canonic (Eq. (2.10)) equation of state read

$$\frac{p'}{\overline{p}}=\frac{\rho'}{\overline{\rho}}+\frac{Y_k'}{\overline{Y}_k}+\frac{T'}{\overline{T}}, \tag{2.14}$$

$$e'=\overline{c}_{\mathrm{v}}T'+\overline{e}_k Y_k' \tag{2.15}$$

and

$$e'=\overline{T}s'+\frac{\overline{p}}{\overline{\rho}^2}\rho'+\overline{g}_k Y_k'. \tag{2.16}$$

All other constitutive equations in Sec. 2.2 are linearized accordingly. The interested reader is referred to Avdonin *et al.* [17] and Meindl *et al.* [161] for the complete set of linearized equations. Note that all flow variables as well as material properties, e.g. viscous, thermal and compositional diffusivities, must be linearized to obtain a set of linearized equations that is fully consistent with the original non-linear problem stated in Sec. (2.3) [17].

The LRF equations are linear in the perturbed quantities and consequently less expensive to solve numerically than the non-linear system of reactive flow equations (2.3). Furthermore, the LRF equations within an ALE or Lagrangian reference frame can be derived analogously to the formulation in the Eulerian reference frame (Eq. (2.12)) by starting the linearization procedure from the reactive flow equations in the corresponding reference frame.

		acoustic Π^+/Π^-	vortical $\mathfrak{v}_j$	entropic $\mathfrak{s}$	compositional $\mathfrak{c}_k$
Pressure	p'	✓	-	-	-
Vorticity	Ω'_j	-	✓	-	-
Entropy	s'	-	-	✓	-
Mass fraction	Y'_k	-	-	-	✓
Velocity	u'_j	✓	✓	-	-
Density	ρ'	✓	-	✓	✓
Temperature	T'	✓	-	✓	✓

Table 2.1: Impact of acoustic waves, vortical perturbations, entropic inhomogenities [50, 150] and compositional inhomogenities on various primitive flow variables.

2.4 Characteristic flow decomposition

In the absence of chemical reactions and diffusive effects as well as assuming a uniform base flow field, the LRF equations 2.12 can be decomposed into four types of non-interacting perturbations – namely acoustic waves, vortical perturbations as well as entropic and compositional inhomogeneities [50, 119, 150, 153]. The decomposition in these four types of canonical perturbations is highly illustrative for understanding the spatiotemporal dynamics in a combustor possibly contributing to thermoacoustic instabilities. Diffusive effects, chemical reactions or other flow non-uniformities in the LRF equations (2.12) can be understood as generation, destruction and conversion mechanisms of these canonic perturbations.

Acoustic waves Π^+/Π^- are isentropic, irrotational and isochemical perturbations propagating with the speed of sound superposed on the base flow velocity, $\overline{c}+\overline{u}_j$. In subsonic flows, acoustic waves are the only type of perturbation able to travel upstream and are, therefore, essential for closing a thermoacoustic feedback loop. In contrast, vortical perturbations $\mathfrak{v}_j$ as well as entropic $\mathfrak{s}$ and compositional $\mathfrak{c}_k$ inhomogeneities are convected with the mean flow velocity $\overline{u}_j$ and, thus, are only able to propagate downstream. Vortical perturbations are incompressible, isentropic and isochemical. Entropic inhomogeneities are incompressible, irrotational and isochemical, whereas compositional waves are incompressible, isentropic, and irrotational.

Table 2.1 provides an overview of primitive variables affected by these canonical perturbations. For small perturbations, p' is a purely acoustic perturbation. Disturbances of vorticity, entropy and composition are exclusive to vortical, entropic and compositional disturbances, respectively. Density, temperature and velocity perturbations are affected by more than one perturbation type.

Note that while the decomposition in vortical, entropic and compositional perturbation as detailed in this section and Tab. 2.1 is common, it is not unique [50, 150] for the convected perturbations. In thermoacoustics, non-acoustic temperature fluctuations are sometimes used as perturbation types instead of entropic disturbances. The corresponding canonic perturbation related to changes in composition would be isobaric, irrotational and isothermal.

2.5 Transformation to the Laplace Domain

For many investigations of thermoacoustic systems, an analysis in frequency space is required or advantageous over the time domain formulation. To obtain the frequency space representation of the LRF equations, Eq. (2.12) is projected onto a harmonic time dependency via the Laplace transform,

$$\hat{\psi}(\mathbf{x}, s) = \int_0^\infty \psi'(\mathbf{x}, t) e^{-st} \, \mathrm{d}t \,. \tag{2.17}$$

The angular frequency ω and the growth rate σ of the corresponding harmonic time dependency are encoded in the Laplace variable

$$s = \sigma + i\omega \,. \tag{2.18}$$

The Laplace transform replaces the temporal derivative in the LRF equation (2.12) by a multiplication with the Laplace variable s,

$$\left.\frac{\partial \psi'(\mathbf{x}, t)}{\partial t}\right|_{\mathrm{x}} \Rightarrow s\hat{\psi}(\mathbf{x}, s) \,. \tag{2.19}$$

In numerical simulations, this removes the necessity for a time-stepping procedure and the corresponding constraints on the numerical time step. Consequently, the frequency space formulation offers a computationally cheaper way to perform, e.g. a (frequencywise) input-output analysis to determine transfer matrices (Sec. 3.2) or transfer functions (Sec. 3.3). Furthermore, the frequency space formulation is required to perform a linear stability analysis for a thermoacoustic system (see Sec. 4).

In addition to the classical Eulerian formulation, this thesis uses the LRF equations expressed in an ALE reference frame. In a general ALE reference frame, spatially varying Doppler shifts originating from the local mesh velocity $u_{\mathrm{s},j}$ appear and the frequency space formulations of the two reference frames would not be comparable. However, the mesh velocity of the ALE framework is limited to small movements ($\overline{u_{\mathrm{s},j}} = 0$, $u_{\mathrm{s},j} = u'_{\mathrm{s},j}$) in this work. The mesh velocity is consequently much smaller than the propagation velocities of the acoustic and convective perturbations. The Doppler shift appears as a second-order effect under these assumptions and can be neglected.

3 Hybrid linearized thermoacoustic models

Thermoacoustic phenomena pose a multi-scale problem with physical mechanisms acting on very different time and length scales. These range from thin flame fronts ($\mathcal{O}(10^{-4}\mathrm{m})$) with intricate chemical and diffusive mechanisms to large-scale acoustic waves ($\mathcal{O}(10^{0}\mathrm{m})$) propagating relatively fast with the speed of sound augmented by the mean flow velocity [158, 195]. This is challenging for monolithic numerical simulations such as high-fidelity CFD simulations or solving the LRF equations since the accurate computation of reactive and diffusive processes in the flame front requires a high spatial resolution, restricting the local mesh size. Combined with the strong non-linearity of the chemical reaction rates, this results in a stiff numerical problem [158, 195]. For time-domain simulations, the time step is additionally restricted due to the combination of small local cell sizes and the high propagation velocity of acoustic waves [158, 195].

Hybrid linearized thermoacoustic modeling approaches leverage the disparity in scales to separate the large-scale acoustic from the small-scale chemical processes. Instead of explicitly resolving the perturbed chemical processes, the perturbed heat release rate $\dot{\omega}'_{\mathrm{T}}$ resulting from flow-flame interactions is modeled externally. The onset of thermoacoustic instabilities is subsequently assessed by evaluating the propagation and generation of acoustic waves (and potentially other convective perturbations) utilizing the external model of $\dot{\omega}'_{\mathrm{T}}$. In this work, linearized thermoacoustic models that require linearized perturbations such as the perturbed heat release rate $\dot{\omega}'_{\mathrm{T}}$ as an external input are denoted as *hybrid*. In contrast, linearized models such as the LRF equations (Sec. 2.3) resolve all linearized perturbations internally and are referred to as *monolithic*. However, note that all linearized methods require steady base flow fields as an input and thus are not standalone approaches for thermoacoustic stability analysis.

3.1 Spatially resolved three-dimensional hybrid models

A variety of hybrid linearized models for three-dimensional thermoacoustic problems exist conceptually. All these models may be derived by introducing additional assumptions into the most general linear system of equations, the LRF equations (2.12). Note that introducing additional assumptions typically reduces the numerical effort in solving the corresponding system of equations while the accuracy of the computed results decreases simultaneously. Listed with increasing simplifications, the most common hybrid linearized thermoacoustic models for three-dimensional problems are:

- The *Linearized Navier-Stokes equations* (LNSE), e.g. [92, 93, 134–136, 160], omit the

species balance equations and the reaction mechanism. Neglecting the $N_Y - 1$ species balance equations significantly reduces the number of degrees of freedom (DOF) of the discretized LNSE compared to the discretized LRF equations. For example, neglecting the four species balance equations of a simple 2-step reaction mechanism such as the 2S-CM2 [24, 161] in a three-dimensional problem reduces the DOF by 44 %. Additionally, dropping the chemical reaction mechanism reduces the stiffness of the linear system of equations. On the downside, compositional inhomogeneities are no longer explicitly resolved, but their effect on the perturbed heat release rate $\dot{\omega}'_{\mathrm{T}}$ may be modeled by the external input.

- The *Linearized Euler Equations* (LEE), e.g. [105, 111, 112, 221], are obtained by additionally neglecting diffusive effects ($\tau = 0$, $\lambda = 0$, $V_k = 0$). In regions with significant diffusive effects, e.g. propagation-stabilized flames or shear/boundary layers, a coarser mesh can be used since these effects are neglected and consequently do not need to be resolved. However, neglecting diffusive effects omits the damping of convective waves as well as acoustic-convective dissipation mechanisms such as acoustic-vorticity dissipation. Furthermore, note that besides the accuracy decrease resulting from the neglect of diffusive effects, spurious perturbations, e.g. spurious vortical perturbations in boundary layers [135, 159], may be generated by inconsistencies between the LEE and the corresponding base flow field if the latter retains viscous effects. This is the case in many technically relevant combustion applications in which the diffusive effects play a prominent role in the flame stabilization.

- The *Acoustic Perturbation Equations* (APE) [36, 77] are obtained by filtering the LEE or LNSE to retain only the acoustic wave propagation in arbitrary complex mean flow fields. The interaction of the resolved acoustic waves with vortical or entropic perturbations may be introduced as an external input (modeled or from high-fidelity simulation) or is neglected altogether. A coarser mesh may be used since the short convective perturbations are not explicitly resolved [104]. This comes at the cost of a complex modeling of the acoustic-convective interaction terms or an additional reduction in accuracy if neglected [104].

- The classical *acoustic wave equation* (time-domain) or *Helmholtz equation* (frequency domain), e.g. [93, 166, 167, 182], is obtained from the LEE[1] by assuming a stagnant fluid ($\overline{u}_j = 0$) and neglecting all convective perturbations. Disregarding all convective perturbations omits all acoustic-convective interaction mechanisms and thus discards all acoustic-convective thermoacoustic feedback loops. Additionally, acoustic-convective dissipation mechanism such as acoustic-vorticity dissipation are neglected. Furthermore, mean flow effects are essential in many thermoacoustic systems and crucial for accurately predicting acoustic reflection and transmission coefficients and, therefore, for an accurate stability assessment of the whole system, e.g. [63, 93, 159]. Thus, the assumption of a stagnant fluid should be chosen with great care.

[1] The acoustic wave equation or Helmholtz equation may be alternatively derived from the APE by assuming a stagnant fluid ($\overline{u}_j = 0$) and omitting the acoustic-convective interaction and dissipation terms

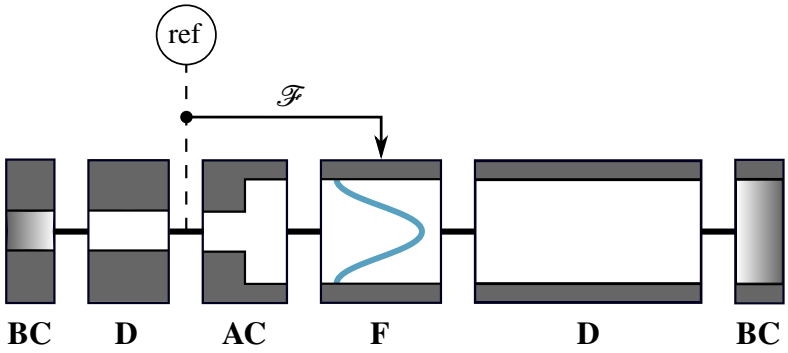

Figure 3.1: Illustrative network model of a ducted slit flame. The model is stacked as a sequence of two compact elements, representing a flame (**F**) and an area change (**AC**), and two non-compact elements, representing ducts (**D**). The flame transfer function $\mathscr{F}$ referenced to the reference point "ref" provides the flow-flame interaction closure (see Sec. 3.3) to the flame element. Boundary conditions (**BC**) at the in- and outlet complete the model.

3.2 Thermoacoustic network models

In contrast to fully resolving a three-dimensional thermoacoustic system with all its complex features, network models lump the thermoacoustic system into independently modeled subsystems and interconnect them via predefined - often quasi-one-dimensional - interfaces. Fig. 3.1 shows an illustrative network model of a ducted slit flame. Each subsystem - a so-called *network element* - is characterized via its transfer matrix **T** or its scattering matrix **S**. Both matrices are lumped representations of the scattering, conversion, generation or destruction of the characteristic perturbations (see Sec. 2.4) within the corresponding element.

The transfer matrix relates the primitive states upstream (index '1') and downstream (index '2') of the element. For example, the transfer matrix of a 2-port system is defined as

$$\begin{bmatrix} u'_2 \\ p'_2 \\ s'_2 \\ Y'_{k,2} \\ (\Omega'_{j,2}) \end{bmatrix} = \mathbf{T} \begin{bmatrix} u'_1 \\ p'_1 \\ s'_1 \\ Y'_{k,1} \\ (\Omega'_{j,1}) \end{bmatrix} \tag{3.1}$$

and is schematically displayed on the right side of Fig. 3.2. Deriving the transfer matrix of an element starting from the fundamental balance equations is straightforward due to the use of primitive variables. However, evaluating the transfer matrix regarding the impact of the corresponding element on the network model is difficult since the primitive variables do not feature a well-defined direction of propagation.

The scattering matrix directly links the characteristic perturbations Π^+/Π^-, $\mathfrak{s}$, $\mathfrak{c}_{k,j}$ and $(\mathfrak{v}_{j,1})^2$

[2]The vortical perturbations are usually neglected in network models assuming quasi-onedimensional interfaces.

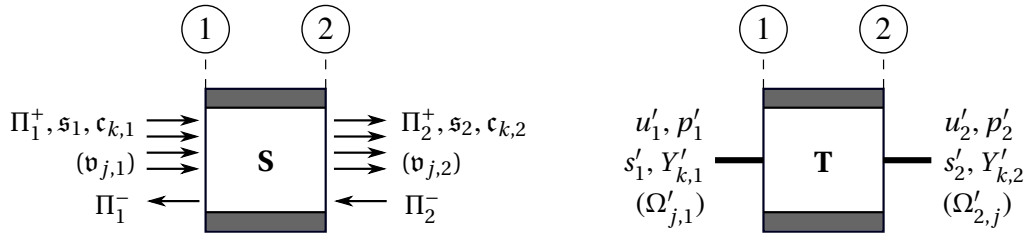

Figure 3.2: Schematic depiction of an exemplary 2-port network element represented in terms of (left) the scattering matrix **S** with the corresponding characteristic input and output disturbances, and (right) the transfer matrix **T** with the upstream and downstream primitive variables.

and is defined as

$$\begin{bmatrix} \Pi_2^+ \\ \Pi_1^- \\ \mathfrak{s}_2 \\ \mathfrak{c}_{k,2} \\ (\mathfrak{v}_{j,2}) \end{bmatrix} = \mathbf{S} \begin{bmatrix} \Pi_1^+ \\ \Pi_2^- \\ \mathfrak{s}_1 \\ \mathfrak{c}_{k,1} \\ (\mathfrak{v}_{j,1}) \end{bmatrix} \tag{3.2}$$

in case of a 2-port system. The left side of Fig. 3.2 illustrates the scattering matrix in this case. Since the direction of propagation of all these characteristic perturbations are well-defined, the scattering matrix offers a useful form for interpreting the internal causality of the element and its impact on a thermoacoustic network model.

The scattering/transfer matrices of the individual subsystems may be determined from experimental measurement data or numerical simulations. Alternatively, analytical or semi-empirical models can be derived from a linearized set of balance equations $\mathscr{L}$, either the full LRF equations (2.12) or any of the simplified models detailed in Sec. 3.1. These models may be classified in acoustically/convectively compact[3] and non-compact elements. Compactness of a subsystem assumes that its spatial extent Δx is much smaller than the shortest wavelength $\lambda_{\min}$ of a characteristic perturbation corresponding to a maximum frequency $f_{\max}$ of interest,

$$\Delta x \ll \lambda_{\min}\,. \tag{3.3}$$

The transfer/scattering matrix of non-compact elements typically results from the analytical solutions of the linearized conservation equations of simple elements such as ducts with or without changes in area and/or temperature [67, 76, 210, 251]. In contrast, compact elements - so-called jump conditions - lump the whole subsystem into a localized discontinuity in the flow variables by analytically approximating the volume integral over the whole subsystem Ω,

$$\int_\Omega \mathscr{L}\,\mathrm{d}\mathbf{x} \longmapsto \mathbf{S}\,\mathrm{or}\,\mathbf{T}\,. \tag{3.4}$$

[3]The assumption of convective compactness is required if convective perturbations such as entropic, vortical or compositional perturbations are included in the derivation of a thermoacoustic jump condition. If only acoustic perturbations are considered, acoustic compactness is sufficient.

In the limit of acoustic/convective compactness, the volume integral in Eq. (3.4) is then evaluated in the limit of a vanishing Helmholtz (acoustically compact case)

$$\mathrm{He} = \frac{\Delta \mathrm{x}}{\lambda} = \frac{\Delta \mathrm{x}}{\overline{c}} f \to 0 \tag{3.5}$$

or Strouhal number (convectively compact case)

$$\mathrm{St} = \frac{\Delta \mathrm{x}}{\lambda} = \frac{\Delta \mathrm{x}}{\overline{u}} f \to 0\,. \tag{3.6}$$

Additional assumptions, such as a reduced order in Mach number, constant gas properties, or a restriction to a subset of characteristic perturbations (see Sec. 2.4) are typically introduced during the derivation of jump conditions to simplify the analytical evaluation of the volume integral [169]. Classical examples of thermoacoustic jump conditions are flames [65, 88, 146, 169, 230], area jumps [65, 69, 103, 219], compact nozzles [59, 60, 153, 155] or junctions [127].

Low-order network modeling, e.g. [28, 64, 70, 76, 131, 165, 186, 218], is a computationally inexpensive technique to describe and predict thermoacoustic phenomena in confined combustion systems with a widespread range of applications. Network models have been proven useful to gain a fundamental understanding of basic phenomena in the dynamics of confined combustion systems, e.g. intrinsic thermoacoustic modes [29, 75, 110] or mode clustering in annular and can-annular combustors [39, 84, 85, 241, 242]. Additionally, network models are exceptionally suited for extensive parameter studies, e.g., in the early design phase of developing a gas turbine combustor, due to the low computational cost. Furthermore, network models may be used in the post-processing of experimental measurements such as for the extraction of the thermoacoustic transfer behavior of the flame, e.g. [253] or PAPER-MBI [74]. Alternatively, network models may be combined with experimental measurement data to infer unknown model parameters to increase the accuracy of model predictions and to provide uncertainty bounds [124, 254].

3.3 Flow-flame interactions

The flow-flame interactions for hybrid linearized thermoacoustic approaches are typically modeled by assuming that the perturbed heat release rate $\dot{\omega}'_{\mathrm{T}}$ results from one or multiple different time-lagged perturbations $\psi'_{\mathrm{ref}}(t-\tau)$ at a reference plane (index $(\cdot)_{\mathrm{ref}}$) with the normal vector $n_{\mathrm{ref},j}$. In the limit of small amplitude perturbations (see Sec. 2.3), this interaction may be modeled in the frequency domain as a Multiple-Input-Single-Output (MISO) system,

$$\frac{\hat{\dot{\omega}}_{\mathrm{T}}(s,\mathbf{x})}{\int_\Omega \overline{\dot{\omega}}_{\mathrm{T}}\,\mathrm{d}\mathbf{x}} = \begin{bmatrix} \mathscr{F}_{\mathrm{u}}(s,\mathbf{x}) & \mathscr{F}_{\mathrm{p}}(s,\mathbf{x}) & \mathscr{F}_{\mathrm{s}}(s,\mathbf{x}) & \mathscr{F}_{\mathrm{Y},k}(s,\mathbf{x}) \end{bmatrix} \begin{bmatrix} \frac{\hat{u}_j\, n_j}{\overline{u}_j\, n_j} \\ \frac{\hat{p}}{\overline{p}} \\ \frac{\hat{s}}{\overline{c}_{\mathrm{p}}} \\ \frac{Y'_k}{\overline{Y}_k} \end{bmatrix}_{\mathrm{ref}}, \tag{3.7}$$

superpositioning the contributions of different linearly independent (see Sec. 2.4) flow perturbations. The flame transfer function (FTF) $\mathscr{F}_\psi$ determines the gain and phase relation between $\dot{\omega}'_{\mathrm{T}}$ and an perturbed quantity ψ'. Depending on the flame type, a flame may be sensitive to all

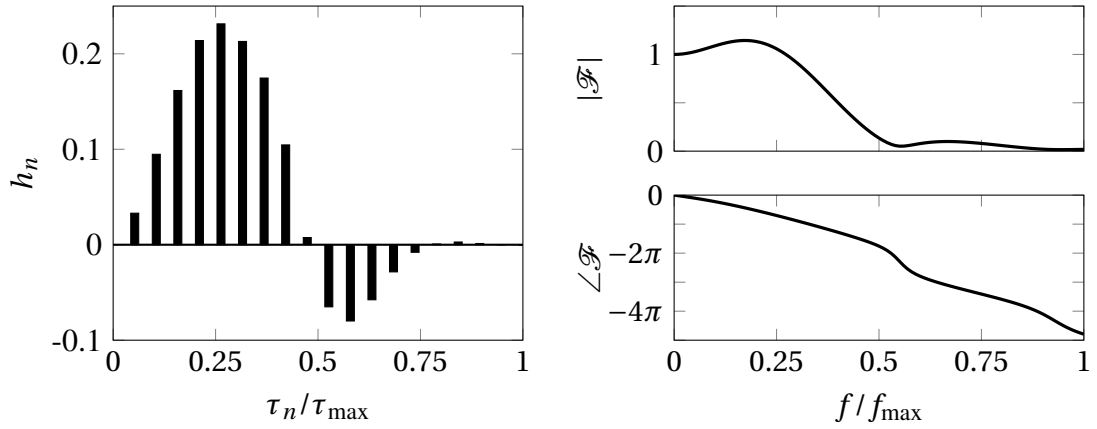

Figure 3.3: Flame response data in the form of (left) the *unit impulse response* and (right) the bode plot of the corresponding FTF $\mathscr{F}(s)$ evaluated for zero growth rate ($\mathrm{Re}(s) = \sigma = 0$).

flow perturbations u', p', s' and Y_k', e.g. autoignition flames [31, 86, 169, 258], or only to a subset thereof. In general, the FTFs $\mathscr{F}(s,\mathbf{x})$ in Eq. (3.7) are functions of frequency and space. However, it is impractical to determine spatially resolved FTFs for each frequency for most application cases. Thus, only the global dynamics of the flow-flame interaction

$$\frac{\int_\Omega \hat{\dot{\omega}}_\mathrm{T}\,\mathrm{d}\mathbf{x}}{\int_\Omega \overline{\dot{\omega}}_\mathrm{T}\,\mathrm{d}\mathbf{x}}(s) = \begin{bmatrix}\mathscr{F}_\mathrm{u}(s) & \mathscr{F}_\mathrm{p}(s) & \mathscr{F}_\mathrm{s}(s) & \mathscr{F}_{\mathrm{Y},k}(s)\end{bmatrix} \begin{bmatrix} \frac{\hat{u}_j\, n_j}{\overline{u}_j\, n_j} \\ \frac{\hat{p}}{\overline{p}} \\ \frac{\hat{s}}{\overline{c}_\mathrm{p}} \\ \frac{Y_k'}{\overline{Y}_k} \end{bmatrix}_\mathrm{ref} \tag{3.8}$$

are usually determined, while the spatial distribution

$$\mathscr{Q}(s,\mathbf{x}) = \frac{\mathscr{F}(s,\mathbf{x})}{\mathscr{F}(s)} \tag{3.9}$$

is modeled if required.

The flow-flame coupling is very complex and highly specific to the thermoacoustic system at hand and the FTFs are typically determined from high-fidelity simulations or experimental measurements. For simplistic academic cases, approximations via analytical models might be used. However, the theoretical functional form of an FTF throughout the complex plane is known in the limit of small perturbations. In this limit, the flame acts as a linear time-invariant system and is fully characterized by its unit impulse response (time domain) [197]. The generalized functional form of the FTFs throughout the complex plane in the frequency domain is then given by the (discrete) Laplace transform of a (discrete) unit impulse response [197],

$$\mathscr{F}(s) = \sum_n h_n \exp(-s\tau_n)\,. \tag{3.10}$$

FTFs of the fundamental functional form stated in Eq. (3.10) are called *Distributed Time Delay* (DTD) models. The coefficients h_n and τ_n of the DTD models may be identified from broadband forced high-fidelity simulations via system identification methods [198, 200]. Fig. 3.3 displays an illustrative example of a unit impulse response and the corresponding FTF.

In the case of a harmonically forced[4] flame, the FTF is only determined at individual frequencies. This is typically the case for experimental measurement data, e.g. [4, 74, 140, 203, 219]. A continuous description of the FTF throughout the complex plane is then typically approximated via rational fitting [101, 185],

$$\mathscr{F}(s) = \frac{\sum_{p=0}^{P} a_p s^p}{\sum_{q=0}^{Q} b_q s^q} \quad \text{with} \quad P < Q\,. \tag{3.11}$$

Alternatively, semi-empirical approximations of Eq. (3.10) with presumed functional forms of the time delay distribution (e.g. [140], [4]) may be used to approximate continuous FTFs.

[4] Separate forcing of individual frequencies.

4 The thermoacoustic eigenvalue problem

All Laplace-transformed systems of linearized balance equations (Sec. 2.3, 3.1, 3.2) can be reformulated into an eigenvalue problem after numerical discretization, e.g. with Finite Volume, Finite Elements or in terms of "network elements", and closure with the necessary input data. The thermoacoustic eigenvalue problem of the general form

$$\mathscr{N}(s)\hat{\mathbf{v}} = 0, \quad \hat{\mathbf{v}} \neq 0, \tag{4.1}$$

is linear in the perturbed states $\hat{\mathbf{v}}$ but typically non-linear in the Laplace-variable s, even though it results from reformulating a linearized set of balance equations. This non-linear dependence on s of the operator $\mathscr{N}(s)$ results either from (semi-)analytical solutions of simple elements in network models, e.g. the wave propagation in ducts, or from lumped parameters modeling unresolved processes, e.g. the flow-flame interaction in hybrid thermoacoustic models (Sec. 3) or the thermoacoustic scattering outside of the resolved domain enforced by complex boundary conditions.

Table 4.1 lists the structure of the operator $\mathscr{N}(s)$ for various linearized models. The matrix $\mathbf{Q}_n(s)$ denotes the non-linear s-dependencies from underresolved source regions within the discretized thermoacoustic system, e.g. a combustion chamber. For example, the FTFs (Sec. (3.3)) used in hybrid thermoacoustic models are lumped parameters approximating the flow-flame interaction instead of fully resolving the linearized chemical reactions. The index n corresponds to the n-th underresolved source region. The matrix $\mathbf{Z}_m(s)$ expresses the non-linear s-dependencies of boundary conditions of the discretized thermoacoustic system. Frequency-dependent boundary conditions may be understood as lumped models approximating the relevant scattering of acoustic and convective perturbations outside of the spatially resolved domain. Examples are rotor and stator stages of a turbine downstream of a combustion chamber [22, 58, 125, 126, 145, 177, 178] or multi-perforated liners [43, 180, 232, 260, 261] at combustor walls. The index m corresponds to the m-th boundary condition. The matrix $\mathbf{M}$ relates with the corresponding prefactor s to the Laplace-transformed time derivative of the local flow perturbations. Note that for the Helmholtz

Linearized models	$\mathscr{N}(s)$
LRF	$s\mathbf{M} + \mathbf{K} + \mathbf{Z}_m(s) + \mathbf{Q}_n$
LEE/LNSE	$s\mathbf{M} + \mathbf{K} + \mathbf{Z}_m(s) + \mathbf{Q}_n(s)$
Helmholtz	$s^2\mathbf{M} + \mathbf{K} + \mathbf{Z}_m(s) + \mathbf{Q}_n(s)$
Network models	$\mathbf{K} + \mathbf{Z}_m(s) + \mathbf{Q}_n(s) + \mathbf{A}_p(s)$

Table 4.1: Structure of the operator $\mathscr{N}(s)$ for different linearized models.

equations, the prefactor s^2 appears due to the second-order time derivative in the wave equation. The matrix $\mathbf{A}_p(s)$ denotes the non-linear s-dependencies of (semi-)analytical solutions used in network models, e.g. for the wave propagation in ducts. The index p corresponds to the p-th analytical solution. The matrix $\mathbf{K}$ includes all other frequency-independent terms. Note that the explicit form of the matrices $\mathbf{M}$, $\mathbf{K}$, $\mathbf{Z}_m$ and $\mathbf{Q}_n$ depends on the underlying system of linearized balance equations, the discretization scheme as well as the chosen closure models.

4.1 Special structures of the thermoacousic eigenvalue problem

Non-linear eigenvalue problems (NLEVP) do not exhibit a closed-form solution, and the number of eigenpairs of an NLEVP is (potentially) infinite [102]. NLEVPs are, therefore, significantly harder to solve than their linear counterpart, and solution methods are tailored to the problem at hand [102, 243]. For fast and efficient computation, solution strategies may exploit certain structures of the NLEVP. Thus, this section lists special structures of the thermoacoustic NLEVP that arise under certain modeling assumptions. Specific solution strategies, namely outer iteration methods, contour integration methods, and methods based on approximation and reformulation are discussed in the Sec. 5.4 contextualizing the results from PAPER-NLEVP [167].

The structure of the thermoacoustic NLEVP is determined mainly by the models used to approximate the unresolved physical processes within ($\mathbf{Q}_n$) and outside[1] ($\mathbf{Z}_m$) the spatially resolved domain. In addition, partial (semi-)analytical solutions ($\mathbf{A}_p$) impact the structure of the NLEVP arising from network models. In the particular case that all these models are approximated via rational functions, the thermoacoustic NLEVP takes the form of a so-called rational eigenvalue problem (REVP, $\mathscr{N}(s) = \mathscr{R}(s)$). The modeling of the unresolved processes via rational functions is typical if the flow-flame feedback (Sec. 3.3) and the boundary impedances are determined experimentally. The approximation via rational functions of partial (semi-)analytical solutions in network models such as the wave propagation in ducts [76] is not uncommon. The REVP has the favorable property that it can be reformulated in an equivalent linear eigenvalue problem of higher dimension [231] for which many well-established solution methods exist, e.g. [207].

The thermoacoustic eigenvalue problem becomes linear if all relevant physical sources within the spatially discretized domain are resolved ($\mathbf{Q}_n(s) = \mathbf{Q}_n$), simple frequency-independent boundary conditions are applicable ($\mathbf{Z}_m(s) = \mathbf{Z}_m$) and no partial (semi-)analytical solutions are used ($\mathbf{A}_p(s) = \mathbf{A}_p$),

$$\mathscr{N}(s) := \mathscr{L}(s) = s\mathbf{M} + \mathbf{K} + \mathbf{Z}_m + \mathbf{Q}_n\,. \tag{4.2}$$

If frequency-independent boundary conditions are applicable, LEVPs arise if the thermoacoustic system is described via the monolithic LRF equations (2.12), e.g. [35, 240].

[1] Underresolved processes outside of the spatially resolved domain are represented by s-dependent boundary conditions.

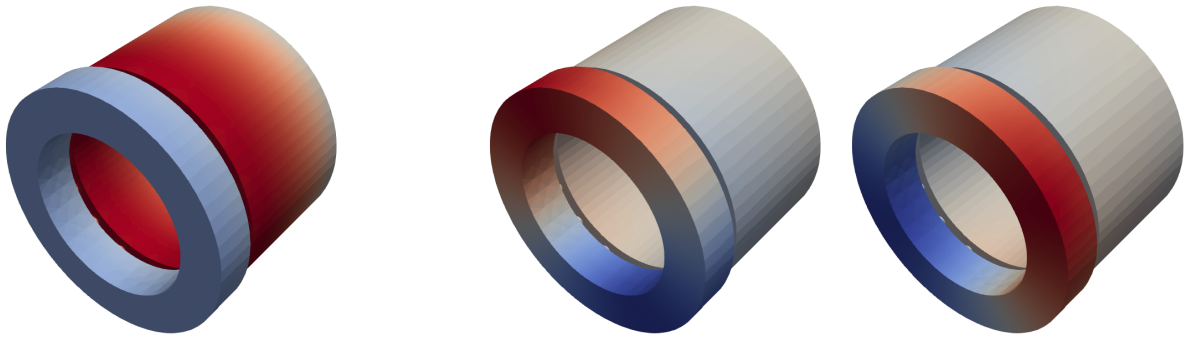

(a) **(b)**

Figure 4.1: Illustrative example of the real part of eigenvectors $\mathrm{Re}(\hat{\mathbf{v}})$ in an annular combustor corresponding to (a) a simple eigenpair, and (b) a semi-simple eigenpair with $N_\mathrm{a} = N_\mathrm{g} = 2$.

4.2 Eigenpairs and their classification

The solutions of the thermoacoustic eigenvalue problem are the eigenpairs $(s,\hat{\mathbf{v}})$ constituting of the eigenvalue s and the eigenvector $\hat{\mathbf{v}}$. The eigenvalue $s = \sigma + i\omega$ (see Eq. (2.18)) provides information about the natural angular frequency ω and the growth rate σ, which expresses the linear asymptotic stability of the thermoacoustic system. The system is linearly stable if for all eigenvalues $\sigma < 0$. In case of an unstable thermoacoustic system, the mode shapes $\hat{\mathbf{v}}$ may be used for an effective placement of acoustic dampers, e.g. [162].

Eigenvalues are mathematically classified via their algebraic N_a and geometric multiplicities N_g. The algebraic multiplicity N_a of an eigenvalue s equates to the number of roots of the determinant of the non-linear operator $\mathcal{N}(s)$ ($\det(\mathcal{N}(s)) = 0$). The geometric multiplicity N_g is the number of the independent eigenvectors $\hat{\mathbf{v}}$ corresponding to an eigenvalue s. Mathematically, the eigenvalues of a system are classified as simple ($N_\mathrm{a} = N_\mathrm{g} = 1$), semi-simple ($N_\mathrm{a} = N_\mathrm{g} > 1$) or defective ($N_\mathrm{a} > N_\mathrm{g}$) (see e.g. [102, 207]). In a thermoacoustic system, simple eigenmodes correspond to, e.g., longitudinal modes [39, 40, 167]. Figure 4.1a illustrates such a longitudinal mode in an annular model combustor. Semi-simple eigenmodes appear, e.g., in systems with rotational symmetry such as annular and can-annular combustors [39, 40, 84, 85, 167, 174, 242] (typically with $N_\mathrm{a} = N_\mathrm{g} = 2$ [173]). For example, Figure 4.1b shows the two eigenmodes corresponding to a semi-simple eigenvalue in an annular model combustor. Defective eigenvalues are, e.g., exceptional points [106, 163, 211]. Note that in numerical computations, a defective eigenpair cannot be obtained exactly due to round-off errors [163].

4.3 Spurious eigenpairs and incomplete spectra

Besides the strict mathematical classifications of eigenvalues, one may distinguish between physical and spurious eigenpairs. Spurious eigenpairs are additional eigenpairs in the spectrum of the eigenvalue problem, which are not valid solutions of the underlying physical system and result as a by-product of approximations applied throughout the modeling cascade. Anal-

ogously, eigenpairs may vanish due to approximations resulting in the determination of an incomplete eigenspectrum. The approximations applied throughout the modeling cascade may be distinguished in the following three steps:

1. Analytical modeling of a real-world problem.
2. Numerical discretization of the analytical model.
3. Approximations applied for the efficient solving of the thermoacoustic eigenvalue problem.

This work focuses on the approximations applied in the third step of the modeling cascade and all spurious eigenpairs and incomplete spectra discussed result from the corresponding approximations. Spurious eigenpairs or incomplete spectra corresponding to the approximations made in the first or second step of the modeling cascade are not further analyzed.

5 Contextualization and Discussion of Publications

5.1 Consistent analysis of source terms in thermoacoustic systems

Analyzing source terms that contribute to the generation of acoustic and convective perturbations offers insight into the underlying physical mechanisms and their importance in various physical configurations. For a *consistent* analysis, these source terms must be strictly separated from propagation terms in the flow differential equations. In the general case of a source region in motion, this strict separation requires the tracking of the source region (see PAPER-ALE [168]). In thermoacoustic systems, the most prominent source region is the exothermic reaction zone of the flame, which may generate acoustic, vortical, entropic or compositional perturbations in response to various disturbances.

For the source terms of entropy perturbations generated by a flame, several studies, e.g. [68, 176], derive from the entropy balance equations in differential form that the generation of entropy disturbances originates from a perturbation of the heat-to-flow power ratio $(\dot{\omega}_\mathrm{T}/pu)'$ and conclude that the total unsteady heat release rate of a flame contributes to the generation of entropy waves. Several jump conditions derived from the same balance equations share this conclusion [65, 107, 144, 244]. However, all these studies assume a flame at rest. In contrast, a realistic flame moves in response to various disturbances (e.g. acoustics, upstream flow velocity, vortical flow structures, turbulence, fuel concentration, hot spots). Bauerheim showed for a premixed flame that the assumption of a flame at rest results in the paradox that in the zero Mach number limit, a resting flame obeys volume instead of mass conservation [21]. Strobio Chen *et al.* [230] resolved that paradox by taking the flame movement into account. Furthermore, Strobio Chen *et al.* [230] analytically showed, utilizing a jump condition, that neglecting the flame motion results in a spurious generation of entropy inhomogeneities. Meindl *et al.* [161] visualized this spurious generation in spatially discretized numerical simulations for a propagation-stabilized, one-dimensional flame and a two-dimensional duct flame. Instead of the heat-to-flow power ratio, the heat-added-per-unit-mass $(\dot{\omega}_\mathrm{T}/\rho u)'$ may be identified from theoretical considerations or jump conditions accounting for the flame motion as the dominant mechanism generating entropy disturbances in premixed flames, e.g. [132, 199, 209, 214, 230]. For jump conditions, the need to account for the flame movement to accurately predict the generation of entropy perturbations in premixed flames is widely accepted [46, 88, 95, 171, 226, 227] and introduced in the derivation. In contrast, the effect of the flame motion on the source terms of entropy disturbances in the integral/differential equation is not apparent, and their isolation is not straightforward. This resulted in the misinterpreta-

tion of some analytical terms as sources in several studies, e.g. [79, 256]. PAPER-ALE [168] *consistently* isolates the source terms of entropy perturbations in *general* three-dimensional reactive flows by tracking the source region utilizing an ALE framework. In agreement with the theoretical and quasi-one-dimensional results, this approach identifies the perturbed heat release rate per unit mass (aligned with the mean entropy gradient) as the dominant contribution to generating entropy perturbations in premixed flames. In addition, PAPER-ALE combines temperature-entropy diagrams with an order of magnitude analysis to discuss all non-diffusive sources of entropy perturbations in the low-frequency and low-Mach number limit of premixed flames.

For acoustic perturbations, the local displacement of the flame was identified as an essential driving mechanism for transverse high-frequency thermoacoustic modes [172, 222]. In addition, Meindl *et al*. [161] observed that neglecting the flame movement results in a spurious generation of acoustic perturbations when this modeling assumption simultaneously alters the mass flow rate across the flame front. Meindl *et al*. [161] demonstrated this numerically for a spatially discretized one-dimensional, premixed, propagation-stabilized, passive ($\dot{\omega}'_{\mathrm{T}} = 0$) flame. While this spurious generation of acoustic waves does not appear in the analysis of Strobio Chen *et al*.[230] due to the assumptions intrinsic to the corresponding jump condition (constant gas properties and retaining only terms up to first order in Mach number), PAPER-JUMP [169] provides a *comprehensive* jump condition for arbitrary premixed flames incorporating this effect. PAPER-JUMP [169] visualize this spurious acoustic wave generation for a flame at rest for a one-dimensional autoignition flame. Overall, the framework in PAPER-ALE [168] can be applied to derive an acoustic analogy to *consistently* identify the acoustic source terms of a moving flame front in three-dimensional flows (see Appendix A.2).

Furthermore, note that the procedure for *consistently* isolating source terms detailed in PAPER-ALE [168] applies to any balance equations of perturbed quantities. Thus, it can also be used to identify the source terms corresponding to vortical or compositional perturbations for a moving flame front.

Besides the *consistent* isolation of source terms, PAPER-ALE [168] offers an analytical framework to analyze the modeling errors corresponding to various models $\widetilde{u}'_{\mathrm{s},j}$, e.g., a flame at rest ($\widetilde{u}'_{\mathrm{s},j} = 0$), approximating the flame displacement velocity $u'_{\mathrm{s},j}$. The modeling error is determined by subtracting the source terms identified with the procedure in PAPER-ALE [168] from the approximate differential equation obeying $\widetilde{u}'_{\mathrm{s},j}$. For convective perturbations ψ' such as entropic, vortical or compositional disturbances, the direct error ϵ_{conv} of neglecting the flame movement ($\widetilde{u}'_{\mathrm{s},j} = 0$) is for example given by (see Appendix A.1)

$$\epsilon_{\mathrm{conv}} = -u'_{\mathrm{s},j}\frac{\partial\overline{\psi}}{\partial x_j}. \tag{5.1}$$

ϵ_{conv} becomes maximal if the flame is displaced in the direction of the mean gradient of ψ and vanishes in case the displacement is orthogonal to the mean gradient of ψ. Analogously, the direct error ϵ_{ac} in the generation of acoustic perturbations resulting from neglecting the flame movement ($\widetilde{u}'_{\mathrm{s},j} = 0$) is identified as (see Appendix A.2)

$$\epsilon_{\mathrm{ac}} = \frac{\partial}{\partial t}\left(u'_{\mathrm{s},j}\frac{\partial\overline{\rho}}{\partial x_j}\right)\bigg|_{\chi} - \frac{\partial}{\partial x_i}\left(u'_{\mathrm{s},j}\frac{\partial\overline{\rho}\,\overline{u}_i}{\partial x_j}\right) + 2\overline{u}_i\frac{\partial}{\partial x_i}\left(u'_{\mathrm{s},j}\frac{\partial\overline{\rho}}{\partial x_j}\right). \tag{5.2}$$

Publication	$\frac{\breve{\omega}_\mathrm{T}(s,\mathbf{x})}{\bar{\dot{\omega}}_\mathrm{T}(\mathbf{x})}$	$\hat{u}_{\mathrm{s},j}(s,\mathbf{x})$	mixed term
Zellhuber *et al.* [259]	$\frac{\hat{p}}{\bar{\gamma}\bar{p}}$[1]	$\hat{u}_j$	
Méry [170]	$-\frac{1}{s}\frac{\partial \hat{u}_j}{\partial x_j}$	$\hat{u}_j$	
Heilmann *et al.* [105]	–	$\hat{u}_j$	
Avdonin [16]	$-\frac{1}{s}\frac{\partial \hat{u}_j}{\partial x_j}$	$\hat{u}_j$	$\hat{\omega}_\mathrm{Avdonin}$

Table 5.1: Closure models for the spatial distribution $\mathscr{Q}(s,\mathbf{x})$

ϵ_ac represents spurious acoustic sources of monopole and dipole type resulting from a spurious mass flux $u'_{\mathrm{s},j}\frac{\partial\bar{\rho}}{\partial x_j}$ and a spurious momentum flux $u'_{\mathrm{s},j}\frac{\partial\bar{\rho}\bar{u}_i}{\partial x_j}$, respectively, through the flame front.

Understanding the mechanisms that result in the generation of spurious perturbations is important to assess the quality and applicability of various models $\widetilde{u}'_{\mathrm{s},j}$ for specific application cases. Especially for hybrid linearized thermoacoustic models based on partial differential equations (LNSE, LEE, APE, Helmholtz) using global flame transfer functions $\mathscr{F}(s)$, incorporating the flame movement poses a problem. In this case, a model approximating the spatial distribution of the heat release perturbation $\mathscr{Q}(s,\mathbf{x})$ (Eq. (3.9)) is required. The flame displacement velocity $\hat{u}_{\mathrm{s},j}(s,\mathbf{x})$ (frequency space) is intrinsically encoded in $\mathscr{Q}(s,\mathbf{x})$. In low-frequency applications, a common assumption is to assume that this spatial distribution follows the mean heat release rate (e.g. [17, 92, 160, 182])

$$\mathscr{Q}(s,\mathbf{x}) = \frac{\bar{\dot{\omega}}_\mathrm{T}(\mathbf{x})}{\int_\Omega \bar{\dot{\omega}}_\mathrm{T}\,\mathrm{d}\mathbf{x}}. \tag{5.3}$$

However, Meindl *et al.* [161] showed that this approximation intrinsically neglects the flame movement. Instead, tracking the flame displacement with an ALE framework provides the general spacial distribution [105, 259]

$$\mathscr{Q}(s,\mathbf{x}) = \frac{1}{\mathscr{F}(s)}\left[\underbrace{\frac{\breve{\dot{\omega}}_\mathrm{T}(s,\mathbf{x})}{\int_\Omega \bar{\dot{\omega}}_\mathrm{T}\,\mathrm{d}\mathbf{x}}}_{\mathrm{I}} - \underbrace{\frac{1}{s}\hat{u}_{\mathrm{s},j}(s,\mathbf{x})\frac{\partial}{\partial x_j}\left(\frac{\bar{\dot{\omega}}_\mathrm{T}(\mathbf{x})}{\int_\Omega \bar{\dot{\omega}}_\mathrm{T}\,\mathrm{d}\mathbf{x}}\right)}_{\mathrm{II}}\right]. \tag{5.4}$$

The first term (I) corresponds to the fluctuations within the ALE reference frame tracking the flame. The second term (II) represents the fluctuations observed locally in an Eulerian framework due to the displacement of the flame. However, the application of Eq. (5.4) in hybrid thermoacoustic models requires closure models for the heat release rate perturbation observed in the moving reference frame $\breve{\dot{\omega}}_\mathrm{T}(s,\mathbf{x})$ and the mesh velocity $\hat{u}_{\mathrm{s},j}(s,\mathbf{x})$. In literature, various models have been proposed and are listed in Tab. 5.1. The models proposed by Zellhuber *et al.* [259], Méry [170] and Heilmann *et al.* [105] assume the displacement of the exothermic reaction

[1] Zellhuber *et al.* [259] provide an additional term $\left(\widetilde{\dot{\omega}}_\mathrm{T}/\bar{\rho}\right)'/\overline{\left(\widetilde{\dot{\omega}}_\mathrm{T}/\bar{\rho}\right)}$ corresponding to the mass-specific heat release rate in the moving reference frame. However, this term itself requires a closure model, which is not provided by Zellhuber *et al.* [259]. Therefore, this term has been neglected in all applications of the Zellhuber model [16] and is consequently neglected in Tab. 5.1.

zone to occur simply as a response to velocity perturbations. However, $\hat{u}_{\mathrm{s},j}(s,\mathbf{x})$ may be affected also by changes to the local reaction velocity. For example, the local reaction velocity of propagation-stabilized flames might be affected by perturbations of the local flame front curvature, which alters local diffusive effects such as thermal preheating. In autoignition flames, the reaction velocity is additionally sensitive to pressure, temperature and compositional fluctuations [31, 86, 169, 258]. Avdonin [16] reformulates the monolithic LRF equations utilizing a tabulated chemistry approach to formulate a model for $\mathscr{Q}(s,\mathbf{x})$. The resulting model adds an additional correction term $\hat{\dot{\omega}}_{\mathrm{Avdonin}}$ to the model of Méry [170] corresponding to the reaction-rate perturbations of the progress variable. However, the perturbation of the progress variable is not explicitly resolved in hybrid thermoacoustic models and the formulation of Avdonin [16] can not be used directly. Ultimately, better models for $\mathscr{Q}(s,\mathbf{x})$ and, therefore, for $\breve{\dot{\omega}}_{\mathrm{T}}(s,\mathbf{x})$ and $\hat{u}_{\mathrm{s},j}$ are required for the use in hybrid thermoacoustic models.

5.2 Consistent inference of global flame transfer functions from experimental pressure measurements

Two established approaches exist to determine global flame transfer functions $\mathscr{F}(s)$ from experimental measurements - the optical and the acoustic approach.

The *optical* approach measures the filtered chemiluminescence intensity I of free radicals such as CH* [19, 66], OH* [5, 19, 26, 133] or C_2* [201] in the reaction zone of the flame. The heat release rate perturbation $\dot{\Omega}'_{\mathrm{T}}/\overline{\dot{\Omega}}_{\mathrm{T}}$, necessary to identify the global FTFs (Eq. (3.8)), is then determined by correlation with the intensity perturbations $I'/\overline{I}$. For fully premixed flames in low Mach number flows and assuming small perturbations, $I'/\overline{I}$ and $\dot{\Omega}'_{\mathrm{T}}/\overline{\dot{\Omega}}_{\mathrm{T}}$ linearly depend on each other and can be used interchangeably. In this case, the optical approach works well [19, 26]. This changes for cases where I and $\dot{\Omega}_{\mathrm{T}}$ show distinct sensitivities to more than one perturbed flow variable, e.g., for partially premixed flames [26, 216, 217]. For partially premixed flames, the heat release rate depends linearly on both the mass flow rate through the flame front and the equivalence ratio. In contrast, the intensity shows a linear dependence on the mass flow rate but an exponential dependence on the equivalence ratio [108]. For such cases, Schuermans *et al*. [217] proposed to measure the chemiluminescence of several free radicals to separately identify the contributions to $I'/\overline{I}$, such as the mass flow rate and equivalence ratio perturbations in a partially premixed flame, by solving the inverse problem. $\dot{\Omega}'_{\mathrm{T}}/\overline{\dot{\Omega}}_{\mathrm{T}}$ is built from this result in a subsequent step. While the method proposed by Schuermans *et al*. [217] is consistent, it is susceptible to measurement errors [218]. In high-pressure applications, the optical approach is additionally restricted by constraints regarding the optical access, heat radiation from combustor walls and a reduced chemiluminescence intensity due to a lower probability of forming the free radicals [218]. Overall, the optical approach is not well suited for cases such as partially premixed flames or spray flames, in particular at engine-like operating conditions.

The *acoustic* approach reconstructs the flame transfer matrix from measured acoustic pressure perturbations with two microphone arrays located in a duct upstream and downstream, respectively, of an acoustically forced combustor. The global FTF is determined in a subsequent step from the flame transfer matrix. The acoustic approach is based on the direct evaluation of acous-

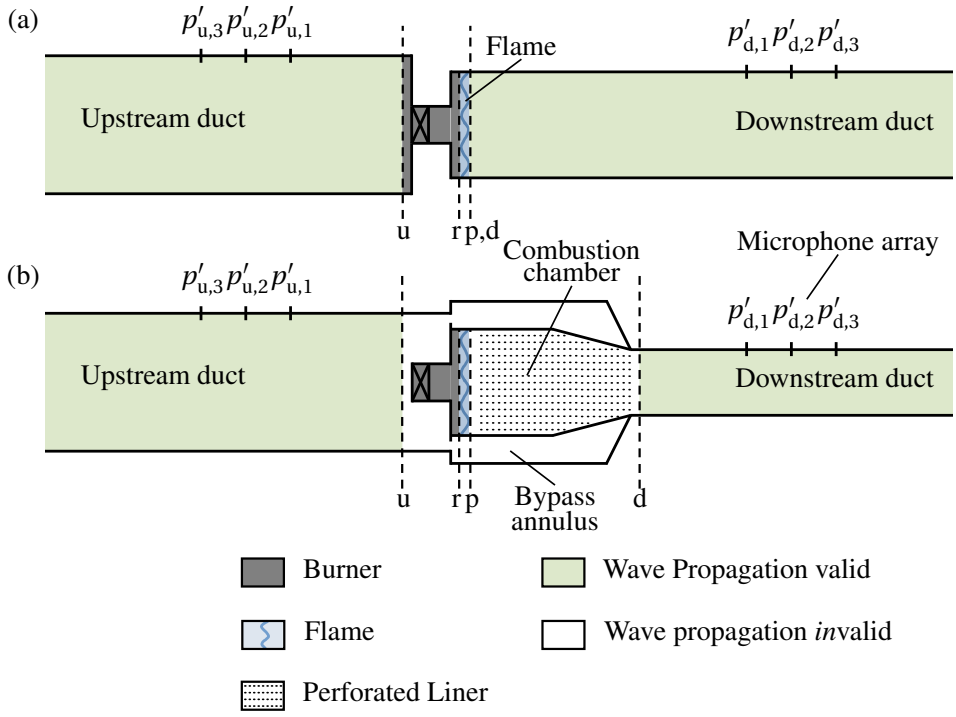

Figure 5.1: Schematic representation of (a) a simple test rig and (b) a test rig with a realistic gas turbine combustor as test section, both under reactive ("hot") conditions. Sirens are not shown.

tic sources and is applicable independent of the level of premixedness, fuel composition or operating pressure. Therefore, the acoustic approach is not limited by the restrictions of the optical approach. However, the post-processing of the measurement data is more demanding in comparison [26]. The acoustic approach can be subdivided in the following steps:

1. The acoustic pressure signals of each microphone array are used to reconstruct locally the complex wave amplitudes of the upstream and downstream traveling acoustic waves. This reconstruction requires two acoustically independent test states [1] and assumes plain acoustic waves propagating with a constant velocity in a duct of constant cross-section (green regions in Fig. 5.1). Theoretically, this reconstruction may be performed with two microphones per array (two-microphone method [51, 122, 223]). However, to increase the robustness of the reconstruction, at least three microphones per array (multi-microphone method [192, 193]) are typically used nowadays. Paschereit and Polifke [186–188] were the first to adopt the multi-microphone method for combustion applications.

2. The locally reconstructed acoustic wave amplitudes are used to determine the transfer matrix of the combustor **C** enclosed by the two microphone arrays. The resulting **C** is a black box model of the combustor section between the reference positions 'u' and 'd' (see Fig. 5.1).

3. The flame transfer matrix **F** is an intrinsic part of **C** and needs to be isolated. The established approach [214, 216] treats the combustor as a sequence of a burner section and the

flame. The corresponding combustor transfer matrix is modeled as the product of **F** and the burner transfer matrix **B**,

$$\mathbf{C} = \mathbf{F}\mathbf{B}. \tag{5.5}$$

Under this assumption, **C** is referred to as the "burner-flame transfer matrix" (BFTM), and thus, the overall approach is called the "BFTM approach" throughout this work. The BFTM approach uses a second measurement at the same operating point without fuel injection ("cold" combustor, $\mathbf{F} = \mathbf{I}$) to determine **B**, assuming an unchanged transfer behavior of the burner section [214, 216]. Then, the flame transfer matrix $\mathbf{F} = \mathbf{C}\mathbf{B}^{-1}$ can be ultimately inferred. The BFTM approach has been successfully applied for a wide variety of flame response studies in simplistic test rigs with a burner section in between two ducts, e.g. [18, 26, 27, 53, 54, 129, 156, 212], as displayed in Fig. 5.1a.

For test rigs with more complex features, such as the combustor section displayed in Fig. 5.1b, the assumptions of the BFTM approach no longer hold [9, 72]. In such a test rig, acoustic branches bypassing the flame, e.g. through the bypass annulus and the effusion cooling holes, or acoustic scattering within the combustor section, e.g. at an area contraction at the end of the combustion chamber, invalidate Eq. (5.5). PAPER-MBI [74] visualizes the resulting inconsistency of the BFTM approach for SCARLET (SCaled Acoustic Rig for Low Emission Technology) [82, 83], a rig to test aero-engine burners under realistic engine conditions at a low technology readiness level. Significant errors in the computed **F** showcase the need for more sophisticated models to represent the interior dynamics of the combustor section in test rigs with complex features. Thus, PAPER-MBI [74] develops a *consistent* framework to infer **F** from **C** in such cases,

$$\mathbf{F} = \left[\mathbf{T}_{\mathrm{ru}} \left(\mathbf{C} - \mathbf{T}_{\mathrm{du}}\right)^{-1} \mathbf{T}_{\mathrm{dp}} + \mathbf{T}_{\mathrm{rp}}\right]^{-1}. \tag{5.6}$$

In contrast to the BFTM approach, a second measurement of the non-reacting test rig is insufficient to fully characterize the interior dynamics of the combustor. Instead, the novel method relies strongly on the accurate modeling of the acoustic interaction encased in the transfer matrices $\mathbf{T}_{\mathrm{ru}}$, $\mathbf{T}_{\mathrm{du}}$, $\mathbf{T}_{\mathrm{dp}}$ and $\mathbf{T}_{\mathrm{rp}}$, bridging the gap between the states 'u','d','r' and 'p' in Fig. 5.1b. Eq. (5.6) is referred to as the *Model-Based Inference* (MBI) method. PAPER-MBI [74] uses a low-order network model to apply the MBI method to SCARLET, showcasing the capabilities of the method and its applicability to complex test rigs. A follow-up study[2] [113] indicated that the usage of additional measurement of the non-reacting test rig (not necessarily at the same operating point) may be used to reduce systematic modeling errors and to improve the robustness of the MBI method.

4. The global flame transfer functions can be approximated from **F** by utilizing an analytical model such as the Rankine-Hugoniot jump condition, e.g. [88, 230] or PAPER-JUMP [169].

5.3 Comprehensive thermoacoustic jump conditions

Jump conditions that describe the coupling of perturbations across compact elements, e.g. flames [65, 88, 146, 169, 230], area jumps [65, 69, 103, 219], compact nozzles [59, 60, 153, 155]

[2] student thesis of Thomas Hollweck [113] supervised by the author

Paper	$\mathcal{O}(M^x)$	c_p	Π^+/Π^-	$\mathfrak{s}$	$\mathfrak{c}_k$	u'_s
Chu [48]	$\mathcal{O}\left(\overline{\mathrm{M}}^1\right)$	$c_\mathrm{p}(Y_k)$	✓	(✓)[3]	-	✓
Dowling and Stow [65]	$\mathcal{O}\left(\overline{\mathrm{M}}^0\right)$	c_p	✓	(✓)[4]	-	-
Schuermans [214]	$\mathcal{O}\left(\overline{\mathrm{M}}^1\right)$	$c_\mathrm{p}(Y_k)$	✓	(✓)[5]	(✓)	✓
Strobio Chen *et al.* [230]	$\mathcal{O}\left(\overline{\mathrm{M}}^1\right)$	c_p	✓	✓	(✓)	✓
Li and Morgans [146]	$\mathcal{O}\left(\overline{\mathrm{M}}^0\right)$	$c_\mathrm{p}(T, Y_k)$	✓	-	-	-
Gant *et al.* [88]	$\mathcal{O}\left(\overline{\mathrm{M}}^{1\|2-3}\right)$	c_p	✓	✓	-	✓
PAPER-JUMP [169]	$\mathcal{O}\left(\overline{\mathrm{M}}^\infty\right)$	$c_\mathrm{p}(T, Y_k)$	✓	✓	✓	✓

Table 5.2: Established jump conditions derived for premixed flames and the assumptions used. The table marks the subset of the modelled characteristics (acoustic Π^+/Π^-, entropic $\mathfrak{s}$, compositional $\mathfrak{c}_k$), the usage of simplified gas properties (c_p), the approximation order in Mach number ($\mathcal{O}(\overline{\mathrm{M}}^x)$) and if the flame movement u'_s is accounted for. Lumped compositional perturbations, e.g., in terms of equivalence perturbations, are checked in brackets. Two exponents are detailed for $\mathcal{O}(\overline{\mathrm{M}}^x)$ if the approximation order in Mach number is chosen differently for the mean field (first exponent) and the perturbed fields (second exponent). More details are found in PAPER-JUMP [169]. (Table adopted from PAPER-JUMP [169])

or junctions [127], are key elements of every thermoacoustic network model. Their transfer/scattering matrices provide insight into the coupling of characteristic perturbations across the compact elements and may help to gain a fundamental understanding of the underlying physical mechanisms. Depending on the application case, applying jump conditions (standalone or as a subsystem in network models) requires a trade-off between accuracy and computational efficiency. Additional assumptions may be used to reduce the complexity or increase the numerical efficiency. The most common simplifications are to assume simplified gas properties, use a reduced order in Mach number approximation, or restrict the derivation to a subset of perturbations, e.g., neglect convective perturbations. Jump conditions with low complexity or high numerical efficiency are mostly favored, focusing on gaining a fundamental understanding or performing extensive parameter studies. Problematically, the corresponding simplifications are typically introduced *a priori* or during the derivation of the jump condition. While the corresponding result is valid for a specific application, the *a priori* introduction of simplifications strongly limits the generality of the derived element. The jump condition must be rederived from scratch if another application case violates one of the initial assumptions or has more stringent accuracy requirements. An illustrative example of a repeatedly derived compact element is the premixed flame. Table 5.2 provides an overview of some established jump conditions of premixed flames in chronological order.

PAPER-JUMP [169] proposes a Jacobian-based framework to derive jump conditions with wide

[3] Chu [48] considers only the incoming entropy perturbation s'_1.
[4] Dowling and Stow [65] consider only entropy waves downstream of the flame.
[5] Schuermans [214] considers only entropy waves downstream of the flame.

generality and flexibility to prevent the repeated derivation of the same jump condition for various application cases. The proposed framework minimizes the assumptions made during the derivation of jump conditions, resulting in a highly accurate[6] formulation accounting for acoustic, entropic and compositional perturbations. Application-specific assumptions may be introduced *a posteriori* to simplify the highly accurate jump condition to a formulation with increased efficiency and reduced complexity. Furthermore, the Jacobian modularity of the proposed framework provides a structure that might be exploited for a numerically efficient implementation of the resulting jump conditions. The proposed framework is applicable for deriving a variety of compact elements. The procedure is showcased in PAPER-JUMP [169] to derive a highly accurate model for a lean premixed flame. The lean premixed flame model is then validated utilizing a one-dimensional autoignition flame burning a hydrogen-vitiated air mixture typical for the second stage of the reheat combustion system [94]. The autoignition flame is sensitive to all incoming perturbations [31, 86, 258], has a non-negligible mean flow Mach number and hydrogen as a fuel ensures a change in gas properties across the flame. The jump condition derived in PAPER-JUMP [169] shows an excellent agreement with the reference solution. Finally, PAPER-JUMP [169] investigates the impact of the most frequently used simplifications (reduced order in Mach number, constant gas properties, flame at rest) on the accuracy of the method.

Highly accurate jump conditions are typically required when used within network models to infer information from experimental data, e.g., [253] or PAPER-MBI [74] since already small inconsistencies in a jump condition might accumulate to significant errors in a complex network model [252].

5.4 Coherent solution strategies for the thermoacoustic eigenvalue problems

In the most general case and as discussed in Sec. 4, the eigenvalue problem resulting from linearized thermoacoustic models is nonlinear. Since the number of eigenpairs of a nonlinear eigenvalue problem is potentially infinite [102], it is usually not possible to compute all eigenpairs. On the other hand, missing an unstable eigenpair is a potentially catastrophic case for the thermoacoustic system. Thus, any method used for solving the thermoacoustic eigenvalue problem must meet the following requirements to perform a reliable thermoacoustic stability analysis:

(I) The solution procedure computes all relevant eigenpairs (a) reliably, (b) accurately and (c) efficiently.

(II) The solution procedure avoids the computation of spurious eigenpairs if possible.

Relevant eigenpairs correspond to eigenvalues within and close to the unstable half-plane. Additionally, an application-specific cut-off frequency can be determined since high-frequency

[6] Highly accurate in the context of jump conditions.

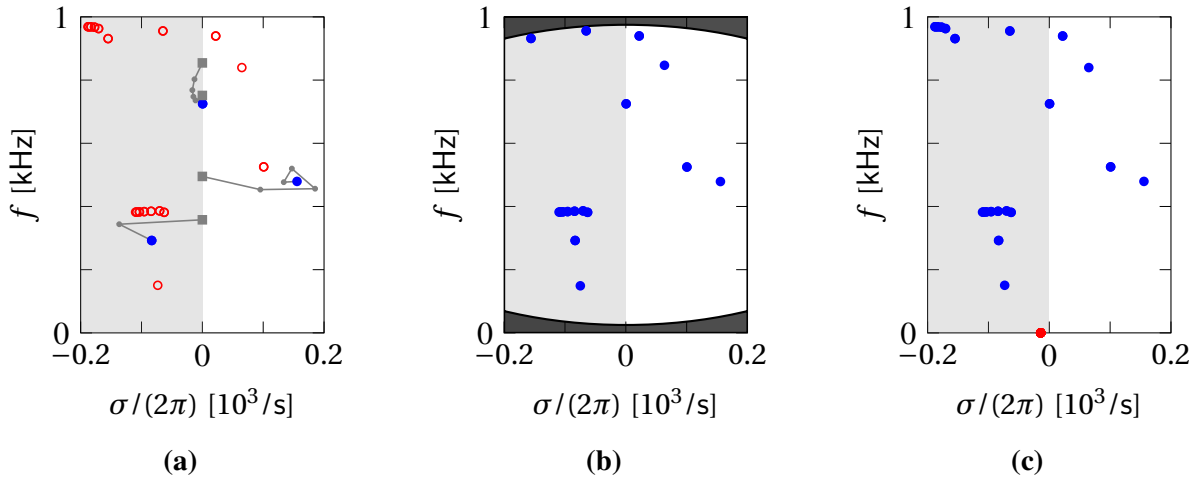

Figure 5.2: Eigenvalues of the MICCA combustor [32, 143] at EM2C (CentraleSupérlec) computed with different solution strategies. Displayed are the computed physical eigenvalues (•), the missed physical eigenvalues (◦) and computed spurious eigenvalues (•) calculated with (a) a fixed-point iteration (outer iteration method) with the passive thermoacoustic modes as initial guesses (▪) as proposed by Nicoud and Benoit [182], (b) Beyn's method [23] (contour integration) utilizing the contour displayed, and (c) the Krylov-Schur algorithm [228, 229] applied to an approximated REVP. (Results are adopted from (a) Buschmann *et al.* [40] and (b) & (c) PAPER-NLEVP [167])

perturbations are damped more strongly[7] and are typically subject to lower driving rates resulting from the flow-flame feedback[8]. The cut-off frequency depends on the geometrical dimensions, the feedback mechanism and the operating conditions of a thermoacoustic system. It may range from several hundred Hz for longitudinal instabilities up to several kHz for high-frequent transverse modes. An additional challenge for solution methods of the thermoacoustic eigenvalue problem is a high number of eigenvalues, e.g. due to clusters of (intrinsic) eigenmodes in annular or can-annular combustors [39, 84, 85, 241, 242], complex geometries [194] or hydrodynamic processes [159]. Overall, three basic methodologies have been used to solve the thermoacoustic NLEVP:

- *Outer iteration methods*, e.g. fixed-point iteration [40, 164, 182], Newton's method [102, 123, 164] or more generally Householder's method [115, 164], iterate from an initial guess of an eigenvalue to a solution of the system. An initial guess within the basin of attraction of each relevant eigenvalue is needed to fulfill requirement **(Ia)**. For thermoacoustic systems, Nicoud and Benoit [182] proposed to use a fixed-point iteration starting from the eigenvalues of the "passive" thermoacoustic system. The "passive" system denotes the thermoacoustic system ("active" system), additionally assuming a steady heat release from the flame ($\dot{\omega}'_T = 0$). However, this approach has severe shortcomings. First, relevant eigenpairs in the "active" thermoacoustic system may not exist or are way outside the relevant region in the "passive" thermoacoustic system. For example, intrinsic ther-

[7] The impact of diffusive effects on perturbations typically increasing with frequency.
[8] The flow-flame feedback in form of the FTF typically shows a low pass filter behavior.

moacoustic (ITA) modes [29, 75, 110] do not exist in the "passive" thermoacoustic system [114, 224]. Second, the basin of attractions of the individual eigenpairs of the "active" system are complex-shaped and of different sizes. Thus, it is common that an eigenpair of the "passive" system is not located within the basin of attraction of the corresponding eigenpair of the "active" system. Buschmann *et al.* [40] discussed the first and second shortcomings. Figure 5.2a shows their results, visualizing numerous missed eigenpairs by the fixed-point iteration applied. Furthermore, Mensah *et al.* [164] showed that ITA modes can be repellors for the fixed-point iteration. In contrast, Newton's method, or generally Householder's method[9], uses additional gradient information and guarantees all thermoacoustic eigenvalues to be attractors. The basin of attraction of ITA modes increases with increasing order of Householder's method. On the downside, an increasing portion of initial guesses does not converge at all. Overall, the lack of a general methodology for choosing initial guesses requires a grid search throughout the relevant part of the stability map. In combination with an unknown and potentially large number of eigenpairs with complex shaped and different-sized basins of attractions, this approach is neither reliable nor efficient for computing all relevant eigenpairs. Therefore, outer iteration methods violate the requirements **(Ia)** and **(Ic)** and should not be used for a thermoacoustic stability analysis.

- *Contour integration* methods, e.g. Beyn's method [23] or the Sakurai-Sugiura method [15, 208, 255], are based on Cauchy's integral theorem [44] combined with Keldysh's expansion [130] of the operator $\mathcal{N}(s)^{-1}$ (see Eq. (4.1)) [102]. The contour integration uses a user-defined closed contour within the complex stability map to filter [239] the spectrum. All eigenpairs within the contour are retained and are found – in theory. In practice, the accuracy and completeness of the computed spectrum within the contour depend on user-defined parameters. Those parameters may include the number of quadrature points used to discretize the specified contour, an estimated upper bound of the summed geometric multiplicities of all eigenvalues within the contour and some tolerance values to remove spurious eigenmodes from the spectrum. Buschmann *et al.* [39, 40] applied Beyn's method to thermoacoustic systems based on the Helmholtz equation, proving its capabilities of finding eigenpairs of simple or semi-simple type, even if they are clustered in a small region (see Fig. 5.2b). A direct comparison of Buschmann *et al.* [40] between Beyn's method and the fixed-point iteration proposed by Nicoud and Benoit [182] demonstrates the superiority of Beyn's method for thermoacoustic systems concerning the computation of a complete eigenspectrum. PAPER-NLEVP [166, 167] utilizes analogous test cases as Buschmann *et al.* [40] to investigate in more detail the role of the user-defined parameters in Beyn's method on the completeness and the precision of the computed eigenspectrum. With respect to the requirements formulated for a reliable method of solving the thermoacoustic eigenvalue problem, Beyn's method performs as follows:

  (Ia) Beyn's method provides a theoretical guarantee of finding all eigenvalues in a specified contour [23]. In practice, this guarantee holds as long as the estimate of the summed geometric multiplicities is larger than the actual number of geometric multiplicities within the contour.

  (Ib) The accuracy of the computed eigenpairs in Beyn's method strongly depends on

[9] Householder's method is a generalization of Newton's method to higher perturbations.

the interplay of the user input parameters and is typically unknown *a priori*. Especially eigenpairs in proximity but outside of the specified contour substantially impact the accuracy of the computed eigenspectrum. These eigenpairs are not fully filtered out from the spectrum due to the numerical discretization of the contour [239]. Thus, these eigenpairs should be accounted for when estimating the upper bound of summed geometric multiplicities inside the filter spanned by the discretized contour. This is highly relevant for thermoacoustic systems with a large number of eigenmodes. In addition, a subsequent iterative scheme may be used to converge the computed eigenvalues to the required accuracy level.

(Ic) Beyn's method requires N independent LU-decompositions, where N is the number of quadrature points used to discretize the specified contour. The method scales well for parallel computations due to the independence of these LU-decompositions. However, for efficient computations, it is recommended to choose N relatively low and increase the estimate of the summed geometric multiplicities within the filter spanned by the contour instead.

(II) The number of computed spurious eigenpairs may be as high as the difference between the actual sum of geometric multiplicities inside the filter spanned by the discretized contour and its estimated upper bound. Consequently, each eigenpair has to be double-checked, e.g. via the residual [23] or with a subsequent iterative procedure [40].

Contour integration methods to solve the thermoacoustic eigenvalue problem have been used by [39, 40, 166, 167, 184].

- The last strategy is to approximate the NLEVP with a LEVP for which a multitude of well-established LEVP solution methods [207] can be applied, e.g. the Arnoldi [14] or the Krylov-Schur [228, 229] algorithm combined with a shift-and-invert spectral transform. Therefore, the NLEVP is reformulated in two steps. First, the NLEVP is approximated via an NLEVP of a simpler structure, such as a REVP (see Sec. 4.1). Since the REVP typically approximates the NLEVP well only in a limited region of the complex domain, care has to be taken that this approximation is sufficiently accurate in the region of interest. Criteria on the quality of this approximation, e.g. [102], can be used to define regions of confidence [213]. In a second step, the REVP is recast into a LEVP of higher dimension [231]. For a direct comparison with Beyn's method (contour integration), PAPER-NLEVP [166, 167] computed the same testcases with this approach utilizing the Krylov-Schur algorithm and a shift-and-invert spectral transform. With respect to the requirements set for a reliable method to solve the thermoacoustic eigenvalue problem, this approach has the following properties:

  (Ia) The completeness of the spectrum within the region of interest cannot be guaranteed, if the REVP results from a general NLEVP (see discussion in Sec. 4.3). However, no problems with incomplete spectra have been observed in PAPER-NLEVP [166, 167] for testcases including mode clusters as well as eigenpairs of simple, semi-simple and almost defective types (see Fig. 5.2c). If the thermoacoustic NLEVP is already of rational type (see discussion in Sec. 4.1), no approximations are needed and the eigenspectrum is complete.

(Ib) The accuracy of the computed eigenpairs depends mainly on how well the REVP approximates the NLEVP locally. If the thermoacoustic NLEVP is already of rational type, the requested accuracy is easily set in the solvers used to solve the linear eigenvalue problem.

(Ic) Assuming a single shift[10], the main computational effort in solving the linear eigenvalue problem results from a single LU-decomposition. Note that the reformulated linear eigenvalue problem has more degrees of freedom than the REVP or NLEVP. However, especially for large eigenvalue problems this increase is typically negligible. An exception is the quadratic dependence on s in the Helmholtz equation (see Tab. 4.1), which doubles the degrees of freedom.

(II) For the spurious eigenvalues, analogous arguments to **(Ia)** and Sec. 4.3 apply.

For thermoacoustic systems, this method has been used extensively, e.g. [17, 30, 76, 160, 215].

PAPER-NLEVP [166, 167] compares the contour integration method and the approach utilizing a rational approximation directly. They conclude that for the contour integration, the combination of an a priori unknown accuracy level combined with an unknown but potentially large sum of geometric multiplicities inside and in the proximity of the contour renders the user-defined input parameters hard to set efficiently. In contrast, the approximation with a rational eigenvalue problem has been found to compute the complete eigenspectrum with only a few spurious eigenpairs. In addition, the computation of the higher dimensional LEVP usually results in a speed-up and avoids hard-to-set user parameters. The errors introduced by the rational approximation have been small and found to be minor in comparison to the advantages of the approach. In addition, no approximation error exists if the NLEVP is already rational, which is a quite common case in practical applications.

[10] shift-and-invert spectral transform

6 Outlook

In this publication-based thesis, several linearized thermoacoustic models have been developed and analyzed. A focus on *consistency* and *comprehensiveness* renders the developed models and frameworks applicable for a wide range of application cases. The developed models and performed analysis contribute to the understanding and prediction of thermoacoustic phenomena and build a solid groundwork to accelerate future research and development on various thermoacoustic systems.

To further strengthen the basis laid out by the developed methodologies, the following projects have been identified for future research:

1. *Analyzing additional sets of linear balance equations and methodologies concerning the implication of the flame front movement:*

   The framework in PAPER-ALE [168] provides a comprehensive approach to understanding the physical mechanisms underlying the generation of various perturbations for sources in motion in three-dimensional reactive flows. Within this thesis and PAPER-ALE [168], the framework is applied to the LRF equations to identify the effects of flame movement on the sources of the characteristic perturbations. Furthermore, spurious sources of perturbations resulting from modeling errors are identified analytically for cases in which a flame model approximating the flame movement is used. For example, knowing these spurious sources is essential to assess the quality of flame models used in hybrid linear thermoacoustic models. The formulations detailed in Appendix A directly apply to the LNSE and the LEE.

   However, besides the LRF, LNSE and LEE, additional sets of linearized equations and linear methodologies are used to analyze thermoacoustic systems. To indentify inconsistencies and misinterpretations, the framework in PAPER-ALE [168] should be used to identify the implications of flame front motion and the sensitivities to modeling errors within additional methodologies such as:

   a. *The Acoustic Perturbation Equations.*

      The APE framework [36, 77] has been used in previous studies, e.g. [36–38, 89, 189, 190], to analyze thermo-acoustic sources in reactive flows. These studies identified source terms of significant strength in addition to the unsteady heat release rate contributing to the overall sound emission. In particular, accelerating entropy gradients were identified as a significant or even dominant contributor [189, 190]. However, this finding contradicts the established understanding of unsteady heat release rate as the sole - or at least predominant - acoustic source in thermoacoustic systems.

      So far, this controversy has not been resolved. A hypothesis is that the additional sources may be spurious, arising from a misrepresentation of flame movement. This

effect is thought to be similar to the generation of spurious perturbations in LNSE simulations, which occur when the closure model of the perturbed heat release rate $\dot{\omega}'_{\mathrm{T}}$ fails to adequately capture the flame movement [161]. Thus, a consistent analysis of the APE framework concerning the influence of flame movement would be valuable for identifying potential inconsistencies, either supporting or refuting this hypothesis. To perform the corresponding derivations, the steps in deriving the APE (see [36, 77]) should be applied to the LRF equations formulated in an ALE reference frame. Furthermore, a strict separation between propagation and source terms may be obtained by applying the framework in PAPER-ALE [168].

b. *Energy-based methods.*

Starting from the early works of Lord Rayleigh [202], energy-based methods have been used to define stability criteria for thermoacoustic systems and analyze various processes contributing to the amplification or damping of thermoacoustic instabilities. By recombining the perturbed reactive flow equations, energy-based methods define a balance equation of a predefined perturbation energy $\mathscr{E}$,

$$\frac{\partial \mathscr{E}}{\partial t} + \frac{\partial W_{\mathscr{E},j}}{\partial x_j} = \dot{\omega}_{\mathscr{E}} \,. \tag{6.1}$$

The perturbation energy $\mathscr{E}$ increases when the sources $\dot{\omega}_{\mathscr{E}}$ exceed the energy losses via fluxes $\frac{\partial W_{\mathscr{E},j}}{\partial x_j}$,

$$\frac{\partial \mathscr{E}}{\partial t} > 0 \quad \Leftrightarrow \quad \dot{\omega}_{\mathscr{E}} > \frac{\partial W_{\mathscr{E},j}}{\partial x_j} \,. \tag{6.2}$$

Eq. (6.2) balances the perturbation energy locally and instantaneously. However, global energy budgets,

$$\int_\Omega \frac{\partial \mathscr{E}}{\partial t} \,\mathrm{d}\mathbf{x} > 0 \quad \Leftrightarrow \quad \int_\Omega \dot{\omega}_{\mathscr{E}} \,\mathrm{d}\mathbf{x} > \int_\Omega \frac{\partial W_{\mathscr{E},j}}{\partial x_j} \,\mathrm{d}\mathbf{x} \,, \tag{6.3}$$

energy budgets averaged over one perturbation period,

$$\oint \frac{\partial \mathscr{E}}{\partial t} \,\mathrm{d}t > 0 \quad \Leftrightarrow \quad \oint \dot{\omega}_{\mathscr{E}} \,\mathrm{d}t > \oint \frac{\partial W_{\mathscr{E},j}}{\partial x_j} \,\mathrm{d}t \,, \tag{6.4}$$

or a combination of both are more relevant to assessing the stability properties of a thermoacoustic system. Examples of perturbation energy budgets are the Rayleigh criterion [202], extended Rayleigh criteria [181], and balances of acoustic [42, 175] or generalized perturbation energies [34, 49, 179].

Perturbation energy budgets are typically formulated in an Eulerian reference frame and, hence, do not track the movement of the flame front. Following the argumentation in PAPER-ALE [168], this results in the incomplete separation between propagation and source terms and may result in misinterpreting source mechanisms of perturbation energy and misleading local energy budgets. Thus, the framework of PAPER-ALE [168] should be applied to the derivation of perturbation energy budgets to strictly separate propagation and source terms, identifying the effect of local

flame movement. For this purpose, the steps in deriving the individual energy budgets should be applied to the reactive flow equations[1] formulated in an ALE reference frame. A strict separation between propagation and source terms is obtained by following the framework in PAPER-ALE [169].

As a short remark, even though budgets of perturbation energy are widely used, the meaningful definition of disturbance energy $\mathscr{E}$ remains a topic of active research [90, 91].

2. *Developing a comprehensive model for the flame front movement in various three-dimensional application cases:*

   A prerequisite to quantifying sources in three-dimensional flows or deriving quantitative flame models, e.g. for hybrid linear stability analysis, is a closed form of the underlying set of linearized balance equations. A specific model for the mesh velocity $u'_{\mathrm{s},j}$ is required to obtain a closed form for any set of linearized balance equations formulated in the ALE reference frame[2]. Thus, mathematical conditions or quantities characteristic to the source region of interest, e.g. the exothermic reaction zone of a flame, must be defined to enable its tracking[3]. Overall, three conditions are required in the general three-dimensional case since the mesh velocity $u'_{\mathrm{s},j}$ is a vector. For example, a progress rate of reaction in combination with the stretch and the curvature of the flame front may be used to track the exothermic reaction zone of a flame.

   Next, the mesh velocity $u'_{\mathrm{s},j}$ may be identified after specifying the ALE tracking conditions. Note that the displacement of the flame is intrinsic to the LRF equations [161] – independently of the reference frame. Thus, combining the LRF equations and the ALE tracking conditions provides a closed system of analytical differential equations. Their solution is the mesh velocity as a function of all other perturbed and base flow field quantities,

$$u'_{\mathrm{s},j} = f\left(\rho', u'_i, E', Y'_k, \overline{\rho}, \overline{u}_i, \overline{p}, \overline{E}, \overline{Y}_k, ...\right). \tag{6.5}$$

   The remaining question is whether a closed-form analytical solution of $u'_{\mathrm{s},j}$ can be found. In pursuit of a closed form of $u'_{\mathrm{s},j}$, the derivation may be eased by performing it in several steps for systems with increased complexity, e.g. for a one-dimensional kinematically stabilized flame, a one-dimensional autoignition flame, and eventually a three-dimensional propagation-stabilized flame without and with diffusion all first for perfectly and then partially premixed flames. Taking advantage of the linearity of the underlying system of equations, the different effects adding to $u'_{\mathrm{s},j}$ can be superpositioned. In addition, the triple decomposition proposed by Heilmann *et al.* [105] may help to solve the system of partial differential equations to find a closed form for $u'_{\mathrm{s},j}$.

   For hybrid linearized models, the general solution of the mesh velocity $u'_{\mathrm{s},j}$ is not directly applicable due to some unresolved perturbed quantities. For example, the LNSE do not

[1] Since the perturbation energy is a second-order perturbation, the first-order LRF equations, as stated in Sec. 2.3, are useless for deriving perturbation energy balances. Thus, deriving a consistent balance equation for the perturbation energy must start from the reactive flow equations (Sec. 2.2).

[2] Note that the Eulerian ($u'_{\mathrm{s},j} = 0$) and the Lagrangian ($u'_{\mathrm{s},j} = u'_j$) reference frames are specific forms of an ALE framework with very particular choices of $u'_{\mathrm{s},j}$. Thus, both – the Lagrangian and the Eulerian reference frame – provide closed forms for any set of linearized balance equations since the mesh velocity $u'_{\mathrm{s},j}$ is defined by default.

[3] The tracking is perfect when the source region of interest is at rest in the ALE reference frame.

resolve the species mass fractions Y_k'. Thus, the unresolved perturbed quantities must be approximated via the available variables, e.g. for the LNSE

$$Y_k' = f\left(\rho', u_i', E', \overline{\rho}, \overline{u}_i, \overline{p}, \overline{E}, \overline{Y}_k, ...\right). \tag{6.6}$$

Eventually, an approximated mesh velocity $u_{\mathrm{s},j}'$ for hybrid linearized models is obtained by substituting these approximate perturbations into Eq. (6.5).

3. *Extending the MBI method to increase accuracy and reliability of flame transfer matrix predictions:*

   The MBI method relies strongly on accurately modeling the inner dynamics of the thermoacoustic system. Systematic modeling errors directly falsify the inferred flame transfer matrices. Furthermore, assessing the quality of the predicted flame transfer matrix coefficients is difficult since the corresponding uncertainty bounds are unknown in the current formulation of the MBI method. Incorporating measurement and model parameter uncertainties and combining the MBI method with statistical procedures such as Bayesian inference (see [33, 152] for the mathematical details) may relax these constraints. The statistical procedures enable the determination of the most probable model parameters for a given model, the uncertainties of model parameters, and the uncertainties in the model prediction [124, 253, 254]. Additional measurements, e.g. of the cold combustor, may be used to reduce uncertainty bounds and to rate the quality of various models in representing the thermoacoustic system [124, 253, 254]. Note that choosing the most suitable model will reduce but not erase systematic modeling errors. Especially when experimental data is limited or for test rigs with complex features, relevant systematic modeling errors may remain. A promising idea for further reducing the impact of systematic modeling errors on the identified flame transfer matrix is to take advantage of the correlation between systematic modeling errors of the hot and cold combustor [113]. A first analysis of the MBI method in this direction shows promising results [113]. However, a systematic approach still must be developed. Future studies in this direction should focus on establishing criteria to determine if a viable correlation between the hot and cold combustor matrices exists. Additionally, future studies should work on optimizing the placement of correction terms to minimize the impact of systematic modeling errors on the identified flame transfer function when a viable correlation is present.

4. *Building a network modeling toolbox based on the framework in PAPER-JUMP [169]:*

   So far, the Jacobian-based framework detailed in PAPER-JUMP [169] has only been used for deriving comprehensive jump conditions for compact premixed flames [169] and area changes (Supplementary Material to PAPER-JUMP [169]). However, other compact elements exist that are essential to representing thermoacoustic systems with network models. The framework in PAPER-JUMP [169] should be applied to derive such models. Examples of additional essential compact elements are various types of junctions. Appendix B comments on the procedure to derive compact jump conditions for two types of junctions – the flow split (1-N junction) and the flow merge (N-1 junction). Eventually, a network modeling toolbox should be built incorporating the

derived models and taking advantage of the Jacobian-based structure of the framework in PAPER-JUMP [169].

5. *Extending the framework in PAPER-JUMP [169] for non-compact elements:*

   The assumption of compactness limits the validity range of jump conditions. Especially in low Mach number flows when taking convective perturbations such as entropic or compositional disturbances into account, the assumption of convective compactness is a substantial restriction.

   In the derivation of jump conditions, the assumption of (convective) compactness is introduced by approximating all perturbed volume integrals, e.g. the accumulation term (see PAPER-JUMP [169])

$$\mathbf{P}' \coloneqq \frac{\partial}{\partial t}\left(\int_\Omega \mathbf{U}\,\mathrm{d}\mathbf{x}\right)' \quad \text{with} \quad \mathbf{U} = \left[\rho, \rho u, \rho E, \rho Y_k\right]^T , \tag{6.7}$$

   in the limit of vanishing Strouhal numbers[4] $\mathrm{St} = 0$ ($\mathscr{O}(\mathrm{St}^0)$),

$$\mathbf{P}' \approx \mathbf{P}'\big|_{\mathrm{St}=0} . \tag{6.8}$$

   Higher approximation orders $\mathscr{O}(\mathrm{St}^n)$ must be taken into account to relax the assumption of (convective) compactness,

$$\mathbf{P}' \approx \sum_{n=0}^{N} \left.\frac{\mathrm{d}^n \mathbf{P}'}{\mathrm{d}\,\mathrm{St}^n}\right|_{\mathrm{St}=0} \frac{\mathrm{St}^n}{n!} . \tag{6.9}$$

   Determining higher-order approximations is not straightforward. However, especially for area changes, examples of transfer and scattering matrices relaxing the assumption of compactness exist in the literature. For example, the L-ζ-model of Schuermans *et al.* [219] relaxes the assumption of acoustic compactness to first order in He[5]. Furthermore, Duran and Moreau [67] utilize a Magnus expansion [25] to derive a solution for quasi-onedimensional nozzle flows for arbitrary orders in St and He. For determining higher-order approximations for the accumulation term (Eq. (6.7)) of a premixed flame, Appendix C outlines a first concept. Two cases are considered – a non-compact flame with and infinitely thin flame front (Appendix C.1) and a non-compact flame sheet (Appendix C.2). The examples in Appendix (C) should serve as a first guideline on how to relax the assumption of compactness within the framework of PAPER-JUMP [169]. This guideline should be used to complete the derivation of a non-compact premixed flame element as well as to extend the procedure to other network elements.

   To better understand the effects of non-compactness, filter matrices

$$\mathbf{H}_T = \mathbf{T}_\mathrm{c}^{-1}\mathbf{T}_\mathrm{nc} \quad \text{and} \quad \mathbf{H}_S = \mathbf{S}_\mathrm{c}^{-1}\mathbf{S}_\mathrm{nc} \tag{6.10}$$

   relating the compact (index 'c') and non-compact (index 'nc') transfer and scattering matrices can be used. For example, Yoon [256] derived a spatial low-pass filter behavior for sources generating entropy perturbations within a convectively non-compact constant temperature gradient at rest in a one-dimensional domain.

[4] or Helmholtz $\mathrm{He} = 0$ ($\mathscr{O}(\mathrm{He}^0)$) if only acoustic compactness is of concern

[5] The Helmholtz number He is the equivalent parameter to the Strouhal number St when considering acoustic instead of convective compactness.

7 Summary of Papers

7.1 An Arbitrary Lagrangian-Eulerian framework for the consistent analysis of entropy wave generation

Label: PAPER-ALE [168]

Original Abstract: Entropy waves are generated in many technically relevant flow processes such as combustion, mixing, or convective heat transfer. When accelerated, entropy waves generate acoustic waves that contribute to the overall sound emission and can lead to self-excited thermoacoustic instabilities, especially at low frequencies. In order to reduce or prevent these undesirable byproducts of the flow, an understanding of the generation mechanisms of entropy waves is key. This study derives the analytical source terms of entropy disturbances for moving sources in general three-dimensional reactive flows. In this general setup, the consistent derivation of the generation mechanisms requires the tracking of the moving source for which an Arbitrary Lagrangian-Eulerian (ALE) framework is utilized. The derived differential equations provide a fundamental understanding of the underlying source mechanisms.

In addition, the general three-dimensional differential equations are reduced to a quasi-one-dimensional jump condition to unify the analysis of the entropy wave generation. This unified framework is used for an in-depth analysis of a premixed flame, where all source terms that generate entropy disturbances are analyzed and their relative importance are quantified. The dominant contribution of unsteady heat addition per unit mass to the generation of entropy waves is reaffirmed for lean premixed flames. Finally, by comparison with the entropy generation mechanisms of a heated gauze at rest, it is emphasized once more that a heat source at rest is an invalid model for a premixed flame.

Relevance for the thesis: Framework to *consistently* analyze the generation of various perturbations resulting from general sources in motion. Exemplified for sources generating entropy perturbations.

CRediT author statement: M. Merk: Conceptualization, Methodology, Validation, Formal analysis, Visualization, Writing - original draft, Writing - review & editing. **A. J. Eder:** Conceptualization, Methodology, Validation, Formal analysis, Visualization, Writing - original draft, Writing - review & editing, Project administration. **W. Polifke:** Conceptualization, Methodology, Validation, Writing - review & editing, Supervision, Funding acquisition.

Status: Published in *Combustion and Flame*.

Review process: Peer-reviewed, Scopus listed.

Reference: M. Merk*, A. J. Eder*, and W. Polifke. An Arbitrary Lagrangian-Eulerian framework for the consistent analysis of entropy wave generation. *Combustion and Flame* 262:113334, 2024. doi: 10.1016/j.combustflame.2024.113334. Reproduced on p. 63 ff.
(*Joint first authors)

7.2 Model-based inference of flame transfer matrices from acoustic measurements in an aero-engine test rig

Label: PAPER-MBI [74]

Original Abstract: Flame dynamics in the form of a flame transfer matrix (FTM) is not directly measurable in a test rig, but must be deduced from transfer matrix measurements of the combustion system. The burner-flame transfer matrix (BFTM) approach for estimating the FTM is based on local pressure signals from two microphone arrays located upstream and downstream of the combustor. It combines acoustic transfer matrix measurements in non-reacting and reacting conditions, where the latter implicitly includes the flame dynamics. A simple matrix operation then yields the FTM. However, this approach assumes that there is loss-free wave propagation at a constant speed of sound with no change in cross-sectional area between the microphone locations and the burner/flame. The present work demonstrates the limitations of these assumptions when applied to a test rig with complex features, such as effusion cooling, bypass annulus, and downstream end contraction. To remedy the shortcomings of the BFTM approach, this work proposes a novel method to infer the FTM for complex combustors by combining reactive transfer matrix measurements of the entire combustor with an accurate low-order thermoacoustic network model (LOM) of the test rig. This generalized method reduces to the BFTM approach as a special case.

In this work, the Rolls-Royce Scaled Acoustic Rig for Low Emission Technology (SCARLET) operated under realistic engine conditions ($T_{\text{in}} \approx 825$ K, $p_{\text{in}} \approx 25$ bar, kerosene) is used to analyze the capabilities of the proposed model-based inference method and the limitations of the BFTM approach. In a first step, a LOM based on the geometry and operating point of SCARLET is formulated using a generic FTM. This generic model is used to visualize the limitations of the BFTM approach in terms of various physical and geometrical parameters. Finally, experimental measurement data is used to deduce the FTM of SCARLET using the proposed approach.

Relevance for the thesis: *Consistent* and quantitatively accurate framework for the inference of flame transfer matrices and flame transfer functions from acoustic measurements.

CRediT author statement: A. J. Eder: Conceptualization, Methodology, Software, Validation, Investigation, Formal analysis, Data curation, Visualization, Writing - original draft, Writing - review & editing, Project administration. **M. Merk:** Conceptualization, Methodology, Software, Validation, Investigation, Formal analysis, Data curation, Visualization, Writing - original draft, Writing - review & editing. **T. Hollweck:** Conceptualization, Software, Validation, Investigation, Formal analysis, Data curation, Visualization, Writing - review & editing. **A. Fischer:** Conceptualization, Validation, Investigation, Formal analysis, Data curation, Writing - review & editing draft. **C. Lahiri:** Conceptualization, Validation, Investigation, Formal analysis, Data curation, Writing - review & editing draft. **C. F. Silva:** Conceptualization, Writing review & editing draft. **W. Polifke:** Conceptualization, Writing - review & editing, Supervision, Funding acquisition.

Status: Published in *Journal of Engineering for Gas Turbines and Power*.

Review process: Peer-reviewed, Scopus listed.

Reference: A. J. Eder*, M. Merk*, T. Hollweck, A. Fischer, C. Lahiri, C. F. Silva, and W. Polifke. Model-based inference of flame transfer matrices from acoustic measurements in an aero-engine test rig. *Journal of Engineering for Gas Turbines and Power*, 147(3):031022, 2025. doi: 10.1115/1.4066366. Reproduced on p. 74 ff.
(*Joint first authors)

Comment: A first version of this publication was presented and published in the proceedings of the *ASME Turbo Expo 2024: Turbomachinery Technical Conference and Exposition* [73].

7.3 A Jacobian-based framework for the derivation of comprehensive thermoacoustic jump conditions

Label: PAPER-JUMP [169]

Original Abstract: Low-order network models are an efficient framework to describe and predict thermoacoustic phenomena in confined combustion systems. These models are based on the interconnection of compact and non-compact elements representing the main features of the system. Assumptions such as reduced Mach number approximations or constant gas properties, are typically applied in the derivation of these elements.

This work proposes a Jacobian-based framework for the derivation of comprehensive thermoacoustic jump conditions (compact elements) accounting for acoustic, entropic, and compositional perturbations. The modularity provided by the Jacobian-based formulation renders the framework easily applicable for the derivation of a variety of compact elements and provides a straightforward implementation guideline. Application-specific assumptions to increase computational efficiency or to ease the implementation may be included *a posteriori*, enabling easy switching between accurate and efficient formulations without rederivation. The capabilities of this framework are demonstrated by deriving a novel, highly accurate lean premixed flame model. This novel flame model is validated via a lean premixed H_2 autoignition flame.

Relevance for the thesis: A framework for deriving thermoacoustic jump conditions applicable to a wide variety of thermoacoustic systems, accounting for acoustic, entropic and compositional perturbations.

CRediT author statement: M. Merk: Project administration, Conceptualization, Methodology, Software, Validation, Investigation, Formal analysis, Visualization, Writing - original draft, Writing - review & editing. **F. Schily:** Conceptualization, Methodology, Writing - review & editing. **W. Polifke:** Conceptualization, Supervision, Writing - review & editing.

Status: Published in *Combustion and Flame*

Review process: Peer-reviewed, Scopus listed.

Reference: M. Merk, F. Schily, and W. Polifke. A Jacobian-based framework for the derivation of comprehensive thermoacoustic jump conditions. *Combustion and Flame*, 274:113958, 2025. doi: 10.1016/j.combustflame.2024.113958. Reproduced on p. 85 ff.

7.4 The Nonlinear Thermoacoustic Eigenvalue Problem and Its Rational Approximations: Assessment of Solution Strategies

Label: PAPER-NLEVP [167]

Original Abstract: Nonlinear eigenvalue problems (NLEVPs) arise in thermoacoustics by considering the temporal evolution of small perturbations in the relevant governing equations. In this work, two solution strategies are compared: (i) a contour-integration-based method that guarantees to provide all eigenvalues in a given domain and (ii) a method that approximates the NLEVP by a rational eigenvalue problem, which is generally easier to solve. The focus lies on numerical speed, the completeness of the computed spectrum, and the appearance of spurious modes, i.e., modes that are not part of the original spectrum but appear as a result of the approximation. To this end, two prototypical thermoacoustic systems are considered: a single-flame Rijke tube and an annular model combustor. The comparison of both methods is preceded by a detailed analysis of the user-defined input parameters in the contour-integration-based method. Our results show that both methods can resolve all types of considered eigenvalues with sufficient accuracy for applications. However, the recast linear problem is overall faster to solve and allows a priori precision estimates – unlike the contour-integration-based method. Spurious modes as a by-product of the NLEVP approximation are found to play a minor role, and recommendations are given on how to eliminate them.

Relevance for the thesis: Assessment of different strategies to solve large eigenvalue problems from spatially discretized thermoacoustic systems *reliably*, *accurately* and *efficiently*.

CRediT author statement: M. Merk: Project administration, Conceptualization, Methodology, Software, Validation, Investigation, Formal Analysis, Visualization, Writing - original draft, Writing - review & editing. **P. E. Buschmann:** Conceptualization, Methodology, Software, Investigation, Formal Analysis, Visualization, Writing - original draft, Writing - review & editing. **J. P. Moeck:** Conceptualization, Formal Analysis, Writing - review & editing, Supervision. **W. Polifke:** Conceptualization, Formal Analysis, Writing - review & editing, Supervision.

Status: Published in *Journal of Engineering for Gas Turbines and Power*.

Review process: Peer-reviewed, Scopus listed.

Reference: M. Merk, P. E. Buschmann, J. P. Moeck and W. Polifke. The Nonlinear Thermoacoustic Eigenvalue Problem and Its Rational Approximations: Assessment of Solution Strategies. *Journal of Engineering for Gas Turbines and Power*, 145(2):021028,2023. doi:10.1115/1.4055583. Reproduced on p. 102 ff.

Comments:

- A first version of this publication was presented and published in the proceedings of the *ASME Turbo Expo 2022: Turbomachinery Technical Conference and Exposition* [166].
- In PAPER-NLEVP, there is a formatting error. Sec. 2 should not be a section and all references to sections within the paper should be incremented by unity.

Appendices

A Modeling errors of $u'_{\mathrm{s},j}$: Spurious generation of disturbances in three-dimensional linearized flows

The ALE framework enables the tracking of moving source regions of convective and acoustic disturbances, e.g. a flame, in three-dimensional reactive flows. The physical source terms are isolated analytically using the framework provided in PAPER-ALE [168]. Among these sources, terms related to the movement of the source region $u'_{\mathrm{s},j}$ appear explicitly in the differential balance equation.

In practical applications, the absolute velocity $u'_{\mathrm{s},j}$ of a flame front is not always known and may be modeled via $\widetilde{u}'_{\mathrm{s},j}$. The requirements for a good model may be assessed by formulating a balance equation of spurious perturbations

$$\psi'_\epsilon = \widetilde{\psi}' - \psi'. \tag{A.1}$$

Such a balance equation can be derived by subtracting the physical from the approximated balance equations. $\widetilde{(\cdot)}'$ denotes an arbitrary physical quantity obeying the balance equation approximating the movement of the source region.

The following two sections identify the balance equations of spurious characteristic flow disturbances (see Sec. 2.4) generated by modeling errors of $\widetilde{u}'_{\mathrm{s},j}$. The corresponding spurious source terms are an analytical representation of the spurious perturbations analysed by Strobio Chen *et al.*[1] [230] and Meindl *et al.*[2] [161] generalized to arbitrary modeling errors $\widetilde{u}'_{\mathrm{s},j}$ and arbitrary spurious convective (Sec. A.1) and acoustic (Sec. A.2) disturbances in three-dimensional reactive flows.

A.1 Convective characteristics

The balance equation for each convectively propagated characteristic perturbation (entropic, vortical, compositional) expressed from the viewpoint of the moving source region may be expressed as (see PAPER-ALE [168])

$$\left.\frac{\partial \psi'}{\partial t}\right|_{\chi} + \overline{u}_j \frac{\partial \psi'}{\partial x_j} = u'_{\mathrm{s},j} \frac{\partial \overline{\psi}}{\partial x_j} + \dot{\omega}'_\psi . \tag{A.2}$$

[1] Chen *et al.* [230] analysed spurious entropic disturbances for a flame at rest ($\widetilde{u}'_{\mathrm{s},j} = 0$).

[2] Meindl *et al.* [161] analysed spurious entropic disturbances and spurious acoustic waves for a flame at rest ($\widetilde{u}'_{\mathrm{s},j} = 0$).

In contrast, the approximated balance equation utilizing the model $\widetilde{u}'_{s,j}$ deteriorates to

$$\left.\frac{\partial \widetilde{\psi}'}{\partial t}\right|_{\chi} + \overline{u}_j \frac{\partial \widetilde{\psi}'}{\partial x_j} = \widetilde{u}'_{s,j} \frac{\partial \overline{\psi}}{\partial x_j} + \widetilde{\dot{\omega}}'_{\psi} . \tag{A.3}$$

Then, substracting Eq. (A.2) from Eq. (A.3) results in the balance equation for the spurious convective characteristics

$$\left.\frac{\partial \psi'_{\epsilon}}{\partial t}\right|_{\chi} + \overline{u}_j \frac{\partial \psi'_{\epsilon}}{\partial x_j} = \underbrace{\left(\widetilde{u}'_{s,j} - u'_{s,j}\right) \frac{\partial \overline{\psi}}{\partial x_j}}_{\text{I}} + \underbrace{\dot{\omega}'_{\psi,\epsilon}}_{\text{II}} . \tag{A.4}$$

Term I describes the direct generation of spurious convective perturbations resulting from a mismatch between $u'_{s,j}$ and the corresponding model $\widetilde{u}'_{s,j}$. Term I vanishes if this mismatch is oriented orthogonally to $\partial\overline{\psi}/\partial x_j$. Consequently, the model $\widetilde{u}'_{s,j}$ only needs to match $u'_{s,j}$ in the direction of $\partial\overline{\psi}/\partial x_j$ to avoid the generation of spurious convective characteristics. After the initial generation of spurious perturbations, term II describes the physical interaction of the spurious perturbations[3] with the mean flow while propagated, resulting in an additional generation/destruction/conversion of spurious convective perturbations.

A.2 Acoustic perturbations

Analogously to the balance equation for the spurious convective characteristics, an acoustic analogy for the spurious acoustic waves can be derived. Utilizing an ALE reference frame and the framework proposed in PAPER-ALE [169], the acoustic analogy is derived starting from the conservation equation of mass,

$$\left.\frac{\partial \rho'}{\partial t}\right|_{\chi} + \frac{\partial \left(\rho u_j\right)'}{\partial x_j} = u'_{s,j} \frac{\partial \overline{\rho}}{\partial x_j} \tag{A.5}$$

and the conservation equation of momentum,

$$\left.\frac{\partial \left(\rho u_i\right)'}{\partial t}\right|_{\chi} + \frac{\partial \left(\rho u_j u_i\right)'}{\partial x_j} + \frac{\partial p'}{\partial x_j}\delta_{ij} = u'_{s,j} \frac{\partial \overline{\rho u}_j}{\partial x_j} + \frac{\partial \zeta'_{\text{mom},ij}}{\partial x_j} . \tag{A.6}$$

The acoustic analogy is then derived by taking the temporal derivative (in the ALE framework) of Eq. (A.5),

$$\left.\frac{\partial^2 \rho'}{\partial t^2}\right|_{\chi} + \left.\frac{\partial}{\partial t}\left(\frac{\partial \left(\rho u_j\right)'}{\partial x_j}\right)\right|_{\chi} = \left.\frac{\partial}{\partial t}\left(u'_{s,j} \frac{\partial \overline{\rho}}{\partial x_j}\right)\right|_{\chi} \tag{A.7}$$

subtracting the divergence of Eq. (A.6),

$$\left.\frac{\partial}{\partial t}\left(\frac{\partial \left(\rho u_i\right)'}{\partial x_i}\right)\right|_{\chi} + \frac{\partial^2 \left(\rho u_j u_i\right)'}{\partial x_i \partial x_j} + \frac{\partial^2 p'}{\partial x_i \partial x_j}\delta_{ij} = \frac{\partial}{\partial x_i}\left(u'_{s,j} \frac{\partial \overline{\rho u}_j}{\partial x_j}\right) + \frac{\partial^2 \zeta'_{\text{mom},ij}}{\partial x_i \partial x_j} \tag{A.8}$$

[3] Not only a specific convective perturbation but all spurious convective and acoustic perturbations.

from it and replacing density fluctuations via

$$\rho' = \frac{p'}{\overline{c}^2} + \rho'_{\mathfrak{s}} + \rho'_{\mathfrak{c}_k}\,. \tag{A.9}$$

$p'/\overline{c}^2$, $\rho'_{\mathfrak{s}}$ and $\rho'_{\mathfrak{c}_k}$ are the density fluctuations related to acoustic, entropic and compositional disturbances. Moving all terms related to $u'_{\mathrm{s},j}$, mean flow gradients as well as non-acoustic density fluctuations to the right-hand side yields the wave equation in the ALE framework of the form

$$\begin{aligned}\frac{1}{\overline{c}^2}\left(\left.\frac{\partial^2 p'}{\partial t^2}\right|_\chi + 2\overline{u}_j\,\frac{\partial}{\partial t}\left(\frac{\partial p'}{\partial x_j}\right)\right|_\chi + \overline{u}_i\overline{u}_j\frac{\partial^2 p'}{\partial x_i \partial x_j}\right) - \frac{\partial^2 p'}{\partial x_i \partial x_j}\delta_{ij} \\ = \left.\frac{\partial}{\partial t}\left(u'_{\mathrm{s},j}\frac{\partial \overline{\rho}}{\partial x_j}\right)\right|_\chi - \frac{\partial}{\partial x_i}\left(u'_{\mathrm{s},j}\frac{\partial \overline{\rho u}_i}{\partial x_j}\right) + 2\overline{u}_i\frac{\partial}{\partial x_i}\left(u'_{\mathrm{s},j}\frac{\partial \overline{\rho}}{\partial x_j}\right) + \dot{\omega}'_{\mathrm{a}}\end{aligned} \tag{A.10}$$

$\dot{\omega}'_{\mathrm{a}}$ includes all acoustic sources unrelated to $u'_{\mathrm{s},j}$.

Utilizing the model $\widetilde{u}'_{\mathrm{s},j}$, Eq. (A.10) is approximated by

$$\begin{aligned}\frac{1}{\overline{c}^2}\left(\left.\frac{\partial^2 \widetilde{p}'}{\partial t^2}\right|_\chi + 2\overline{u}_j\,\frac{\partial}{\partial t}\left(\frac{\partial \widetilde{p}'}{\partial x_j}\right)\right|_\chi + \overline{u}_i\overline{u}_j\frac{\partial^2 \widetilde{p}'}{\partial x_i \partial x_j}\right) - \frac{\partial^2 \widetilde{p}'}{\partial x_i \partial x_j}\delta_{ij} \\ = \left.\frac{\partial}{\partial t}\left(\widetilde{u}'_{\mathrm{s},j}\frac{\partial \overline{\rho}}{\partial x_j}\right)\right|_\chi - \frac{\partial}{\partial x_i}\left(\widetilde{u}'_{\mathrm{s},j}\frac{\partial \overline{\rho u}_i}{\partial x_j}\right) + 2\overline{u}_i\frac{\partial}{\partial x_i}\left(\widetilde{u}'_{\mathrm{s},j}\frac{\partial \overline{\rho}}{\partial x_j}\right) + \widetilde{\dot{\omega}}'_{\mathrm{a}}\,.\end{aligned} \tag{A.11}$$

Substracting Eq. (A.10) from Eq. (A.11) yield the wave equation of spurious acoustic waves

$$\begin{aligned}&\frac{1}{\overline{c}^2}\left(\left.\frac{\partial^2 p'_\epsilon}{\partial t^2}\right|_\chi + 2\overline{u}_j\,\frac{\partial}{\partial t}\left(\frac{\partial p'_\epsilon}{\partial x_j}\right)\right|_\chi + \overline{u}_i\overline{u}_j\frac{\partial^2 p'_\epsilon}{\partial x_i \partial x_j}\right) - \frac{\partial^2 p'_\epsilon}{\partial x_i \partial x_j}\delta_{ij} \\ &= \underbrace{\left.\frac{\partial}{\partial t}\left(\left(\widetilde{u}'_{\mathrm{s},j} - u'_{\mathrm{s},j}\right)\frac{\partial \overline{\rho}}{\partial x_j}\right)\right|_\chi}_{\text{Ia}} \underbrace{- \frac{\partial}{\partial x_i}\left(\left(\widetilde{u}'_{\mathrm{s},j} - u'_{\mathrm{s},j}\right)\frac{\partial \overline{\rho u}_i}{\partial x_j}\right)}_{\text{Ib}} \underbrace{+ 2\overline{u}_i\frac{\partial}{\partial x_i}\left(\left(\widetilde{u}'_{\mathrm{s},j} - u'_{\mathrm{s},j}\right)\frac{\partial \overline{\rho}}{\partial x_j}\right)}_{\text{Ic}} \underbrace{+ \dot{\omega}'_{\mathrm{a},\epsilon}}_{\text{II}}\end{aligned} \tag{A.12}$$

The source term Ia denotes a spurious acoustic monopole resulting from a spurious mass flux through the exothermic reaction zone of the flame. The source terms Ib and Ic represent dipole sources due to a spurious momentum flux and spurious mass flux through the flame region, respectively. Source term II again represents the physical interaction of the spurious perturbations[4] with mean flow gradients after the initial generation, resulting in additional generation/ scattering/refraction/conversion of spurious acoustic perturbations.

[4]Not only acoustic but also convective perturbations.

B On the derivation of comprehensive jump conditions of junctions

This chapter comments on the derivation of two different types of junctions – a flow split (1-N-junction) and a flow merge (N-1-junction) – utilizing the procedure detailed in PAPER-JUMP [169]. This chapter does not detail all six steps of the derivation procedure in PAPER-JUMP [169], but only outlines first ideas on modeling the junctions and highlights specifics one should keep in mind.

B.1 The flow split – a 1-N-junction

This section considers the flow split, as illustrated in Fig. B.1. The junction is located in a duct of constant cross-section

$$A = A_1 = \sum_n^N A_{2n}\,, \tag{B.1}$$

and viscous losses are assumed to be negligible. The flow split may be separated in N flow tubes that are only coupled via the pressure acting on the interfacing streamlines. Thus, the inflow cross-section may be split into sub-cross-sections,

$$A = A_1 = \sum_n^N A_{1n}. \tag{B.2}$$

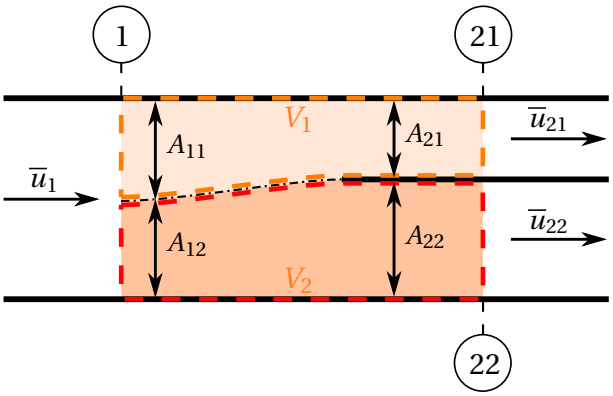

Figure B.1: Schematic representation of a 1-N-junction with $N = 2$. The junction is separated in $N = 2$ flow tubes with the volumes V_1 ( ) and V_2 ( ). The flow tubes are coupled only via the pressure on the interfacing streamline (-··-). The junction is enclosed in a duct of constant cross section.

However, note that the inlet cross-sections of the individual flow tubes depend on the flow properties and can be perturbed ($A'_{1n} \neq 0$), in contrast to the fixed geometrical outlet cross-sections ($A'_{2n} = 0$).

For this model, N volume integrations over the individual flow tubes are performed in step 2 of the procedure in PAPER-JUMP [169], providing N times $3 + (N_Y - 1)$ equations. After linearizing these equations (step 3) and choosing the local perturbed state vectors (step 4), closure models for the pressure coupling between the flow tubes must be defined. If the junction encloses a finite volume, additional closures for the accumulation terms (see PAPER-JUMP [169]) are required. Eventually, the jump condition of the 1-N-junction is determined in step 6. The $N(3 + (N_Y - 1))$ equations are used to determine u'_{2n}, s'_{2n} and $Y'_{k,2n}$ at all outflows, p'_1 at the inflow in addition to the perturbed inflow cross-sections A'_{1n} of $N-1$ flow tubes. The linearized version of Eq. (B.2) defines the N-th cross-section A'_{1N}. All other perturbations are required as an input. Note that the number of inputs equals the number of characteristic perturbations entering the system. The resulting transfer matrix $\mathbf{T}$ of the flow split is rectangular.

B.2 The flow merge – a N-1-junction

This section considers the flow merge, as illustrated in Fig. B.2. The junction is located in a duct of constant cross-section

$$A = \sum_{n}^{N} A_{1n} = A_2. \tag{B.3}$$

Viscous losses in the shear layer between the inflow streams should be considered. In contrast to the flow split (Sec. B.1), separating the junction into weakly coupled flow tubes is impossible due to the mixing of the N inflows within the junction. Thus, only a single volume integration over the entire control volume V is performed in step 2 of the framework in PAPER-JUMP [169]. This provides $3 + (N_Y - 1)$ coupling relations. However, $N + 2 + (N_Y - 1)$ coupling relations, equal to the number of characteristic perturbations leaving a N-1-junction, are required to derive the transfer matrix of the system. Thus, additional $N-1$ coupling relations

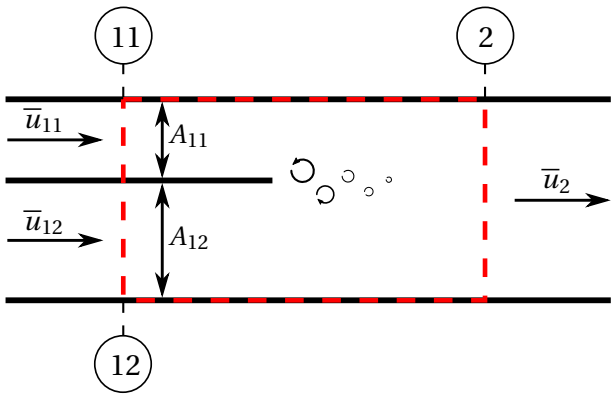

Figure B.2: Schematic representation of a N-1-junction with $N = 2$ enclosed by the control volume V (– –). The junction is enclosed in a duct of constant cross-section.

must be determined[1]. When these additional coupling relations are identified and appropriate closure models for the viscous losses (and potentially the accumulation terms (see Sec. B.1)) are defined, the procedure detailed in PAPER-JUMP [169] is straightforward. The resulting transfer matrix $\mathbf{T}$ of the N-1-junction is once again rectangular.

[1] The $N-1$ missing relations most likely couple the inflow and outflow pressures.

C Towards relaxing the assumption of compactness for jump conditions of premixed flames

This chapter outlines a concept towards relaxing the assumption of compactness for the comprehensive jump condition of a premixed flame derived in PAPER-JUMP [169]. Therefore, an expansion of the volume integrals appearing within the derivation to higher orders in Strouhal St (convective compactness) or Helmholtz He (acoustic compactness) number is required. The following sections illustrate this expansion for the accumulation term (Eq. (6.7)) for two specific examples - a non-compact premixed flame with an infinitely thin flame front (Sec. C.1) as well as a non-compact flame sheet (Sec. C.2). Combining the two approaches is required when both effects contribute to the non-compactness of the premixed flame.

C.1 A non-compact premixed flame with an infinitely thin flame front

This section considers the non-compact premixed flame schematically depicted in Fig. C.1. The flame is placed in a duct of constant cross-section A, and the control volume

$$V = \int_{\Omega} \mathrm{d}\mathbf{x} \tag{C.1}$$

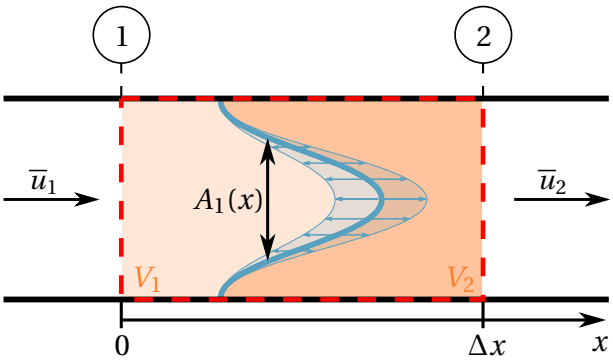

Figure C.1: Schematic representation of a non-compact premixed flame (——) including a moving flame front. The infinitely thin flame front separates the control volume V (– –) into the subvolumes V_1 ( ) and V_2 ( ).

encloses the flame at every instance. The flame front is assumed to be infinitely thin, separating the control volumes into the subvolumes V_1 upstream and V_2 downstream of the flame. The flame front displaces in response to incoming perturbations, oscillating around its mean position. The mean state vectors $\overline{\mathbf{U}}_1$ and $\overline{\mathbf{U}}_2$ are considered constant within V_1 and V_2, respectively. Under these assumption, the accumulation term (Eq. (6.7)) simplifies to

$$\frac{\partial}{\partial t}\left(\int_\Omega \mathbf{U}\,\mathrm{d}\mathbf{x}\right)' = \underbrace{\left(\overline{\mathbf{U}}_1 - \overline{\mathbf{U}}_2\right)\frac{\partial V_1'}{\partial t}}_{\mathbf{I}} + \underbrace{\frac{\partial}{\partial t}\int_\Omega \mathbf{U}_1'\,\mathrm{d}\mathbf{x}_1}_{\mathbf{IIa}} + \underbrace{\frac{\partial}{\partial t}\int_\Omega \mathbf{U}_2'\,\mathrm{d}\mathbf{x}_2}_{\mathbf{IIb}}. \tag{C.2}$$

Term **I** is related to the movement of the flame front and equivalent to the term derived in PAPER-JUMP [169] assuming compactness. In contrast, the terms **IIa** and **IIb** vanish in the limit of compactness ($\mathrm{St}, \mathrm{He} \to 0$) [169]. Relaxing the assumption of compactness requires the derivation of higher-order approximations of terms **IIa** and **IIb**.

Next, the characteristic disturbances within V_1 and V_2 are assumed to propagate without damping ($s = i\omega$, $\sigma = 0$) in x-direction only. Then, the perturbed state vectors

$$\mathbf{U}_i' = \bar{\mathbf{J}}_{U,i}\mathbf{w}_i' \tag{C.3}$$

may be expressed via the vector of characteristic perturbations

$$\mathbf{w}_i' = \begin{bmatrix} \Pi_i^+ \\ \Pi_i^- \\ \mathfrak{s}_i \\ \mathfrak{c}_{k,i} \end{bmatrix} = \begin{bmatrix} \Pi_i^+(t)\exp\left(-\frac{s(x-x_i)}{\overline{u}_1+\overline{c}_1}\right) \\ \Pi_i^-(t)\exp\left(-\frac{s(x-x_i)}{\overline{u}_1-\overline{c}_1}\right) \\ \mathfrak{s}_i(t)\exp\left(-\frac{s(x-x_i)}{\overline{u}_1}\right) \\ \mathfrak{c}_{k,i}(t)\exp\left(-\frac{s(x-x_i)}{\overline{u}_1}\right) \end{bmatrix} \quad \text{with} \quad x_1 = 0 \quad \text{and} \quad x_2 = \Delta x, \tag{C.4}$$

and the corresponding jacobian matrix

$$\bar{\mathbf{J}}_{U,i} = \frac{\partial \mathbf{U}_i'}{\partial \mathbf{w}_i'}. \tag{C.5}$$

Utilizing Eq. (C.3), the volume integrals over the perturbed state vectors within terms **IIa** and **IIb** in Eq. (C.2) simplify to

$$\frac{\partial}{\partial t}\int_\Omega \mathbf{U}_i'\,\mathrm{d}\mathbf{x}_i = \bar{\mathbf{J}}_{U,i}\frac{\partial}{\partial t}\int_0^{\Delta x} \mathbf{w}_i' A_i(x)\,\mathrm{d}x \tag{C.6}$$

$A_i(x)$ is the local cross-section of the corresponding subvolume V_i (see Fig. C.1). Approximating the cross-sections $A_1(x)$ and $A_2(x)$ via a Taylor series of order N,

$$A_1(x) \approx \sum_{n=0}^{N} \left.\frac{\mathrm{d}^n A_1^n}{\mathrm{d}x^n}\right|_0 \frac{x^n}{n!} \quad \text{and} \quad A_2(x) = A - A_1(x), \tag{C.7}$$

and moving all spatially independent factors out of the integral (Eq. (C.6)) yields only integrals of the general form

$$\int_0^{\Delta x} x^n \exp\left(\frac{s(x-x_i)}{\overline{u}_{\mathrm{ch},i}}\right)\mathrm{d}x = \sum_{p=0}^{n}(-1)^p\left(\frac{\overline{u}_{\mathrm{ch},i}}{s}\right)^{p+1}\frac{n!}{(n-p)!}\left[x^{n-p}\exp\left(\frac{s(x-x_i)}{\overline{u}_{\mathrm{ch},i}}\right)\right]_0^{\Delta x}. \tag{C.8}$$

In Eq. (C.8), $\overline{u}_{\mathrm{ch},i}$ denotes the characteristic propagation velocity and may take the values $\overline{u}_i+\overline{c}_i$, $\overline{u}_i-\overline{c}_i$ or $\overline{u}_i$ depending on the investigated characteristic. ! is the factorial.

The maximum approximation order of Eq. (C.8) in terms of St or He is n. This is shown in the following. For example, assuming a convective disturbance ($\overline{u}_{\mathrm{ch},1}=\overline{u}_1$) propagating through the subvolume V_1 ($x_1=0$), Eq. (C.8) yields

$$\begin{aligned}\int_0^{\Delta x} x^n \exp\left(\frac{sx}{\overline{u}_1}\right)\mathrm{d}x = \sum_{p=0}^{n-1}(-1)^p\left(\frac{\overline{u}_1}{s}\right)^{2p-n+1}\frac{n!}{(n-p)!}\left(2\pi i\,\mathrm{St}_1\right)^{n-p}\exp\left(2\pi i\,\mathrm{St}_1\right)\\ +(-1)^n\left(\frac{\overline{u}_1}{s}\right)^{n+1} n!\left(\exp\left(2\pi i\,\mathrm{St}_1\right)-1\right).\end{aligned} \tag{C.9}$$

Overall, the maximum value of n in Eq. (C.2) is set via the approximation order N of the cross section $A_1(x)$ (Eq. (C.7)). Furthermore, note that Eq. (C.9) vanishes in the limit of compactness ($\mathrm{St}_1=0$) as discussed for Eq. (C.2). Finally, note that Eq. (C.9) can be formulated analogously for the subvolume V_2 or for acoustic perturbations. He replaces St in case of the acoustic perturbations.

C.2 A non-compact flame sheet

This section considers the non-compact flame sheet displayed in Fig. C.2. In contrast to Sec. C.1, the flame is quasi-onedimensional with a flame front of finite thickness. Analogously to Sec. C.1, the flame is located in a duct of constant cross-section A and, at every instance, enclosed by the control volume V (Eq. (C.1)). The flame sheet with the center position $x_f(t)$ oscillates around its mean position $\overline{x}_f$ in response to incoming perturbations. Furthermore, we assume that the state vector

$$\mathbf{U}=\mathbf{U}_1+(\mathbf{U}_2-\mathbf{U}_1)\,g(x-x_f(t)) \tag{C.10}$$

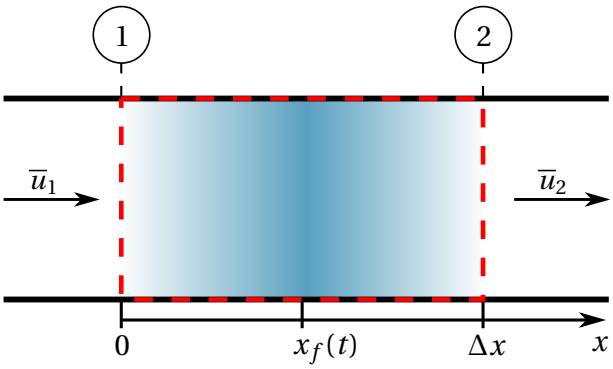

Figure C.2: Schematic representation of a non-compact premixed flame sheet (■) enclosed in the control volume V (– –). The center position of the flame sheet $x_f(t)$ displaces with time.

can be interpolated from the states upstream ($\mathbf{U}_1$) and downstream ($\mathbf{U}_2$) of the flame via the function g. g is an user-defined function, which fulfills the conditions

$$g(x_1) = 0 \quad \text{and} \quad g(x_2) = 1\,. \tag{C.11}$$

Linearizing Eq. (C.10) yields the perturbed state vector

$$\mathbf{U}' = \mathbf{U}_1' + \left(\mathbf{U}_2' - \mathbf{U}_1'\right) g(x - \overline{x_f}) + \left(\overline{\mathbf{U}}_2 - \overline{\mathbf{U}}_1\right) \overline{\frac{\mathrm{d}g}{\mathrm{d}x_f}}\, x_f'(t)\,. \tag{C.12}$$

Utilizing Eq. (C.12), the accumulation term (Eq. (6.7)) simplifies to

$$\begin{aligned}\frac{\partial}{\partial t}\left(\int_\Omega \mathbf{U}\,\mathrm{d}\mathbf{x}\right)' &= \frac{\partial}{\partial t}\int_\Omega \mathbf{U}'\,\mathrm{d}\mathbf{x} \\ &= \underbrace{\left(\overline{\mathbf{U}}_1 - \overline{\mathbf{U}}_2\right) A \frac{\partial x_f'(t)}{\partial t} \int_0^{\Delta x} \overline{\frac{\mathrm{d}g}{\mathrm{d}x_f}}\,\mathrm{d}x}_{\mathbf{I}} + \underbrace{A\int_0^{\Delta x} \mathbf{U}_1' + \left(\mathbf{U}_2' - \mathbf{U}_1'\right) g(x - \overline{x}_f)\,\mathrm{d}x}_{\mathbf{II}}\end{aligned} \tag{C.13}$$

Term **I** is related to the displacement of the flame sheet. In the compact case, this term simplifies to the accumulation term derived in PAPER-JUMP [169]. Term **II** vanishes in the compact case, but must be expanded to higher orders to relax the assumption of compactness.

For this purpose, the function $g(x - \overline{x}_f)$ is approximated by a Taylor series of order N expanded around the flame center $\overline{x}_f$,

$$g(x) \approx \sum_{n=0}^{N} \left.\frac{\mathrm{d}^n g^n}{\mathrm{d}x^n}\right|_{\overline{x}_f} \frac{(x - \overline{x}_f)^n}{n!}\,, \tag{C.14}$$

and the perturbed state vectors as formulated in Eq. (C.3) are used. Utilizing these approximations, the integrals in term **II** (Eq. (C.13)) yield again the general form in Eq. (C.8). The rest of the derivation procedure is equivalent to Sec. (C.1).

D Reproduction of peer-reviewed publications

In this chapter, all publications that contributed to this thesis are reproduced in the following. The papers are ordered analogously to chapter 7.

D.1 PAPER-ALE

Combustion and Flame 262 (2024) 113334

Contents lists available at ScienceDirect

Combustion and Flame

journal homepage: www.sciencedirect.com/journal/combustion-and-flame

An Arbitrary Lagrangian–Eulerian framework for the consistent analysis of entropy wave generation

Moritz Merk [*,1], Alexander J. Eder[1], Wolfgang Polifke

Technical University of Munich, TUM School of Engineering and Design, Department of Engineering Physics and Computation, Boltzmannstr. 15, Garching, 85747, Germany

ARTICLE INFO

Keywords:
Entropy wave generation
Moving sources
Arbitrary Lagrangian–Eulerian framework
Three-dimensional reactive flows
Quasi-one-dimensional jump condition

ABSTRACT

Entropy waves are generated in many technically relevant flow processes such as combustion, mixing, or convective heat transfer. When accelerated, entropy waves generate acoustic waves that contribute to the overall sound emission and can lead to self-excited thermoacoustic instabilities, especially at low frequencies. In order to reduce or prevent these undesirable byproducts of the flow, an understanding of the generation mechanisms of entropy waves is key. This study derives the analytical source terms of entropy disturbances for moving sources in general three-dimensional reactive flows. In this general setup, the consistent derivation of the generation mechanisms requires the tracking of the moving source for which an Arbitrary Lagrangian–Eulerian (ALE) framework is utilized. The derived differential equations provide a fundamental understanding of the underlying source mechanisms.

In addition, the general three-dimensional differential equations are reduced to a quasi-one-dimensional jump condition to unify the analysis of the entropy wave generation. This unified framework is used for an in-depth analysis of a premixed flame, where all source terms that generate entropy disturbances are analyzed and their relative importance are quantified. The dominant contribution of unsteady heat addition per unit mass to the generation of entropy waves is reaffirmed for lean premixed flames. Finally, by comparison with the entropy generation mechanisms of a heated gauze at rest, it is emphasized once more that a heat source at rest is an invalid model for a premixed flame.

Novelty and significance statement

The analytical terms of entropy wave generation are derived consistently for moving sources in a general three-dimensional reactive flow. It is shown and emphasized that a consistent derivation requires the tracking of the local entropy sources. Therefore, an Arbitrary Lagrangian–Eulerian framework is used.

The derived equations provide a fundamental insight into the generation of entropy disturbances in reactive flows, e.g. premixed flames. Furthermore, the derived equations can be seen as a starting point to consistently extract sources of entropy waves from numerical simulations.

1. Introduction

Isobaric and irrotational disturbances [1] – so-called *entropy waves* – occur in many technically relevant unsteady flow processes such as combustion, mixing, or convective heat transfer. These entropic disturbances are convected with the mean flow velocity and generate a dipole-type acoustic sound source when accelerated [2–5]. In gas turbines, aero-engines, or rocket engines, entropy waves generated in the combustion chamber are accelerated as they enter a high-pressure turbine stage or a downstream nozzle. The acoustic waves generated – some leaving the combustor and some propagating back – affect the system in two ways. The outward propagating acoustic wave contributes to the overall sound emission of the engine [6–8], while the inward propagating wave can result in self-excited low-frequency thermoacoustic combustion instability. This type of oscillation, often referred to as "rumble" [9–11], has been an active area of research [12–16] since the early work of Keller et al. [17,18] in the 1980's and can lead to reduced combustor lifetime or even system failure [6,19,20]. In order to prevent instability or to reduce the contribution to overall sound emissions, an understanding and accurate modeling of the generation, dispersion, and convection of entropy waves, and their conversion to acoustic energy is essential. This work focuses on a consistent description of entropy wave generation by unsteady combustion.

* Corresponding author.
E-mail address: moritz.merk@tfd.mw.tum.de (M. Merk).
[1] Joint first authors.

https://doi.org/10.1016/j.combustflame.2024.113334
Received 10 November 2023; Received in revised form 18 January 2024; Accepted 19 January 2024
Available online 3 February 2024

Nomenclature

Roman letters

A_s	Surface of source region (m^2)
c_p	Isobaric heat capacity ($\frac{\mathrm{J}}{\mathrm{kgK}}$)
f	Frequency (Hz)
g	Mass specific sensible-plus-chemical Gibbs' free enthalpy ($\frac{\mathrm{J}}{\mathrm{kg}}$)
h	Mass specific sensible-plus-chemical enthalpy ($\frac{\mathrm{J}}{\mathrm{kg}}$)
h_s	Mass specific sensible enthalpy ($\frac{\mathrm{J}}{\mathrm{kg}}$)
H	Mass specific total non-chemical enthalpy ($\frac{\mathrm{J}}{\mathrm{kg}}$)
$\dot{m}_\mathrm{s}$	Mass flux density relative to the local entropy source region ($\frac{\mathrm{kg}}{\mathrm{m}^2\mathrm{s}}$)
M	Mach number (-)
$\dot{M}_\mathrm{s}$	Mass flux relative to the local entropy source region ($\frac{\mathrm{kg}}{\mathrm{s}}$)
n	Normal vector (-)
p	Pressure ($\frac{\mathrm{kg}}{\mathrm{ms}^2}$)
$\dot{q}$	Volumetric heat release rate ($\frac{\mathrm{W}}{\mathrm{m}^3}$)
$\dot{Q}$	Integral heat release rate (W)
s	Mass specific sensible-plus-chemical entropy ($\frac{\mathrm{J}}{\mathrm{kgK}}$)
t	Time (s)
T	Temperature (K)
u	Flow velocity ($\frac{\mathrm{m}}{\mathrm{s}}$)
u_s	Velocity of entropy source region ($\frac{\mathrm{m}}{\mathrm{s}}$)
V	Volume (m^3)
V_k	Diffusion velocity of species k ($\frac{\mathrm{m}}{\mathrm{s}}$)
x	Eulerian coordinate (spatially fixed) (m)
x_s	(Eulerian) coordinate of the entropy source region (m)
Y	Mass fraction (-)

Greek letters

α	Heat transfer coefficient ($\frac{\mathrm{W}}{\mathrm{m}^2\mathrm{K}}$)
γ	Ratio of specific heats (-)
λ	Heat conductivity ($\frac{\mathrm{W}}{\mathrm{mK}}$)
ρ	Mass density ($\frac{\mathrm{kg}}{\mathrm{m}^3}$)
τ_{ij}	Viscous stress tensor ($\frac{\mathrm{kg}}{\mathrm{ms}^2}$)
ϕ	Equivalence ratio (-)
χ	ALE coordinate (moving with u_s) (m)
ψ	Source term of entropy generation ($\frac{\mathrm{W}}{\mathrm{m}^3\mathrm{K}}$)
Ψ	Integral source term of entropy generation ($\frac{\mathrm{W}}{\mathrm{K}}$)
$\dot{\omega}_k$	Volumetric reaction rate of species k ($\frac{\mathrm{kg}}{\mathrm{m}^3\mathrm{s}}$)
$\dot{\Omega}_k$	Integral reaction rate of species k ($\frac{\mathrm{kg}}{\mathrm{s}}$)

Operators

δ	Delta distribution
Δ	Difference
$\mathcal{H}$	Heaviside function
$\mathcal{O}$	Order of magnitude

Subscript

diff	Due to diffusive effects
gen	Generated
p	Acoustic contribution
$\vert_p$	Derivative at constant pressure
ref	Reference value
s	Entropic contribution
$\vert_s$	Derivative at constant sensible-plus-chemical entropy
$\vert_x$	Derivative at fixed Eulerian coordinate x
$\vert_\chi$	Derivative at fixed Arbitrary Lagrangian–Eulerian coordinate χ
Y	Compositional contribution
$\vert_Y$	Derivative at constant mass fraction
$\dot{\omega}_k$	Due to chemical reaction
1	Gas state in front of the reaction zone
2	Gas state behind the reaction zone
$\parallel$	Parallel to the local $\bar{s}$ gradient

Superscript

$\bar{}$	Mean
$'$	Perturbation

Abbreviations

ALE	Arbitrary Lagrangian–Eulerian
LHS	Left-hand side
Q1D	Quasi one-dimensional
RHS	Right-hand side

To develop a fundamental understanding of the processes leading to the generation of entropy waves in exothermic reaction zones, analytical [21–24] and numerical [25–29] procedures are the methods of choice in the literature. Many experimental studies concentrate on the convection and acoustic response of entropy waves [30–33] and on the conversion to acoustic energy when accelerated [34,35], but not on the underlying generation mechanisms, except e.g. [36]. In contrast, numerical calculations provide comprehensive access to the fields of all relevant physical quantities. Depending on the trade-off between accuracy and computational time, there are numerical methods of varying complexity, ranging from high-fidelity simulations, e.g., large eddy simulation, to semi-analytic network models, some of which use simplistic analytical solutions such as quasi-one dimensional (Q1D) jump conditions. In any case, analytical tools are needed to provide *a priori* the underlying system of equations and *a posteriori* guidelines for visualizing and interpreting effects of interest in the simulation results. Closed-form analytical solutions exist only for simplistic situations but can provide an in-depth understanding of physical mechanisms. A proper understanding of the analytical equations is essential for the correct interpretation of both numerical and analytical results.

Starting from analytically derived entropy balance equations in differential form, several studies such as Morgans and Duran [8] or Duran et al. [7] argue that the total unsteady heat release rate of a flame contributes to the generation of entropy waves and that a perturbation of the heat-to-flow power ratio is the origin of entropic perturbations [37]. Derived from the same balance equations, several analytically reduced quasi-one-dimensional jump conditions agree with this conclusion [36,38–40]. However, all of these studies consider the flame as a heat source at rest. In contrast, a premixed flame front exhibits local displacements in response to various disturbances (e.g. acoustics, upstream flow velocity, vortical flow structures, turbulence, fuel concentration). This neglect of flame motion leads problematically to the spurious generation of entropy waves, as shown by Strobio Chen et al. [22] for a Q1D jump condition across a premixed flame, or by Meindl et al. [27] in one- and two-dimensional numerical simulations. This conclusion is widely accepted for quasi-one-dimensional jump conditions [41–46]. However, especially in differential/integral equations, the effect of flame motion on the source term of entropy waves is not

obvious, and the resulting source terms have been misinterpreted [23, 47].

Other studies, e.g. [13,17,37,48,49], argue from theoretical considerations or the derivation of one-dimensional jump conditions that perturbations of the heat added per unit mass are the only important generation mechanism of entropy waves in exothermic reaction zones. However, to the best of the authors' knowledge, the corresponding source terms have never been isolated adequately in differential/integral equations.

The objective of this work is (i) to consistently derive the source terms of entropy disturbances for moving sources in general three-dimensional reactive flows, and (ii) to unify the description of entropy wave generation of moving sources from the three-dimensional differential equations to the limit of quasi-one-dimensional jump conditions. An Arbitrary Lagrangian–Eulerian (ALE) reference frame [50] is used to explicitly take into account the movement of the source region.

The paper is structured as follows: In Section 2.1, the general three-dimensional differential balance equation for entropy disturbances is derived, and the entropy source terms of general sources in motion are identified. Section 2.2 reduces the differential equation to a quasi-one-dimensional jump condition to simplify the subsequent analysis of the individual source terms and recover the results of Strobio Chen et al. [22]. Section 3 evaluates the jump condition for two exemplary cases – a moving lean premixed flame front and a fixed heated source such as a heated gauze – including a detailed source term analysis for the lean premixed flame. Section 4 provides a conclusion and outlook for future work.

2. Analytical framework

Analyzing the source terms of entropy perturbations in flow differential equations provides an insight into the underlying physical mechanisms *and* their importance in various physical configurations. For a meaningful analysis, the isolation of terms generating entropy perturbations from simple transport terms is crucial. In the most general case of a moving entropy source region, the displacement of its time-invariant part does not generate entropy perturbations [22, 27,51]. The strict separation between mechanisms of transport and generation in the differential equations requires the tracking of the local displacement of the entropy source region. Analytically, this is achieved by using an Arbitrary Lagrangian–Eulerian coordinate system [50] following the entropy source region as proposed by Heilmann et al. [51].

This paragraph utilizes the example of a one-dimensional, perfectly premixed exothermic reaction zone in the limit of negligible diffusive effects to illustrate the need for entropy source tracking to strictly separate the generation and transport mechanisms of entropy disturbances. The investigated reaction zone is kinematically stabilized and responds to incoming velocity perturbations by a displacement of the reaction zone. No entropy disturbances are generated [22] since the global entropy generation remains time-invariant. This simplistic example is shown in Fig. 1(a) in an Eulerian coordinate system x (spatially fixed) with a relative motion between the coordinate system and the entropy source region. In the subfigure on the left, the spatial distribution of entropy is displayed. The subfigure on the right shows the respective temporal entropy signal observed at the fixed coordinate x^*. In the case of the fixed coordinate system, a *non-constant, time-dependent* entropy signal is observed at x^*, which might be interpreted as the result of a source of entropy waves. However, this signal is not evidence for the generation of a convected entropy disturbance but merely an artifact of the relative motion of the entropy source region relative to x^*. This artifact disappears when the exothermic reaction zone is expressed in an ALE coordinate system χ that perfectly tracks the entropy source region (see Fig. 1(b)). In this case there is no relative movement between the entropy source region and the coordinate system (Fig. 1(b) (left)) and the expected *constant, time-invariant* entropy signal is observed at the coordinate χ^* (Fig. 1(b) (right)).

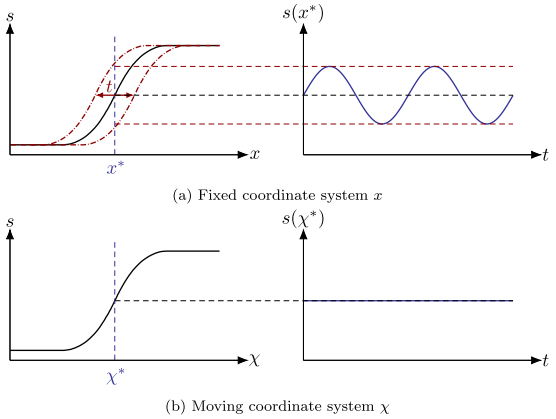

(a) Fixed coordinate system x

(b) Moving coordinate system χ

Fig. 1. One-dimensional fully premixed exothermic reaction zone perturbed by incoming velocity perturbations expressed in (a) a fixed (Eulerian) coordinate system x and (b) a moving (ALE) coordinate system χ perfectly tracking the corresponding entropy source region. The subplots on the left depict the spatial entropy distribution in the different coordinate system. The subplots on the right show the temporal entropy signal at the fixed coordinates x^* and χ^*, respectively.

In this work, the ALE framework [50] is used to unify the analytical source formulation of entropy disturbances from the general three-dimensional balance equations to the quasi-one-dimensional jump condition. The derivations throughout this work involve the transformation between the ALE, the Eulerian, and the Lagrangian (coordinate system moving with a reference mass) frameworks. Expressed in the fixed spatial coordinates x, the three-dimensional coordinate transformation between the different systems is performed by simply rewriting the convective operator [50]. Using Einstein notation, the convective operator of the different coordinate systems expressed in the fixed spatial coordinates x reads

$$\underbrace{\frac{\mathrm{D}}{\mathrm{D}t}}_{\text{Lagrangian}} = \underbrace{\left.\frac{\partial}{\partial t}\right|_{\chi} + \left(u_j - u_{\mathrm{s},j}\right)\frac{\partial}{\partial x_j}}_{\text{ALE}} = \underbrace{\left.\frac{\partial}{\partial t}\right|_{x} + u_j\frac{\partial}{\partial x_j}}_{\text{Eulerian}}. \tag{1}$$

This expression of the ALE framework in the non-moving coordinates x is chosen for a more straightforward application in numerical simulations. We refer to Donéa and Huerta [50] for a detailed derivation of this corresponding coordinate transformation. In Eq. (1), $u_{\mathrm{s},j}$ is the local velocity between the moving ALE coordinates χ and the fixed Eulerian coordinates x. Since the ALE framework perfectly tracks the entropy source regions throughout this work, $u_{\mathrm{s},j}$ is equal the local movement of these regions. $\partial/\partial t|_x$ and $\partial/\partial t|_\chi$ refer to the time derivatives at the fixed coordinate x and χ, respectively. The difference between the two time derivatives is the displacement operator

$$\left.\frac{\partial}{\partial t}\right|_{x} - \left.\frac{\partial}{\partial t}\right|_{\chi} = -u_{\mathrm{s},j}\frac{\partial}{\partial x_j}. \tag{2}$$

Its effect is visualized in Fig. 1(a) (right) for the perturbed one-dimensional fully premixed flame. The explicit appearance of the displacement operator in (Eq. (2)) in the ALE framework is key to the strict separation of generation and transport mechanisms in differential equations.

2.1. General balance equation for entropy disturbance

The derivation of the balance equation for entropy disturbances in general three-dimensional reacting flows of an ideal gas mixture starts

from the Gibbs' equation of a multi-component gas [52–55]:

$$T\,\mathrm{d}s = \mathrm{d}h - \frac{\mathrm{d}p}{\rho} - \sum_{k=1}^{N} g_k \mathrm{d}Y_k \,, \tag{3}$$

where ρ, p, T, $h = \sum_{k=1}^{N} h_k Y_k$ and $s = \sum_{k=1}^{N} s_k Y_k$ are the density, the pressure, the temperature, the sensible-plus-chemical enthalpy, and entropy. Y_k and $g_k = h_k - T s_k$ are the mass fraction and the sensible-plus-chemical Gibbs' free enthalpy of the kth of N species, respectively.

For flow problems, the total differentials d in Eq. (3) are replaced by the material derivatives D/Dt (Lagrangian framework) and after multiplication with ρ/T, Eq. (3) reads

$$\rho\frac{\mathrm{D}s}{\mathrm{D}t} = \frac{1}{T}\left(\rho\frac{\mathrm{D}h}{\mathrm{D}t} - \frac{\mathrm{D}p}{\mathrm{D}t}\right) - \sum_{k=1}^{N}\frac{g_k}{T}\rho\frac{\mathrm{D}Y_k}{\mathrm{D}t} \,. \tag{4}$$

Next, the balance equation for sensible-plus-chemical enthalpy [55,56]

$$\rho\frac{\mathrm{D}h}{\mathrm{D}t} - \frac{\mathrm{D}p}{\mathrm{D}t} = \tau_{ji}\frac{\partial u_j}{\partial x_i} + \frac{\partial}{\partial x_j}\left(\lambda\frac{\partial T}{\partial x_j}\right) - \frac{\partial}{\partial x_j}\left(\rho\sum_{k=1}^{N} h_k Y_k V_{k,j}\right) \,, \tag{5}$$

and the species balance equations [56]

$$\rho\frac{\mathrm{D}Y_k}{\mathrm{D}t} = -\frac{\partial}{\partial x_j}\left(\rho Y_k V_{k,j}\right) + \dot{\omega}_k \,, \tag{6}$$

are used to gain a better insight into the mechanisms of entropy generation. In Eqs. (5) and (6), volume forces and volumetric heat sources (e.g. an electric spark or a radiative flux) are neglected. τ_{ij}, λ, V_k and $\dot{\omega}_k$ are the viscous stress tensor, the heat conductivity, the diffusion velocity and the volumetric reaction rate of specie k. Substituting Eqs. (5) and (6) into Eq. (4) and transforming from the Lagrangian to the ALE framework (see Eq. (1)) yields the entropy balance equation for a general three-dimensional reacting flow

$$\rho\frac{\mathrm{D}s}{\mathrm{D}t} = \rho\left.\frac{\partial s}{\partial t}\right|_{\chi} + \underbrace{\rho\left(u_j - u_{\mathrm{s},j}\right)}_{\dot{m}_{\mathrm{s},j}}\frac{\partial s}{\partial x_j} = \psi_{\dot{\omega}_k} + \psi_{\mathrm{diff}} \,. \tag{7}$$

The mass flux density $\dot{m}_{\mathrm{s},j}$ is introduced for brevity and describes the local mass flux density relative to the local entropy source region, which is moving with the local velocity $u_{\mathrm{s},j}$. The two source terms on the right-hand side (RHS) of Eq. (7)

$$\psi_{\dot{\omega}_k} = -\sum_{k=1}^{N}\frac{g_k}{T}\dot{\omega}_k = \frac{\dot{q}}{T} - \sum_{k=1}^{N}\frac{h_{\mathrm{s},k}}{T}\dot{\omega}_k + \sum_{k=1}^{N} s_k\dot{\omega}_k \,, \tag{8}$$

and

$$\psi_{\mathrm{diff}} = \frac{1}{T}\tau_{ji}\frac{\partial u_j}{\partial x_i} + \frac{1}{T}\frac{\partial}{\partial x_j}\left(\lambda\frac{\partial T}{\partial x_j}\right) + \sum_{k=1}^{N} s_k\frac{\partial}{\partial x_j}\left(\rho Y_k V_{k,j}\right) - \frac{1}{T}\sum_{k=1}^{N}\frac{\partial h_k}{\partial x_j}\rho Y_k V_{k,j} \,, \tag{9}$$

correspond to the entropy generation due to chemical reactions and due to diffusive effects, respectively. In Eq. (8), $\psi_{\dot{\omega}_k}$ is further divided into three processes [28]. The first term corresponds to the entropy generation due to the volumetric chemical heat release rate $\dot{q} = -\sum_{k=1}^{N}\Delta h^0_{f,k}\dot{\omega}_k$ - the energy conversion process from chemical into sensible enthalpy. The second and third terms take into account the changes in sensible[2] enthalpy h_{s} and the sensible-plus-chemical entropy due to a change in the composition of the gas mixture. The source term ψ_{diff} is divided into four contributions, namely (from left to right in Eq. (9)) viscous dissipation, heat conduction, entropy transport by species diffusion and enthalpy transport by species diffusion.

[2] Note that the "chemical part" of the sensible-plus-chemical enthalpy h is already included in the first term $\dot{q}/T$ via the definition of the volumetric heat release rate.

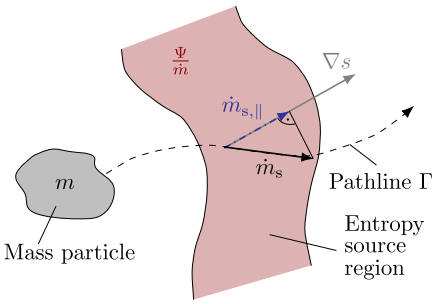

Fig. 2. Mass particle m convects along its pathline Γ across a source region with the entropy source density $\psi/\dot{m}_{\mathrm{s},\parallel} = \left(\psi_{\dot{\omega}_k} + \psi_{\mathrm{diff}}\right)/\dot{m}_{\mathrm{s},\parallel}$.

Eq. (7) is valid for general unsteady flows. The aim of the following paragraph is to derive the balance equation for low-amplitude entropy perturbations based on a first-order perturbation ansatz, which is introduced into Eq. (7) by expressing all physical quantities $Y(x,t) = \overline{Y}(x) + Y'(x,t)$ as the sum of a time-invariant mean $\overline{Y}(x)$ and a small fluctuating part $Y'(x,t) \ll \overline{Y}(x)$. Then, applying a subsequent separation of scales allows to split Eq. (7) into its mean (zeroth-order perturbation)

$$\overline{\dot{m}}_{\mathrm{s},j}\frac{\partial\overline{s}}{\partial x_j} = \overline{\psi}_{\dot{\omega}_k} + \overline{\psi}_{\mathrm{diff}} \,, \tag{10}$$

and its linearized (first-order perturbation) part

$$\overline{\rho}\left.\frac{\partial s'}{\partial t}\right|_{\chi} + \overline{\dot{m}}_{\mathrm{s},j}\frac{\partial s'}{\partial x_j} = -\dot{m}'_{\mathrm{s},j}\frac{\partial\overline{s}}{\partial x_j} + \psi'_{\dot{\omega}_k} + \psi'_{\mathrm{diff}} \,. \tag{11}$$

In Eqs. (10) and (11), the terms $\overline{\dot{m}}_{\mathrm{s},j}\frac{\partial\overline{s}}{\partial x_j}$ and $\dot{m}'_{\mathrm{s},j}\frac{\partial\overline{s}}{\partial x_j}$ represent the projection of the mean and perturbed mass flux densities onto the local mean sensible-plus-chemical entropy gradient and can be reformulated as

$$\overline{\dot{m}}_{\mathrm{s},j}\frac{\partial\overline{s}}{\partial x_j} = \overline{\dot{m}}_{\mathrm{s},\parallel}n_j\frac{\partial\overline{s}}{\partial x_j} \qquad \text{and} \qquad \dot{m}'_{\mathrm{s},j}\frac{\partial\overline{s}}{\partial x_j} = \dot{m}'_{\mathrm{s},\parallel}n_j\frac{\partial\overline{s}}{\partial x_j} \,, \tag{12}$$

with the amplitudes of the mean $\overline{\dot{m}}_{\mathrm{s},\parallel}$ and perturbed $\dot{m}'_{\mathrm{s},\parallel}$ mass flux densities in the direction of the mean sensible-plus-chemical entropy gradient $\partial\overline{s}/\partial x_j$ (see Fig. 2), and the corresponding normal vector

$$n_j = \frac{\frac{\partial\overline{s}}{\partial x_j}}{\left|\frac{\partial\overline{s}}{\partial x_i}\right|} \,. \tag{13}$$

Then, by taking advantage of the projection property in Eq. (12), the mean sensible-plus-chemical entropy gradient in the linearized entropy balance equation (11) is substituted with the mean entropy balance equation (10), yielding

$$\begin{aligned}\underbrace{\overline{\rho}\left.\frac{\partial s'}{\partial t}\right|_{\chi} + \overline{\dot{m}}_{\mathrm{s},j}\frac{\partial s'}{\partial x_j}}_{\text{Transport}} &= \overline{\psi}_{\dot{\omega}_k}\left(\frac{\psi'_{\dot{\omega}_k}}{\overline{\psi}_{\dot{\omega}_k}} - \frac{\dot{m}'_{\mathrm{s},\parallel}}{\overline{\dot{m}}_{\mathrm{s},\parallel}}\right) + \overline{\psi}_{\mathrm{diff}}\left(\frac{\psi'_{\mathrm{diff}}}{\overline{\psi}_{\mathrm{diff}}} - \frac{\dot{m}'_{\mathrm{s},\parallel}}{\overline{\dot{m}}_{\mathrm{s},\parallel}}\right) \\ &= \underbrace{\overline{\dot{m}}_{\mathrm{s},\parallel}\left(\frac{\psi_{\dot{\omega}_k}}{\dot{m}_{\mathrm{s},\parallel}}\right)' + \overline{\dot{m}}_{\mathrm{s},\parallel}\left(\frac{\psi_{\mathrm{diff}}}{\dot{m}_{\mathrm{s},\parallel}}\right)'}_{\text{Generation}} \,,\end{aligned} \tag{14}$$

with

$$\left(\frac{\Psi_{\dot\omega_k}}{\dot m_{\mathrm{s},\parallel}}\right)' = \frac{\overline{\dot q}}{\overline{\dot m}_{\mathrm{s},\parallel}\overline{T}}\left[\frac{\left(\frac{\dot q}{\dot m_{\mathrm{s},\parallel}}\right)'}{\left(\frac{\dot q}{\dot m_{\mathrm{s},\parallel}}\right)} - \frac{T'}{\overline{T}}\right] - \sum_{k=1}^{N}\frac{\overline{h}_{s,k}}{\overline{T}}\frac{\overline{\dot\omega}_k}{\overline{\dot m}_{\mathrm{s},\parallel}}\left[\frac{\left(\frac{\dot\omega_k}{\dot m_{\mathrm{s},\parallel}}\right)'}{\left(\frac{\dot\omega_k}{\dot m_{\mathrm{s},\parallel}}\right)} + \left(\frac{\overline{c}_{\mathrm{p},k}\overline{T}}{\overline{h}_{s,k}} - 1\right)\frac{T'}{\overline{T}}\right] + \sum_{k=1}^{N}\overline{s}_k\frac{\overline{\dot\omega}_k}{\overline{\dot m}_{\mathrm{s},\parallel}}\left[\frac{\left(\frac{\dot\omega_k}{\dot m_{\mathrm{s},\parallel}}\right)'}{\left(\frac{\dot\omega_k}{\dot m_{\mathrm{s},\parallel}}\right)} + \frac{s_k'}{\overline{s}_k}\right] \tag{15}$$

and

$$\left(\frac{\Psi_{\mathrm{diff}}}{\dot m_{\mathrm{s},\parallel}}\right)' = \left(\frac{\tau_{ji}\frac{\partial u_j}{\partial x_i}}{\dot m_{\mathrm{s},\parallel}\overline{T}}\right)' + \left(\frac{\frac{\partial}{\partial x_j}\left(\lambda\frac{\partial T}{\partial x_j}\right)}{\dot m_{\mathrm{s},\parallel}T}\right)' + \left(\frac{\sum_{k=1}^{N} s_k\frac{\partial \rho Y_k V_{k,j}}{\partial x_j}}{\dot m_{\mathrm{s},\parallel}}\right)' - \left(\frac{\sum_{k=1}^{N}\frac{\partial h_k}{\partial x_j}\rho Y_k V_{k,j}}{\dot m_{\mathrm{s},\parallel}T}\right)' . \tag{16}$$

Eq. (14) is the balance equation for small sensible-plus-chemical entropy perturbations strictly separating terms related to transport (left-hand side (LHS)) and generation (RHS).

The generation terms on the RHS of Eq. (14) show that small-scale entropy perturbations are generated only by disturbances of the local sources $\psi_{\dot\omega_k}/\dot m_{\mathrm{s},\parallel}$ (unit J/(kg m K)) or $\psi_{\mathrm{diff}}/\dot m_{\mathrm{s},\parallel}$ (unit J/(kg m K)). By analyzing the corresponding units, two important contributions can be identified: First, the length-based density[3] (unit 1/m) of the local energy addition per unit mass (unit J/kg). Integration of this quantity along the path of a mass particle moving through an entropy source region gives its total energy change per unit mass. To the local entropy generation, only the mass flux density parallel to the local entropy gradient contributes. The second important effect is the temperature at which the local energy addition per unit mass density takes place (unit J/(kg m)). The local entropy generation decreases with increasing temperature for a constant length-based density of the local energy addition per unit mass. The total entropy generated per unit mass across an entropy source region is then given by the path integral

$$s_{\mathrm{gen}} = \int_\Gamma \frac{\psi_{\dot\omega_k} + \psi_{\mathrm{diff}}}{\dot m_{\mathrm{s},\parallel}}\,\mathrm{d}x \tag{17}$$

as shown in Fig. 2.

2.2. Jump condition for entropy disturbance across a moving heat source

This section derives a Q1D jump condition that models the generation of entropy perturbations across a source region. The Q1D jump condition is an explicit analytical solution of the general balance equation (14) of entropy perturbations integrated over a convectively compact control volume enclosing an infinitesimally thin source sheet (see Fig. 3). Diffusive effects are assumed to be negligible ($\psi_{\mathrm{diff}} \approx 0$). The source sheet is a continuous, two-dimensional surface in motion. All state variables Y (e.g. $\dot m_{\mathrm{s}}$, ρ, p, T, s) are modeled via step functions

$$Y \equiv Y_1 + (Y_2 - Y_1)\mathcal{H}\left(\mathbf{x} - \mathbf{x}_{\mathrm{s}}(t)\right) , \tag{18}$$

[3] A length-based density of a quantity Y refers to this quantity per unit length. This definition is analogous to area-based densities such as the mass flux density $\dot m_{\mathrm{s}}$ (mass flux $\dot M_{\mathrm{s}}$ per unit area) or to volume-based densities such as the mass density ρ (mass per unit volume).

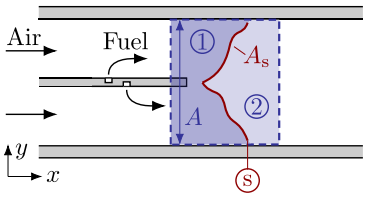

Fig. 3. Spatially fixed control volume V (dark blue, dashed line) enclosing an entropy source region in motion (s, dark red, wrinkled solid line). The flow states in front (1, dark blue) and after (2, light blue) the source region are indicated. The example is based on a generic partially premixed burner. (For interpretation of the references to color in this figure legend, the reader is referred to the web version of this article.)

with the Heaviside function defined as

$$\mathcal{H}\left(\mathbf{x} - \mathbf{x}_{\mathrm{s}}(t)\right) \equiv \begin{cases} 0, & \mathbf{x} < \mathbf{x}_{\mathrm{s}}(t) \\ \mathrm{ref}, & \mathbf{x} = \mathbf{x}_{\mathrm{s}}(t) \\ 1, & \mathbf{x} > \mathbf{x}_{\mathrm{s}}(t) \end{cases} . \tag{19}$$

State variables upstream and downstream of the entropy source region are assumed to be constant and are denoted by $(\cdot)_1$ and $(\cdot)_2$, respectively. $\mathbf{x}$ is the spatial coordinate and $\mathbf{x}_{\mathrm{s}}(t)$ is the time-dependent location of the source region. 'ref' denotes a reference value of the variable in the source region. We refer to Laksana et al. [57] for how to choose this reference value for reactive flows.

The volumetric heat release rate $\dot q$ as well as the volumetric reaction rates $\dot\omega_k$ are modeled as

$$\begin{aligned} \dot q &\equiv \frac{\dot Q}{A_{\mathrm{s}}}\,\delta\left(\mathbf{x} - \mathbf{x}_{\mathrm{s}}(t)\right) \quad &\Rightarrow \quad \dot Q &= \int \dot q\,\mathrm{d}V \\ \dot\omega_k &\equiv \frac{\dot\Omega_k}{A_{\mathrm{s}}}\,\delta\left(\mathbf{x} - \mathbf{x}_{\mathrm{s}}(t)\right) \quad &\Rightarrow \quad \dot\Omega_k &= \int \dot\omega_k\,\mathrm{d}V \end{aligned} \tag{20}$$

with the integral heat release rate $\dot Q$, the integral reaction rates $\dot\Omega_k$, the delta distribution δ and the surface of the source region A_{s} (see Fig. 3).

Integrating over a control volume V as shown in Fig. 3 under the Q1D assumptions and for negligible diffusive effects, Eq. (7) simplifies to

$$\dot M_{\mathrm{s}}\left(s_2 - s_1\right) = \Psi_{\dot\omega_k} , \tag{21}$$

with

$$\Psi_{\dot\omega_k} = \frac{\dot Q}{T_{\mathrm{ref}}} - \sum_{k=1}^{N}\left(\frac{h_{\mathrm{s},k}}{T}\right)_{\mathrm{ref}}\dot\Omega_k + \sum_{k=1}^{N} s_{k,\mathrm{ref}}\dot\Omega_k , \tag{22}$$

where $\dot M_{\mathrm{s}} = \int \dot m_{\mathrm{s},j}\,\mathrm{d}A_s$ is the mass flux across the entropy source region. Analogous to Section 2.1, the introduction of the first-order perturbation ansatz and the subsequent separation of scales yields the Q1D entropy jump condition as

$$\underbrace{\overline{\dot M}_{\mathrm{s}}\left(s_2' - s_1'\right)}_{\text{Transport}} = \underbrace{\overline{\dot M}_{\mathrm{s}}\left(\frac{\Psi_{\dot\omega_k}}{\dot M_{\mathrm{s}}}\right)'}_{\text{Generation}} , \tag{23}$$

with the source term

$$\left(\frac{\Psi_{\dot\omega_k}}{\dot M_{\mathrm{s}}}\right)' = \frac{\overline{\dot Q}}{\overline{\dot M}_{\mathrm{s}}\overline{T}_{\mathrm{ref}}}\left[\frac{\left(\frac{\dot Q}{\dot M_{\mathrm{s}}}\right)'}{\left(\frac{\dot Q}{\dot M_{\mathrm{s}}}\right)} - \frac{T'_{\mathrm{ref}}}{\overline{T}_{\mathrm{ref}}}\right] - \sum_{k=1}^{N}\left(\frac{\overline{h}_{s,k}}{\overline{T}}\right)_{\mathrm{ref}}\frac{\overline{\dot\Omega}_k}{\overline{\dot M}_{\mathrm{s}}}\left[\frac{\left(\frac{\dot\Omega_k}{\dot M_{\mathrm{s}}}\right)'}{\left(\frac{\dot\Omega_k}{\dot M_{\mathrm{s}}}\right)} + \left(\frac{\overline{c}_{\mathrm{p},k}\overline{T}}{\overline{h}_{s,k}} - 1\right)_{\mathrm{ref}}\frac{T'_{\mathrm{ref}}}{\overline{T}_{\mathrm{ref}}}\right] + \sum_{k=1}^{N}\overline{s}_{k,\mathrm{ref}}\frac{\overline{\dot\Omega}_k}{\overline{\dot M}_{\mathrm{s}}}\left[\frac{\left(\frac{\dot\Omega_k}{\dot M_{\mathrm{s}}}\right)'}{\left(\frac{\dot\Omega_k}{\dot M_{\mathrm{s}}}\right)} + \frac{s'_{k,\mathrm{ref}}}{\overline{s}_{k,\mathrm{ref}}}\right] . \tag{24}$$

An extensive derivation of the Q1D jump condition is given in Section 1 of the supplementary material.

Comparing the reactive entropy source term of the Q1D jump condition in Eq. (24) and the general 3D formulation in Eq. (15), their identical structure is evident. Note that the vectorial mass flux density $\dot{m}_{s,j}$ and the amplitude of the mass flux density parallel $\dot{m}_{s,\parallel}$ to the mean density gradient in Eq. (15) both coincide in the mass flux $\dot{M}_s$ in Eq. (24) due to the quasi-one-dimensional assumption. In analogy to Section 2, the source term of entropy disturbances (Eq. (24)) in the quasi-one-dimensional limit results from an energy addition per unit mass added at a given temperature level. It includes a contribution of the heat addition per unit mass.

For consistency, the derivation of the jump condition (Eq. (23)) in this work is based on the general entropy balance equation derived in Section 2.1. However, this approach requires the explicit definition of a reference state within the source region to approximate integrals such as $\int \dot{q}/T \mathrm{d}V$. This difficulty is avoided if the derivation of the entropy disturbance jump condition is based on the energy equation as is usually done in the literature [22,43]. Both derivation approaches are equivalent if the reference temperature is chosen as

$$T_{\mathrm{ref}} = \frac{h_{s,2} - h_{s,1}}{s_2 - s_1} - \frac{1}{2}\frac{u_2^2 - u_1^2}{s_2 - s_1}. \tag{25}$$

Utilizing this reference temperature and introducing constant gas properties, no species fluctuations and an approximation to the first and third order in Mach number into Eq. (23) yields the jump conditions derived by Strobio Chen et al. [22] and Gant et al. [43], respectively. More details are found in Section 2 of the supplementary material.

In the following section, the similarity between the three-dimensional balance equation of entropy disturbances Eq. (14) and the quasi-one-dimensional jump condition Eq. (23) is used to better understand the general source terms.

3. Generation of entropy waves by moving and fixed heat sources

Numerous unsteady physical processes generate entropy waves, and Section 2 presents a unified framework for consistently analyzing the underlying mechanisms responsible for their generation. In this section, the framework is applied to two exemplary cases – a lean premixed flame in convective balance and a heated wire at rest – to understand the dominant mechanisms that generate entropy waves in both cases. The comparison of the two cases highlights the inherent difference in the generation of entropy waves for sources at rest and in motion.

3.1. Heat source in motion - A lean premixed flame

A *lean premixed flame* is an exothermic reaction zone, where fuel reacts with an excess of oxidizer. In analytical descriptions, the reaction mechanism models the reaction kinetics, while the species balance equations express the transport of individual species. The analysis of the dominant entropy generation mechanism in a premixed flame is divided into two parts. The first part investigates the non-diffusive entropy source terms based on the formulation of the Q1D jump condition in Eq. (24) following an order of magnitude analysis. In addition, the non-diffusive generation mechanisms are explained using temperature-entropy diagrams. The second part provides a rule of thumb for the consideration of diffusive terms (see Eq. (16)).

3.1.1. The non-diffusive entropy generation mechanisms of a premixed flame

Assuming complete combustion and infinitely fast reaction, the heat added per unit mass and the mass of species k reacting per unit mass of a lean premixed flame can be written as [22,58,59]

$$\frac{\dot{Q}}{\dot{M}_s} = \Delta h_r \phi \quad \text{and} \quad \frac{\dot{\Omega}_k}{\dot{M}_s} = Y_{2,k} - Y_{1,k} = \Delta Y_k\,, \tag{26}$$

with the heat of reaction Δh_r and the equivalence ratio ϕ. Then, the linearization of Eq. (26) under the assumption of a constant fuel composition ($\Delta h_r' = 0$) yields

$$\frac{\left(\frac{\dot{Q}}{\dot{M}_s}\right)'}{\left(\frac{\dot{Q}}{\dot{M}_s}\right)} = \frac{\phi'}{\overline{\phi}} \quad \text{and} \quad \frac{\left(\frac{\dot{\Omega}_k}{\dot{M}_s}\right)'}{\left(\frac{\dot{\Omega}}{\dot{M}_s}\right)} = \frac{Y_{2,k}' - Y_{1,k}'}{\overline{Y}_{2,k} - \overline{Y}_{1,k}} = \frac{\Delta Y_k'}{\Delta \overline{Y}_k}\,. \tag{27}$$

Substituting Eq. (27) into Eq. (23) leads to the Q1D balance equation for entropy waves of a lean premixed flame

$$\overline{\dot{M}}_s \left(s_2' - s_1'\right) = \overline{\dot{M}}_s \left[\left(\frac{\Psi_{\dot{\omega}_k}}{\dot{M}_s}\right)_{\mathrm{I}}' + \left(\frac{\Psi_{\dot{\omega}_k}}{\dot{M}_s}\right)_{\mathrm{II}}' + \left(\frac{\Psi_{\dot{\omega}_k}}{\dot{M}_s}\right)_{\mathrm{III}}'\right], \tag{28}$$

where the generation of entropy waves by the energy conversion from chemical to internal energy at a specific temperature level T_{ref} is expressed as

$$\left(\frac{\Psi_{\dot{\omega}_k}}{\dot{M}_s}\right)_{\mathrm{I}}' = \frac{\overline{\dot{Q}}}{\overline{\dot{M}}_s \overline{T}_{\mathrm{ref}}}\left(\frac{\phi'}{\overline{\phi}} - \frac{T_{\mathrm{ref}}'}{\overline{T}_{\mathrm{ref}}}\right). \tag{29}$$

The remaining source terms in Eq. (28) refer to a change in sensible enthalpy due to either a change in composition or due to the temperature dependence of the gas properties

$$\left(\frac{\Psi_{\dot{\omega}_k}}{\dot{M}_s}\right)_{\mathrm{II}}' = -\sum_{k=1}^{N}\left(\frac{\overline{h}_{s,k}}{\overline{T}}\right)_{\mathrm{ref}} \Delta \overline{Y}_k \left[\frac{\Delta Y_k'}{\Delta \overline{Y}_k} + \left(\frac{\overline{c}_{\mathrm{p},k}\overline{T}}{\overline{h}_{s,k}} - 1\right)_{\mathrm{ref}} \frac{T_{\mathrm{ref}}'}{\overline{T}_{\mathrm{ref}}}\right], \tag{30}$$

and a change in the chemical-plus-sensible entropy once again either due to a change in composition or its dependency on a temperature or pressure change

$$\left(\frac{\Psi_{\dot{\omega}_k}}{\dot{M}_s}\right)_{\mathrm{III}}' = \sum_{k=1}^{N} \overline{s}_{k,\mathrm{ref}} \Delta \overline{Y}_k \left[\frac{\Delta Y_k'}{\Delta \overline{Y}_k} + \frac{s_{k,\mathrm{ref}}'}{\overline{s}_{k,\mathrm{ref}}}\right], \tag{31}$$

respectively.

The source terms on the RHS of Eq. (28) originate from the interaction of an incoming perturbation with the exothermic reaction zone. In the small perturbation limit, incoming disturbances are considered as a superposition of acoustic (p'), entropic (s'), and compositional (ϕ', Y_k') waves.[4] This decomposition may be introduced into Eqs. (29), (30) and (31) by the substitution of the temperature fluctuations with the linearization of the Gibbs equation (3)

$$\frac{T'}{\overline{T}} = \underbrace{\frac{\gamma - 1}{\gamma}\frac{p'}{\overline{p}}}_{\text{acoustic}} + \underbrace{\frac{s'}{\overline{c}_{\mathrm{p}}}}_{\text{entropic}} - \underbrace{\sum_k \frac{\overline{s}_k}{\overline{c}_{\mathrm{p}}} Y_k'}_{\text{compositional}}, \tag{32}$$

and the linearization of the sensible-plus-chemical entropy of species k

$$s_k' = \underbrace{\left.\overline{\frac{\partial s_k}{\partial p}}\right|_{s,Y_k} p'}_{\text{acoustic}} + \underbrace{\left.\overline{\frac{\partial s_k}{\partial s}}\right|_{p,Y_k} s'}_{\text{entropic}} + \underbrace{\left.\overline{\frac{\partial s_k}{\partial Y_k}}\right|_{p,s,Y_{l\neq k}} Y_k'}_{\text{compositional}}. \tag{33}$$

In Eq. (33), the explicit formulation of the acoustic, entropic, and compositional subcontributions is omitted here for the sake of simplicity. Instead, Fig. 4 shows individual source mechanisms resulting from the incoming compositional (Fig. 4(a)), acoustic (Fig. 4(b)), and entropic (Fig. 4(c)) waves in the low Mach number ($\mathrm{M} \to 0$) and zero frequency ($f \to 0$) limit via temperature-entropy (T-s) diagrams. In the limit of these assumptions, all perturbations are spatially independent offsets

[4] In the small perturbation limit, only (incoming) acoustic waves affect the pressure fluctuations p'; only (incoming) entropy waves impact the entropy fluctuations s', and solely (incoming) compositional waves affect the mass fraction Y_k' and the equivalence ratio ϕ'. This fact is easily derived from a characteristic decomposition of the 1D reactive Euler equations.

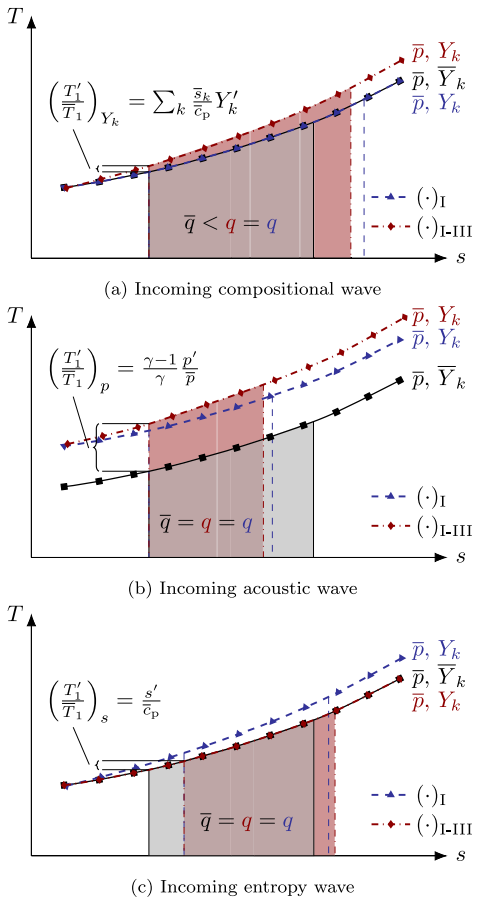

Fig. 4. Temperature-entropy (T-s) diagrams of an exothermic reaction zone in the low Mach number and zero frequency limit visualizing the entropy wave generation mechanisms $(\Psi_{\dot{\omega}_k}/\dot{M}_s)'$ and $(\Psi_{\dot{\omega}_k}/\dot{M}_s)_{\mathrm{I}}'$ for (a) an incoming compositional wave Y_k' ($\phi' > 0$), (b) an incoming acoustic perturbation $p_1' > 0$, (c) an incoming entropy wave $s_1' > 0$. The black (solid), dark blue (dashed) and dark red (dash-dotted) lines correspond to the unperturbed mean state, the perturbed case considering solely $(\Psi_{\dot{\omega}_k}/\dot{M}_s)_{\mathrm{I}}'$ and the perturbed case considering the full source term $(\Psi_{\dot{\omega}_k}/\dot{M}_s)'$.

($f \to 0$) and the combustion process is isobaric [56] (M $\to$ 0). In this case, the *mass-specific* heat released by the reaction,

$$q = \frac{\dot{Q}}{\dot{M}_s} = \int T \mathrm{d}s \,, \tag{34}$$

is equivalent to the area under the isobaric lines in the T-s diagram. In Fig. 4, each sub-figure shows the mean process in black (solid line) and the perturbed process in dark red (dash-dotted line). To visualize the individual effects of the entropy wave sources (Eqs. (29), (30) and (31)) and since neglecting the sources $(\Psi_{\dot{\omega}_k}/\dot{M}_s)_{\mathrm{II}}' + (\Psi_{\dot{\omega}_k}/\dot{M}_s)_{\mathrm{III}}'$ is a common assumption in the literature [6,8,28], the additional process shown in dark red (dashed line) considers solely the effect of the heat release source term $(\Psi_{\dot{\omega}_k}/\dot{M}_s)_{\mathrm{I}}'$.

Fig. 4(a) shows the effect of an incoming compositional wave $Y_{k,1}'$ in the form of an equivalence ratio perturbation $\phi_1' > 0$ ($p_1' = 0$, $s_1' = 0$) of a lean premixed flame. In this case, the incoming perturbation shifts the gas mixture closer to the stoichiometric condition. Consequently, it increases the mass-specific heat release $q > \overline{q}$ (see Eq. (26)) by the chemical reaction. This effect corresponds to the entropy source term $(\Psi_{\dot{\omega}_k}/\dot{M}_s)_{\mathrm{I}}'$ (see Eq. (29)) and is shown by the increased area enclosed by the dark blue dashed lines in Fig. 4a. The effect of the sources $(\Psi_{\dot{\omega}_k}/\dot{M}_s)_{\mathrm{II}}' + (\Psi_{\dot{\omega}_k}/\dot{M}_s)_{\mathrm{III}}'$ is a modulation of the shape of the isobaric curve in the T-s diagram. The modulation results from the change in local gas composition and the corresponding perturbations in gas properties and entropy sensitivities (see Eqs. (30) and (31)). Overall, incoming equivalence ratio fluctuations generate entropy waves in phase.

In Fig. 4(b), an incoming acoustic perturbation $p_1' > 0$ ($s_1' = 0$, $\phi' = 0$, $Y_k' = 0$) shifts the incoming pressure to a higher isobaric line and therefore to higher temperatures, while the mass-specific heat remains unchanged ($q' = 0$, $q = \overline{q}$). Thus, an acoustic wave generates entropy waves solely by changing T_{ref} (and $s_{k,\mathrm{ref}}$). The generated entropy wave is π out of phase with the acoustic wave. The contribution of the entropy source $(\Psi_{\dot{\omega}_k}/\dot{M}_s)_{\mathrm{I}}'$ in this mechanism can be formulated as a shift to another isobaric line, assuming unchanged specific heat $c_{p,k}$ and entropy s_k compared to the mean state. The sources $(\Psi_{\dot{\omega}_k}/\dot{M}_s)_{\mathrm{II}}' + (\Psi_{\dot{\omega}_k}/\dot{M}_s)_{\mathrm{III}}'$ again modulate the new isobaric line by incorporating the temperature (and pressure) dependence of $c_{p,k}$ and s_k.

In Fig. 4(c), an incoming entropy wave $s_1' > 0$ ($p_1' = 0$, $\phi' = 0$, $Y_k' = 0$) at constant pressure shifts the mass-specific heat release to higher entropy levels and thus to higher temperatures. In contrast, the mass-specific heat release $q = \overline{q}$ remains constant. Similar to an acoustic wave, an incoming entropy wave generates additional entropy waves simply by changing T_{ref} (and $s_{k,\mathrm{ref}}$). The generated entropy wave is in antiphase with the incoming wave. Destructive interference typically weakens the resulting entropy wave. In addition to the shift to higher entropy levels, the effect of the source $(\Psi_{\dot{\omega}_k}/\dot{M}_s)_{\mathrm{I}}'$ leads to a modulation of the isobaric line due to the neglect of changes in specific heat $c_{p,k}$ and entropy s_k relative to the mean state. Considering the full source term $(\dot{\omega}_k/\dot{M}_s)'$, the modulation of the isobaric line of $(\dot{\omega}_k/\dot{M}_s)_{\mathrm{I}}'$ is compensated by $(\Psi_{\dot{\omega}_k}/\dot{M}_s)_{\mathrm{II}}' + (\Psi_{\dot{\omega}_k}/\dot{M}_s)_{\mathrm{III}}'$ and the isobaric line remains unchanged.

The understanding of the entropy wave generation mechanisms for the Q1D description in the low Mach number and zero frequency limit gained from Fig. 4 can be extrapolated to higher Mach numbers, higher frequencies as well as to the full three-dimensional description (Section 2.1). At higher frequencies, the integral generation of entropy waves across the flame front exhibits a low-pass filter behavior [23], resulting from the partial cancellation effects across the flame front. The shape of this low-pass filter determines the frequency at which the acoustic/convective compactness assumption and the Q1D jump condition are no longer valid. At higher Mach numbers, the isentropic acceleration of the gas across the flame front becomes significant. Since the acceleration is isentropic, it does not directly affect the generation of entropy waves. However, a distributed flame can modulate the acoustic source mechanism by altering local pressure values. Expanding the interpretation of sub-mechanisms for the non-diffusive three-dimensional flow requires considering the analysis depicted in Fig. 4 as a local analysis, where the reference values $(\cdot)_{\mathrm{ref}}$ only pertain to local quantities.

After gaining a qualitative understanding of the individual source mechanisms from Fig. 4, the following paragraph focuses on an order of magnitude analysis. This analysis aims to quantify the importance of the compositional, acoustic, or entropic source contributions. To simplify the analysis, and since in premixed flames, the source term $(\Psi_{\dot{\omega}_k}/\dot{M}_s)_{\mathrm{I}}'$ is generally the main contributor to entropy wave generation [28,60], this is the only term considered in the following analysis. However, the derived results are assumed to be reasonable estimates even for cases where the source terms $(\Psi_{\dot{\omega}_k}/\dot{M}_s)_{\mathrm{II}}' + (\Psi_{\dot{\omega}_k}/\dot{M}_s)_{\mathrm{III}}'$ are more prominent, since previous analysis showed that the source $(\Psi_{\dot{\omega}_k}/\dot{M}_s)_{\mathrm{II}}' + (\Psi_{\dot{\omega}_k}/\dot{M}_s)_{\mathrm{III}}'$ may be of the same order of magnitude as $(\Psi_{\dot{\omega}_k}/\dot{M}_s)_{\mathrm{I}}'$, but is generally not the dominant contributor [28].

First, the relative order of magnitude of the different perturbations must be clarified. This study employs the normalized velocity perturbation $u_1'/\overline{u}_1$ in front of the reaction zone as a standard reference for other perturbations. All remaining perturbations are related to this quantity as follows:

1. Equivalence ratio perturbations are typically generated by a velocity perturbation at the fuel injector. The corresponding normalized equivalence ratio perturbation is of the same order of magnitude as the velocity perturbation [61–63]

$$\mathcal{O}\left(\frac{\phi'}{\overline{\phi}}\right) \approx \mathcal{O}\left(\frac{u_1'}{\overline{u}_1}\right). \tag{35}$$

2. Perturbations in the incoming normalized equivalence ratio $\phi'/\overline{\phi}$ can be expressed by perturbations in the incoming species mass fraction $Y_{k,1}'/\overline{Y}_{k,1}$ with a similar order of magnitude. In addition, the order of magnitude of $Y_k'/\overline{Y}_k$ can be assumed constant throughout the exothermic reaction zone due to the chosen normalization:

$$\mathcal{O}\left(\frac{Y_{k,1}'}{\overline{Y}_{k,1}}\right) \approx \mathcal{O}\left(\frac{Y_{k,\mathrm{ref}}'}{\overline{Y}_{k,\mathrm{ref}}}\right) \approx \mathcal{O}\left(\frac{\phi'}{\overline{\phi}}\right) \approx \mathcal{O}\left(\frac{u_1'}{\overline{u}_1}\right). \tag{36}$$

3. In the absence of acoustic sources, the acoustic characteristic variables

$$\Pi^{\pm} = \frac{1}{2}\left(\frac{p'}{\overline{p}} \pm \gamma \mathrm{M}_1 \frac{u'}{\overline{u}}\right), \tag{37}$$

remain constant. At the inlet, the normalized pressure perturbation relates to the normalized velocity disturbance via the Mach number M. Furthermore, the order of magnitude of the normalized pressure fluctuations remains constant throughout the reaction zone for low to moderate Mach numbers [22,43]:

$$\mathcal{O}\left(\frac{p_1'}{\overline{p}_1}\right) \approx \mathcal{O}\left(\frac{p_{\mathrm{ref}}'}{\overline{p}_{\mathrm{ref}}}\right) \approx \mathcal{O}\left(\mathrm{M}\frac{u_1'}{\overline{u}_1}\right). \tag{38}$$

4. The entropy perturbations at the reference point are generated either by incoming compositional, acoustic or entropic waves (see Fig. 4):

$$\left(\frac{s'}{\overline{c}_\mathrm{p}}\right)_{\mathrm{ref}} = \underbrace{\left(\frac{s'}{\overline{c}_\mathrm{p}}\right)_{\mathrm{ref},Y_k}}_{\text{compositional}} + \underbrace{\left(\frac{s'}{\overline{c}_\mathrm{p}}\right)_{\mathrm{ref},p}}_{\text{acoustic}} + \underbrace{\left(\frac{s'}{\overline{c}_\mathrm{p}}\right)_{\mathrm{ref},s}}_{\text{entropic}}. \tag{39}$$

Assuming that incoming acoustic, entropic, and compositional waves continuously generate entropy waves, it can be inferred that the entropy fluctuation at the reference point and behind the flame follow the same functional dependence. In the low Mach number limit, the order of magnitude of the sources in Eq. (39) are known, deriving from the Q1D jump condition proposed by Strobio Chen et al. [22, Eq. (42)]:

$$\begin{aligned}
&\mathcal{O}\left(\left(\frac{s'}{\overline{c}_\mathrm{p}}\right)_{\mathrm{ref},Y_k}\right) \leq \mathcal{O}\left(\frac{\phi'}{\overline{\phi}}\right) = \mathcal{O}\left(\frac{u_1'}{\overline{u}_1}\right),\\
&\mathcal{O}\left(\left(\frac{s'}{\overline{c}_\mathrm{p}}\right)_{\mathrm{ref},p}\right) \leq \mathcal{O}\left(\frac{p_1'}{\overline{p}_1}\right) = \mathcal{O}\left(\mathrm{M}_1\frac{u_1'}{\overline{u}_1}\right),\\
&\mathcal{O}\left(\left(\frac{s'}{\overline{c}_\mathrm{p}}\right)_{\mathrm{ref},s}\right) = \mathcal{O}\left(\frac{s_1'}{\overline{c}_\mathrm{p}}\right).
\end{aligned} \tag{40}$$

The Q1D jump condition for the generation of entropy waves is given in Eq. (28). Considering only the heat release source mechanism, the generation of entropy waves normalized with $\zeta = \dot{\overline{Q}}/(\overline{\dot{M}}_s\overline{T}_{\mathrm{ref}})$ reads

$$\frac{s_2'}{\zeta} - \frac{s_1'}{\zeta} = \frac{\phi'}{\overline{\phi}} + \left(\sum_k \frac{\overline{s}_k\overline{Y}_k}{\overline{c}_\mathrm{p}}\frac{Y_k'}{\overline{Y}_k}\right)_{\mathrm{ref}} - \left(\frac{\overline{\gamma}-1}{\overline{\gamma}}\frac{p'}{\overline{p}}\right)_{\mathrm{ref}} - \left(\frac{s'}{c_\mathrm{p}}\right)_{\mathrm{ref}}. \tag{41}$$

If present, the non-diffusive generation of entropy waves is dominated by fluctuations in incoming equivalence ratio

$$\mathcal{O}\left(\frac{\phi'}{\overline{\phi}} + \left(\frac{s'}{\overline{c}_\mathrm{p}}\right)_{\mathrm{ref},Y_k}\right) = \mathcal{O}\left(\frac{u_1'}{\overline{u}_1}\right). \tag{42}$$

Compositional temperature fluctuations at the reference point,

$$\mathcal{O}\left(\left(\frac{T'}{\overline{T}}\right)_{\mathrm{ref},Y_k}\right) = \mathcal{O}\left(-\sum_k\left(\frac{\overline{s}_k\overline{Y}_k}{\overline{c}_\mathrm{p}}\right)_{\mathrm{ref}}\frac{Y_{k,1}'}{\overline{Y}_{k,1}}\right) \lessapprox \mathcal{O}\left(10^{-1}\frac{\phi'}{\overline{\phi}}\right), \tag{43}$$

are typically at least an order of magnitude smaller than the effect of the equivalence ratio perturbation, as shown by Patki et al. [28]. This is true even though $\mathcal{O}\left(Y_k'/\overline{Y}_k\right) \approx \mathcal{O}\left(\phi'/\overline{\phi}\right)$ and results from a partial cancellation of the summands due to different signs of the species mass fraction fluctuations $Y_k'/\overline{Y}_k$ for different species.

The contribution of incoming acoustic waves to the generation of entropy waves

$$\mathcal{O}\left(-\frac{\overline{\gamma}-1}{\overline{\gamma}}\frac{p'}{\overline{p}} - \left(\frac{s'}{\overline{c}_\mathrm{p}}\right)_{\mathrm{ref},p}\right) \approx \mathcal{O}\left(-\mathrm{M}_1\frac{u_1'}{\overline{u}_1}\right) \tag{44}$$

increases proportionally with the equivalence ratio and the Mach number M_1 upstream of the flame. As the Mach number approaches zero, this term vanishes. For $\mathrm{M} \to 1$, the acoustic contribution equals the importance of equivalence ratio perturbations.

Incoming entropy waves generate entropy waves of the same order of magnitude

$$\mathcal{O}\left(-\left(\frac{s'}{\overline{c}_\mathrm{p}}\right)_{\mathrm{ref},s}\right) = \mathcal{O}\left(\frac{s_1'}{\overline{c}_{\mathrm{p},1}}\right). \tag{45}$$

However, the generated entropy waves are out of phase by π (see Fig. 4), resulting in destructive interference across the flame front. Typically, the amplitude of the incoming entropy wave is reduced across the flame front.

3.1.2. The diffusive entropy generation mechanisms of a premixed flame

Diffusion effects are essential to most flames. Species diffusion is necessary for mixing fuel and oxidizer in diffusion flames [64] and is responsible for local equivalence ratio fluctuations in hydrogen fuel blends [29]. Thermal diffusion is essential for stabilizing and anchoring many flames, while viscous heating gains significance in high-speed flows due to strong velocity gradients. Due to the dissipative nature of all diffusion effects, they contribute to the generation of entropy (see Eq. (9)) and their perturbations — to the generation of entropy waves (see Eq. (16)). However, an order of magnitude analysis as performed for the non-diffusive mechanisms in Section 3.1.1 to estimate their relative importance for the generation of entropy waves is not straightforward. As a conservative rule of thumb, the contribution of the diffusive mechanisms to the local generation of entropy disturbances should be considered non-negligible in regions with leading order contributions of the diffusive mechanisms to the generation of entropy in the mean flow.

3.2. Heat source at rest - A heated wire gauze

In this section, a *heated wire gauze* in a flow field, as applied in a typical Rijke tube [65], is used as an example for the generation of entropy waves in a heat source at rest ($u_s = 0$). In this case, incoming flow field perturbations affect the heat transfer between the flow and the heated wire grid, leading to entropy wave generation. This mechanism is analyzed in more detail using the Q1D jump condition

(Section 2.2). Therefore, the heat flux between the wire gauze and the flow is modeled by Newton's law

$$\dot{Q} = \alpha A_s \Delta T, \tag{46}$$

with the heat transfer coefficient α, the surface area of the heated wire A_s and the temperature difference between the fluid and the wire surface ΔT. For a given geometry and fluid, the heat transfer coefficient

$$\alpha(\dot{M}_s, T_{ref}) \tag{47}$$

depends only on the mass flux $\dot{M}_s$ and a reference temperature T_{ref} for the temperature-dependent fluid properties. The exact functional form of Eq. (47) is typically given via correlations. Then, the mass-specific heat flux is given by

$$\frac{\dot{Q}}{\dot{M}_s} = \frac{\alpha(\dot{M}_s, T_{ref}) A_s \Delta T}{\dot{M}_s}, \tag{48}$$

and the corresponding linearization

$$\frac{\left(\frac{\dot{Q}}{\dot{M}_s}\right)'}{\left(\frac{\dot{Q}}{\dot{M}_s}\right)} = \left(\frac{\frac{\partial \alpha}{\partial \dot{M}_s}\Big|_{\overline{T}_{ref}}}{\overline{\alpha}} - 1 \right) \frac{\dot{M}_s'}{\overline{\dot{M}_s}} + \frac{\frac{\partial \alpha}{\partial T_{ref}}\Big|_{\overline{\dot{M}_s}}}{\overline{\alpha}} \left(\frac{T'}{\overline{T}} \right)_{ref} + \frac{\Delta T'}{\overline{\Delta T}} \tag{49}$$

with

$$\frac{\dot{M}_s'}{\overline{\dot{M}_s}} = \frac{u_1'}{\overline{u}_1} + \frac{1}{\overline{\gamma}_1} \frac{p_1'}{\overline{p}_1} - \frac{s_1'}{\overline{c}_{p,1}}. \tag{50}$$

The index $(\cdot)_1$ denotes the inflow condition. Then, the generation of entropy waves is given by

$$\overline{\dot{M}_s} \left(s_2' - s_1' \right) = \frac{\overline{\dot{Q}}}{\overline{T}_{ref}} \left[\varsigma \frac{\dot{M}_s'}{\overline{\dot{M}_s}} + \left(\frac{\frac{\partial \alpha}{\partial T_{ref}}\Big|_{\overline{\dot{M}_s}}}{\overline{\alpha}} - 1 \right) \left(\frac{T'}{\overline{T}} \right)_{ref} + \frac{\Delta T'}{\overline{\Delta T}} \right] \tag{51}$$

with the prefactor of the perturbed mass flux

$$\varsigma = \left(\frac{\frac{\partial \alpha}{\partial \dot{M}_s}\Big|_{\overline{T}_{ref}}}{\overline{\alpha}} - 1 \right) \neq 0. \tag{52}$$

Since the prefactor ς does not vanish, the interaction of incoming velocity perturbations with the heated wire gauze generates entropy waves due to a perturbation of the convective heat transfer. This is in contrast to the lean premixed flame in Section 3.1, which is insensitive to velocity perturbations.

A similar effect of a non-vanishing prefactor ς of the perturbed mass flux appears when the flame in Section 3.1 is assumed to be at rest. However, although this assumption is often made in the literature [36,38–40], the corresponding velocity sensitivity of the entropy wave generation is spurious [22].

4. Conclusion

This study provides an analytical framework for the consistent analysis of moving sources of entropy disturbances for general three-dimensional reactive flows and in the limit of a quasi-one-dimensional jump condition. The source terms of entropy perturbations are strictly separated from transport mechanisms by an Arbitrary Lagrangian–Eulerian framework that moves with the source itself.

The unified framework for the analysis of entropy perturbations derived in this study provides a deep insight into the underlying physical processes. As an example, the analytical framework is applied to a lean premixed flame (entropy source in kinematic balance with the flow) and a heated wire gauze (entropy source at rest). For the lean premixed flame, temperature-entropy diagrams and an order of magnitude analysis are used to explain the different non-diffusive mechanisms of entropy wave generation and quantify their relative importance. In addition, and in agreement with earlier studies in quasi-one-dimensional frameworks, this analysis reaffirms the dominant contribution of equivalence ratio perturbations to the generation of entropy disturbances [13,22,25,48]. Furthermore, it highlights the heat release per unit mass as the key quantity for entropy wave generation in premixed flames. A comparison between the premixed flame and a heated wire gauze shows the fundamentally different mechanisms of entropy wave generation of sources in motion and at rest. In agreement with Strobio Chen et al. [22] and Meindl et al. [27], this reemphasizes the fact that premixed flames cannot be modeled via heat sources at rest.

The necessity of the Arbitrary Lagrangian–Eulerian framework for a clear separation between transport and generation effects has direct implications for the source analysis in numerical simulations. The derived analytical framework can be understood as a first step towards correcting the numerical analysis of entropy wave generation mechanisms.

CRediT authorship contribution statement

Moritz Merk: Conducted research, Wrote paper. **Alexander J. Eder:** Conducted research, Wrote paper. **Wolfgang Polifke:** Supervised research, Wrote paper.

Declaration of competing interest

The authors declare that they have no known competing financial interests or personal relationships that could have appeared to influence the work reported in this paper.

Data availability

No data and code used in the present work.

Acknowledgments

We wish to thank Dr. Camilo F. Silva for helpful comments on the draft. Moreover, the authors gratefully acknowledge the German Research Foundation (Deutsche Forschungsgemeinschaft, DFG) for financial support to Alexander J. Eder under the DFG Transfer Project NoiSI (PO 710/23-1).

Appendix A. Supplementary data

Supplementary material related to this article can be found online at https://doi.org/10.1016/j.combustflame.2024.113334.

References

[1] B.T. Chu, L.S.G. Kovasznay, Non-linear interactions in a viscous heat-conducting compressible gas, J. Fluid Mech. 3 (1957) 495–514.
[2] J.E. Ffowcs Williams, M.S. Howe, The generation of sound by density inhomogeneities in low Mach number nozzle flows, J. Fluid Mech. 70 (1975) 605–622.
[3] N.A. Cumpsty, F.E. Marble, The interaction of entropy fluctuations with turbine blade rows; A mechanism of turbojet engine noise, Proc. R. Soc. A: Math. 357 (1977) 323–344.
[4] F.E. Marble, S.M. Candel, Acoustic disturbance from gas non-uniformities convected through a nozzle, J. Sound Vib. 55 (1977) 225–243.
[5] J.J. Keller, Production and propagation of sound in a duct, J. Acoust. Soc. Am. 65 (1979) 25–31.
[6] A.P. Dowling, Y. Mahmoudi, Combustion noise, Proc. Combust. Inst. 35 (2015) 65–100.
[7] I. Duran, S. Moreau, F. Nicoud, T. Livebardon, E. Bouty, T. Poinsot, Combustion noise in modern aero-engines, AerospaceLab 7 (2014) 1–11.
[8] A.S. Morgans, I. Duran, Entropy noise: A review of theory, progress and challenges, Int. J. Spray Combust. Dyn. 8 (4) (2016) 285–298.

[9] G.E. Abouseif, J.A. Keklak, T.Y. Toong, Ramjet rumble: The low-frequency instability mechanism in coaxial dump combustors, Combust. Sci. Technol. 36 (1984) 83–108.
[10] J. Eckstein, E. Freitag, C. Hirsch, T. Sattelmayer, Experimental study on the role of entropy waves in low-frequency oscillations in a RQL combustor, J. Eng. Gas Turbines Power 128 (2006) 264–270.
[11] Z. Yao, Y. Gao, M. Zhu, A.P. Dowling, K.N.C. Bray, Combustion rumble prediction with integrated computational-fluid-dynamics/low-order-model methods, J. Propuls. Power 28 (2012) 1015–1025.
[12] M.A. Macquisten, A.P. Dowling, Low-frequency combustion oscillations in a model afterburner, Combust. Flame 94 (1993) 253–264.
[13] W. Polifke, C.O. Paschereit, K. Döbbeling, Constructive and destructive interference of acoustic and entropy waves in a premixed combustor with a choked exit, Int. J. Acoust. Vib. 6 (2001) 135–146.
[14] F. Nicoud, T. Poinsot, Thermoacoustic instabilities: Should the Rayleigh criterion be extended to include entropy changes? Combust. Flame 142 (2005) 153–159.
[15] C.S. Goh, A.S. Morgans, The influence of entropy waves on the thermoacoustic stability of a model combustor, Combust. Sci. Technol. 185 (2013) 249–268.
[16] E. Motheau, F. Nicoud, T. Poinsot, Mixed acoustic-entropy combustion instabilities in gas turbines, J. Fluid Mech. 749 (2014) 542–576.
[17] J.J. Keller, W. Egli, J. Hellat, Thermally induced low-frequency oscillations, Z. Angew. Math. Phys. 36 (1985) 250–274.
[18] J.J. Keller, Thermoacoustic oscillations in combustion chambers of gas turbines, AIAA J. 33 (1995) 2280–2287.
[19] T. Lieuwen, Modeling premixed combustion - acoustic wave interactions: A review, J. Propuls. Power 19 (2003) 765–781.
[20] T. Poinsot, Prediction and control of combustion instabilities in real engines, Proc. Combust. Inst. 36 (2017) 1–28.
[21] K. Nishida, T. Takagi, S. Kinoshita, Analysis of entropy generation and exergy loss during combustion, Proc. Combust. Inst. 29 (2002) 869–874.
[22] L. Strobio Chen, S. Bomberg, W. Polifke, Propagation and generation of acoustic and entropy waves across a moving flame front, Combust. Flame 166 (2016) 170–180.
[23] M. Yoon, The entropy wave generation in a heated one-dimensional duct, J. Fluid Mech. 883 (2020) A44.
[24] J. Nan, J. Li, A.S. Morgans, L. Qin, L. Yang, Theoretical analysis of sound propagation and entropy generation across a distributed steady heat source, J. Sound Vib. 536 (2022) 117170.
[25] T. Steinbacher, M. Meindl, W. Polifke, Modeling the generation of temperature inhomogeneities by a premixed flame, Int. J. Spray Combust. Dyn. 10 (2018) 111–130.
[26] B. Semlitsch, T. Hynes, I. Langella, N. Swaminathan, A.P. Dowling, Entropy and vorticity wave generation in realistic gas turbine combustors, J. Propuls. Power 35 (2019) 839–849.
[27] M. Meindl, C.F. Silva, W. Polifke, On the spurious entropy generation encountered in hybrid linear thermoacoustic models, Combust. Flame 223 (2021) 525–540.
[28] P. Patki, V. Acharya, T. Lieuwen, Entropy generation mechanisms from exothermic chemical reactions in laminar, premixed flames, Proc. Combust. Inst. 39 (2022) 1607–1614.
[29] A.J. Eder, B. Dharmaputra, M. Désor, C.F. Silva, A.M. Garcia, B. Schuermans, N. Noiray, W. Polifke, Generation of entropy waves by fully premixed flames in a non-adiabatic combustor with hydrogen enrichment, J. Eng. Gas Turbines Power 145 (2023) 111001.
[30] A. Giusti, N.A. Worth, E. Mastorakos, A.P. Dowling, Experimental and numerical investigation into the propagation of entropy waves, AIAA J. 55 (2017) 446–458.
[31] D. Wassmer, B. Schuermans, C. Paschereit, J.P. Moeck, Measurement and modeling of the generation and the transport of entropy waves in a model gas turbine combustor, Int. J. Spray Combust. Dyn. 9 (2017) 299–309.
[32] M. Weilenmann, U. Doll, R. Bombach, A. Blondé, D. Ebi, Y. Xiong, N. Noiray, Linear and nonlinear entropy-wave response of technically-premixed jet-flames-array and swirled flame to acoustic forcing, Proc. Combust. Inst. 38 (2021) 6135–6143.
[33] B. Dharmaputra, S. Shcherbanev, A. Blondé, B. Schuermans, N. Noiray, Entropy transfer function measurement with tunable diode laser absorption spectroscopy, Proc. Combust. Inst. 39 (2022) 4621–4630.
[34] F. Bake, C. Richter, B. Mühlbauer, N. Kings, I. Röhle, F. Thiele, B. Noll, The entropy wave generator (EWG): A reference case on entropy noise, J. Sound Vib. 326 (2009) 574–598.
[35] F. De Domenico, E.O. Rolland, J. Rodrigues, L. Magri, S. Hochgreb, Compositional and entropy indirect noise generated in subsonic non-isentropic nozzles, J. Fluid Mech. 910 (2021) A5.
[36] G. Wang, X. Liu, S. Wang, L. Li, F. Qi, Experimental investigation of entropy waves generated from acoustically excited premixed swirling flame, Combust. Flame 204 (2019) 85–102.
[37] A.P. Dowling, The calculation of thermoacoustic oscillation, J. Sound Vib. 180 (1995) 557–581.
[38] A.P. Dowling, S.R. Stow, Acoustic analysis of gas turbine combustors, J. Propul. Power 19 (2003) 751–764.
[39] P.A. Hield, M.J. Brear, S.H. Jin, Thermoacoustic limit cycles in a premixed laboratory combustor with open and choked exits, Combust. Flame 156 (2009) 1683–1697.
[40] M. Leyko, F. Nicoud, T. Poinsot, Comparison of direct and indirect combustion noise mechanisms in a model combustor, AIAA J. 47 (2009) 2709–2716.
[41] Y. Méry, Dynamical response of a perfectly premixed flame and limit behavior for high power density systems, Combust. Flame 192 (2018) 410–425.
[42] Y. Chen, L.J. Ayton, D. Zhao, Modelling of intrinsic thermoacoustic instability of premixed flame in combustors with changes in cross section, Combust. Sci. Technol. 192 (2019) 832–851.
[43] F. Gant, A. Cuquel, M.R. Bothien, Autoignition flame transfer matrix: Analytical model versus large eddy simulations, Int. J. Spray Combust. Dyn. 14 (2022) 72–81.
[44] Y. Song, X. Liu, J. Li, L. Yang, Effect of the flame motion on azimuthal combustion instabilities, Aerosp. Sci. Technol. 130 (2022) 107930.
[45] Y. Song, J. Li, L. Yang, Effect of flame motion on longitudinal combustion instabilities, Aerosp. Sci. Technol. 122 (2022) 107427.
[46] H.S. Gopalakrishnan, A. Gruber, J.P. Moeck, Computation and prediction of intrinsic thermoacoustic oscillations associated with autoignition fronts, Combust. Flame 254 (2023) 112844.
[47] A. Fattahi, N. Karimi, N. Hajialigol, Dynamics of entropy wave generation in a simplified model of gas turbine combustor: A theoretical investigation, Phys. Fluids 32 (2020) 106107.
[48] T. Sattelmayer, Influence of the combustor aerodynamics on combustion instabilities from equivalence ratio fluctuations, J. Eng. Gas Turbines Power 125 (2003) 11–19.
[49] B. Schuermans, Modeling and Control of Thermoacoustic Instabilities (Ph.D. thesis), École Polytechnique Fédérale de Lausanne, Lausanne, Switzerland, 2003.
[50] J. Donéa, A. Huerta, Finite Element Methods for Flow Problems, Wiley, Hoboken, NJ, USA, 2003.
[51] G. Heilmann, T. Liu, P. Romero Vega, T. Sattelmayer, A novel decomposition approach preventing spurious entropy generation in hybrid thermoacoustic stability computations, J. Eng. Gas Turbines Power 144 (2022) 091013.
[52] L. Magri, On indirect noise in multicomponent nozzle flows, J. Fluid Mech. 828 (2017) R2.
[53] L. Magri, J. O'Brien, M. Ihme, Effects of nozzle Helmholtz number on indirect combustion noise by compositional perturbations, J. Eng. Gas Turbines Power 140 (2018) 031501.
[54] E.O. Rolland, Sound Produced by Entropic and Compositional Inhomogeneities (Ph.D. thesis), University of Cambridge, Cambridge, UK, 2018.
[55] T.C. Lieuwen, Unsteady Combustor Physics, Cambridge University Press, New York, NY, USA, 2021.
[56] T. Poinsot, D. Veynante, Theoretical and Numerical Combustion, Edwards, Philadelphia, PA, USA, 2005.
[57] A. Laksana, P. Patki, T. John, V. Acharya, T. Lieuwen, Distributed heat release effects on entropy generation by premixed, laminar flames, Int. J. Spray Combust. Dyn. 15 (2023) 139–146.
[58] B. Schuermans, V. Bellucci, F. Guethe, F. Meili, P. Flohr, O. Paschereit, A Detailed Analysis of Thermoacoustic Interaction Mechanisms in a Turbulent Premixed Flame, ASME Turbo Expo 2004, 2004.
[59] T. Schuller, T. Poinsot, S. Candel, Dynamics and control of premixed combustion systems based on flame transfer and describing functions, J. Fluid Mech. 894 (2020) P1.
[60] J.M. Truffaut, G. Searby, L. Boyer, Sound emission by non-isomolar combustion at low Mach numbers, Combust. Theory Model. 2 (1998) 423–428.
[61] W. Polifke, C.J. Lawn, On the low-frequency limit of flame transfer functions, Combust. Flame 151 (2007) 437–451.
[62] A. Huber, W. Polifke, Dynamics of practical premix flames, part I: Model structure and identification, Int. J. Spray Combust. Dyn. 1 (2009) 199–228.
[63] H. Schwarz, L. Zimmer, D. Durox, S. Candel, Detailed measurements of equivalence ratio modulations in premixed flames using laser Rayleigh scattering and absorption spectroscopy, Exp. Fluids 49 (2010) 809–821.
[64] N. Peters, Turbulent Combustion, Cambridge University Press, Cambridge, UK, 2000.
[65] P.L. Rijke, Notiz über eine neue Art, die in einer an beiden Enden offenen Röhre enthaltene Luft in Schwingungen zu versetzen, Ann. Physics 183 (1859) 339–343.

D.2 PAPER-MBI

ASME Journal of Engineering for Gas Turbines and Power
Online journal at:
https://asmedigitalcollection.asme.org/gasturbinespower

Alexander J. Eder[1,2]
Department of Engineering Physics and Computation,
TUM School of Engineering and Design,
Technical University of Munich,
Garching D-85748, Germany
e-mail: alexander.eder@tum.de

Moritz Merk[1]
Department of Engineering Physics and Computation,
TUM School of Engineering and Design,
Technical University of Munich,
Garching D-85748, Germany

Thomas Hollweck
Department of Engineering Physics and Computation,
TUM School of Engineering and Design,
Technical University of Munich,
Garching D-85748, Germany

André Fischer
Combustion and Turbine Department,
Rolls-Royce Deutschland,
Blankenfelde-Mahlow, D-15827, Germany

Claus Lahiri
Combustion and Turbine Department,
Rolls-Royce Deutschland,
Blankenfelde-Mahlow D-15827, Germany

Camilo F. Silva
Department of Engineering Physics and Computation,
TUM School of Engineering and Design,
Technical University of Munich,
Garching D-85748, Germany

Wolfgang Polifke
Department of Engineering Physics and Computation,
TUM School of Engineering and Design,
Technical University of Munich,
Garching D-85748, Germany

Model-Based Inference of Flame Transfer Matrices From Acoustic Measurements in an Aero-Engine Test Rig

Flame dynamics, represented as a flame transfer matrix (FTM), is not directly measurable in test rigs and must be deduced from transfer matrix measurements of the combustion system. The burner-flame transfer matrix (BFTM) approach for FTM estimation is based on local pressure signals from microphones located upstream and downstream of the combustor. It combines acoustic measurements in nonreacting and reacting conditions, with the latter implicitly including flame dynamics. A simple matrix operation yields the FTM. However, this approach assumes loss-free wave propagation at constant speed of sound with no change in cross-sectional area between the microphones and the burner/flame. The present work demonstrates the limitations of these assumptions when applied to a test rig with effusion cooling, bypass annulus, and end contraction. This work proposes a method to infer the FTM for complex combustors by combining reactive transfer matrix measurements of the entire combustor with an accurate low-order model (LOM) of the test rig. This generalized method reduces to the BFTM approach as a special case. The Rolls-Royce SCARLET test rig, operating under realistic engine conditions, is used to analyze the capabilities of the proposed model-based inference method and the limitations of the BFTM approach. First, a LOM based on SCARLET's geometry and operating point is formulated using a generic FTM. This model visualizes the limitations of the BFTM approach concerning various physical and geometrical parameters. Finally, experimental data is used to infer the FTM of SCARLET using the proposed approach. [DOI: 10.1115/1.4066366]

1 Introduction

Lean-burn, low-emission combustion systems, such as modern aero-engines, are susceptible to thermoacoustic combustion instabilities that can restrict their operational range, increase wear, or even damage the engine [1,2]. To prevent these self-excited instabilities in future engine development programs, accurate and efficient prediction tools are essential. Low-order thermoacoustic network modeling [3–9] has been demonstrated to be an efficient technique for predicting thermoacoustic instabilities in confined combustion systems like aero-engine combustors. Such a low-order model encompasses the main geometric features of the combustion system and is based on the interconnection of compact (e.g., area

Turbo Expo, June 24–28, 2024. GT2024.
[1]Joint first authors.
[2]Corresponding author.
Manuscript received July 16, 2024; final manuscript received August 6, 2024; published online October 15, 2024. Editor: Jerzy T. Sawicki.

change, end reflection, flow splits, flame) and noncompact (e.g., duct) quasi-one-dimensional acoustic elements [10,11]. The local transfer behavior of each network element may be represented by its transfer matrix, which links the upstream and downstream acoustic pressure and velocity fluctuations, respectively. The transfer matrix can be described for many elements using simple analytical models based on linearized governing equations. However, transfer matrices extracted from numerical simulations or experimental measurements are used for elements with more complex dynamics.

The intricate dynamics of a flame require sophisticated methods to model with accuracy. Apart from simulation-based approaches [12–15], the flame transfer matrix (FTM) [16] is usually estimated using measured data from a thermoacoustic test rig. However, since a direct measurement of the FTM is not possible, it is usually postprocessed from measured pressure signals. In this setup, the model combustor is placed between two measurement ducts that are equipped with microphone arrays. A siren modulates the air mass flow of the thermoacoustically stable experimental setup, exciting the flame at distinct frequencies. The microphone arrays with a spatial distribution in the axial direction then measure the resulting acoustic pressure fluctuations. Starting from the measured pressure data, two modeling steps are required to estimate the FTM. First, the acquired pressure fluctuations enable the reconstruction of upstream and downstream propagating plane acoustic waves while assuming a constant speed of sound and no changes in cross section between the individual microphones. This technique was first proposed by Munjal and Doige [17] and later extended to the multimicrophone method (MMM) by Peters et al. [18]. Paschereit, Polifke and Schuermans [16,19–21] adopted it for combustion applications. The reconstructed acoustic waves may be utilized to relate the acoustic pressure and velocity fluctuations upstream and downstream of the combustor via a transfer matrix. This transfer matrix is a black-box representation of the acoustic behavior of the combustor. In a second step, the established approach for estimating the FTM combines two transfer matrices obtained from measurements in nonreacting ("cold") and reacting ("hot") conditions. This approach assumes that the transfer behavior of the hot burner can be expressed as a sequence of the cold burner transfer matrix and the flame. The FTM is then computed by simple matrix multiplication of the hot and cold burner transfer matrices [20,22]. This methodology has been successfully employed in various studies [23–26] on premixed flames in simplistic test rigs.

However, as pointed out in recent studies by Alanyaloğlu [27] and Eder [28], this approach is not valid for complex configurations such as aero-engine combustors. The primary discrepancies to simplistic test rigs investigated in prior studies are an additional acoustic communication path between the upstream and the downstream duct via an effusion cooling bypass annulus and more complex combustion chamber geometries. While the FTM remains an intrinsic part of the hot measurement, the assumption that the hot burner transfer matrix is a simple sequence of the cold burner transfer matrix and the flame does not hold anymore. Therefore, the established approach is no longer applicable.

To remedy the limitations of the aforementioned approach, this work presents a novel method that provides a consistent inference of the FTM for complex test rigs. The proposed method combines acoustic transfer matrix measurements of the full combustor under hot conditions with a low-order thermoacoustic network model of the test rig. The capabilities of the model-based method are analyzed using the Rolls-Royce Scaled Acoustic Rig for Low Emission Technology (SCARLET) [29,30], which comprises a single sector aero-engine combustor and is operated under realistic engine conditions (high pressure, preheating temperatures and mass fluxes).

The paper is structured as follows. Section 2 describes the established method to postprocess the FTM from experimental measurements and introduces the model-based inference method. The experimental setup, acoustic transfer matrix measurements, and a low-order thermoacoustic network model of SCARLET are presented in Sec. 3. In Sec. 4, the network model is used to visualize the limitations of the established method for test rigs with complex features like SCARLET. In addition, the model-based inference method is shown to be exact in the absence of modeling errors. In Sec. 5, the model-based inference method is applied to experimental data of SCARLET and the advantages and drawbacks of the novel method are discussed. Finally, the work is concluded in Sec. 6.

2 Modeling Approach

In experimental setups, many quantities of interest cannot be measured directly but must be postprocessed from the acquired data utilizing models. The quality and validity of the postprocessed quantities are therefore limited by the modeling assumptions used. It is essential to understand these limitations.

2.1 Determination of Transfer Matrices From Acoustic Pressure Measurements. The multimicrophone method [16,18–21,31] is a postprocessing technique to approximate the acoustic velocity and pressure perturbations at a reference point x_{ref} based on pressure signals acquired from an axially-distributed microphone array. Under the assumption of plane acoustic wave propagation at constant speed and no changes in cross section, the Fourier transformed pressure signals of the individual microphones

$$\begin{pmatrix} p'_1 \\ \vdots \\ p'_k \end{pmatrix} = \bar{\rho}\bar{c}\mathbf{A}\begin{pmatrix} f_{\mathrm{ref}} \\ g_{\mathrm{ref}} \end{pmatrix} \tag{1}$$

can be expressed in terms of the acoustic wave amplitudes $f = \left(p'/(\bar{\rho}\bar{c}) + u'\right)/2$ and $g = \left(p'/(\bar{\rho}\bar{c}) - u'\right)/2$ at x_{ref}. The matrix

$$\mathbf{A} = \begin{pmatrix} \exp\left(-\dfrac{i\omega}{\bar{c}+\bar{u}}\Delta x_1\right) & \exp\left(-\dfrac{i\omega}{\bar{c}-\bar{u}}\Delta x_1\right) \\ \vdots & \vdots \\ \exp\left(-\dfrac{i\omega}{\bar{c}+\bar{u}}\Delta x_k\right) & \exp\left(-\dfrac{i\omega}{\bar{c}-\bar{u}}\Delta x_k\right) \end{pmatrix} \tag{2}$$

accounts for the phase shift resulting from the acoustic wave propagation between the microphones and the reference point, $\Delta x_k = x_k - x_{\mathrm{ref}}$. ω, p, ρ, c, and u are the angular frequency, pressure, density, speed of sound, and flow velocity. The superscripts $\bar{\psi}$ and ψ' denote the time-invariant mean value and a small perturbation of an arbitrary quantity ψ. Then, the approximated acoustic wave amplitudes at the reference point are retrieved as the least-squares minimization of Eq. (1), e.g., by applying the Moore–Penrose generalized inverse [32]

$$\begin{pmatrix} f_{\mathrm{ref}} \\ g_{\mathrm{ref}} \end{pmatrix} = \frac{1}{\bar{\rho}\bar{c}}\left(\mathbf{A}^H\mathbf{A}\right)^{-1}\mathbf{A}^H\begin{pmatrix} p'_1 \\ \vdots \\ p'_k \end{pmatrix} \tag{3}$$

where $(\cdot)^H$ and $(\cdot)^{-1}$ are the Hermitian transpose and the matrix inverse. Finally, f_{ref} and g_{ref} can be decomposed into the pressure and velocity fluctuations at the x_{ref} via

$$\begin{pmatrix} p'_{\mathrm{ref}} \\ \bar{\rho}\bar{c} \\ u'_{\mathrm{ref}} \end{pmatrix} = \begin{pmatrix} 1 & 1 \\ 1 & -1 \end{pmatrix}\begin{pmatrix} f_{\mathrm{ref}} \\ g_{\mathrm{ref}} \end{pmatrix} \tag{4}$$

The transfer behavior of a system can be represented by a transfer matrix $\mathbf{T}$, which relates the pressure and the velocity perturbations at the boundaries of a system, generally defined as

$$\begin{pmatrix} \dfrac{p'}{\bar{\rho}\bar{c}} \\ u' \end{pmatrix}_j = \mathbf{T}\begin{pmatrix} \dfrac{p'}{\bar{\rho}\bar{c}} \\ u' \end{pmatrix}_i \tag{5}$$

Transfer matrices can be determined from acoustic measurements by enclosing a system between the reference points of two microphone arrays ($i = \mathrm{u}$, $j = \mathrm{d}$). Additionally, the measurement

of at least two acoustically independent test states is needed. See Åbom [33] for various possibilities of producing different test sets. For two test states A and B, the transfer matrix can be obtained using

$$\widetilde{\mathbf{T}} = \begin{pmatrix} \frac{p'^{\mathrm{A}}_{\mathrm{d}}}{\overline{\rho c}} & \frac{p'^{\mathrm{B}}_{\mathrm{d}}}{\overline{\rho c}} \\ u'^{\mathrm{A}}_{\mathrm{d}} & u'^{\mathrm{B}}_{\mathrm{d}} \end{pmatrix} \begin{pmatrix} \frac{p'^{\mathrm{A}}_{\mathrm{u}}}{\overline{\rho c}} & \frac{p'^{\mathrm{B}}_{\mathrm{u}}}{\overline{\rho c}} \\ u'^{\mathrm{A}}_{\mathrm{u}} & u'^{\mathrm{B}}_{\mathrm{u}} \end{pmatrix}^{-1} \tag{6}$$

Note that transfer matrices determined by the measurement procedure detailed in this section are denoted with $\widetilde{(\cdot)}$ throughout this work.

2.2 Estimation of the Flame Transfer Matrix From Two Measurements - the Burner-Flame Transfer Matrix Approach. The flame transfer matrix $\mathbf{F}$ is an intrinsic part of the transfer matrix $\widetilde{\mathbf{T}}^{\mathrm{h}}$ of the reactive ("hot") test rig. To extract $\mathbf{F}$ from the experimentally determined $\widetilde{\mathbf{T}}^{\mathrm{h}}$, the established postprocessing approach [23–26] assumes that $\mathbf{T}^{\mathrm{h}}$ can be modeled as a series of the burner transfer matrix $\mathbf{B}$ and the flame transfer matrix $\mathbf{F}$

$$\mathbf{T}^{\mathrm{h}} := \mathbf{F}\mathbf{B} \tag{7}$$

$\mathbf{T}^{\mathrm{h}}$ is called burner-flame transfer matrix (BFTM) in this case. In addition, the burner transfer matrix $\mathbf{B}$ is assumed to remain unchanged by the combustion processes [22,34]. $\mathbf{B}$ is then determined by the transfer behavior $\widetilde{\mathbf{T}}^{\mathrm{c}}$ of the nonreactive ("cold") test rig at the same inlet conditions

$$\widetilde{\mathbf{T}}^{\mathrm{c}} := \mathbf{B} \tag{8}$$

Assuming that the model in Eq. (7) accurately represents the measured hot test rig ($\widetilde{\mathbf{T}}^{\mathrm{h}} = \mathbf{T}^{\mathrm{h}}$), the flame transfer matrix can be estimated via

$$\mathbf{F} = \widetilde{\mathbf{T}}^{\mathrm{h}} \left(\widetilde{\mathbf{T}}^{\mathrm{c}}\right)^{-1} \tag{9}$$

Analogously to $\widetilde{\mathbf{T}}^{\mathrm{h}}$, $\widetilde{\mathbf{T}}^{\mathrm{c}}$ is determined from experimental measurements using the MMM detailed in Sec. 2.1. Throughout this work, the method represented by Eq. (9) is referred to as the *BFTM approach* due to the key modeling assumption in Eq. (7).

Figure 1(*a*) shows a simple test rig consisting of a burner section between two ducts. In this simplistic case, the reference points of the MMM can be chosen to enclose solely the burner and the flame. The assumptions of the BFTM approach hold. For combustor test rigs with complex features such as effusion cooling, bypass annulus, and downstream end contraction as shown in Fig. 1(*b*), the reference points of the MMM typically brackets the full combustor. Considering Fig. 1(*b*) it is evident that the transfer matrices $\widetilde{\mathbf{T}}^{\mathrm{c}}$ and $\widetilde{\mathbf{T}}^{\mathrm{h}}$ measured with the MMM should be recognized as the combustor transfer matrices $\widetilde{\mathbf{C}}^{\mathrm{c}}$ and $\widetilde{\mathbf{C}}^{\mathrm{h}}$ for the "cold" and "hot" operating conditions, respectively. In this case, the modeling assumption (Eq. (7)) of the BFTM postprocessing approach is no longer valid [27,28] and a new method is required to deduce $\mathbf{F}$ from $\widetilde{\mathbf{C}}^{\mathrm{h}}$.

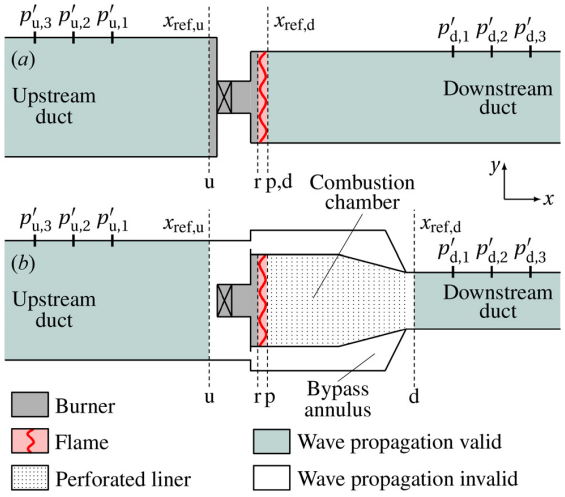

Fig. 1 Schematic representation of (*a*) a simplistic and (*b*) an aero-engine test rig under reactive conditions. Sirens are not shown. The indices "*u*," "*r*," "*p*," and "*d*" stand for upstream, reactants, products, and downstream, respectively.

2.3 Model-Based Inference of the Flame Transfer Matrix in General Setups. In general, the inference of $\mathbf{F}$, defined as (Fig. 2, top right)

$$\mathbf{v}_{\mathrm{p}} = \mathbf{F}\,\mathbf{v}_{\mathrm{r}} \tag{10}$$

from the measured hot combustor transfer matrix $\widetilde{\mathbf{C}}^{\mathrm{h}}$, defined as (Fig. 2, top left)

$$\mathbf{v}_{\mathrm{d}} = \widetilde{\mathbf{C}}^{\mathrm{h}}\mathbf{v}_{\mathrm{u}} \tag{11}$$

Requires a model that connects the states

$$\mathbf{v}_i = \begin{pmatrix} \frac{p'}{\overline{\rho c}} \\ u' \end{pmatrix}_i \tag{12}$$

upstream ($i = \mathrm{r}$, "reactants") and downstream ($i = \mathrm{p}$, "products") of the flame to the states upstream ($i = \mathrm{u}$) and downstream ($i = \mathrm{d}$) of the combustor. This connector model (Fig. 2, center) is an interconnection of different transfer matrices representing the complexity of the underlying system. The subelements can be modeled individually, e.g., via low-order models (LOM), or provided from experimental measurements or numerical simulations. The resulting connector transfer matrix can be expressed by the general model [35]

$$\begin{pmatrix} \mathbf{v}_{\mathrm{r}} \\ \mathbf{v}_{\mathrm{d}} \end{pmatrix} = \begin{pmatrix} \mathbf{T}_{\mathrm{ru}} & \mathbf{T}_{\mathrm{rp}} \\ \mathbf{T}_{\mathrm{du}} & \mathbf{T}_{\mathrm{dp}} \end{pmatrix} \begin{pmatrix} \mathbf{v}_{\mathrm{u}} \\ \mathbf{v}_{\mathrm{p}} \end{pmatrix} \tag{13}$$

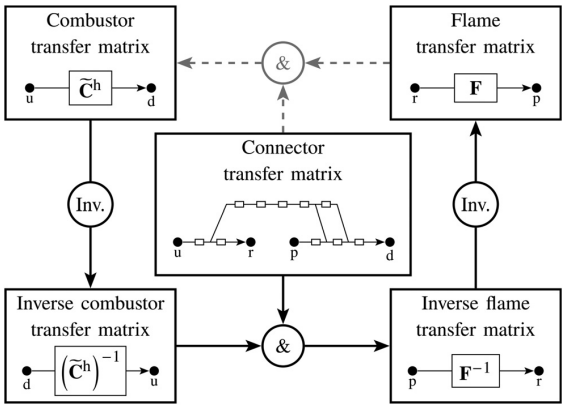

Fig. 2 Visualization of the model-based inference method (solid arrows) to infer the flame transfer matrix (top right) from the measured combustor transfer matrix (top left) utilizing a connector model (center). "Inv." denotes the inversion of a transfer matrix and "&" the interconnection of two models. The gray dashed arrows display the methodology to calculate the system response from a known flame transfer matrix.

In Eq. (13), $\mathbf{v}_u$ and $\mathbf{v}_p$ are chosen as inputs while $\mathbf{v}_r$ and $\mathbf{v}_d$ are treated as outputs of the connector model. Note that this choice is arbitrary and could be changed. The connector model's subtransfer matrices $\mathbf{T}_{ru}$, $\mathbf{T}_{rp}$, $\mathbf{T}_{du}$ and $\mathbf{T}_{dp}$ each depend on the reflection and transmission coefficients of all subelements of the connector model. $\mathbf{T}_{ru}$, $\mathbf{T}_{rp}$, $\mathbf{T}_{du}$, and $\mathbf{T}_{dp}$ can be extracted utilizing existing low-order network toolboxes such as the open source MATLAB® package taX[2] [35] developed at TUM. Note that Eq. (13) is valid for connector models of arbitrary complexity.

To derive a closed-form representation of $\mathbf{F}$, the inverse hot combustor transfer matrix $(\widetilde{\mathbf{C}}^{\mathrm{h}})^{-1}$ (Fig. 2, lower left) is used as a closure model to remove $\mathbf{v}_u$ and $\mathbf{v}_d$ from the connector transfer matrix (Eq. (13)). Mathematically, this interconnection is expressed in the following two steps. First, the bottom row of Eq. (13) is used to substitute $\mathbf{v}_d$ in the definition of the inverse combustor transfer matrix

$$\begin{aligned}\mathbf{v}_u &= (\widetilde{\mathbf{C}}^{\mathrm{h}})^{-1}\mathbf{v}_d \\ &= (\widetilde{\mathbf{C}}^{\mathrm{h}})^{-1}(\mathbf{T}_{du}\mathbf{v}_u + \mathbf{T}_{dp}\mathbf{v}_p)\end{aligned} \tag{14}$$

This reveals an expression of the state $\mathbf{v}_u$ in terms of the state $\mathbf{v}_p$ only

$$\mathbf{v}_u = \left(\widetilde{\mathbf{C}}^{\mathrm{h}} - \mathbf{T}_{du}\right)^{-1}\mathbf{T}_{dp}\,\mathbf{v}_p \tag{15}$$

Second, Eq. (15) is used to substitute $\mathbf{v}_u$ in the top row of Eq. (13). The result is the inverse flame transfer matrix $\mathbf{F}^{-1}$ (Fig. 2) that expresses the state $\mathbf{v}_r$ in sole dependence of the state $\mathbf{v}_p$

$$\mathbf{v}_r = \underbrace{\left[\mathbf{T}_{ru}\left(\widetilde{\mathbf{C}}^{\mathrm{h}} - \mathbf{T}_{du}\right)^{-1}\mathbf{T}_{dp} + \mathbf{T}_{rp}\right]}_{\mathbf{F}^{-1}}\mathbf{v}_p \tag{16}$$

Finally, a simple matrix inversion provides the general rule for the inference of the FTM from the measured hot combustor transfer matrix

$$\mathbf{F} = \left[\mathbf{T}_{ru}\left(\widetilde{\mathbf{C}}^{\mathrm{h}} - \mathbf{T}_{du}\right)^{-1}\mathbf{T}_{dp} + \mathbf{T}_{rp}\right]^{-1} \tag{17}$$

Throughout this work, the utilization of Eq. (17) is referred to as the *model-based inference* (MBI) method, where the individual steps to derive it are visualized in Fig. 2.

In contrast to the BFTM approach, described in Sec. 2.2, the MBI method does not require the additional measurement of the cold combustor transfer matrix $\widetilde{\mathbf{C}}^{\mathrm{c}}$ at the same operating point as $\widetilde{\mathbf{C}}^{\mathrm{h}}$ to infer the FTM, reducing the experimental effort. Therefore, the superscript "h" has been omitted throughout this section for simplicity. Note, however, that the MBI method relies heavily on the connector model's accurate representation of the internal combustor dynamics. Equation (17) shows that any modeling error in the connector transfer matrices $\mathbf{T}_{ru}$, $\mathbf{T}_{rp}$, $\mathbf{T}_{du}$, and $\mathbf{T}_{dp}$ directly impact the inferred $\mathbf{F}$. Therefore, the quality of the connector model must be ensured for reliable FTM predictions. In this work, the comparison of a measured cold combustor transfer matrix $\widetilde{\mathbf{C}}^{\mathrm{c}}$ with the corresponding model

$$\mathbf{C}^{\mathrm{c}} = \mathbf{T}^{\mathrm{c}}_{dp}\left(\mathbf{I} - \mathbf{T}^{\mathrm{c}}_{rp}\right)^{-1}\mathbf{T}^{\mathrm{c}}_{ru} + \mathbf{T}^{\mathrm{c}}_{du} \tag{18}$$

is used to indicate the accuracy of the connector model. Equation (18) is derived from the connector model (Eq. (13)) in the absence of a flame, $\mathbf{v}_p = \mathbf{I}\,\mathbf{v}_r$, where $\mathbf{I}$ is the identity matrix. The superscript "c" for the connector matrices $\mathbf{T}_{ru}$, $\mathbf{T}_{rp}$, $\mathbf{T}_{du}$, and $\mathbf{T}_{dp}$ denotes their evaluation for the cold combustor. See Appendix for a detailed derivation of the combustor model $\mathbf{C}^{\mathrm{c}}$ (and $\mathbf{C}^{\mathrm{h}}$).

[2]https://gitlab.lrz.de/tfd/tax

Note that the MBI method applies not only to reduced-order network models—as used in the present work—but also to spatially resolved models based on linearized equations, e.g., Helmholtz equation, linearized Euler equations or linearized Navier-Stokes equation. In this case, the input and output state vectors $\mathbf{v}_u$, $\mathbf{v}_r$, $\mathbf{v}_p$, and $\mathbf{v}_d$ of the connector model include numerous states and Eq. (13) remains valid.

2.4 The Burner-Flame Transfer Matrix Approach—a Special Case of the Model-Based Inference Method. The postprocessing approach presented in Sec. 2.2 is a special case of the generalized MBI method proposed in Sec. 2.3. In the absence of an acoustic branch bypassing the flame, the transfer matrices $\mathbf{T}_{du}$ and $\mathbf{T}_{rp}$ of the connector model vanish ($\mathbf{T}_{du} = \mathbf{0}$, $\mathbf{T}_{rp} = \mathbf{0}$). Additionally, assuming a combustion chamber with constant cross section ($\mathbf{T}_{dp} = \mathbf{D}_{dp}$), Eq. (17) simplifies to

$$\mathbf{F} = \left(\mathbf{D}^{\mathrm{h}}_{dp}\right)^{-1}\widetilde{\mathbf{C}}^{\mathrm{h}}\left(\mathbf{T}^{\mathrm{h}}_{ru}\right)^{-1} \tag{19}$$

Under the additional assumption that $\mathbf{T}^{\mathrm{h}}_{ru}$ is not affected by the flame ($\mathbf{T}^{\mathrm{h}}_{ru} = \mathbf{T}^{\mathrm{c}}_{ru} = \mathbf{T}_{ru} = \mathbf{B}$) [22,34], $\mathbf{T}^{\mathrm{h}}_{ru}$ can be deduced from the cold combustor transfer matrix $\widetilde{\mathbf{C}}^{\mathrm{c}} = \mathbf{D}^{\mathrm{c}}_{dp}\mathbf{T}^{\mathrm{h}}_{ru}$ and Eq. (19) further reduces to

$$\mathbf{F} = \underbrace{\left(\mathbf{D}^{\mathrm{h}}_{dp}\right)^{-1}\widetilde{\mathbf{C}}^{\mathrm{h}}}_{\mathbf{FB}}\underbrace{\left(\widetilde{\mathbf{C}}^{\mathrm{c}}\right)^{-1}\mathbf{D}^{\mathrm{c}}_{dp}}_{\mathbf{B}^{-1}} \tag{20}$$

In this simple setup, the terms $\left(\mathbf{D}^{\mathrm{h}}_{dp}\right)^{-1}\widetilde{\mathbf{C}}^{\mathrm{h}}$ and $\left(\mathbf{D}^{\mathrm{c}}_{dp}\right)^{-1}\widetilde{\mathbf{C}}^{\mathrm{c}}$ are equal to the BFTM (Eq. (7)) and the burner transfer matrix (Eq. (8)), respectively. Accordingly, Eq. (20) is equivalent to the BFTM approach (Eq. (9)).

3 Thermoacoustic Test Rig

In this study, the BFTM approach (Sec. 2.2) and the proposed MBI method (Sec. 2.3) are used to estimate the flame transfer matrix from acoustic measurement data in an aero-engine test rig. The experimental setup and a thermoacoustic low-order network model of the rig are presented below.

3.1 Experimental Setup. The Rolls-Royce SCARLET test rig [29,30] comprises a single-sector aero-engine combustion chamber and is located in the HBK-3 (high-pressure combustion chamber) test facility at the DLR (German Aerospace Center) in Cologne, Germany. It was developed for efficient testing of liquid fuel injectors under realistic engine conditions. The inlet conditions of the rig represent the outlet conditions of the compressor stage in the engine with a maximum pressure of 30 bar, a maximum preheating temperature of 950 K, and a maximum air mass flow of 4 kg/s. The operating point investigated in this work is given in Table 1, where kerosene is used as the liquid fuel. The measurements aim to determine the cold and hot combustor transfer matrices $\widetilde{\mathbf{C}}^{\mathrm{c}}$ and $\widetilde{\mathbf{C}}^{\mathrm{h}}$, respectively, using the multimicrophone method described in Sec. 2.1. These measurements are conducted in an acoustically controlled environment and, therefore, guarantee a thermoacoustically stable operation.

Table 1 Operating condition of SCARLET

Parameter	Value	Unit
Inlet pressure	25	bar
Inlet mass flow	3	kg s^{-1}
Inlet temperature	825	K
Thermal power	4.2	MW

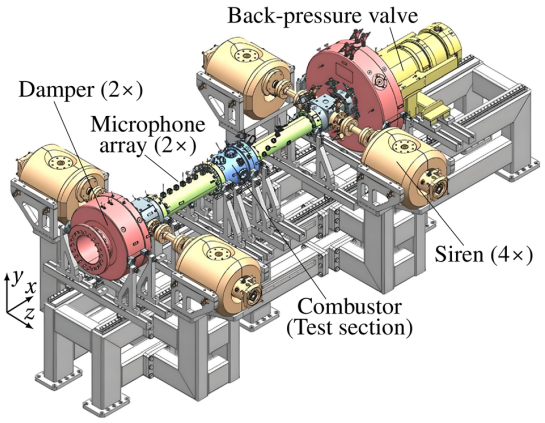

Fig. 3 Isometric view of SCARLET. Flow in *x*-direction.

The rig, shown in Fig. 3, consists of a back-pressure valve, two dampers, four sirens, two acoustic measurement sections (constant cross section) with an array of microphones, and an aero-engine combustion chamber (test section). A variable back-pressure valve restricts the total mass flow to adjust the pressure drop across the installed injector unit from about 2% to 4% to the inlet pressure. Upstream and downstream dampers ensure control of the acoustic boundaries, thus minimizing end reflections and dampening the occurrence of longitudinal modes. Two opposing sirens upstream and downstream of the test section provide sinusoidal acoustic excitation in the frequency range of approximately 100–1000 Hz, with the amplitude controlled by variations in the phase relation. The two acoustic measurement sections for reconstructing the upstream and downstream acoustic fields consist of five flush-mounted microphones each, whereas the downstream ones are water-cooled. The rig has approximately 200 static transducers to measure temperatures, static pressures, mass flows, and differences of static pressure with acquisition rates of 1 Hz. These measurements include upstream and downstream pressures, upstream temperature, pressure drops across the injector and liner, and air mass flow. The static pressures and pressure differences are measured at three radial positions and then averaged. The downstream temperature is not measured but estimated based on the fuel concentration, net caloric value of the fuel, upstream pressure, and upstream temperature, whereas the impact of wall cooling is neglected.

The test section is shown schematically in Fig. 4(*a*). It is situated amidst the microphone arrays and consists of an injector unit with a fuel spray nozzle and five axial swirlers, and a combustion chamber with a bypass annulus for effusion cooling. The main air is split at the injector in three streams (through the injector for combustion, through the bypass annulus, and through the heat shield as cooling air). The combustion chamber walls are cooled by effusion cooling (transpiration cooling), achieved by moving air from the outer annulus through the liner structure (thousands of small holes). Due to its application in an aero-engine, the geometry of the single-sector axis-symmetrical combustor has a typical shape that tapers in diameter toward its outlet (i.e., turbine inlet). The entire test section (between the black dots) can be considered as a black-box by means of the combustor transfer matrix as shown in Fig. 4(*b*). The postprocessed combustor transfer matrices $\widetilde{\mathbf{C}}^{\mathrm{c}}$ (no flame) and $\widetilde{\mathbf{C}}^{\mathrm{h}}$ (flame) are shown in Fig. 5. All frequencies in this work are nondimensionalized using a Strouhal number for confidentiality

$$\mathrm{St} = f\frac{L_{\mathrm{ref}}}{u_{\mathrm{ref}}} \tag{21}$$

where f is the frequency, L_{ref} is the diameter of the injector, and u_{ref} is the bulk velocity of the inlet air stream.

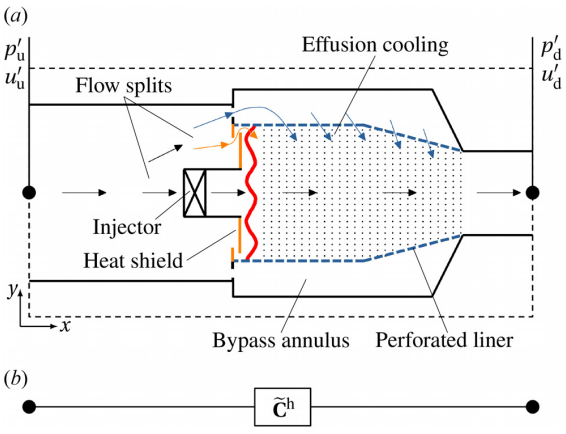

Fig. 4 (*a*) Schematic representation and (*b*) black-box model of the SCARLET test section in Fig. 3. The five axial swirlers are encompassed in the simplistic representation of the injector.

3.2 Acoustic Network Model. The model-based inference of the flame transfer matrix presented in Sec. 2.3 combines acoustic transfer matrix measurements with an acoustic network model of the test rig. The network model of SCARLET used in this work is built using taX [35] and consists of 185 elements in total, including duct segments, area changes with and without pressure losses, converging and diverging junctions, and a compact flame element (in hot conditions). The *ducts* are modeled based on the one-dimensional acoustic wave equation [35] and are discretized with a third-order upwind scheme. The shortest wavelength of interest is highly resolved with 100 base points. Sudden *area changes* are represented with the $L-\zeta$ model [16,36]. The injector, bypass entry, effusion holes, and heat shield are penalized with a pressure loss coefficient ζ calculated from measured pressure differences, while effective and reduced lengths are set to zero [36]. Even though the geometry of the injector unit is highly complex, the axially arranged swirl vanes may be reasonably assumed to have acoustically transparent behavior [37]. Experimentally or numerically determined transfer matrices

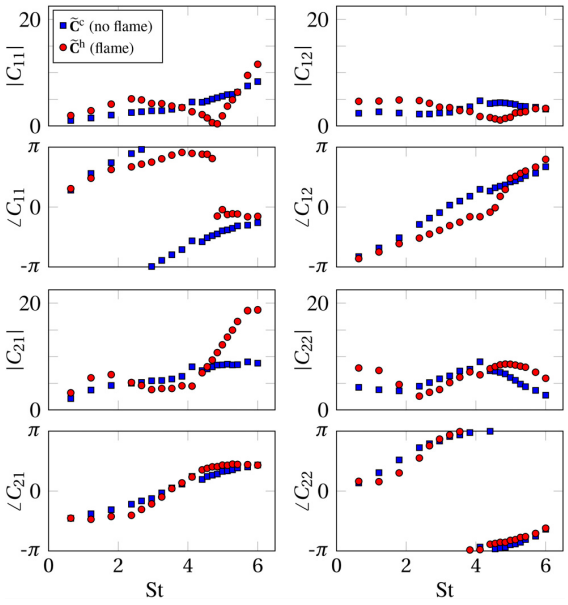

Fig. 5 Gain and phase of the coefficients of the experimental combustor transfer matrices of SCARLET

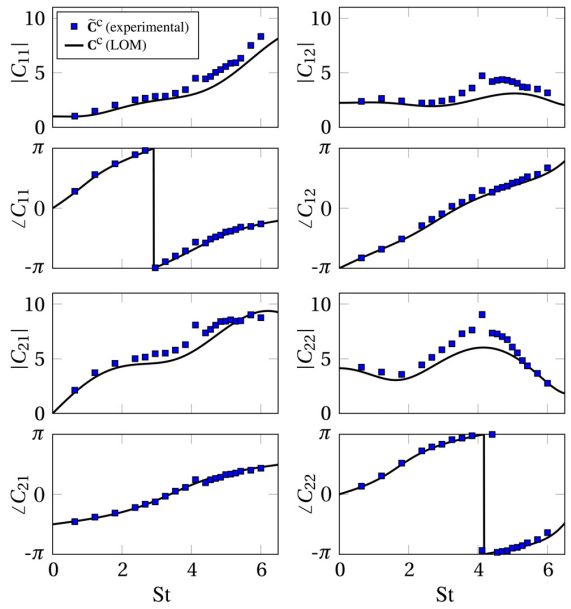

Fig. 6 Gain and phase of the coefficients of the combustor transfer matrix for cold conditions obtained from experimental data $\mathbf{C}^c$ and LOM $\mathbf{C}^c$

should be used to increase the model's accuracy, especially at higher frequencies [20,38,39]. The convergent part of the combustion chamber is modeled as ten consecutive series of duct and area change. The real combustor has several thousand cooling holes in the acoustic liner. These holes are lumped into 20 branches in the LOM, each as a series of area change-duct-area change. Increasing the number of branches does not improve the results. The upstream and downstream boundaries are treated as nonreflective since they do not affect the determination of the combustor transfer matrix (acoustic/geometric changes outside the test section are irrelevant). Furthermore, the dependence of material properties on the temperature and mixture is neglected ($c_p \neq f(T, Y_i) = \text{const.}$ and $R \neq f(Y_i) = \text{const.}$, i.e., $\gamma = c_p/(c_p - R) \neq f(T, Y_i) = \text{const.}$) and low Mach numbers ($\mathcal{O}(\mathrm{M}^1)$) are assumed in all elements, which are common (yet questionable) assumptions made in thermoacoustic network models [14,40–42].

The acoustic network model in this work is based on geometrical information (lengths, diameters, areas) and static measurements (upstream and downstream pressure, upstream temperature, upstream mass flow) of SCARLET. The downstream temperature is estimated as described in Sec. 3. The flow splits are determined using low-order model calculations for the flow, and the effective surface area of the injector is approximated. The underlying model is physics-based and does not rely on spurious tuning parameters. This ensures a reasonably accurate modeling of the internal system dynamics, whereas fitting model parameters solely to global behavior (i.e., combustor transfer matrix) would violate this approach. A comparison of the cold combustor transfer matrix from measurements $\tilde{\mathbf{C}}^c$ and the acoustic network model $\mathbf{C}^c$ (Eq. (18)) is shown in Fig. 6. Both the gain and phase of the LOM are in quantitative agreement with experiments. Together with the physics-based approach of the LOM (internal system dynamics), this agreement ensures accurate modeling of the global behavior.

4 Limitations of the Burner-Flame Transfer Matrix Approach

The BFTM method, as described in Sec. 2.2, is appealing due to its simplicity and use of solely experimental input data. Unfortunately,

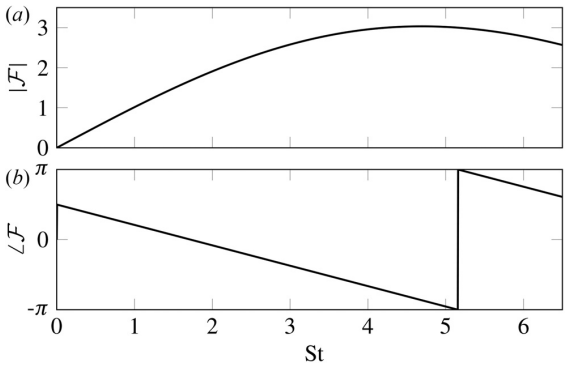

Fig. 7 (*a*) Gain and (*b*) phase of the generic flame transfer function $\mathcal{F}^*$

it is inconsistent for combustor geometries such as the present one with effusion cooling, bypass annulus, and downstream end contraction [27,28]. The goal of this section is to visualize this inconsistency.

A method is consistent if it can recover the reference solution without modeling errors, measurement inconsistencies, and uncertainties. To generate such a fully consistent dataset in combination with a known reference FTM, this section combines the LOM of SCARLET (see Sec. 3.2) with a generic FTM to generate $\tilde{\mathbf{C}}^h$. Additionally, $\tilde{\mathbf{C}}^c$ at the same operating point is generated using the LOM. Note that in this section, the transfer matrices $\mathbf{F}^*$, $\tilde{\mathbf{C}}^h$, and $\tilde{\mathbf{C}}^c$ are therefore purely analytical, while the flow quantities of the LOM are based on the realistic engine condition given in Table 1. The generic FTM has been generated using the Rankine–Hugoniot relations [5,20]

$$\mathbf{F}_{\mathrm{RH}} = \begin{pmatrix} \frac{\rho_c c_c}{\rho_h c_h} & -\theta \mathrm{M}_h (1 + \mathcal{F}(\omega)) \\ -\gamma\theta \mathrm{M}_c & 1 + \theta\mathcal{F}(\omega) \end{pmatrix} \tag{22}$$

where $\theta = (T_h/T_c - 1)$, T is the temperature, ρc is the acoustic impedance, M is the Mach number, and $\mathcal{F}(\omega)$ is the flame transfer function (FTF) of a velocity-sensitive flame used as closure for the heat release rate fluctuations. The FTF is defined as

$$\mathcal{F}(\omega) \equiv \frac{\dot{Q}'(\omega)/\bar{\dot{Q}}}{u_c'(\omega)/\bar{u}_c} \tag{23}$$

where $\dot{Q}$ is the heat release rate and u_c is the velocity in the cold region upstream of the flame. This work uses a generic distributed time delay (DTD) model [43] of a partially premixed flame $\mathcal{F}^*$ as shown in Fig. 7. The corresponding generic FTM is obtained by incorporating $\mathcal{F}^*$ into Eq. (22) and is referred to as $\mathbf{F}^*$.

Figure 8 shows the FTMs postprocessed from the generic combustor transfer matrices of the SCARLET LOM via the BFTM approach (dash-dotted line) and the MBI method (solid line) and compares them to the reference solution $\mathbf{F}^*$. The MBI method is consistent, and its result coincides with the reference solution for the generic dataset used. In Fig. 8, $\mathbf{F}^*$ and the MBI results are represented by the same (solid) line. In contrast, the FTM postprocessed with the BFTM method shows large deviations from $\mathbf{F}^*$ in all transfer matrix coefficients. These discrepancies in the FTM originate solely from the inconsistency of the BFTM method for complex thermoacoustic test rigs like SCARLET and demonstrate furthermore its inapplicability in such cases.

In SCARLET, the inconsistency of the BFTM method is due to three features as summarized in Table 2—the area contraction at the end of the combustion chamber (C) as well as the acoustics (A) and the mean flow (M) bypassing the flame through the effusion holes. The following paragraph analyzes their contributions to the

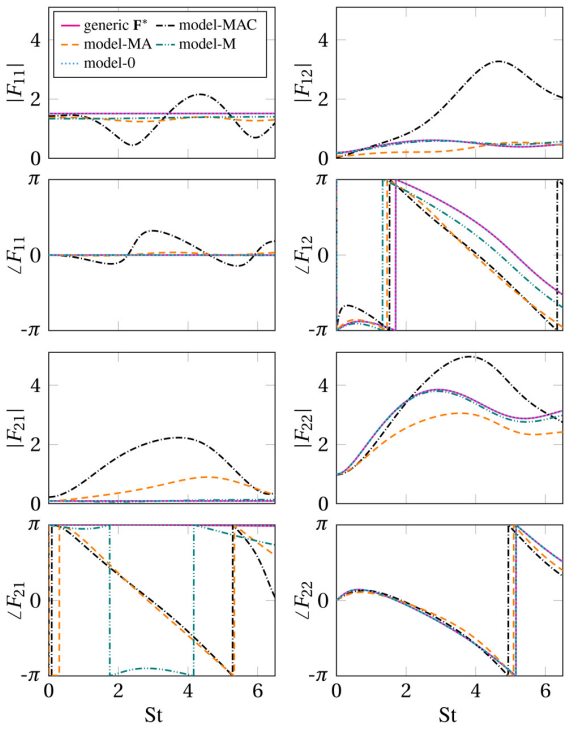

Fig. 8 Gain and phase of the coefficients of the generic $\mathbf{F}^*$ and the flame transfer matrices postprocessed from the generic SCARLET models detailed in Fig. 9 via the BFTM approach: model-MAC (original LOM), model-MA, model-M, and model-0. Note that model-0 and $\mathbf{F}^*$ overlap. The MBI result coincides with $\mathbf{F}^*$ in all cases and is therefore represented by the same solid line.

Table 2 Geometrical and flow features of different generic SCARLET low-order models used in this section. Important features are the meanflow bypass (M), the acoustic bypass (A) and the area contraction at the end of the combustion chamber (C).

	M	A	C
model-MAC	✓	✓	✓
model-MA	✓	✓	
model-M	✓		
model-0			

deviations of the BFTM method. Therefore, the SCARLET LOM is gradually adapted three times, removing the features M, A, and C. Figure 9 displays the corresponding generic SCARLET models. All other key features besides M, A, and C, like the FTM $\mathbf{F}^*$, mass flow splits, and pressure losses, remain unchanged. The SCARLET LOM detailed in Sec. 3.2 includes all features and is therefore awarded the short name *model-MAC* (Fig. 9(*a*)). In the *model-MA* (Fig. 9(*b*)), the area contraction of the combustion chamber is removed by adapting the diameter of the downstream duct. The *model-M* (Fig. 9(*c*)) additionally eliminates the acoustic bypass through the effusion holes and the heat shield. This is achieved by inserting a fully reflective, acoustically energy-conserving element into each effusion hole and the heat shield. Finally, the *model-0* (Fig. 9(*d*)) also removes the bypass mean flow by venting all bypass air through a nozzle at the end of the bypass annulus.

The FTMs postprocessed with the BFTM approach for the generic SCARLET model-MAC, model-MA, model-M, and model-0 are visualized in Fig. 8 in addition to the MBI result. In the case of SCARLET, the area contraction at the end of the combustion chamber contributes most to the deviations of the BFTM method in all transfer coefficients of $\mathbf{F}^*$ (see the difference between model-MAC and model-MA). The magnitude of this deviation is directly linked to the area contraction and increases with stronger area contractions and vice versa. Compared to the deviations introduced by C, the deviations corresponding to the acoustic bypass (difference between model-MA and model-M) are smaller but yet in the same order of magnitude. This contribution's magnitude and frequency content depend strongly on the flow characteristics and the geometry of the bypass. Which of the two features, A or C, dominates the deviations in a given setup, and whether they partially cancel each other out, highly depends on the problem. Overall, both A and C should be assumed to invalidate the BFTM method for a specific setup unless proven otherwise. The final deviation of the cooling air reentering the combustion chamber (difference between model-M and model-0) is inferior to the other two effects. For model-0, the FTM postprocessed with the BFTM method coincides with the reference $\mathbf{F}^*$, proving that all features that render the BFTM method inconsistent have been removed.

5 Application to Experimental Measurements

The model-based inference method is applicable for complex thermoacoustic test rigs. As shown in Secs. 2.3 and 4, it is furthermore exact if the available combustor transfer matrix and the corresponding LOM are fully consistent. However, postprocessing of real experimental measurement data has to deal with combustor transfer matrices and LOMs subject to modeling and measurement errors. Therefore, the available combustor transfer matrices and the LOM are never fully consistent. This section discusses the capabilities and functionality of the model-based inference method in this case.

5.1 Flame Transfer Matrix of SCARLET. The model-based inference method relies on the accuracy of the LOM used. Therefore, to infer reliable results, it is necessary to ensure that the LOM well approximates the combustor's global and internal system dynamics. The accuracy of the LOM concerning the global dynamics of the combustor was assessed by first comparing the experimental combustor transfer matrix $\tilde{\mathbf{C}}^c$ with the corresponding model $\mathbf{C}^c$ (Eq. (18)) in Fig. 6. As a second measure for the accuracy of the LOM, this section computes the FTM using the BFTM method (Eq. (20)) with $\tilde{\mathbf{C}}^c$ and with $\mathbf{C}^c$, respectively. The results are plotted in Fig. 10. Note that although the BFTM method does not determine the correct FTM (see Sec. 4), the two FTMs of the BFTM method

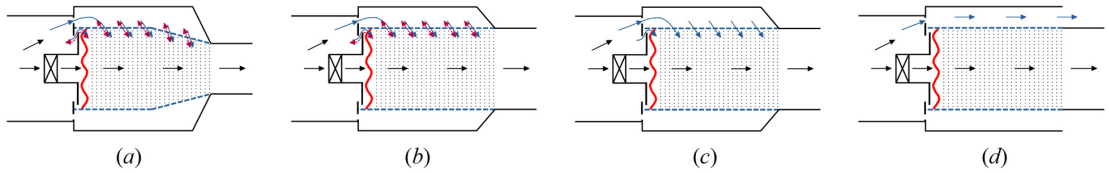

Fig. 9 Schematic representation of the generic SCARLET models. Bypass mean flow and bypass acoustics are indicated by arrows and double arrows, respectively: (*a*) model-MAC, (*b*) model-MA, (*c*) model-M, and (*d*) model-0.

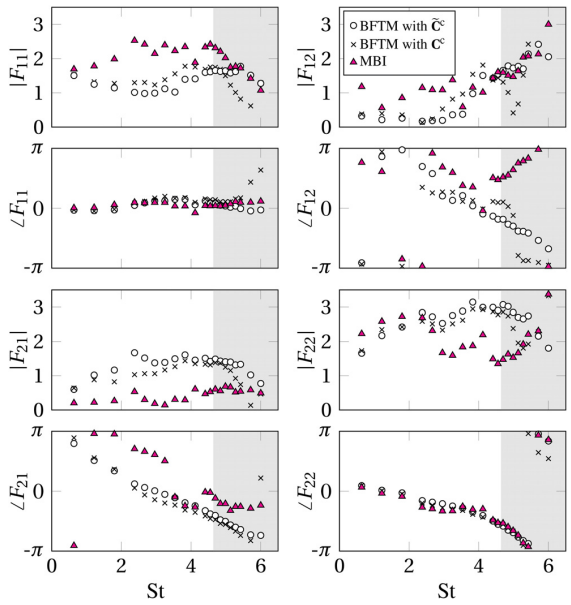

Fig. 10 Gain and phase of the coefficients of the flame transfer matrices of SCARLET computed with the MBI method and obtained with the BFTM approach using the experimental hot combustor transfer matrix $\tilde{\mathbf{C}}^h$ in combination with the experimental or modeled cold combustor transfer matrix $\tilde{\mathbf{C}}^c$ or $\mathbf{C}^c$, respectively, for comparison reasons and as an indicator for the accuracy of the LOM used

should coincide in case of a perfect model. The magnitude of discrepancy, on the other hand, will indicate to what extent inadequacies of the model $\tilde{\mathbf{C}}_c$ impact the determination of the FTM. Figure 10 shows a good agreement between the two FTMs for $\mathrm{St} \leq 4.5$. For $\mathrm{St} > 4.5$, the two FTMs diverge in all coefficients, and it is concluded that the LOM is inaccurate in this frequency range. Figure 10 is therefore grayed out for $\mathrm{St} > 4.5$.

Finally, the LOM described in Sec. 3.2 is used to infer the FTM from the experimental combustor transfer matrix $\tilde{\mathbf{C}}^h$ of SCARLET shown in Fig. 5. The model-based inference method uses the LOM to calculate the FTM of SCARLET. The resulting FTM is shown in Fig. 10 as triangles. Analogous to Sec. 4, the FTM coefficients of the BFTM approach and the model-based inference method differ from each other. This is expected due to the inconsistency of the BFTM method. However, in contrast to the ideal case in Sec. 4, the FTM of the model-based inference method is subject to modeling and measurement errors resulting in potential discrepancies between the experimental combustor transfer matrix $\tilde{\mathbf{C}}^h$ and the corresponding LOM. At this point, no quantitative statement can be made about the accuracy of the FTM due to the lack of a reference solution of SCARLET or a quantitative quality measure for the LOM applied. Qualitatively, a comparison between the FTM obtained with the model-based inference method and the BFTM approach shows similar effects as in Fig. 8. The phase of F_{11} is flattened. The coefficient F_{21} is strongly reduced in amplitude. The maximum amplitude of the coefficient F_{22} is shifted to lower Strouhal numbers, and at higher frequencies, the overall amplitude is reduced. The phase of coefficient F_{22} remains nearly unchanged. The outlier in the combustor transfer matrices $\tilde{\mathbf{C}}^c$ and $\tilde{\mathbf{C}}^h$ at $\mathrm{St} \approx 4$ (see Figs. 5 and 6) is present in all coefficients of the FTMs.

The inferred FTM in Fig. 10 suggests that the Rankine-Hugoniot relations (Eq. (22)) together with the FTF in Eq. (23) are applicable in the present case. For low Mach number flows ($\mathrm{M_c} \ll 1$), the F_{22} element in Eq. (22) is commonly used to determine the flame dynamics via $\mathcal{F}(\omega) = 1/\theta(F_{22} - 1)$ [23–26]. Figure 11 shows the flame transfer function of SCARLET under these assumptions. The upcoming section discusses possible ways to enhance the quantification of model accuracy for the model-based inference method.

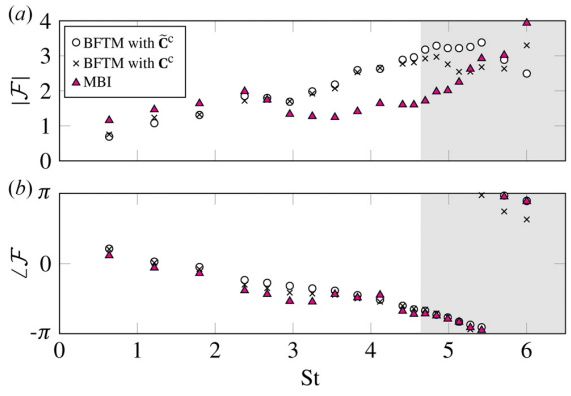

Fig. 11 (*a*) Gain and (*b*) phase of the flame transfer function of SCARLET computed with the MBI method and obtained with the BFTM approach using the experimental hot combustor transfer matrix $\tilde{\mathbf{C}}^h$ in combination with the experimental or modeled cold combustor transfer matrix $\tilde{\mathbf{C}}^c$ or $\mathbf{C}^c$, respectively

5.2 Discussion. The model-based inference method is a mathematically consistent approach to determining the FTM from the experimental combustor transfer matrices of complex thermoacoustic test rigs. However, its dependence on a LOM introduces a sensitivity to modeling errors. Any inaccuracies of the acoustic LOM will manifest as errors in the FTM. Therefore, it is crucial to ensure a good approximation of the global behavior and inner system dynamics of the combustor by the LOM.

Combining the model-based inference method with statistical procedures, such as Bayesian inference [44,45], may relax these constraints. Explicitly accounting for uncertainties in the experimental combustor transfer matrices and model input parameters would help to quantify the propagation of errors in the FTM. Additionally, the computation of uncertainty bounds for the FTM would visualize the reliability of the inferred result. Furthermore, quality measures could be systematically computed, facilitating the assessment of different LOMs in terms of their alignment with experimental combustor transfer matrices.

To ensure the fidelity of the internal system dynamics, it is imperative to construct the LOM with a high degree of physical realism. Introducing modeling assumptions, such as low Mach number flows or constant gas properties, should be avoided or chosen with meticulous care. In general, the LOM should be designed to minimize the number of uncertain input parameters, thereby enhancing its reliability in representing the intricacies of the system's internal system dynamics. If available, subelements or subsections of the LOM may be replaced by scattering matrices obtained from additional experiments or numerical simulations. In this case, the quality of the LOM would increase with the development of the combustor.

6 Conclusion and Outlook

This work focuses on the inference of the flame transfer matrix from experimental combustor transfer matrices of thermoacoustic test rigs with complex features, such as acoustic cross-communication bypassing the flame or area contractions at the combustion chamber outlet. The BFTM approach to postprocess the FTM simply combines the experimentally determined transfer matrices of the hot and cold burner at the same inlet conditions. Note that the BFTM approach achieves robustness by heavily constraining the internal system dynamics. This work shows that this approach is mathematically inconsistent for test rigs with complex features. Instead, a model-based inference method utilizing a LOM

to approximate the internal system dynamics of the combustor is proposed—a generalized framework to infer the FTM in complex setups. In addition, using a LOM can reduce the experimental effort as cold measurements are only required to validate the same but not at every operation point. The model-based inference method converges to the BFTM method in the absence of complex test rig features. The capabilities of the model-based inference method are analyzed by applying it to generic and experimental data sets of the Rolls-Royce SCARLET test rig operated under realistic engine conditions.

Formulating an accurate LOM is the most challenging part of the model-based inference method. A physics-based approach with minimal assumptions is used in this study. For future work, we propose to couple the MBI method with statistical procedures such as Bayesian inference. This coupling promises the systematic computation of quality measures to compare different LOMs, uncertainty bounds for the inferred FTM, and a reduced error propagation in the FTM.

Acknowledgment

The authors gratefully acknowledge the German Research Foundation (Deutsche Forschungsgemeinschaft, DFG) for financial support under the DFG Transfer Project (No. PO 710/23-1) NoiSI. We also acknowledge the support of the DLR test crew.

Funding Data

- Deutsche Forschungsgemeinschaft (DFG) (Award No. PO 710/23-1; Funder ID: 10.13039/501100001659).

Data Availability Statement

The datasets generated and supporting the findings of this article are obtainable from the corresponding author upon reasonable request.

Nomenclature

$\mathbf{B}$ = burner transfer matrix
$\mathbf{C}$ = combustor transfer matrix
c = speed of sound (m s^{-1})
$\mathbf{D}$ = duct transfer matrix
$\mathcal{F}$ = flame transfer function
$\mathbf{F}$ = flame transfer matrix
f, g = acoustic Riemann invariants
M = Mach number
p = pressure (kg m^{-1} s^{-2})
$\dot{Q}$ = heat release rate (W m^{-3})
St = Strouhal number
$\mathbf{T}$ = transfer matrix
u = velocity (m s^{-1})

Greek Symbols

γ = heat capacity ratio
θ = temperature ratio
ρ = density (kg m^{-3})
ω = angular frequency (Hz)

Subscripts

r = reactants
ref = reference position
p = products
u = upstream

Superscripts

c = cold
h = hot
$*$ = generic
$\sim$ = measurement

Abbreviations

BFTM = burner-flame transfer matrix
DTD = distributed time delay
FTF = flame transfer function
FTM = flame transfer matrix
LOM = low-order model
MBI = model-based inference
MMM = multi-microphone method

Appendix: Derivation of Combustor Transfer Matrix Models

Analogously to the derivations in Sec. 2.3, a model for the hot combustor matrix $\mathbf{C}^{\mathrm{c}}$ can be derived by interconnecting the connector model (Fig. 2, center) with a known flame transfer matrix $\mathbf{F}$ (Fig. 2, upper right). For that purpose, the first row of Eq. (13) is used to substitute $\mathbf{v}_{\mathrm{r}}$ in Eq. (10)

$$\begin{aligned}\mathbf{v}_{\mathrm{p}} &= \mathbf{F}\mathbf{v}_{\mathrm{r}} \\ &= \mathbf{F}\left(\mathbf{T}^{\mathrm{h}}_{\mathrm{ru}}\mathbf{v}_{\mathrm{u}} + \mathbf{T}^{\mathrm{h}}_{\mathrm{rp}}\mathbf{v}_{\mathrm{p}}\right)\end{aligned} \quad \Rightarrow \quad \mathbf{v}_{\mathrm{p}} = \left(\mathbf{F}^{-1} - \mathbf{T}^{\mathrm{h}}_{\mathrm{rp}}\right)^{-1}\mathbf{T}^{\mathrm{h}}_{\mathrm{ru}}\mathbf{v}_{\mathrm{u}} \tag{A1}$$

Subsequently, Eq. (A1) is used to replace $\mathbf{v}_{\mathrm{p}}$ in the bottom row of Eq. (13) to retrieve $\mathbf{C}^{\mathrm{h}}$

$$\mathbf{v}_{\mathrm{d}} = \underbrace{\left[\mathbf{T}^{\mathrm{h}}_{\mathrm{dp}}\left(\mathbf{F}^{-1} - \mathbf{T}^{\mathrm{h}}_{\mathrm{rp}}\right)^{-1}\mathbf{T}^{\mathrm{h}}_{\mathrm{ru}} + \mathbf{T}^{\mathrm{h}}_{\mathrm{du}}\right]}_{\mathbf{C}^{\mathrm{h}}}\mathbf{v}_{\mathrm{u}} \tag{A2}$$

This procedure is displayed in Fig. 2 by the gray dashed arrows. The cold combustor matrix model $\tilde{\mathbf{C}}^{\mathrm{c}}$ is retrieved from Eq. (2) by replacing with the identity matrix $\mathbf{I}$ and evaluating $\mathbf{T}_{\mathrm{ru}}$, $\mathbf{T}_{\mathrm{rp}}$, $\mathbf{T}_{\mathrm{du}}$, and $\mathbf{T}_{\mathrm{dp}}$ for cold conditions

$$\mathbf{C}^{\mathrm{c}} = \mathbf{T}^{\mathrm{c}}_{\mathrm{dp}}\left(\mathbf{I} - \mathbf{T}^{\mathrm{c}}_{\mathrm{rp}}\right)^{-1}\mathbf{T}^{\mathrm{c}}_{\mathrm{ru}} + \mathbf{T}^{\mathrm{c}}_{\mathrm{du}} \tag{A3}$$

References

[1] Lieuwen, T., and Yang, V., eds., 2005, *Combustion Instabilities in Gas Turbine Engines*, Vol. 210, AIAA, Reston, VA.
[2] Poinsot, T., 2017, "Prediction and Control of Combustion Instabilities in Real Engines," Proc. Combust. Inst., **36**(1), pp. 1–28.
[3] Merk, H. J., 1957, "Analysis of Heat-Driven Oscillations of Gas Flows," Appl. Sci. Res., **6**(4), pp. 317–336.
[4] Bohn, D., and Deucker, E., 1993, "An Acoustical Model to Predict Combustion Driven Oscillations," 20th International Congress on Combustion Engines, CIMAC, London, UK, Mar. 17–20.
[5] Keller, J. J., 1995, "Thermoacoustic Oscillations in Combustion Chambers of Gas Turbines," AIAA J., **33**(12), pp. 2280–2287.
[6] Paschereit, C. O., and Polifke, W., 1997, "Characterization of Lean Premixed Gas Turbine Burners as Acoustic Multi-Ports," APS/DFD Annual Meeting, APS, San Francisco, NC, Nov. 23–25.
[7] Dowling, A. P., 1999, "Thermoacoustic Instability," 6th International Congress on Sound and Vibration, Copenhagen, Denmark, pp. 3277–3292.
[8] Eckstein, J., and Sattelmayer, T., 2006, "Low-Order Modeling of Low-Frequency Combustion Instabilities in Aeroengines," J. Propul. Power, **22**(2), pp. 425–432.
[9] Schuermans, B., Guethe, F., Pennell, D., Guyot, D., and Paschereit, C. O., 2010, "Thermoacoustic Modeling of a Gas Turbine Using Transfer Functions Measured Under Full Engine Pressure," ASME J. Eng. Gas Turbines Power, **132**(11), p. 111503.
[10] Munjal, M. L., 2014, *Acoustics of Ducts and Mufflers*, 2nd ed., Wiley, Chichester, UK.
[11] Emmert, T., 2016, "State Space Modeling of Thermoacoustic Systems With Application to Intrinsic Feedback," Ph.D. thesis, Technical University of Munich, Munich, Germany.
[12] Pankiewitz, C., Fischer, A., Hirsch, C., and Sattelmayer, T., 2003, "Computation of Transfer Matrices for Gas Turbine Combustors Including Acoustics/Flame Interaction," AIAA Paper No. 2003-3295.

[13] Bothien, M., Lauper, D., Yang, Y., and Scarpato, A., 2019, "Reconstruction and Analysis of the Acoustic Transfer Matrix of a Reheat Flame From Large-Eddy Simulations," ASME J. Eng. Gas Turbines Power, **141**(2), p. 021018.

[14] Gant, F., Cuquel, A., and Bothien, M. R., 2022, "Autoignition Flame Transfer Matrix: Analytical Model Versus Large Eddy Simulations," Int. J. Spray Combust. Dyn., **14**(1–2), pp. 72–81.

[15] Reinhardt, H., Alanyal Ioğlu, Ç. O., Fischer, A., Lahiri, C., Nicolai, H., and Hasse, C., 2023, "Simulation of the Thermoacoustic Response of an Aero-Engine Gas Turbine Fuel Injector Using a Hybrid CFD-CAA Method," ASME J. Eng. Gas Turbines Power, **145**(11), p. 111016.

[16] Schuermans, B., Polifke, W., and Paschereit, C. O., 1999, "Modeling Transfer Matrices of Premixed Flames and Comparison With Experimental Results," ASME Paper No. 99-GT-132.

[17] Munjal, M. L., and Doige, A. G., 1990, "Theory of a Two Source-Location Method for Direct Experimental Evaluation of the Four-Pole Parameters of an Aeroacoustic Element," J. Sound Vib., **141**(2), pp. 323–333.

[18] Peters, M. C. A. M., Hirschberg, A., Reijnen, A. J., and Wijnands, A. P. J., 1993, "Damping and Reflection Coefficient Measurements for an Open Pipe at Low Mach and Low Helmholtz Numbers," J. Fluid Mech., **256**, pp. 499–534.

[19] Paschereit, C. O., and Polifke, W., 1998, "Investigation of the Thermo-Acoustic Characteristics of a Lean Premixed Gas Turbine Burner," ASME Paper No. 98-GT-582.

[20] Paschereit, C. O., Schuermans, B., Polifke, W., and Mattson, O., 2002, "Measurement of Transfer Matrices and Source Terms of Premixed Flames," ASME J. Eng. Gas Turbines Power, **124**(2), pp. 239–247.

[21] Bellucci, V., Schuermans, B., Nowak, D., Flohr, P., and Paschereit, C. O., 2005, "Thermoacoustic Modeling of a Gas Turbine Combustor Equipped With Acoustic Dampers," ASME J. Turbomach., **127**(2), pp. 372–379.

[22] Schuermans, B., 2003, "Modeling and Control of Thermoacoustic Instabilities," Ph.D. thesis, École Polytechnique Fédérale de Lausanne, Lausanne, Switzerland.

[23] Schimek, S., Göke, S., Schrödinger, C., and Paschereit, C. O., 2012, "Flame Transfer Function Measurements With CH4 and H2 Fuel Mixtures at Ultra Wet Conditions in a Swirl Stabilized Premixed Combustor," ASME Paper No. GT2012-69788.

[24] Bobusch, B. C., Moeck, J. P., Paschereit, C. O., and Sadig, S., 2012, "Thermoacoustic Stability Analysis of a Kerosene-Fueled Lean Direct Injection Combustor Employing Acoustically and Optically Measured Transfer Matrices," ASME Paper No. GT2012-69034.

[25] Bade, S., Wagner, M., Hirsch, C., Sattelmayer, T., and Schuermans, B., 2014, "Influence of Fuel-Air Mixing on Flame Dynamics of Premixed Swirl Burners," ASME Paper No. GT2014-25381.

[26] Blondé, A., Schuermans, B., Pandey, K., and Noiray, N., 2023, "Effect of Hydrogen Enrichment on Transfer Matrices of Fully and Technically Premixed Swirled Flames," ASME J. Eng. Gas Turbines Power, **145**(12), p. 121009.

[27] Alanyal Ioğlu, C., Reinhardt, H., Fischer, A., Lahiri, C., Nicolai, H., and Hasse, C., 2023, "Comparison of Acoustic, Optic, and Heat Release Rate Based Flame Transfer Functions for a Lean-Burn Injector Under Engine-Like Conditions," Symposium on Thermoacoustics in Combustion, Zurich, Switzerland, Sept. 11–14.

[28] Eder, A. J., Fischer, A., Lahiri, C., Merk, M., Staufer, M., Eggels, R., Silva, C. F., and Polifke, W., 2023, "Identification of the Dynamics of a Turbulent Spray Flame at High Pressure," Symposium on Thermoacoustics in Combustion, Zurich, Switzerland, Sept. 11–14.

[29] Fischer, A., Lahiri, C., and Doerr, T., 2017, "Design, Build, and Commissioning of the New Thermo-Acoustics Combustion Test Rig SCARLET," Rolls-Royce Deutschland, Report No. DLRK2017-450116.

[30] Fischer, A., and Lahiri, C., 2021, "Ranking of Aircraft Fuel-Injectors Regarding Low Frequency Thermoacoustics Based on an Energy Balance Method," ASME Paper No. GT2021-59561.

[31] Lavrentjev, J., Åbom, M., and Bodén, H., 1995, "A Measurement Method for Determining the Source Data of Acoustic Two-Port Sources," J. Sound Vib., **183**(3), pp. 517–531.

[32] Ben-Israel, A., and Greville, T. N. E., 2003, *Generalized Inverses: Theory and Applications*, 2nd ed., Springer, New York.

[33] Åbom, M., 1992, "A Note on the Experimental Determination of Acoustical Two-Port Matrices," J. Sound Vib., **155**(1), pp. 185–188.

[34] Schuermans, B., Bellucci, V., Guethe, F., Meili, F., Flohr, P., and Paschereit, C. O., 2004, "A Detailed Analysis of Thermoacoustic Interaction Mechanisms in a Turbulent Premixed Flame," ASME Paper No. GT2004-53831.

[35] Emmert, T., Meindl, M., Jaensch, S., and Polifke, W., 2016, "Linear State Space Interconnect Modeling of Acoustic Systems," Acta Acust. United Acust., **102**(5), pp. 824–833.

[36] Gentemann, A., Fischer, A., Evesque, S., and Polifke, W., 2003, "Acoustic Transfer Matrix Reconstruction and Analysis for Ducts With Sudden Change of Area," AIAA Paper No. 3142.

[37] Kim, K. T., Lee, J. G., Quay, B. D., and Santavicca, D. A., 2010, "Spatially Distributed Flame Transfer Functions for Predicting Combustion Dynamics in Lean Premixed Gas Turbine Combustors," Combust. Flame, **157**(9), pp. 1718–1730.

[38] Van Horn, E. M., and Scarborough, D. E., 2022, "Low-Frequency Acoustic Response of Gas Turbine Perforated Plate and Axial Swirler," ASME J. Eng. Gas Turbines Power, **144**(5), p. 051008.

[39] Meindl, M., Merk, M., Fritz, F., and Polifke, W., 2019, "Determination of Acoustic Scattering Matrices From Linearized Compressible Flow Equations," J. Theor. Comput. Acoust., **27**(3), p. 1850027.

[40] Dowling, A. P., 1995, "The Calculation of Thermoacoustic Oscillation," J. Sound Vib., **180**(4), pp. 557–581.

[41] Dowling, A. P., and Stow, S. R., 2003, "Acoustic Analysis of Gas Turbine Combustors," J. Propul. Power, **19**(5), pp. 751–764.

[42] Strobio Chen, L., Bomberg, S., and Polifke, W., 2016, "Propagation and Generation of Acoustic and Entropy Waves Across a Moving Flame Front," Combust. Flame, **166**, pp. 170–180.

[43] Polifke, W., 2020, "Modeling and Analysis of premixed flame Dynamics by Means of Distributed Time Delays," Prog. Energy Combust. Sci., **79**, p. 100845.

[44] MacKay, D. J., 2003, *Information Theory, Inference, and Learning Algorithms*, Cambridge University Press, New York.

[45] Yoko, M., and Juniper, M. P., 2023, "Data-Driven Modelling of Thermoacoustic Instability in a Ducted Conical Flame," Symposium on Thermoacoustics in Combustion, Zurich, Switzerland, Sept. 11–14.

D.3 PAPER-JUMP

Combustion and Flame 274 (2025) 113958

Contents lists available at ScienceDirect

Combustion and Flame

journal homepage: www.sciencedirect.com/journal/combustion-and-flame

A Jacobian-based framework for the derivation of comprehensive thermoacoustic jump conditions

Moritz Merk *, Felix Schily, Wolfgang Polifke

Technical University of Munich, TUM School of Engineering and Design, Department of Engineering Physics and Computation, Boltzmannstr. 15, Garching, 85747, Germany

ARTICLE INFO

Keywords:
Jump conditions
Jacobian-based framework
Partially premixed flame
Autoignition flame
Thermoacoustics
Network modeling

ABSTRACT

Low-order network models are an efficient framework to describe and predict thermoacoustic phenomena in confined combustion systems. These models are based on the interconnection of compact and non-compact elements representing the main components of the system. Assumptions such as small Mach numbers or constant gas properties are typically applied in the derivation of these elements.

This work proposes a Jacobian-based framework for the derivation of comprehensive thermoacoustic jump conditions (compact elements) accounting for acoustic, entropic, and compositional perturbations. The modularity provided by the Jacobian-based formulation renders the framework easily applicable for the derivation of a variety of compact elements and provides a straightforward implementation guideline. Application-specific assumptions to increase computational efficiency or, conversely, to ease the implementation may be included *a posteriori*, enabling easy switching between accurate and efficient formulations without rederivation. The capabilities of this framework are demonstrated by deriving a novel, highly accurate lean premixed flame model. This novel flame model is validated for the case of a lean premixed H_2 autoignition flame.

Novelty and Significance

This study proposes a novel framework for developing jump conditions for compact elements of thermoacoustic network models. Unlike the established approach of deriving case-specific jump conditions by hand, our Jacobian-based method generates jump conditions valid for a wide range of application cases with a modularity that eases implementation and the possibility of straightforward a posteriori customization for specific application cases. For the first time, jump conditions for acoustic, entropic and compositional perturbations across a lean premixed flame that allow for arbitrary Mach numbers, realistic gas properties as well as flame movement are developed, showcasing the capabilities of the proposed framework. The proposed framework adds flexibility to thermoacoustic network models that enable a quick adjustment to vary application-specific requirements concerning accuracy and efficiency.

1. Introduction

Lean-burn combustion systems, such as low emission gas turbines or aero-engines, are prone to thermoacoustic combustion instabilities that can limit the operational range of the engine, increase wear, or even result in system failure [1,2]. Accurate and efficient prediction tools are crucial to aid and accelerate the design process in engine development programs to prevent these self-excited instabilities.

Low-order network modeling [3–10] has been proven to be an efficient technique in the description and prediction of thermoacoustic phenomena in confined combustion systems. These models are based on the interconnection of acoustically/convectively compact as well as non-compact elements. Examples for compact elements are flames [11–14], area jumps [11,15–17], compact nozzles [18–21] or junctions [22]. Non-compact elements are, for example, ducts with or without changes in area and/or temperature [10,23–25]. The application of low-order network models is versatile. They are used to gain a fundamental understanding of basic phenomena in the dynamics of combustion systems (e.g. mode clustering in annular and can-annular combustors [26–29]) and played a crucial role in the discovery of intrinsic thermoacoustic modes [30,31]. Their low numerical cost renders low-order network models exceptionally suited for extensive parameter studies, e.g. in early design phases. Additionally, low-order network models may be used in the post-processing of experimental measurements to get more accurate system stability predictions with uncertainty bounds [32] or to extract the thermoacoustic transfer behavior of the flame from microphone measurements [33].

* Corresponding author.
E-mail address: moritz.merk@tfd.mw.tum.de (M. Merk).

https://doi.org/10.1016/j.combustflame.2024.113958
Received 24 June 2024; Received in revised form 28 December 2024; Accepted 28 December 2024
Available online 21 January 2025

Nomenclature

a	number of carbon atoms (fuel species) (–)
a_Σ	relative gain error (–)
A	area (m^2)
b	number of hydrogen atoms (fuel species) (–)
c	speed of sound ($\frac{m}{s}$)
c_p	specific heat capacity at constant pressure ($\frac{J}{kg\,K}$)
f	frequency (Hz)
$\mathcal{F}$	flame transfer function (–)
$\mathbf{F}$	flux vector
$\mathbf{F}_\nabla$	convective flux vector
$\mathbf{F}_p$	surface flux vector
h	sensible enthalpy ($\frac{J}{kg}$)
Δh^0	enthalpy of formation ($\frac{J}{kg}$)
H	total non-chemical enthalpy ($\frac{J}{kg}$)
He	Helmholtz number (–)
$\mathbf{J}$	Jacobian matrix
L	length (m)
L_τ	distance between the input and the maximum heat release rate (m)
M	Mach number (–)
$\mathbf{n}$	normal vector (–)
N	number of species (–)
p	pressure (Pa)
P	approximation order in Mach number (–)
R	specific gas constant ($\frac{J}{kg\,K}$)
s	entropy ($\frac{J}{kg\,K}$)
$\mathbf{S}$	scattering matrix
St	Strouhal number (–)
t	time (s)
T	temperature (K)
$\mathbf{T}$	transfer matrix
u	velocity ($\frac{m}{s}$)
u_q	absolute flame velocity in a fixed reference system ($\frac{m}{s}$)
$\mathbf{U}$	state vector of conserved quantities
$\mathbf{v}$	state vector of perturbations
V	volume (m^3)
$\mathbf{w}$	vector of perturbation characteristics
$\mathbf{x}$	spatial coordinate (m)
$\mathbf{X}$	vector of mole fractions (–)
X	mole fraction (–)
$\mathbf{Y}$	vector of mass fractions (–)
Y	mass fraction (–)

Greek letters

γ	ratio of specific heats (–)
$\mathbf{\Gamma}$	filter matrix (–)
δ	Kronecker delta (–)
λ	wavelength (m)
$\mathbf{\Lambda}$	boundary matrix (–)
ν	stoichiometric coefficients (–)
ρ	density ($\frac{kg}{m^3}$)
$\mathbf{\Sigma}$	approximation error (–)
ϕ	equivalence ratio (–)
φ	phase (–)
φ_Σ	phase error (–)
ψ	arbitrary physical quantity
$\dot{\omega}_T$	volumetric heat release rate ($\frac{W}{m^3}$)
$\dot{\boldsymbol{\omega}}_Y$	vector of volumetric species reaction rates ($\frac{\frac{kg}{s}}{m^3 s}$)
$\dot{\boldsymbol{\omega}}$	volumetric source vector
$\mathbf{\Omega}$	integral source vector
$\dot{\Omega}_T$	integral heat release rate (W)
$\dot{\mathbf{\Omega}}_Y$	vector of integral species reaction rates ($\frac{kg}{s}$)

Operators

d	differential
lim	limes
$\mathcal{O}$	order of magnitude

Subscript

$(\cdot)_{air}$	air
$(\cdot)_d$	duct
$(\cdot)_f$	fuel
$(\cdot)_k$	of species k
$(\cdot)_i$	at location i
$(\cdot)_{in}$	characteristic perturbations entering the system
$(\cdot)_{max}$	maximum value
$(\cdot)_{out}$	characteristic perturbations leaving the system
$(\cdot)_{ref}$	at a reference point
$(\cdot)_w$	at the wall

Superscript

$(\cdot)^{A/B/C/D/E/F}$	forcing case A/B/C/D/E/F
$\overline{(\cdot)}$	mean quantity
$(\cdot)'$	perturbed quantity
$(\cdot)^+$	non-dimensionalized perturbed quantity
$\hat{(\cdot)}$	approximation

Abbreviations

FTF	flame transfer function
Q1D	quasi-one-dimensional
3D	three-dimensional

The individual elements of network models, represented by transfer/ scattering matrices, can be determined by experiments or numerical simulations. Alternatively, models for the individual elements can be derived from first principle. Such analytical models give insight into the basic coupling of perturbations in the corresponding physical system between the "ports" of the element. However, their application typically requires a trade-off between accuracy and computational efficiency, where the typical focus on extensive parameter studies or fundamental insight favors efficiency or reduced complexity. Deriving these elements, the focus on efficiency or reduced complexity commonly results in *a priori* assumptions, e.g., assuming constant gas properties or approximating to first-order in Mach number. Problematically, introducing assumptions *a priori* limits the range of validity of the elements. A rederivation is required when a different application case violates any of these assumptions or has more stringent accuracy requirements. Let us consider the example of a compact flame element. Chu [34] derived the acoustic transfer behavior for a discontinuity in motion, including terms up to first order in Mach number and calorically perfect gas mixtures with different mixtures upstream and downstream of the flame front. Dowling and Stow [11]

as well as Schuermans [35] revisited this problem, additionally taking into account entropic disturbances generated by the flame. While Schuermans [35] retained the flame motion and the assumption of a calorically perfect gas mixture, Dowling and Stow [11] introduced the additional assumption of constant gas properties and a heat source at rest. Strobio Chen et al. [12] derived the jump condition for a flame with constant gas properties taking the flame movement back into account and emphasized that the assumption of a flame at rest results in the generation of spurious entropy. In addition, including the movement of the flame naturally resolves the paradox [36] that in the zero Mach number limit, a flame at rest should conserve the volume flow rate rather than the mass flow rate. Gant et al. [14] derived the compact flame element for high Mach number autoignition flame since the limitation to first order in Mach number of Strobio Chen et al. [12] was too restrictive for the case under consideration. In parallel, Li and Morgans [13] show a clear impact of non-constant gas properties on thermoacoustic instability predictions for long combustion chambers in the limit of negligible mean flow ($\mathcal{O}(M^0)$). However, flame movement is not taken into account. Note that the list of papers above is not exhaustive, but shows a clear pattern of repeated case-dependent derivations that involve varying combinations of assumptions.

Nowadays, the coupling of low-order network models with experimental measurements receives increased attention. The use of Bayesian inference promises more reliable stability predictions in combination with uncertainty quantification [32], whereas the model-based inference method [33] uses low-order network models to retrieve the thermoacoustic transfer behavior of a flame from experimental measurements in complex test rigs. Both methodologies require an accurate representation of the internal dynamics of the thermoacoustic systems. However, even minor inaccuracies in the transfer behavior of single elements can add up and alter the dynamics of complex thermoacoustic systems significantly [32]. Therefore, the elements used should be as accurate as possible and assumptions should be reduced to only those that are well justified.

In this work, we focus on the derivation of thermoacoustic coupling conditions for compact elements — so-called "jump conditions". The goal of this study is (i) to provide a generalized framework for the derivation of jump conditions with (ii) a wide generality and flexibility. The framework is (iii) easily applicable for the derivation of a variety of compact elements (e.g., flame, area jump) and (iv) provides a straightforward implementation rule. The jump conditions derived are (v) highly accurate and account for all characteristics (acoustic, entropic, and compositional perturbations) in quasi-one-dimensional reactive flows. Application-specific assumptions to increase efficiency or reduce complexity are easily included (vi) *a posteriori* without requiring a rederivation of the jump condition. Finally, the state variables are chosen such that they are of the same order of magnitude for typical application cases so that (vii) the transfer matrix/ scattering matrix coefficients are non-dimensionalized and at the same time represent the relative importance of the different incoming perturbations in generating velocity, pressure, entropy, or compositional fluctuations.

This paper is structured as follows. Section 2 details the general framework for deriving compact jump conditions with the features mentioned above. The section is subdivided into the underlying fundamental equations (Section 2.1), the Jacobian-based framework (Section 2.2), and *a posteriori* simplifications (Section 2.3). In Section 3, the capabilities of the Jacobian-based framework are demonstrated by deriving a novel jump condition for compact lean premixed flames (Section 3.1). This novel jump condition resolves the transfer behavior of acoustic, entropic, and compositional perturbations, accounts for flame movement as well as realistic gas properties, and is valid for flows of arbitrary Mach number. In Section 3.2, the accuracy of this novel formulation is demonstrated by comparison to numerical results of a one-dimensional H_2 autoignition flame generated with a linearized reactive flow solver. Section 3.3 discusses that the *a posteriori* introduction of frequently invoked assumptions recovers well-known results for jump conditions found in literature. Furthermore, the approximation errors corresponding to the most common approximations are analyzed. Section 4 briefly comments on the application of the Jacobian-based framework for non-reacting cases and Section 5 concludes the paper.

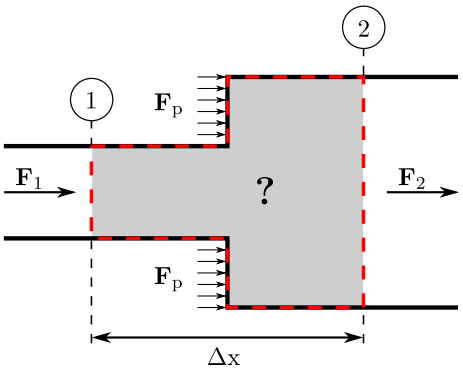

Fig. 1. Schematic representation of illustrative physical system. The control volume V (– –) encloses the system for which the thermoacoustic jump condition is derived. The interior (?) of the system requires a problem-specific model to find a closed representation of the thermoacoustic jump conditions and is not further specified in this example. (For interpretation of the references to color in this figure legend, the reader is referred to the web version of this article.)

2. Generalized jump conditions

Fig. 1 displays an illustrative example of an element of a thermoacoustic network model enclosed by a control volume V with a single input port 1 and a single output port 2. The input and output states are assumed to be quasi-one-dimensional (Q1D) to work as coupling interfaces in Q1D network models. The interior of the system may include three-dimensional (3D) effects. The goal of this work is to provide a framework for deriving generalized coupling relations between the Q1D inputs and outputs of such a system accounting for acoustic, entropic and compositional perturbations. In such a relation, any 3D effects inside the control volume are included in an integral manner, e.g., for an arbitrary physical source $\dot{\omega}_\psi$ via the volume integral

$$\int \dot{\omega}_\psi \, \mathrm{dV}. \tag{1}$$

Analytical or semi-empirical closure models are needed to derive closed-form coupling relations for the volume integrals such as Eq. (1), e.g. models for the heat release rate of a flame [37] or for viscous losses [38].

This work focuses on coupling relations in the limit of *convective compactness* – so-called jump conditions. The assumption of convective compactness is required since this work derives jump conditions that include the description of entropic and compositional disturbances. The assumption of *acoustic compactness* is sufficient if only acoustic waves are considered. Compactness relates to the assumption that the spatial extent Δx of the system (see Fig. 1) is negligible compared to the wavelengths λ of incoming and outgoing perturbations. Mathematically, jump conditions are typically the zeroth order approximation with respect to the Strouhal number (*convectively* compact case)

$$\mathrm{St} = \frac{\Delta x}{\lambda_c} = \frac{\Delta x}{u} f \tag{2}$$

or the Helmholtz number (*acoustically* compact case)

$$\mathrm{He} = \frac{\Delta x}{\lambda_a} = \frac{\Delta x}{c} f \tag{3}$$

of more general coupling relations and can be derived by evaluating all terms in the limit St $\to$ 0 or He $\to$ 0, respectively. f, u and c are the frequency, the flow velocity and the speed of sound. Note that assuming convective compactness strongly restricts the frequency range in which the jump condition approximates the underlying physical system well. For convectively non-compact systems, coupling relations of higher-order in the Strouhal number should be derived. The framework proposed in Section 2.2 is extendable to higher-order coupling relations, even though their explicit derivation is beyond the scope of this paper. With increasing Strouhal number, the convective non-compactness will result in a "spatial" low-pass filter behavior of the sources related to convective effects [39].

Furthermore, note that even though this work focuses on jump conditions of 2-port systems, the Jacobian-based framework proposed in Section 2.2 is applicable to systems with arbitrary numbers of input and output ports.

2.1. The fundamental equations

The basis of any jump condition is a closed system of balance equations that provides the prerequisites for coupling the Q1D input and output states

$$\mathbf{U} = \begin{bmatrix} \rho \\ \rho u \\ \rho H - p \\ \rho \mathbf{Y} \end{bmatrix} \tag{4}$$

of a system (e.g. Fig. 1). p, ρ, u, and $H = \sum_k h_k Y_k + \frac{1}{2}u^2$ are the pressure, density, velocity, and the total non-chemical enthalpy. h_k and Y_k correspond to the sensible enthalpy and the mass fraction of species k. $\mathbf{Y} = [Y_1, \dots, Y_k, \dots, Y_{N-1}]^T$ is the transposed vector of $N-1$ species mass fractions. Note that as a consequence of mass conservation, the Nth species mass fraction

$$Y_N = 1 - \sum_{k=1}^{N-1} Y_k \tag{5}$$

can be expressed via $\mathbf{Y}$ and does not need to be resolved explicitly. The interior dynamics of the system are described by the integral reactive Navier–Stokes equations of the form

$$\frac{\partial}{\partial t}\int \mathbf{U}\mathrm{dV} + \int \mathbf{F}\cdot\mathbf{n}\mathrm{dA} = \int \dot{\boldsymbol{\omega}}\mathrm{dV}\,, \tag{6}$$

where

$$\mathbf{F} = \mathbf{F}_\nabla + \mathbf{F}_p = \begin{bmatrix} \rho u \\ \rho u^2 \\ \rho u H \\ \rho u \mathbf{Y} \end{bmatrix} + \begin{bmatrix} 0 \\ p \\ 0 \\ \mathbf{0} \end{bmatrix} \tag{7}$$

are Q1D fluxes at the boundary of the system providing Q1D coupling interfaces to neighboring elements in a network model. $\mathbf{F}_\nabla$ and $\mathbf{F}_p$ are the convective flux and the surface flux, respectively. $\mathbf{0}$ is a zero vector of corresponding dimensions. The source vector $\dot{\boldsymbol{\omega}}$ describes 3D volumetric source terms, e.g. due to chemical reactions such as the volumetric heat release rate $\dot{\omega}_T$ or the volumetric species reaction rates $\dot{\boldsymbol{\omega}}_Y$. Additionally, diffusive effects such as pressure losses or wall heat losses can be included in $\dot{\boldsymbol{\omega}}$. $\int \mathrm{dV}$ and $\int \mathrm{dA}$ denote the integration over a volume and the corresponding surfaces with the outward-facing normal vector $\mathbf{n}$, respectively. Note that V and A are yet undefined, and Eq. (6) can be applied to any system.

To close Eq. (6), thermal, caloric, and canonical equations of states are required. In this work, the perfect gas law (thermal equation of state)

$$p = \rho \sum_k R_k Y_k T\,, \tag{8}$$

Gibbs' equation of a multi-component gas [20,40–43] (canonic equation of state)

$$\mathrm{d}h = T\mathrm{d}s + \frac{1}{\rho}\mathrm{d}p + \sum_k \left(h_k - T s_k\right)\mathrm{d}Y_k \tag{9}$$

and the caloric equation of state

$$\mathrm{d}h = c_\mathrm{p}\mathrm{d}T + \sum_k h_k \mathrm{d}Y_k \tag{10}$$

are used. R_k, and s_k are the specific gas constant and the mass-specific entropy of the species k. d denotes a differential.

Furthermore, in the case of chemical reactions, modeling the source terms $\dot{\omega}_T$ and $\dot{\boldsymbol{\omega}}_Y$ requires a reaction mechanism and the calculation of the corresponding chemical equilibrium. For example, the following global reaction mechanism

$$\boldsymbol{\nu}_1 \begin{bmatrix} \mathrm{C}_a\mathrm{H}_b \\ \mathrm{O}_2 \\ \mathrm{N}_2 \\ \mathrm{CO}_2 \\ \mathrm{H}_2\mathrm{O} \end{bmatrix} \longrightarrow \boldsymbol{\nu}_2 \begin{bmatrix} \mathrm{C}_a\mathrm{H}_b \\ \mathrm{O}_2 \\ \mathrm{N}_2 \\ \mathrm{CO}_2 \\ \mathrm{H}_2\mathrm{O} \end{bmatrix}, \tag{11}$$

with the stoichiometric coefficients

$$\boldsymbol{\nu}_i := \begin{bmatrix} \nu_{i,\mathrm{C}_a\mathrm{H}_b} & \nu_{i,\mathrm{O}_2} & \nu_{i,\mathrm{N}_2} & \nu_{i,\mathrm{CO}_2} & \nu_{i,\mathrm{H}_2\mathrm{O}} \end{bmatrix}^T, \quad i \in \{1,2\}, \tag{12}$$

can be used for lean combustion ($\phi < 1$) of an arbitrary hydrocarbon fuel $\mathrm{C}_a\mathrm{H}_b$ in a medium temperature range [13,44]. Note that hydrogen is represented by the special case $a = 0$, $b = 2$. In case of the global reaction mechanism in Eq. (11), the stoichiometric coefficients downstream of the reaction zone ν_2 can be expressed in terms of the upstream coefficients ν_1 and are given via

$$\boldsymbol{\nu}_2 = \begin{bmatrix} 0 & 0 & 0 & 0 & 0 \\ -(a+\frac{b}{4}) & 1 & 0 & 0 & 0 \\ 0 & 0 & 1 & 0 & 0 \\ a & 0 & 0 & 1 & 0 \\ \frac{b}{2} & 0 & 0 & 0 & 1 \end{bmatrix} \boldsymbol{\nu}_1. \tag{13}$$

The coefficients a and b are used to represent arbitrary hydrocarbon fuels or hydrogen ($a = 0$, $b = 2$). Note that the inclusion of CO_2 and $\mathrm{H}_2\mathrm{O}$ in the incoming air mixture enables the modeling of vitiated air in axially staged combustors [14,45–49] or humidified air for wet combustion [50,51]. For higher temperatures and fuel-richer conditions, dissociated species cannot be neglected, and additional equations, e.g. $\mathrm{CO}_2 \rightleftharpoons \mathrm{CO} + \frac{1}{2}\mathrm{O}_2$or $\mathrm{H}_2\mathrm{O} \rightleftharpoons \mathrm{H}_2 + \frac{1}{2}\mathrm{O}_2$, would have to be taken into account. Then, the stoichiometric coefficients ν_2 in Eq. (13) must be corrected. We refer to Li and Morgans [13] on how to efficiently correct ν_2 in this case.

Finally, additional closure models are needed if diffusive effects are taken into account in $\dot{\boldsymbol{\omega}}$. However, the corresponding closure models are highly problem-specific and are therefore not further detailed in this section.

2.2. A Jacobian-based framework

On the basis of the general equations stated in Section 2.1, the derivation of any thermoacoustic jump conditions including acoustic, entropic and compositional perturbations can be generalized while minimizing the assumptions made. The derivation is subdivided in the following six steps:

1. *Defining the physical system of interest*, e.g., a flame element or a sudden area jump. In this step, a schematic representation of the system of interest is created, which can be used in the following steps to derive the jump condition. Fig. 1 shows such a schematic representation of an illustrative system of interest, which is enclosed by the control volume V. The interior of the system must be defined in this step. However, since the interior of the system is highly problem-specific, it is not further detailed in the illustrative example of Fig. 1.
2. *Analytical integration over the control volume.* In this step, the integral reactive Navier–Stokes Eqs. (6) are integrated over the control volume V of the system specified in step 1. This allows us to partially evaluate the general terms in Eq. (6) analytically. For

example, applying Eq. (6) to the exemplary system displayed in Fig. 1, the fluxes across the system boundaries can be simplified under the assumption of convective compactness to

$$\lim_{\mathrm{St}\to 0}\int \mathbf{F}\cdot\mathbf{n}\,\mathrm{d}A = \mathbf{F}_2 A_2 - \mathbf{F}_1 A_1 + \lim_{\mathrm{St}\to 0}\int \mathbf{F}_p\cdot\mathbf{n}\,\mathrm{d}A_\mathrm{w}, \tag{14}$$

where the indices $(\cdot)_1$, $(\cdot)_2$ and $(\cdot)_\mathrm{w}$ denote the states upstream, downstream and along the walls of the system of interest, respectively.

3. *Linearization of the integral reactive Navier–Stokes equations.* All physical quantities $\psi = \overline{\psi} + \psi'$ are separated into a time-independent mean part $\overline{\psi}$ and a temporal deviation from that state ψ'. Next, the perturbations are assumed very small ($\psi' \ll \overline{\psi}$) such that the mean quantities are unaffected by the perturbations and may be computed separately. Under these assumptions, the analytically simplified (step 2) Eq. (6) can be separated into two sets of equations — the first describing the mean field and the second detailing the perturbation thereof. Within the perturbed balance equation, higher-order perturbation terms ($\mathcal{O}((\psi')^2)$) are neglected due to the assumed small perturbation amplitudes, rendering the equation linear in the perturbed quantities ψ'.
For example, the flux vector $\mathbf{F}_i$ at the location i is split into

$$\mathbf{F}_i = \overline{\mathbf{F}}_i + \mathbf{F}_i' = \begin{bmatrix} \overline{\rho u} \\ \overline{\rho u}^2 + \overline{p} \\ \overline{\rho u}\,\overline{H} \\ \overline{\rho u}\,\overline{\mathbf{Y}} \end{bmatrix}_i + \begin{bmatrix} \rho'\overline{u} + \overline{\rho}u' \\ \rho'\overline{u}^2 + 2\overline{\rho u}u' + p' \\ (\rho'\overline{u} + \overline{\rho}u')\overline{H} + \overline{\rho u}H' \\ (\rho'\overline{u} + \overline{\rho}u')\overline{\mathbf{Y}} + \overline{\rho u}\mathbf{Y}' \end{bmatrix}_i \tag{15}$$

with $H' = \overline{u}u' + h'$. $\overline{\mathbf{F}}_i$ represents the mean flux vector contributing to the mean balance equation, whereas $\mathbf{F}_i'$ is the linear perturbation of the flux vector contributing to the perturbed balance equation.

The following steps focus on the linearized balance equations since a thermoacoustic jump condition is a closed representation of this set of equations. Nonetheless, it is crucial to note that quantifying the transfer coefficients of a jump condition requires the solution of the mean balance equation as an input.

4. *Defining the local perturbed state vector.* A generalized thermoacoustic jump condition describes the abrupt change in two acoustic, one entropic, and $N-1$ compositional perturbations across a compact element. The local state of the perturbed system is therefore described by $N+2$ perturbations, e.g. via the state vector

$$\mathbf{v}_i^+ = \begin{bmatrix} u_i^+ \\ p_i^+ \\ \overline{M}_i s_i^+ \\ \overline{M}_i(\mathbf{Y}_i^+) \end{bmatrix}, \tag{16}$$

with the non-dimensional perturbations

$$u_i^+ = \frac{u_i'}{\overline{c}_i}, \quad p_i^+ = \frac{p_i'}{\overline{\gamma p}_i}, \quad s_i^+ = \frac{s_i'}{\overline{c}_{\mathrm{p},i}} - \sum_k \frac{\overline{s}_{k,i}}{\overline{c}_{\mathrm{p},i}} Y_{k,i}' \quad \text{and} \quad Y_{k,i}^+ = \frac{Y_{k,i}'}{\overline{Y}_{k,i}}.$$

The superscript $(\cdot)^+$ denotes a non-dimensional perturbation throughout this work. γ, c_p and $\overline{M} = \overline{u}/\overline{c}$ are the ratio of specific heats, the specific heat capacity at constant pressure and the Mach number. The non-dimensional entropy term s^+ equals the non-dimensional, non-acoustic temperature fluctuation. In literature, this term is also known as fluctuation of excess temperature [52]. Note that the choice of $\mathbf{v}_i^+$ in Eq. (16) is not unique and a matter of choice. In Eq. (16) $\mathbf{v}_i^+$ is defined such that the incoming perturbations are of the same order of magnitude $\mathcal{O}$ for typical application cases in the zero frequency limit [43]:

$$\mathcal{O}(u_1^+) \approx \mathcal{O}(p_1^+) \approx \mathcal{O}(\overline{M}_1 \mathbf{Y}_1^+) \lesssim \mathcal{O}(\overline{M}_1 s_1^+). \tag{17}$$

Velocity u^+ and pressure p^+ perturbations are related via the acoustic characteristics $(p^+ \pm u^+)/2$. For a freely propagating plain acoustic wave in the absence of acoustic sources, the acoustic characteristics are constant, and u^+ and p^+ are of the same order in magnitude. Compositional perturbations $\mathbf{Y}^+$ in form of equivalence ratio perturbations are typically generated across a fuel injector and are of the same order as the velocity perturbation $u'/\overline{u} = u^+/\overline{M}$ [53–55]. Entropic inhomogeneities s^+ up to the order of the velocity perturbation $u'/\overline{u} = u^+/\overline{M}$ may be generated across a mixing section. Additionally, s^+ of the order of equivalence ratio perturbations (compositional perturbations $\mathbf{Y}^+$) may be generated across a flame. Overall, note that the scaling of the compositional $\mathbf{Y}^+$ and entropic s^+ perturbations with the Mach number $\overline{M}$ in Eq. (17) is required to relate these perturbations to the velocity perturbation u^+ instead of $u'/\overline{u}$. We refer to Merk et al. [43] for an in-depth discussion on the relation in Eq. (17).
The scaling of each incoming perturbation to the same order of magnitude ultimately results in thermoacoustic jump conditions, where the relative magnitude of the individual transfer matrix coefficients directly represents their relative importance. Furthermore, choosing non-dimensional perturbations results in a non-dimensional transfer matrix with a minimal number of non-dimensional mean input groups.

5. *Closure of the linearized system of equations.* The generalized thermoacoustic jump condition expresses the linearized reactive Navier–Stokes equations solely in terms of the input and output states $\mathbf{v}_i^+$ (Eq. (16)), e.g. $i \in \{1,2\}$ in Fig. 1. Any additional perturbations ψ' must be expressed in terms of the states $\mathbf{v}_i^+$ via the Jacobians $\overline{\mathbf{J}}_{\psi,i}$,

$$\psi' = \sum_i \frac{\partial \psi'}{\partial \mathbf{v}_i^+}\mathbf{v}_i^+ = \sum_i \overline{\mathbf{J}}_{\psi,i}\mathbf{v}_i^+. \tag{18}$$

Additional equations are required to formulate the Jacobians $\overline{\mathbf{J}}_{\psi,i}$. Note that the Jacobians solely depend on mean quantities due to the linearity of the underlying equations with respect to ψ'. This property is emphasized by the overbar.
For example, the perturbations at the interface i in density

$$\rho_i' = \overline{\mathbf{J}}_{\rho,i}\mathbf{v}_i^+ \quad \text{with} \quad \overline{\mathbf{J}}_{\rho,i} = \overline{\rho}\begin{bmatrix} 0 & 1 & -\frac{1}{\overline{M}_i} & -\frac{\widetilde{\mathbf{X}}_i}{\overline{M}_i} \end{bmatrix} \tag{19}$$

and in sensible enthalpy

$$h_i' = \overline{\mathbf{J}}_{h,i}\mathbf{v}_i^+ \quad \text{with} \quad \overline{\mathbf{J}}_{h,i} = \overline{c}_{\mathrm{p},i}\overline{T}_i\begin{bmatrix} 0 & (\overline{\gamma}_i - 1) & \frac{1}{\overline{M}_i} & \frac{\widetilde{\boldsymbol{h}}_i}{\overline{M}_i} \end{bmatrix} \tag{20}$$

are expressed in terms of $\mathbf{v}_i^+$ by combining the linearized versions of the perfect gas law (Eq. (8)), the Gibbs equation for a multi-component gas (Eq. (9)) and the corresponding caloric equation of state (Eq. (10)). In Eq. (19), the vector

$$\widetilde{\mathbf{X}} = [\widetilde{X}_1, \dots, \widetilde{X}_k, \dots, \widetilde{X}_{N-1}] \quad \text{with} \quad \widetilde{X}_k = \overline{X}_k - \frac{\overline{Y}_k}{\overline{Y}_N}\overline{X}_N \tag{21}$$

results from the perturbed specific gas constant $R'/\overline{R} = \widetilde{\mathbf{X}}\mathbf{Y}^+$. X_k is the molar fraction of species k. In Eq. (20), the vector

$$\widetilde{\boldsymbol{h}} = [\widetilde{h}_1, \dots, \widetilde{h}_k, \dots, \widetilde{h}_N] \quad \text{with} \quad \widetilde{h}_k = \frac{(\overline{h}_k - \overline{h}_N)}{\overline{c}_p\overline{T}}\overline{Y}_k \tag{22}$$

relates compositional perturbations to a change in sensible enthalpy. Incorporating Eqs. (19) and (20) into Eq. (15), the linearized flux vector $\mathbf{F}_i$ is given by

$$\mathbf{F}_i' = \overline{\mathbf{J}}_{F,i}\mathbf{v}_i^+ \quad \text{with} \quad \overline{\mathbf{J}}_{F,i} = \overline{\mathbf{E}}_i\widetilde{\mathbf{J}}_{F,i}, \tag{23}$$

where

$$\overline{\mathbf{E}}_i = \overline{\rho}_i\overline{c}_i\,\mathrm{diag}\left(\begin{bmatrix} 1 & \overline{c}_i & \overline{c}_{\mathrm{p},i}\overline{T}_i & \mathbf{1} \end{bmatrix}\right) \tag{24}$$

is a diagonal matrix, and

$$\widetilde{\mathbf{J}}_{F,i} = \begin{bmatrix} 1 & \overline{M}_i & -1 & -\widetilde{\mathbf{X}}_i \\ 2\overline{M}_i & 1+\overline{M}_i^2 & -\overline{M}_i & -\overline{M}_i\widetilde{\mathbf{X}}_i \\ \widetilde{H}_i + \overline{M}_i^2(\overline{\gamma}_i - 1) & \overline{M}_i\left(\widetilde{H}_i + \overline{\gamma}_i - 1\right) & 1-\widetilde{H}_i & \left(\widetilde{\boldsymbol{h}}_i - \widetilde{H}_i\widetilde{\mathbf{X}}_i\right) \\ \overline{\mathbf{Y}}_i & \overline{M}_i\overline{\mathbf{Y}}_i & -\overline{\mathbf{Y}}_i & \mathrm{diag}\left(\overline{\mathbf{Y}}_i\right) - \overline{\mathbf{Y}}_i\widetilde{\mathbf{X}} \end{bmatrix} \tag{25}$$

is the non-dimensional Jacobian. diag() transforms a vector into a diagonal matrix and $\mathbf{1}$ is a vector of ones of corresponding dimensions. $\widetilde{H}_i = \overline{H}_i/(\overline{c}_{p,i}\overline{T})$ is the non-dimensionalized mean total non-chemical enthalpy.

Analogously, closure models are required to express the perturbed source vector

$$\boldsymbol{\Omega}' = \lim_{\mathrm{St}\to 0}\left(\int \dot{\boldsymbol{\omega}}\,\mathrm{dV}\right)' = \sum_i \overline{\mathbf{J}}_{\Omega,i}\mathbf{v}_i^+, \tag{26}$$

the perturbed accumulation term of the system

$$\lim_{\mathrm{St}\to 0}\frac{\partial}{\partial t}\left(\int \mathbf{U}\,\mathrm{dV}\right)' = \sum_i \overline{\mathbf{J}}_{\mathrm{U},i}\mathbf{v}_i^+ \tag{27}$$

and the fluctuating surface flux at walls (see Eq. (14))

$$\lim_{\mathrm{St}\to 0}\left(\int \mathbf{F}_p\cdot\mathbf{n}\,\mathrm{dA_w}\right)' = \sum_i \overline{\mathbf{J}}_{\mathrm{F_w},i}\mathbf{v}_i^+ \tag{28}$$

in terms of $\mathbf{v}_i^+$. The problem-specific forms of $\overline{\mathbf{J}}_{\Omega,i}$, $\overline{\mathbf{J}}_{\mathrm{U},i}$ and $\overline{\mathbf{J}}_{\mathrm{F_w},i}$ depend on the corresponding closure problems.

6. *Formulation of the generalized thermoacoustic jump condition.* After the problem is closed in the previous step, the linearized reactive Navier–Stokes equations can be reformulated into the transfer matrix $\overline{\mathbf{T}}$ of the generalized thermoacoustic jump condition. In the exemplary case displayed in Fig. 1 with a single state upstream and a single state downstream of the system, the transfer matrix $\mathbf{T}$ is generally defined as

$$\mathbf{v}_2^+ = \overline{\mathbf{T}}\mathbf{v}_1^+ \tag{29}$$

and can be expressed via

$$\overline{\mathbf{T}} = \left(\overline{\mathbf{J}}_{\mathrm{U},2} + \overline{\mathbf{J}}_{\mathrm{F},2}A_2 + \overline{\mathbf{J}}_{\mathrm{F_w},2} - \overline{\mathbf{J}}_{\Omega,2}\right)^{-1}\left(-\overline{\mathbf{J}}_{\mathrm{U},1} + \overline{\mathbf{J}}_{\mathrm{F},1}A_1 - \overline{\mathbf{J}}_{\mathrm{F_w},1} + \overline{\mathbf{J}}_{\Omega,1}\right) \tag{30}$$

following the previous steps.

The Jacobian-based derivation procedure proposed in this section is easily applicable for deriving a variety of compact thermoacoustic jump conditions. Furthermore, the Jacobian-based representation renders the jump conditions easily extendable. If an important mechanism was omitted in the definition of the system of interest (step 1), it can be easily included *a posteriori* without rederiving the full jump condition. For example, consider the case that the wall heat transfer should be included in the examplary system of interest defined in step 1 and displayed in Fig. 1. In this case, we simply need to derive a closure for the additional source term of the wall heat transfer $(\cdot)^{\mathrm{wht}}$ following the steps 2–5 and superpose it with the previously derived source Jacobian $(\cdot)^{\mathrm{prev}}$,

$$\overline{\mathbf{J}}_{\Omega,i} = \overline{\mathbf{J}}_{\Omega,i}^{\mathrm{prev}} + \overline{\mathbf{J}}_{\Omega,i}^{\mathrm{wht}}. \tag{31}$$

The general form of the transfer matrix in Eq. (30) does not change. Ultimately, this modularity of the Jacobian-based representation offers a guideline for the straightforward implementation of $\overline{\mathbf{T}}$. Instead of hard-coding the analytical transfer matrix T, it is computationally advantageous to implement all Jacobians individually and then perform the operation detailed in Eq. (30) during run time. This retains the flexibility to quickly exchange the individual closure models encoded in the Jacobians. Additionally, the Jacobian-based approach, compared to the hard-coded implementation, saves computational operations in setting up the transfer matrix due to the factorized formulation, especially for complex transfer matrices.

While the derivation of the transfer matrix $\overline{\mathbf{T}}$ is straightforward, an equivalent representation of the thermoacoustic system – the so-called scattering matrix – is typically used for physical interpretation. The scattering matrix

$$\mathbf{w}_{\mathrm{out}}^+ = \overline{\mathbf{S}}\mathbf{w}_{\mathrm{in}}^+, \tag{32}$$

is expressed in terms of the characteristic amplitudes of the acoustic ($f^+ = \frac{1}{2}\left(p^+ + u^+\right)$, $g^+ = \frac{1}{2}\left(p^+ - u^+\right)$), entropic ($\overline{M}s^+$) and compositional ($\overline{M}\mathbf{Y}^+$) perturbations entering $(\cdot)_{\mathrm{in}}$ and leaving $(\cdot)_{\mathrm{out}}$ the system,

$$\begin{aligned} \mathbf{w}_{\mathrm{in}}^+ &= \left[f_i^+, g_j^+, \overline{M}_i s_i^+ \overline{M}_i \mathbf{Y}_i^+\right]^T \\ \mathbf{w}_{\mathrm{out}}^+ &= \left[f_j^+, g_i^+, \overline{M}_j s_j^+ \overline{M}_j \mathbf{Y}_j^+\right]^T, \end{aligned} \tag{33}$$

here with $i = 1$ and $j = 2$. $\overline{\mathbf{S}}$ is calculated from $\overline{\mathbf{T}}$ by applying the state vector transformation from $\mathbf{v}_1^+$ and $\mathbf{v}_2^+$ to $\mathbf{w}_{\mathrm{in}}^+$ and $\mathbf{w}_{\mathrm{out}}^+$.

2.3. A posteriori simplifications

The generalized thermoacoustic jump conditions derived following the six steps in Section 2.2 account for acoustic, entropic, and compositional perturbations while including changes in gas properties and arbitrary Mach numbers. However, in many applications it may be justified to use only a subset of the resolved perturbations or to introduce additional assumptions to increase efficiency. Starting from the general thermoacoustic jump conditions, simplifications are easily introduced *a posteriori*. The most common assumptions are discussed in the following subsections.

2.3.1. Restriction to a subset of perturbations

The restriction to a subset of perturbations is straightforward. The transfer behavior of any subset of perturbations is represented by a submatrix

$$\overline{\mathbf{T}}_{\mathrm{red}} = \boldsymbol{\Gamma}\overline{\mathbf{T}}\boldsymbol{\Lambda}. \tag{34}$$

of the generalized transfer matrix $\overline{\mathbf{T}}$ (Eq. (30)). The filter matrix $\boldsymbol{\Gamma}$ reduces the state vector $\mathbf{v}_i^+$ to

$$\mathbf{v}_{\mathrm{red},i}^+ = \boldsymbol{\Gamma}\mathbf{v}_i^+. \tag{35}$$

$\boldsymbol{\Gamma}$ is rectangular with the number of columns equal to the length of the complete state vector $\mathbf{v}_i^+$ and the number of rows equal to the length of the reduced state vector $\mathbf{v}_{\mathrm{red},i}^+$. Additionally, $\boldsymbol{\Gamma}$ is binary when reducing to a subset of perturbations, with '1' indicating a perturbation of interest. The boundary matrix $\boldsymbol{\Lambda}$ enforces boundary conditions at the inlet, e.g. $(\cdot)_1$, intrinsic to the reduced jump condition,

$$\mathbf{v}_{\mathrm{bc},1}^+ = \boldsymbol{\Lambda}\mathbf{v}_{\mathrm{red},1}^+. \tag{36}$$

Only perturbations of interest are assumed to enter the system. All other perturbations at the inlet are assumed to be of zero amplitude. For example, if there is a sole interest in coupling velocity and pressure perturbations (acoustic transfer behavior), the filter matrix $\boldsymbol{\Gamma}$ is defined via

$$\begin{bmatrix} u_i^+ \\ p_i^+ \end{bmatrix} = \underbrace{\begin{bmatrix} 1 & 0 & 0 & \mathbf{0} \\ 0 & 1 & 0 & \mathbf{0} \end{bmatrix}}_{\boldsymbol{\Gamma}} \begin{bmatrix} u_i^+ \\ p_i^+ \\ \overline{M}_i s_i^+ \\ \overline{M}_i(\mathbf{Y}_i^+) \end{bmatrix}. \tag{37}$$

In addition, no entropic or compositional perturbations are assumed to enter the system at the inlet boundary ($s_1^+ = 0$, $Y_{k,1}^+ = 0$),

$$\begin{bmatrix} u_1^+ \\ p_1^+ \\ 0 \\ \mathbf{0} \end{bmatrix} = \underbrace{\begin{bmatrix} 1 & 0 \\ 0 & 1 \\ 0 & 0 \\ \mathbf{0} & \mathbf{0} \end{bmatrix}}_{\boldsymbol{\Lambda}} \begin{bmatrix} u_1^+ \\ p_1^+ \end{bmatrix}. \tag{38}$$

Note that $\mathbf{\Lambda} = \mathbf{\Gamma}^T$ holds in general when restricting to a subset of perturbations.

2.3.2. Lumping compositional perturbations

The generalized state vectors $\mathbf{v}_i^+$ are defined by two acoustic, one entropic and $N-1$ compositional perturbations with, e.g. $N-1=4$ considering the global reaction mechanism in Eq. (11). This shows that the accurate representation of all compositional waves Y_k^+ adds significantly to the degrees of freedom of the thermoacoustic jump condition. In the context of network modeling, this increase in degrees of freedom raises the computational effort substantially.

A standard approach in the literature, e.g. [12,15], to reduce the degrees of freedom of thermoacoustic jump conditions is to lump all species into two mixtures, e.g. a fuel mixture $(\cdot)_\mathrm{f}$ and an air mixture $(\cdot)_\mathrm{air}$,

$$Y_\mathrm{f} = \widetilde{\boldsymbol{\alpha}}_\mathrm{f}\mathbf{Y} + \alpha_{\mathrm{f},N} \qquad \text{and} \qquad Y_\mathrm{air} = \left(\mathbf{1} - \widetilde{\boldsymbol{\alpha}}_\mathrm{f}\right)\mathbf{Y} + \left(1 - \alpha_{\mathrm{f},N}\right) \tag{39}$$

with $\widetilde{\boldsymbol{\alpha}}_\mathrm{f} = \left[\widetilde{\alpha}_{\mathrm{f},1}, \dots, \widetilde{\alpha}_{\mathrm{f},k}, \dots, \widetilde{\alpha}_{\mathrm{f},N-1}\right]$ and $\widetilde{\alpha}_{\mathrm{f},k} = \alpha_{\mathrm{f},k} - \alpha_{\mathrm{f},N}$, both of immutable composition ($\boldsymbol{\alpha}_\mathrm{f} = \text{const.}$, $\alpha_{\mathrm{f},k} \in \{0,1\}$). Due to mass conservation ($Y_\mathrm{f} + Y_\mathrm{air} = 1$), only a single compositional perturbation, e.g., the perturbed fuel mass fraction

$$Y_\mathrm{f}^+ = -\frac{1-\overline{Y}_\mathrm{f}}{\overline{Y}_\mathrm{f}} Y_\mathrm{air}^+ = \widetilde{\boldsymbol{\beta}}_\mathrm{f}\mathbf{Y}^+ \tag{40}$$

with $\widetilde{\boldsymbol{\beta}}_\mathrm{f} = \left[\widetilde{\beta}_{\mathrm{f},1}, \dots, \widetilde{\beta}_{\mathrm{f},k}, \dots, \widetilde{\beta}_{\mathrm{f},N}\right]$ and $\widetilde{\beta}_{\mathrm{f},k} = (\widetilde{\alpha}_{\mathrm{f},k}\overline{Y}_k)/(\overline{Y}_\mathrm{f})$, must be computed. Analogously to Section 2.3.1, a filter matrix $\mathbf{\Gamma}$ (see Eq. (35)) reduces the complete state vectors $\mathbf{v}_i^+$ to the corresponding reduced state vector $\mathbf{v}_{\mathrm{red},i}^+$. If the only mixture to be computed is the perturbed fuel mass fraction, the filter matrix takes the form

$$\mathbf{\Gamma} = \begin{bmatrix} 1 & 0 & 0 & \mathbf{0} \\ 0 & 1 & 0 & \mathbf{0} \\ 0 & 0 & 1 & \mathbf{0} \\ 0 & 0 & 0 & \widetilde{\boldsymbol{\beta}}_\mathrm{f} \end{bmatrix}. \tag{41}$$

In contrast to Section 2.3.1, the filter matrix $\mathbf{\Gamma}$ is not binary in this case. Furthermore, when using lumped compositional perturbations, the composition perturbations $Y_{k,1}^+$ at the inlet are assumed to be equal to $Y_{\mathrm{f},1}^+$ or $Y_{\mathrm{air},1}^+$, depending on whether species k is part of the fuel or air mixture,

$$\mathbf{Y}_1^+ = Y_{\mathrm{f},1}^+\boldsymbol{\alpha}_\mathrm{f}^T + Y_{\mathrm{air},1}^+\left(\mathbf{1} - \boldsymbol{\alpha}_\mathrm{f}^T\right) = Y_{\mathrm{f},1}^+\boldsymbol{\eta}_\mathrm{f}^T \tag{42}$$

with $\boldsymbol{\alpha}_\mathrm{f} = \left[\alpha_{\mathrm{f},1}, \dots, \alpha_{\mathrm{f},5}, \dots, \alpha_{\mathrm{f},N-1}\right]$, $\boldsymbol{\eta}_\mathrm{f} = \left[\eta_{\mathrm{f},1}, \dots, \eta_{\mathrm{f},k}, \dots, \eta_{\mathrm{f},N-1}\right]$ and $\eta_{\mathrm{f},k} = \left(\alpha_{\mathrm{f},k} - \left(1-\alpha_{\mathrm{f},k}\right)\overline{Y}_k/\overline{Y}_\mathrm{f}\right)$. The corresponding boundary matrix $\mathbf{\Lambda}$ (see Eq. (36)) then reads

$$\mathbf{\Lambda} = \begin{bmatrix} 1 & 0 & 0 & 0 \\ 0 & 1 & 0 & 0 \\ 0 & 0 & 1 & 0 \\ \mathbf{0} & \mathbf{0} & \mathbf{0} & \boldsymbol{\eta}_\mathrm{f}^T \end{bmatrix}. \tag{43}$$

Eventually, the reduced transfer matrix $\overline{\mathbf{T}}_\mathrm{red}$ for lumped compositional perturbations is computed as defined in Eq. (34).

2.3.3. Simplified gas properties

The gas properties $c_\mathrm{p} = c_\mathrm{p}(T,\mathbf{Y})$, $\gamma = \gamma(T,\mathbf{Y})$ and $R = R(\mathbf{Y})$ of a gas mixture generally depend on the composition $\mathbf{Y}$ and partially on the temperature T. However, common assumptions are to neglect either the dependency on T, e.g. [34,35], or the dependency on both T and $\mathbf{Y}$, e.g. [11,12,14,44], to reduce the numerical effort in computing the thermoacoustic jump conditions.

Neglecting the dependency on temperature renders the specific heat capacities and the ratio of specific heats constant for each species k ($c_{\mathrm{p},k} = \text{const.}$, $\gamma_k = \text{const.}$). This simplifies the temperature-dependency of each species' sensible enthalpy

$$h_k = \int_{T_0}^{T} c_{\mathrm{p},k}\,\mathrm{d}T \approx c_{\mathrm{p},k}\left(T - T_0\right) \tag{44}$$

to a linear relation, where T_0 is the reference temperature at which the enthalpy $h_k(T_0)$ is defined to be zero. Relaxing the non-linear temperature dependence of the sensible enthalpy to a linear one significantly reduces the numerical effort of solving the mean-field equations. The numerical effort of subsequently solving the linearized system (Eq. (29)) is unaffected when neglecting the temperature dependence of the gas properties since the dependence of the perturbed sensible enthalpy

$$h_k' = \overline{c}_{\mathrm{p},k}T' \tag{45}$$

on T' is linear by default.

If the dependence of c_p, γ and R on the composition $\mathbf{Y}$ of the gas mixture is neglected additionally, the gas properties of the overall mixture become constant ($c_\mathrm{p} = \text{const.}$, $\gamma = \text{const.}$, $R = \text{const.}$). This relates to the assumption that the gas properties of all species are equal ($c_{\mathrm{p},k} = c_\mathrm{p}$, $R_k = R$, $\gamma_k = \gamma$). Since all species behave analogously in this case, a detailed computation of the gas mixture composition $\mathbf{Y}$ is no longer necessary. This results in a minor reduction of the computational cost.

2.3.4. Reduced Mach number approximations

In low Mach number flows, higher-order Mach number effects may be neglected. This approximation is introduced *a posteriori* into the generalized jump condition by expanding each Jacobian $\mathbf{J}_i$ in the generalized transfer matrix $\overline{\mathbf{T}}$, e.g. Eq. (30), into a Taylor series up to a specified order P,

$$\mathbf{J}_i \approx \sum_{p=0}^{P} \left.\frac{\mathrm{d}^p\mathbf{J}_i}{\mathrm{d}\overline{M}_i^p}\right|_{\overline{M}=0} \frac{\overline{M}_i^p}{p!}. \tag{46}$$

The Taylor expansion is performed with respect to the mean flow Mach number $\overline{M}_i$ around the expansion point $\overline{M}_i = 0$. ! denotes the factorial.

Note that for a consistent set of balance equations, the mean and the perturbation equations must be expanded to the same order P. Then, analogous to dropping the T-dependency of the gas mixture in Section 2.3.3, neglecting higher-order Mach number terms can decrease the computational effort of solving the mean-field equations by removing non-linear dependencies. For $P \leq 2$, the kinetic energy is neglected and the resulting energy balance equation provides a linear relation between heat addition and a change in sensible enthalpy. For $P \leq 1$, the convective momentum flux is neglected in addition resulting in an isobaric mean field.

The numerical effort for solving the perturbed system of equations (Eq. (29)) is only affected barely by the reduced Mach number assumption since it is linear in the perturbed quantities by definition.

3. The lean premixed flame

The flame element is the core of any thermoacoustic network model representing a combustion system. The general framework detailed in Section 2.2 is therefore applied in the following to derive and validate a generalized jump condition for a lean premixed flame including key features such as realistic gas properties [13] and flame movement [12,14,34,35] while resolving acoustic, entropic and compositional waves.

3.1. General derivation

The six steps (Section 2.2) in the derivation of a jump condition representing a lean premixed flame are detailed in the following.

1. *Defining the physical system of interest.* The schematic representation of the lean premixed flame derived in this section is shown in Fig. 2. The flame is assumed to be located in a duct of constant cross-section $A = A_1 = A_2$. The 3D flame front is assumed to be of infinite thinness and to fully separate the flow upstream and downstream of the flame. The flame is stabilized at an anchoring point and the flame front is, on average, at rest. However, the

local flame front may be displaced in response to incoming flow perturbations, e.g. due to a local kinematic imbalance in propagation stabilized flames or due to perturbations of the autoignition delay time in autoignition flames. Diffusive effects are considered negligible. A fixed control volume V encloses the flame at every time instance.

2. *Analytical integration over the control volume.* Analytical simplifications of the integral reactive Navier–Stokes Eqs. (6) are possible when applied to the lean premixed flame (step 1) in the limit of a compact control volume V. In this case, the accumulation term of the system simplifies to

$$\lim_{\mathrm{St}\to 0}\left(\frac{\partial}{\partial t}\int \mathbf{U}\mathrm{dV}\right) = -\frac{\partial V_1}{\partial t}\left(\mathbf{U}_2-\mathbf{U}_1\right). \tag{47}$$

See Section 1 of the supplementary material for a detailed derivation of Eq. (47). Note that the accumulation term does not vanish even in the limit of compactness due to the movement of the flame front [12,56,57]. The cross-section averaged absolute flame velocity in the reference frame at rest is defined as

$$u_\mathrm{q} = \frac{1}{A}\frac{\partial V_1}{\partial t}. \tag{48}$$

Next, the surface integral in Eq. (6) is simplified for the compact flame element to

$$\lim_{\mathrm{St}\to 0}\int \mathbf{F}\cdot\mathbf{n}\,\mathrm{dA} = \left(\mathbf{F}_2-\mathbf{F}_1\right)A. \tag{49}$$

In contrast to Eq. (14), no wall–fluid interaction is considered as a result of the constant cross-section A.
Neglecting diffusive effects, the source vector of the premixed flame (step 1)

$$\dot{\boldsymbol{\omega}} = \begin{bmatrix} 0 \\ 0 \\ \dot{\omega}_\mathrm{T} \\ \dot{\boldsymbol{\omega}}_\mathrm{Y} \end{bmatrix} \tag{50}$$

includes the volumetric heat release rate $\dot{\omega}_T$ and the species reaction rates $\dot{\boldsymbol{\omega}}_Y$ only. The corresponding volume integral cannot be simplified in the limit of compactness. For the shorter notation in the following steps, the global source vector

$$\boldsymbol{\Omega} = \lim_{\mathrm{St}\to 0}\int \dot{\boldsymbol{\omega}}\mathrm{dV} = \begin{bmatrix} 0 \\ 0 \\ \dot{\Omega}_\mathrm{T} \\ \dot{\boldsymbol{\Omega}}_\mathrm{Y} \end{bmatrix} \tag{51}$$

with the global heat release rate $\dot{\Omega}_T$ and the global species reaction rates $\dot{\boldsymbol{\Omega}}_Y$ is introduced here.
Recombining Eqs. (47), (49) and (51), the integral reactive Navier–Stokes equations simplify for the compact premixed flame to

$$-A\left(\mathbf{U}_2-\mathbf{U}_1\right)u_\mathrm{q} + \left(\mathbf{F}_2-\mathbf{F}_1\right)A = \boldsymbol{\Omega}. \tag{52}$$

Note that u_q and Ω are not mutually independent as will be seen in step 5.

3. *Linearization of the integral reactive Navier–Stokes equations.* In the next step, Eq. (52) is separated into its mean and perturbed parts. The mean equation of the premixed flame takes the form

$$\left(\overline{\mathbf{F}}_2-\overline{\mathbf{F}}_1\right)A = \overline{\boldsymbol{\Omega}}. \tag{53}$$

The mean cross-averaged flame velocity vanishes ($\overline{u}_\mathrm{q}=0$) in Eq. (53) since the flame is stabilized. The linear perturbed system of equation equates to

$$-\left(\overline{\mathbf{U}}_2-\overline{\mathbf{U}}_1\right)Au'_\mathrm{q} + \left(\mathbf{F}'_2-\mathbf{F}'_1\right)A = \boldsymbol{\Omega}'. \tag{54}$$

Eq. (54) includes the movement of the flame u'_q in response to incoming flow perturbations.

4. *Defining the local perturbed state vector.* The perturbed state vector $\mathbf{v}_i^+$ defined in Eq. (16) is used throughout this work. The reasons are detailed in step 4 in Section 2.2.

5. *Closure of the linearized system of equations.* The linearized set of balance equations for the premixed flame (Eq. (54)) is closed by expressing all perturbations u'_q, $\mathbf{F}'_1$, $\mathbf{F}'_2$ and $\boldsymbol{\Omega}'$ (with $\dot{\Omega}'_\mathrm{T}$ and $\dot{\boldsymbol{\Omega}}'_\mathrm{Y}$) in terms of the perturbed state vectors $\mathbf{v}_1^+$ and $\mathbf{v}_2^+$.
Unsteady changes in the surface area of the flame as well as effects directly affecting the reaction velocity alter the fuel consumption rate of the flame and consequently result in a perturbed global heat release rate $\dot{\Omega}'_\mathrm{T}$ and perturbed global species reaction rates $\dot{\boldsymbol{\Omega}}'_\mathrm{Y}$. For realistic flames, these unsteady flame dynamics are highly complex and not easily modeled. Therefore, jump conditions rely on external inputs in the form of so-called flame transfer functions (FTFs) to provide an accurate representation of the dynamics of the flame. The FTFs define $\dot{\Omega}'_\mathrm{T}$ with respect to the perturbed state at a reference point $(\cdot)_\mathrm{ref}$. For a lean premixed flame, $\dot{\Omega}'_\mathrm{T}$ is defined as

$$\frac{\dot{\Omega}'_\mathrm{T}}{\overline{\dot{\Omega}}_\mathrm{T}} = \mathcal{F}_\mathrm{u}\frac{u'_\mathrm{ref}}{\overline{u}_\mathrm{ref}} + \mathcal{F}_\mathrm{p}\frac{p'_\mathrm{ref}}{\overline{p}_\mathrm{ref}} + \mathcal{F}_\mathrm{s}s^+_\mathrm{ref} + \boldsymbol{\mathcal{F}}_\mathrm{Y}\mathbf{Y}^+_\mathrm{ref} + \mathcal{F}_{\mathrm{Y}_N}Y^+_{N,\mathrm{ref}}, \tag{55}$$

where $\mathcal{F}_\mathrm{u}$, $\mathcal{F}_\mathrm{p}$ and $\mathcal{F}_\mathrm{s}$ are the FTFs related to incoming velocity, pressure and entropy perturbations. The vector

$$\boldsymbol{\mathcal{F}}_\mathrm{Y} = \left[\mathcal{F}_{\mathrm{Y}_1},\ \dots,\ \mathcal{F}_{\mathrm{Y}_k},\ \dots,\ \mathcal{F}_{\mathrm{Y}_{N-1}}\right] \tag{56}$$

constitutes of FTFs related to perturbations of the first $N-1$ species mass fractions and $\mathcal{F}_{\mathrm{Y}_N}$ is the FTF of the perturbed specie mass fraction N, respectively. Note that some FTFs may be negligible for some type of flames. However, $\mathcal{F}_\mathrm{u}$, $\mathcal{F}_\mathrm{p}$, $\mathcal{F}_\mathrm{s}$, $\boldsymbol{\mathcal{F}}_\mathrm{Y}$ and $\mathcal{F}_{\mathrm{Y}_N}$ are required for the accurate representation of lean autoignition flames [47,48,58]. The global species reaction rates $\dot{\boldsymbol{\Omega}}_\mathrm{Y}$ are directly linked to the global heat release rate $\dot{\Omega}_\mathrm{T}$ via the enthalpies of formation Δh^0_k,

$$\dot{\Omega}_\mathrm{T} = \sum_k^N \Delta h^0_k \dot{\Omega}_{\mathrm{Y}_k} \quad\Rightarrow\quad \frac{\dot{\Omega}'_\mathrm{T}}{\overline{\dot{\Omega}}_\mathrm{T}} = \sum_k^N \overline{\eta}_k \frac{\dot{\Omega}'_{\mathrm{Y}_k}}{\overline{\dot{\Omega}}_{\mathrm{Y}_k}}. \tag{57}$$

$\overline{\eta}_k = (\Delta h^0_k\overline{\dot{\Omega}}_{\mathrm{Y}_k})/(\sum_k^N \Delta h^0_k\overline{\dot{\Omega}}_{\mathrm{Y}_k})$ with $\sum_k \overline{\eta}_k = 1$ is the relative contribution of the non-dimensional perturbed reaction rate of specie k $\dot{\Omega}'_{\mathrm{Y}_k}/\overline{\dot{\Omega}}_{\mathrm{Y}_k}$ to the non-dimensional perturbed heat release rate $\dot{\Omega}'_\mathrm{T}/\overline{\dot{\Omega}}_\mathrm{T}$. Then, assuming all species reactions to show the same integral dynamics, a direct relation between the perturbed species reaction rates $\dot{\Omega}'_{\mathrm{Y}_k}$ and the heat release rate $\dot{\Omega}'_\mathrm{T}$ is found,

$$\frac{\dot{\Omega}'_\mathrm{T}}{\overline{\dot{\Omega}}_\mathrm{T}} = \frac{\dot{\Omega}'_{\mathrm{Y}_k}}{\overline{\dot{\Omega}}_{\mathrm{Y}_k}}. \tag{58}$$

Ultimately, combining the closure models in Eqs. (55) and (58) and choosing the reference point directly upstream of the flame ($(\cdot)_\mathrm{ref}=(\cdot)_1$) reveals the overall closure of $\boldsymbol{\Omega}'$ as

$$\boldsymbol{\Omega}' = \overline{\mathbf{J}}_{\Omega,1}\mathbf{v}_1^+ \quad\text{with}\quad \overline{\mathbf{J}}_{\Omega,1} = \overline{\boldsymbol{\Omega}}\begin{bmatrix} \frac{\mathcal{F}_\mathrm{u}}{\overline{M}_1} & \overline{\gamma}_1\mathcal{F}_\mathrm{p} & \frac{\mathcal{F}_\mathrm{s}}{\overline{M}_1} & \frac{\widetilde{\mathcal{F}}_\mathrm{Y}}{\overline{M}_1} \end{bmatrix} \quad\text{and}\quad \widetilde{\boldsymbol{\mathcal{F}}}_\mathrm{Y} = \boldsymbol{\mathcal{F}}_\mathrm{Y} - \frac{\overline{\mathbf{Y}}}{\overline{Y}_N}\mathcal{F}_{\mathrm{Y}_N}. \tag{59}$$

A closure model for the perturbed cross-section averaged absolute flame velocity u'_q of a lean premixed flame may be derived from the balance equation of the reacting fuel mass flux,

$$-A\left(\overline{\rho}_2\overline{Y}_{\mathrm{f},2} - \overline{\rho}_1\overline{Y}_{\mathrm{f},1}\right)u'_\mathrm{q} + A\left(\rho_1 u_1\left(Y_{\mathrm{f},2}-Y_{\mathrm{f},1}\right)\right)' = \dot{\Omega}'_{Y_\mathrm{f}}. \tag{60}$$

Under the assumption of complete combustion ($Y_{\mathrm{f},2}=0$)[1] and incorporating the closure model for the fuel species reaction rate from Eq. (59), Eq. (60) yields the closure

$$u'_\mathrm{q} = \overline{\mathbf{J}}_{u_\mathrm{q},1}\mathbf{v}_1^+ \tag{61}$$

[1] For fuel-rich flame, the same procedure as for the lean premixed flame can be used to derive a closure model for u'_q. In this case, the balance equation of the oxidizer instead of the fuel species is used. Additionally, the assumption of complete combustion in a fuel-rich flame equates to $Y_{\mathrm{ox},2}=0$.

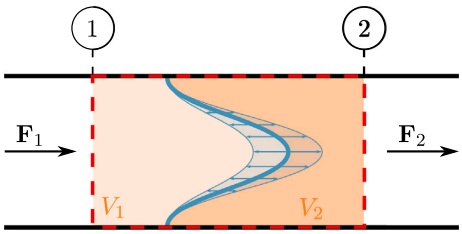

Fig. 2. Schematic representation of a premixed flame including a moving flame front. The moving flame front (——) is at every instance included in the fixed control volume V (— —). The flame separates the control volume V into the sub-volumes V_1 ( ) and V_2 ( ). (For interpretation of the references to color in this figure legend, the reader is referred to the web version of this article.)

with

$$\bar{\mathbf{J}}_{u_q,1} = \bar{c}_1 \left[(1 - \mathcal{F}_u) \quad \overline{M}_1 (1 - \bar{\gamma}_1 \mathcal{F}_p) \quad -(1 + \mathcal{F}_s) \quad (\delta_{if} - \widetilde{\mathbf{X}}_1 - \widetilde{\boldsymbol{\mathcal{F}}}_Y) \right] . \tag{62}$$

The closures of the perturbed flux vectors $\mathbf{F}'_1$ and $\mathbf{F}'_2$ are already known and are defined in Eqs. (23), (24) and (25).

6. *Formulation of the generalized thermoacoustic jump condition.* Finally, the perturbed system of equations for the lean premixed flame (Eq. (54)) is closed using the Jacobian-based closure models for the perturbed fluxes $\mathbf{F}'_1$ and $\mathbf{F}'_2$ (Eq. (23)) with $\bar{\mathbf{J}}_{F,1}$ and $\bar{\mathbf{J}}_{F,2}$ (Eqs. (24),(25)), the perturbed global source term $\boldsymbol{\Omega}'$ with $\bar{\mathbf{J}}_{\Omega,1}$ (Eq. (59)) and the cross-section averaged absolute flame velocity u'_q (Eq. (61)) with $\bar{\mathbf{J}}_{u_q,1}$ (Eq. (62)). The generalized transfer matrix of a lean premixed flame is then defined as

$$\overline{\mathbf{T}} = \left(\bar{\mathbf{J}}_{F,2} A \right)^{-1} \left(\bar{\mathbf{J}}_{F,1} A + \underbrace{A \left(\overline{\mathbf{U}}_2 - \overline{\mathbf{U}}_1 \right) \bar{\mathbf{J}}_{u_q,1}}_{=\bar{\mathbf{J}}_{U,1}} + \bar{\mathbf{J}}_{\Omega,1} \right) . \tag{63}$$

The form of Eq. (63) is analogous to the general Eq. (30) with $\bar{\mathbf{J}}_{F_w,1} = \bar{\mathbf{J}}_{F_w,2} = \mathbf{0}$ (no area change), $\bar{\mathbf{J}}_{U,2} = \mathbf{0}$ and $\bar{\mathbf{J}}_{\Omega,2} = \mathbf{0}$. Note that the explicit analytical formulation of the transfer matrix of the lean premixed flame (Eq. (63)) in the general case is omitted here since it would be far too lengthy to fit this page. Furthermore, a Jacobian-based representation and implementation is advantageous from a computational perspective concerning flexibility and efficiency (see Section 2.2).

3.2. Validation

This section uses the one-dimensional autoignition flame shown in Fig. 3(a) to validate the generalized jump condition of a lean premixed flame (Eq. (63)). The flame is located in a domain of length $L = 5L_\tau$, where L_τ is the location of the maximum heat release of the flame (see Fig. 3(b)). To be consistent with the notation in Section 3.1, the "theoretical" states just upstream and downstream of the flame front are indicated by $(\cdot)_1$ and $(\cdot)_2$, whereas the indices $(\cdot)_0$ and $(\cdot)_3$ denote the states at the domain inlet and outlet, respectively. Furthermore, the investigated flame burns a lean hydrogen (H_2)-vitiated air mixture typical for the second stage in reheat combustion systems [49]. The corresponding species mass fractions, mean flow parameters and the ratio of gas properties of the autoignition flame under investigated are listed in Table 1.

Note that the general model for the lean premixed flame derived in Sec. 3.1 is applicable to 3D flames. However, the case of a one-dimensional H_2 autoignition flame is sufficient and well suited for the validation of the generalized jump condition for the following reasons. First, the generalized jump condition is exact for a one-dimensional flame in the limit of compactness. Second, autoignition flames are sensitive to all incoming perturbations requiring all FTFs $\mathcal{F}_u$, $\mathcal{F}_p$, $\mathcal{F}_s$ and $\widetilde{\boldsymbol{\mathcal{F}}}_Y$ for an accurate representation [47,48,58]. Third, the mean flow

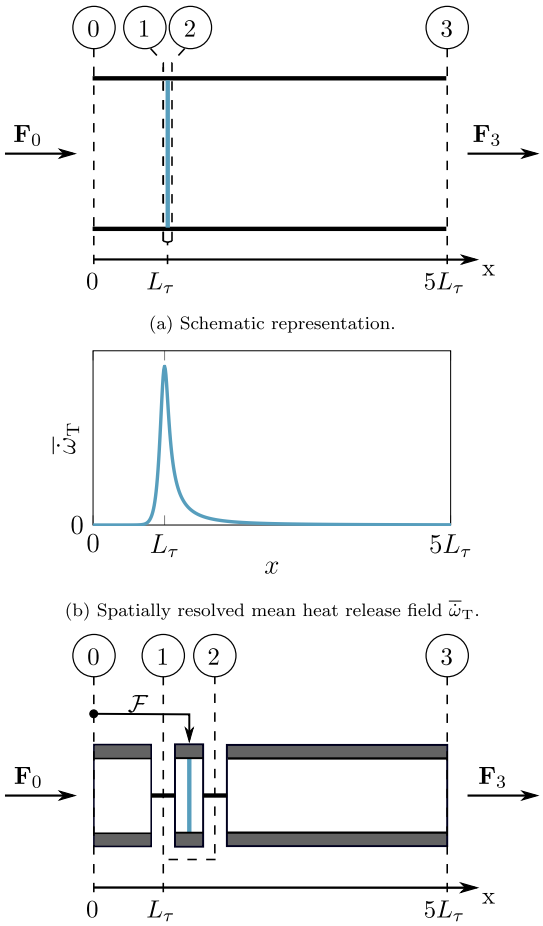

Fig. 3. The one-dimensional H_2 autoignition flame.

Table 1
Mean flow values of the H_2 autoignition flame.

Mean flow parameters	$\bar{p}_0$	101 325	Pa
	$\bar{T}_0$	1100	K
	$\bar{M}_0$	0.1	
	$\bar{L}_\tau$	9.33×10^{-3}	m
Specie mass fractions	$\bar{Y}_{H_2,0}$	0.008	
	$\bar{Y}_{H_2O,0}$	0.050	
	$\bar{Y}_{O_2,0}$	0.180	
	$\bar{Y}_{N_2,0}$	0.762	
Gas properties	$\bar{c}_{p,3}/\bar{c}_{p,0}$	1.074	
	$\bar{\gamma}_3/\bar{\gamma}_0$	0.964	
	$\bar{R}_3/\bar{R}_0$	0.950	

Table 2
The independent characteristic forcing cases A-F computed for the H_2 autoignition flame.

Case	Forced characteristic	Characteristic amplitude
A	acoustic (inlet)	f_0^+
B	acoustic (outlet)	g_3^+
C	entropic (inlet)	s_0^+
D	compositional (inlet)	$\left(Y_{\mathrm{H_2}}^+\right)_0 \mid \left(Y_{\mathrm{N_2}}^+\right)_0$
E	compositional (inlet)	$\left(Y_{\mathrm{O_2}}^+\right)_0 \mid \left(Y_{\mathrm{N_2}}^+\right)_0$
F	compositional (inlet)	$\left(Y_{\mathrm{H_2O}}^+\right)_0 \mid \left(Y_{\mathrm{N_2}}^+\right)_0$

Mach numbers in applications encountering autoignition are typically higher than for propagation stabilized flames. Lastly, hydrogen as a fuel ensures a change in all gas properties of the gas mixtures across the flame (see Table 1). An additional practical reason, validation data for the one-dimensional autoignition flame is easily computed utilizing the current implementation of the spatially discretized linearized reactive flow solver of Meindl et al. [59] (see below). Note that for a 3D flame, the 3D effects would be simply encoded in the FTFs that appear as coefficients in the jump conditions.

The reference solution for the autoignition flame is computed utilizing the spatially discretized linearized reactive Euler equations in combination with the UCSD reaction mechanism [60] reduced for hydrogen/air combustion [61] (9 species, 21 reactions). The corresponding mean fields, such as the mean heat release field in Fig. 3(b), are solved using finite differences with a first-order upwind scheme. The domain is resolved with 10^6 cells. The corresponding linearized fields are solved in the frequency domain utilizing the Discontinuous Galerkin solver detailed in Meindl et al. [59]. Third-order elements and 10^4 cells are used to resolve the computational domain of length L. Non-reflecting characteristic boundary conditions are used at the inlet and outlet [62].

Six linearly independent forcing cases exist to perturb the linearized system of conservation equations, e.g. the six characteristic forcings listed in Table 2. Note that there are only three linearly independent forcings of coupled species perturbations for the four species H_2, O_2, H_2O, and N_2 at the domain inlet. This is a direct consequence of mass conservation (Eq. (5)). Consequently, in combination with the FTFs $\mathcal{F}_\mathrm{u}$, $\mathcal{F}_\mathrm{p}$, $\mathcal{F}_\mathrm{s}$, only three coupled compositional FTFs, e.g. $\mathcal{F}_{Y_{\mathrm{H_2|N_2}}}$, $\mathcal{F}_{Y_{\mathrm{O_2|N_2}}}$ and $\mathcal{F}_{Y_{\mathrm{H_2O|N_2}}}$, as defined in Eq. (59) can be identified from numerical simulations. Harmonic forcing of the six forcing cases in Table 2 enables the frequency-wise determination of $\mathcal{F}_\mathrm{u}$, $\mathcal{F}_\mathrm{p}$, $\mathcal{F}_\mathrm{s}$, $\mathcal{F}_{Y_{\mathrm{H_2|N_2}}}$, $\mathcal{F}_{Y_{\mathrm{O_2|N_2}}}$ and $\mathcal{F}_{Y_{\mathrm{H_2O|N_2}}}$ with respect to the state at the domain inlet $(\cdot)_0$ via

$$\begin{bmatrix} \mathcal{F}_\mathrm{u} \\ \mathcal{F}_\mathrm{p} \\ \mathcal{F}_\mathrm{s} \\ \mathcal{F}_{Y_{\mathrm{H_2|N_2}}} \\ \mathcal{F}_{Y_{\mathrm{O_2|N_2}}} \\ \mathcal{F}_{Y_{\mathrm{H_2O|N_2}}} \end{bmatrix} = \mathbf{A}_0^{-1} \begin{bmatrix} \left(\frac{\dot{\omega}_\mathrm{T}'}{\overline{\dot{\omega}}_\mathrm{T}}\right)^A \\ \left(\frac{\dot{\omega}_\mathrm{T}'}{\overline{\dot{\omega}}_\mathrm{T}}\right)^B \\ \left(\frac{\dot{\omega}_\mathrm{T}'}{\overline{\dot{\omega}}_\mathrm{T}}\right)^C \\ \left(\frac{\dot{\omega}_\mathrm{T}'}{\overline{\dot{\omega}}_\mathrm{T}}\right)^D \\ \left(\frac{\dot{\omega}_\mathrm{T}'}{\overline{\dot{\omega}}_\mathrm{T}}\right)^E \\ \left(\frac{\dot{\omega}_\mathrm{T}'}{\overline{\dot{\omega}}_\mathrm{T}}\right)^F \end{bmatrix} \tag{64}$$

with

$$\mathbf{A}_0 = \begin{bmatrix} \left(\frac{u^+}{\overline{M}}\right)^A & \left(\overline{\gamma}p^+\right)^A & \left(s^+\right)^A & \left(Y_{\mathrm{H_2}}^+\right)^A & \left(Y_{\mathrm{O_2}}^+\right)^A & \left(Y_{\mathrm{H_2O}}^+\right)^A \\ \left(\frac{u^+}{\overline{M}}\right)^B & \left(\overline{\gamma}p^+\right)^B & \left(s^+\right)^B & \left(Y_{\mathrm{H_2}}^+\right)^B & \left(Y_{\mathrm{O_2}}^+\right)^B & \left(Y_{\mathrm{H_2O}}^+\right)^B \\ \left(\frac{u^+}{\overline{M}}\right)^C & \left(\overline{\gamma}p^+\right)^C & \left(s^+\right)^C & \left(Y_{\mathrm{H_2}}^+\right)^C & \left(Y_{\mathrm{O_2}}^+\right)^C & \left(Y_{\mathrm{H_2O}}^+\right)^C \\ \left(\frac{u^+}{\overline{M}}\right)^D & \left(\overline{\gamma}p^+\right)^D & \left(s^+\right)^D & \left(Y_{\mathrm{H_2}}^+\right)^D & \left(Y_{\mathrm{O_2}}^+\right)^D & \left(Y_{\mathrm{H_2O}}^+\right)^D \\ \left(\frac{u^+}{\overline{M}}\right)^E & \left(\overline{\gamma}p^+\right)^E & \left(s^+\right)^E & \left(Y_{\mathrm{H_2}}^+\right)^E & \left(Y_{\mathrm{O_2}}^+\right)^E & \left(Y_{\mathrm{H_2O}}^+\right)^E \\ \left(\frac{u^+}{\overline{M}}\right)^F & \left(\overline{\gamma}p^+\right)^F & \left(s^+\right)^F & \left(Y_{\mathrm{H_2}}^+\right)^F & \left(Y_{\mathrm{O_2}}^+\right)^F & \left(Y_{\mathrm{H_2O}}^+\right)^F \end{bmatrix}_0 . \tag{65}$$

Fig. 4 shows the resulting reference FTFs for forcing frequencies f between 100 Hz and 2000 Hz with an increment of 100 Hz as markers. For an accurate low-frequency limit of the FTFs, an additional data point at 1 Hz is displayed. Note that the respective low-frequency limit ($f \to 0$ Hz) of the individual FTFs may be derived from theoretical considerations [48,53,58]. In a linearized framework, all deviations from the mean, including the displacement of the flame, are assumed to be small. To limit the flame displacement in the low-frequency limit ($f \to 0$ Hz) with an infinite perturbation period, the absolute flame velocity displacing the flame must become infinitesimally small ($u_\mathrm{q}' \to 0$).[2] Thus, the low-frequency limits of the FTFs are evident from Eq. (62) and are $\mathcal{F}_\mathrm{u} = 1$ [53], $\mathcal{F}_\mathrm{p} = 1/\overline{\gamma}_1$ [58], $\mathcal{F}_\mathrm{s} = -1$ [48] and $\widetilde{\boldsymbol{\mathcal{F}}}_\mathrm{Y} = \delta_\mathrm{if} - \widetilde{\mathbf{X}}_1$. The low-frequency limits of the FTFs in Fig. 4 match the theoretically obtained values. Rational fits of the FTFs are represented by the lines in Fig. 4. Note that for an autoignition flame, each species perturbation Y_k' can affect the species reaction rates of all species and consequently have their own FTF. In Fig. 4, this effect is clearly visible from the non-vanishing FTF $\mathcal{F}_{Y_{\mathrm{O_2|N_2}}}$.

In addition to the FTFs, the reference scattering matrix of the test case domain is determined from the six forcing cases A-F listed in Table 2 via

$$\overline{\mathbf{S}} = \mathbf{W}_\mathrm{out}^+ \left(\mathbf{W}_\mathrm{in}^+\right)^{-1} \tag{66}$$

with

$$\mathbf{W}_l^+ = \begin{bmatrix} \left(\mathbf{w}_l^+\right)^A & \left(\mathbf{w}_l^+\right)^B & \left(\mathbf{w}_l^+\right)^C & \left(\mathbf{w}_l^+\right)^D & \left(\mathbf{w}_l^+\right)^E & \left(\mathbf{w}_l^+\right)^F \end{bmatrix} \tag{67}$$

and the state vectors $\mathbf{w}_l^+$ ($l \in \{\mathrm{in}, \mathrm{out}\}$, $i = 0$, $j = 3$) as defined in Eq. (33).

The thermoacoustic scattering of the domain displayed in Fig. 3(a) encasing the one-dimensional autoignition flame can be modeled by the simple network model detailed in Fig. 3(c). The network model is a sequence of two ducts enclosing the compact flame derived in Section 3.1, where the flame is located at the maximum heat release $x = L_\tau$ of the spatially discretized flame (see Fig. 3(b)). The duct element (e.g. [10]) with the scattering matrix

$$\overline{S}_\mathrm{d} = \begin{bmatrix} e^{\varphi_f} & 0 & 0 & \mathbf{0} \\ 0 & e^{\varphi_g} & 0 & \mathbf{0} \\ 0 & 0 & e^{\varphi_c} & \mathbf{0} \\ \mathbf{0} & \mathbf{0} & \mathbf{0} & \mathbf{I}\, e^{\varphi_c} \end{bmatrix} \tag{68}$$

[2] In a linearized framework, all deviations from the mean are assumed to be small. The displacement $\Delta'(t)$ of a flame front is therefore limited to a small maximum value Δ'_max. Now, assuming a harmonic displacement of the flame front $\Delta'(t) = \Delta'_\mathrm{max} \exp(i\omega t)$ around its mean in response to a harmonic perturbation, it becomes obvious that the absolute flame velocity $u_\mathrm{q}' = \frac{\partial \Delta'}{\partial t} = i\omega \Delta'_\mathrm{max} \exp(i\omega t)$ vanishes in the low-frequency limit ($\omega \to 0$). This is necessary to keep a limited displacement while the time to reach the maximum displacement becomes infinitely large. Note that this argument is independent of the physical mechanism displacing the flame front, but solely results from the assumption of small perturbations.

simply apply the phase shifts

$$\varphi_f = -2i\pi f \frac{L_\mathrm{d}}{\overline{c}+\overline{u}}$$
$$\varphi_g = -2i\pi f \frac{L_\mathrm{d}}{\overline{c}-\overline{u}} \tag{69}$$
$$\varphi_c = -2i\pi f \frac{L_\mathrm{d}}{\overline{u}},$$

propagating the acoustic, entropic and compositional disturbances through the duct of length L_d. i is the complex number. Note that the network model in Fig. 3(c) uses the state $(\cdot)_0$ at the domain inlet as a reference for the FTFs. Then, interconnecting the scattering matrices of the individual elements [10] results in the scattering matrix of the domain approximated by the network model.

Fig. 5 compares the scattering matrices of the spatially resolved one-dimensional autoignition flame (Fig. 3(b)) and the corresponding network model (Fig. 3(c)). For conciseness, Fig. 5 shows only the H_2 perturbations at the domain inlet and H_2O perturbations at the domain outlet. Overall, the scattering matrix of the network model shows an excellent agreement in absolute and a very good agreement in phase values with the reference solution. Only the phases of the coefficients S_{sf} and S_{sg} show a deviation between the network model and the reference solution. However, note that the absolute values of the corresponding coefficients are almost zero and the phase information is consequently meaningless and of no concern. The deviation results from minor numerical artifacts in the reference solution. Furthermore, no phase information is plotted for the coefficients $S_{\mathrm{H_2O}f}$, $S_{\mathrm{H_2O}g}$ and $S_{\mathrm{H_2O}s}$ since their absolute values are zero by definition and the phase is consequently undefined.

The entries of the state vector $\mathbf{w}_i^+$ in Eq. (33) are defined to be in the same order of magnitudes for typical application cases [43]. Consequently, the amplitudes of the scattering matrix coefficients directly visualize their relative importance for the thermoacoustic scattering. For example, S_{fs} and S_{gs} indicate a significant acoustic wave generation by incoming entropy waves for the lean autoignition flame. This sensitivity of autoignition flames to incoming entropic/temperature disturbances is well documented in the literature (e.g. [14,47,48]). Furthermore, the fifth row in Fig. 5 clearly shows that incoming entropy disturbances are damped across the flame ($|S_{ss}| < 1$) and that the generation of entropy disturbances by acoustic waves is negligible ($|S_{fs}| \approx 0$, $|S_{gs}| \approx 0$). Entropy disturbances are consequently predominantly generated by disturbances in the fuel mass fractions ($S_{s\mathrm{H_2}}$). This is in line with detailed analytical investigations (e.g. [12,43]).

3.3. Discussion

The generalized jump condition for a lean premixed flame derived in Section 3.1 can be simplified to a multitude of jump conditions in literature by introducing suitable assumptions *a posteriori*. The assumptions necessary to simplify this generalized jump condition to some established results in the literature are listed in Table 3. The essential assumptions listed are the restriction to a subset of perturbations (Section 2.3.1), lumping compositional perturbations (Section 2.3.2), simplified gas properties (Section 2.3.3), reduced Mach number approximations[3] (Section 2.3.4) and the neglect of the flame movement $\overline{\mathbf{J}}_{u_\mathrm{q},1} = \overline{\mathbf{J}}_{u_\mathrm{q},2} = \mathbf{0}$. In addition to their intrinsic assumptions, the jump conditions in the literature typically do not resolve the gas composition (with Li and Morgans [13] being an exception) requiring additional external inputs to close the jump condition. For example, Strobio Chen et al. [12] and Gant et al. [14] use the temperature ratio $\overline{T}_2/\overline{T}_1$ as an additional input. Schuermans et al. [35] requires the lower heating value of the fuel H_u, the fuel mass fraction Y_f and the gas specific ratios $\overline{R}_2/\overline{R}_1$ and $\overline{c}_{\mathrm{p},2}/\overline{c}_{\mathrm{p},1}$ as inputs, whereas Dowling and Stow [11] need the mean heat release rate $\overline{\Omega}_\mathrm{T}$. Note that the external input used can have an impact on the accuracy of the jump condition.

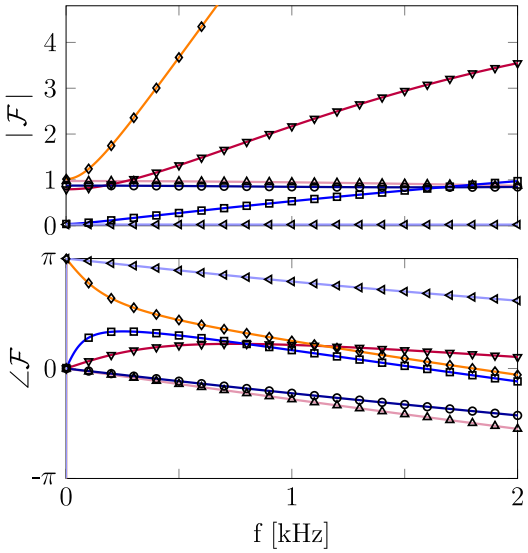

Fig. 4. Flame transfer functions $\mathcal{F}_u$ (△, ——), $\mathcal{F}_p$ (▽, ——), $\mathcal{F}_s$ (◇, ——), $\mathcal{F}_{Y_{\mathrm{H_2IN_2}}}$ (○, ——), $\mathcal{F}_{Y_{\mathrm{O_2IN_2}}}$ (□, ——) and $\mathcal{F}_{Y_{\mathrm{H_2OIN_2}}}$ (◁, ——) for the one-dimensional H_2 autoignition flame. The markers symbolize the reference solution, the lines the corresponding rational fit used to evaluate the jump condition. (For interpretation of the references to color in this figure legend, the reader is referred to the web version of this article.)

In the following, the validation case detailed in Section 3.2 is used to investigate the approximation errors of the corresponding scattering matrix (Fig. 5) resulting from the assumptions of a reduced order in Mach number, constant gas properties, or neglecting the flame movement. The respective simplifications are introduced by following the procedure detailed in Section 2.3. Throughout all cases, the mean global heat release rate $\overline{\Omega}_\mathrm{T}$ is kept constant and the gas compositions upstream ($\overline{\mathbf{Y}}_0$) and downstream ($\overline{\mathbf{Y}}_3$) of the flame are resolved. When assuming constant gas properties, these are chosen equivalent to the gas properties upstream of the flame ($\overline{\gamma} = \overline{\gamma}_0$, $\overline{R} = \overline{R}_0$, $\overline{c}_\mathrm{p} = \overline{c}_{\mathrm{p},0}$). Eventually, the approximation error of the scattering matrix coefficient with index ij is defined as

$$\Sigma_{ij} = \frac{\left|\overline{S}_{ij} - \hat{\overline{S}}_{ij}\right|}{|\overline{S}_{ij}|}, \tag{70}$$

where $\hat{\overline{S}}_{ij}$ is the approximation of the generalized scattering matrix coefficient $\overline{S}_{ij}$ in Fig. 5. Note that the approximation error defined in Eq. (70) subtracts the complex-valued scattering matrix coefficients $\hat{\overline{S}}_{ij}$ and $\overline{S}_{ij}$ from each other, resulting in a measure accounting simultaneously for errors in gain $a_{\Sigma,ij}$ (relative error) and phase $\varphi_{\Sigma,ij}$.[4] Fig. 6 illustrates the definition of the error measure Σ_{ij} in a phasor plot.

[3] In literature, the transfer matrix is expanded into a Taylor series up to order P directly instead of following the procedure detailed in Section 2.3.4. In this case, the transfer matrix itself is the Pth order approximation of the transfer matrix derived by the procedure in Section 2.3.4.

[4] Eq. (70) can be expressed in terms of a relative error in gain $a_{\Sigma,ij}$ and a phase error $\varphi_{\Sigma,ij}$,

$$\Sigma_{ij} = \left[a_{\Sigma,ij}^2 + 2(1-\cos(\varphi_{\Sigma,ij})) + 2a_{\Sigma,ij}(1-\cos(\varphi_{\Sigma,ij}))\right]^{\frac{1}{2}}.$$

A relative approximation error of, for example, 25 % may correspond solely to an amplitude error of $a_{\Sigma,ij} = 0.25$, solely to a phase error of $\varphi_{\Sigma,ij} =$

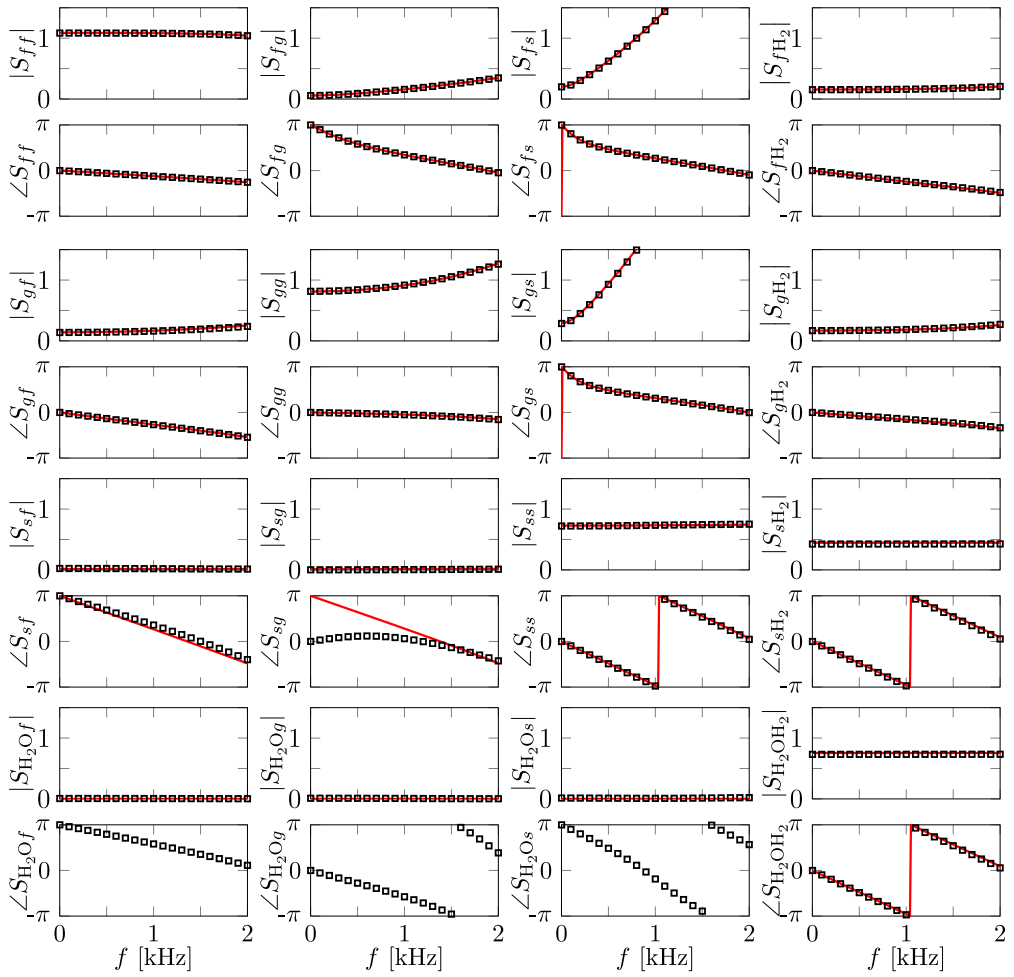

Fig. 5. Scattering matrix coefficients of the H_2 autoignition flame detailed in Table 1. Displayed are the results of the reference solution (¤) and the network model (——). (For interpretation of the references to color in this figure legend, the reader is referred to the web version of this article.)

Table 3
Necessary assumptions to simplify the generalized compact flame element derived in this section *a posteriori* to established results in the literature. The table marks the subset of the resolved characteristics (Section 2.3.1), the usage of simplified gas properties (c_p, Section 2.3.3), approximation order in Mach number ($\mathcal{O}(M^x)$, Section 2.3.4) and the consideration of the flame movement u_q. If only a lumped compositional perturbation (Section 2.3.2) was used, the compositional perturbation Y_k^+ is checked in brackets (✓). Two exponents are detailed for $\mathcal{O}(\overline{M}^x)$ if the approximation order in Mach number are chosen differently for the mean field (first exponent) and the perturbed fields (second exponent).

Paper	$\mathcal{O}(M^x)$	c_p	u^+, p^+	s^+	Y_k^+	u_q
Chu [34]	$\mathcal{O}\left(\overline{M}^1\right)$	$c_p(\mathbf{Y})$	✓	(✓)[a]	–	✓
Dowling and Stow [11]	$\mathcal{O}\left(\overline{M}^0\right)$	c_p	✓	(✓)[b]	–	–
Schuermans [35]	$\mathcal{O}\left(\overline{M}^1\right)$	$c_p(\mathbf{Y})$	✓	(✓)[c]	(✓)	✓
Strobio Chen et al. [12]	$\mathcal{O}\left(\overline{M}^1\right)$	c_p	✓	✓	(✓)	✓
Li and Morgans [13]	$\mathcal{O}\left(\overline{M}^0\right)$	$c_p(T, \mathbf{Y})$	✓	–	–	–
Gant et al. [14]	$\mathcal{O}\left(\overline{M}^{1\|2-3}\right)$	c_p	✓	✓	–	✓
This work	$\mathcal{O}\left(\overline{M}^{\infty}\right)$	$c_p(T, \mathbf{Y})$	✓	✓	✓	✓

[a] Chu [34] considers only the incoming entropy perturbation s_1^+.
[b] Dowling and Stow [11] considers only entropy waves downstream of the flame.
[c] Schuermans [35] considers only entropy waves downstream of the flame.

First, Σ_{ij} of zeroth ($P = 0$), first ($P = 1$) and second ($P = 2$) order Mach number approximations (Section 2.3.4) are investigated and displayed in Fig. 7. The zeroth order approximation is only displayed for the acoustic scattering coefficients since the convective perturbations are no longer propagated in this limit case [63]. As expected, Fig. 7 shows a decreasing Σ_{ij} for all coefficients with increasing order of the Mach number approximation. For the H_2 autoignition flame with an inlet Mach number of $\overline{M}_1 = 0.1$, the zeroth order Mach number approximation is with relative errors between $5 - 70\%$ insufficient for an accurate representation of the acoustic scattering of the flame. The first-order approximations show decent relative errors of $\leq 3\%$ for most coefficients with an exception for Σ_{ss} at higher frequencies where the relative error increases up to $6.5\,\%$. The second-order approximation is already very accurate with relative errors of $\leq 1.6\,\%$ once again with the worst accuracy for Σ_{ss} at higher frequencies. Overall, the approximation error of a reduced Mach number approximation of order P scales with $\overline{M}_1$ via

$$\boldsymbol{\Sigma} \propto \overline{M}_1^{P+1}. \tag{71}$$

For test cases with $\overline{M}_1 > 0.1$, Mach number approximations of higher than first order should be used to obtain an accurate jump condition (see also the argumentation in Gant et al. [14]).

Second, Fig. 7 shows the approximation error due to the assumption of constant gas properties (Section 2.3.3). The relative errors are with up to $25\,\%$ for Σ_{fg} and Σ_{ss} rather large. This stresses the fact that for an accurate jump condition, the change in gas properties must be taken into account (see also Li and Morgans et al. [13]). For the H_2 autoignition flame under investigation, the approximation error corresponding to the assumption of constant gas properties clearly dominates over the error introduced by first or higher-order Mach number approximations. Overall, the change in gas properties depends on the fuel and air composition, the inlet temperature $\overline{T}_1$ and the fuel mass fraction.

Finally, Fig. 7 displays the approximation error resulting from neglecting the flame movement. Here, especially the scattering coefficients connected to the generation of entropy waves Σ_{sf}, Σ_{sg} and Σ_{ss} and Σ_{sH_2} show immense relative errors of almost $6000\,\%$. The neglect of flame movement results in the significant generation of spurious entropic perturbations [12]. Additionally, the acoustic scattering coefficients ($\Sigma \leq 12\,\%$) as well as the entropic-acoustic ($\Sigma \leq 19\,\%$) and the compositional-acoustic coupling ($\Sigma \leq 15\,\%$) are affected when the flame movement is neglected. This results in the additional generation of spurious acoustic waves as previously observed by Meindl et al. [64]. In the low-frequency limit, the absolute flame velocity displacing the flame is infinitesimally small (see Section 3.2). Consequently, the errors resulting from the neglect of the flame movement decrease strongly for low frequencies. That the error is not vanishing results from small errors in the numerically determined FTFs displayed in Fig. 4. Additionally, Eq. (62) shows that the error resulting from the neglect of the flame movement away from the zero frequency limit depends strongly on the underlying flame dynamics and, therefore, the flame transfer functions.

To the best of the authors' knowledge, the jump condition proposed by Gant et al. [14] is the most elaborate and accurate thermoacoustic jump condition for the configuration at hand found in the literature. Therefore, we choose, in addition to the numerical results, the formulation of Gant et al. [14] as a reference in an effort to assess the validity and accuracy of the Jacobian-based framework. Since Gant et al. [14] use a state vector different from $\mathbf{v}_i^+$, the state transformation

$$\begin{bmatrix} \frac{p'}{\overline{\rho}\overline{c}} \\ u' \\ \frac{\overline{R}T'}{\overline{c}} \end{bmatrix}_i = \underbrace{\begin{bmatrix} 0 & \overline{c} & 0 \\ \overline{c} & 0 & 0 \\ 0 & \overline{c}\frac{\gamma-1}{\gamma} & \frac{\overline{c}}{\overline{\gamma}\overline{M}} \end{bmatrix}_i}_{\overline{\mathbf{V}}_i} \begin{bmatrix} u^+ \\ p^+ \\ \overline{M}s^+ \end{bmatrix}_i \tag{72}$$

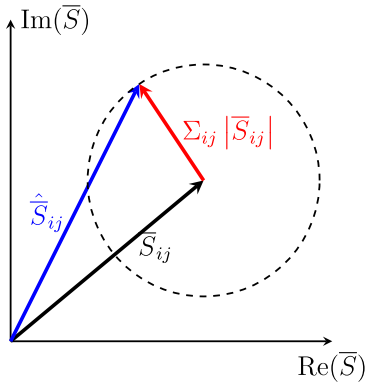

Fig. 6. Phasor plot illustrating the definition of the absolute approximation error $\Sigma_{ij}\,|\overline{S}_{ij}|$ (⟶) as the length of the phasor interconnecting the phasors of the reference $\overline{S}_{ij}$ (⟶) and the approximated $\hat{\overline{S}}_{ij}$ (⟶) scattering matrix coefficients. All approximations on the isoline (- - -) are of the same approximation error $\Sigma_{ij}\,|\overline{S}_{ij}|$. (For interpretation of the references to color in this figure legend, the reader is referred to the web version of this article.)

must be applied to the transfer matrix $\overline{\mathbf{T}}_{\text{Gant}}$ of Gant et al. [14, Eq. (15)] to obtain a transfer matrix

$$\overline{\mathbf{T}}_{\text{Gant,tf}} = \overline{\mathbf{V}}_2^{-1}\overline{\mathbf{T}}_{\text{Gant}}\overline{\mathbf{V}}_1 \tag{73}$$

comparable to Eq. (63). Subsequently, the approximate scattering matrix $\hat{\overline{\mathbf{S}}}_{\text{Gant,tf}}$ is computed by replacing the flame transfer matrix (Eq. (63)) with $\overline{\mathbf{T}}_{\text{Gant,tf}}$ for the validation case (Section 3.2). To determine $\hat{\overline{\mathbf{S}}}_{\text{Gant,tf}}$, the global heat release rate $\overline{\dot{\Omega}}_{\text{T}}$ is held constant and the gas properties are set equal to the inflow properties analogously to the other simplification cases in this section. $\hat{\overline{\mathbf{S}}}_{\text{Gant,tf}}$ is plotted in Fig. 1 of the supplementary material. Eventually, the approximation errors of the jump condition of Gant et al. [14] are computed via Eq. (70) and displayed in Fig. 7.

The jump condition of Gant et al. [14] uses two intrinsic assumptions — constant gas properties and the Mach number approximation $\mathcal{O}(\overline{M}^{1|2-3})$ (see Table 3). In Fig. 7, the approximation errors associated with the jump condition of Gant et al. [14] closely align with the errors arising from the assumption of constant gas properties. This indicates that the errors from assuming constant gas properties dominate over those from the Mach number approximation $\mathcal{O}(\overline{M}^{1|2-3})$. To analyze and visualize the errors associated with the two assumptions separately, the authors derived an extended version of the jump condition of Gant et al. [14], removing the assumption of constant gas properties while retaining the Mach number approximation $\mathcal{O}(\overline{M}^{1|2-3})$. The analytical formulation of the extended jump condition is detailed in Sec. 3 of the supplementary material. In Fig. 7, the approximation errors of the extended jump condition are reduced significantly (roughly by an order of magnitude for most coefficients) in comparison to those of the original jump condition of Gant et al. [14]. This proves that the assumption of constant gas properties dominates the approximation errors of the original jump condition of Gant et al. [14] in the case considered here. The errors associated with the Mach number approximation $\mathcal{O}(\overline{M}^{1|2-3})$ (isolated in the extended jump condition) are minor in comparison and behave similarly to $\mathcal{O}(\overline{M}^1)$. Only the scattering coefficients associated with the generation of entropic disturbances show a slightly smaller order of approximation errors $\mathcal{O}(\overline{M}^{1-2})$. This indicates that the error of the Mach number approximation $\mathcal{O}(\overline{M}^{1|2-3})$ is predominantly influenced by the first-order mean flow approximation used, even though second to third-order Mach number terms are taken into account in the

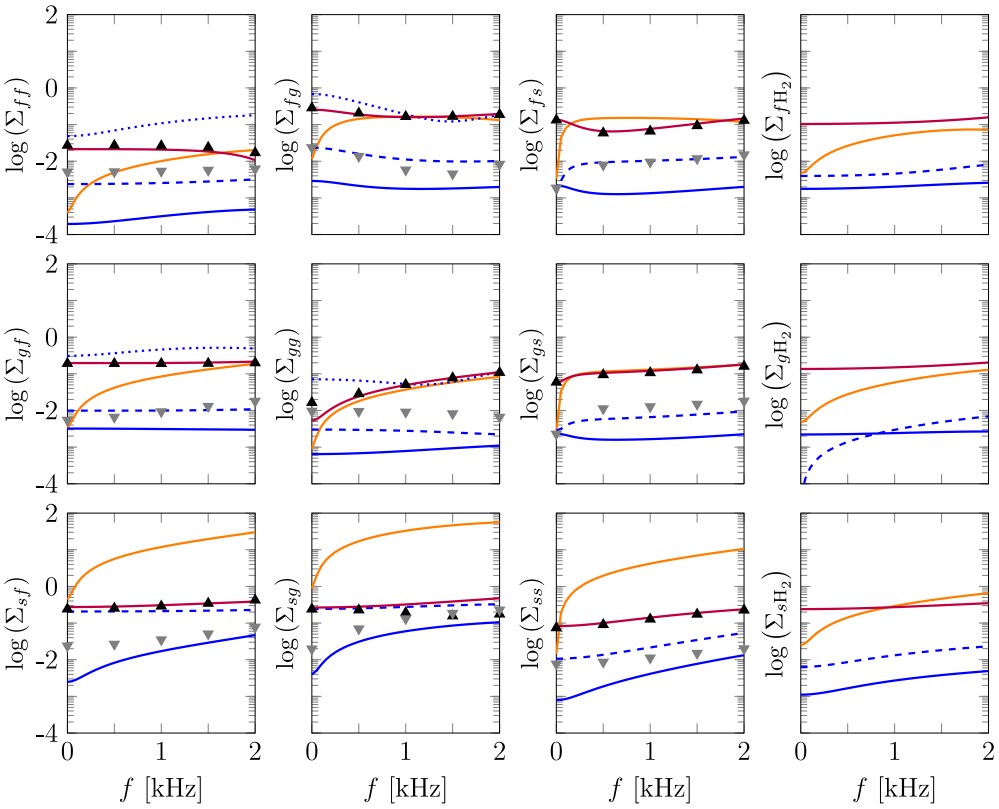

Fig. 7. Approximation errors $\boldsymbol{\Sigma}$ introduced into the generalized scattering matrix of the H_2 autoignition flame (Fig. 5). Displayed are the second ($\mathcal{O}(M^2)$, ——), first ($\mathcal{O}(M^1)$, - - -) and zeroth order ($\mathcal{O}(M^0)$, ·····) Mach number approximations, constant gas properties (——) and the neglect of flame movement (——). The zeroth order Mach approximation is plotted only for the acoustic scattering coefficients. For reference, the approximation error of Gant et al. [14] ($\mathcal{O}(M^{1|2-3})$, constant gas properties, ▲) is plotted at five distinct frequencies. In addition, the approximation error of Gant et al. [14]'s jump condition extended for realistic gas properties ($\mathcal{O}(M^{1|2-3})$, ▼) is displayed to isolate the errors corresponding to the Mach number approximation used by Gant et al. [14]. (For interpretation of the references to color in this figure legend, the reader is referred to the web version of this article.)

perturbed system of equations. Nevertheless, the Mach number approximation $\mathcal{O}(\overline{M}^{1|2-3})$ used by Gant et al. [14] achieves small relative errors $\Sigma \leq 2.4\,\%$ for all coefficients with significant absolute values[5] and is sufficient to achieve highly accurate jump conditions for the validation case considered here.

4. Application to non-reacting cases

The framework proposed in Section 2 is not only applicable for reacting cases such as the lean premixed flame (Section 3) but also for the derivation of comprehensive jump conditions for non-reacting elements such as area changes or junctions. To emphasize this point, Section 4 in the supplementary material provides the exemplary derivation for a shock-free area change with or without pressure loss.

5. Conclusion

This work introduces a Jacobian-based framework for the derivation of comprehensive thermoacoustic jump conditions for different application cases under minimal assumptions. The modularity and generality of the framework render it applicable for the derivation of a wide variety of compact elements. Additionally, the Jacobian-based modularity provides a guideline for efficient and straightforward numerical implementation of these jump conditions. The jump conditions derived within this framework are comprehensive and account for acoustic, entropic and compositional perturbations in reactive flows. Furthermore, the framework provides easily interpretable transfer/scattering matrices by choosing the state variables of the same order of magnitude, resulting in relatable matrix coefficients. Finally, application-specific assumptions to increase efficiency are easily included *a posteriori* without the need for a rederivation of the jump condition.

The easy applicability of the proposed framework is demonstrated in this work by deriving the jump condition of a lean premixed flame. This novel jump condition is subsequently validated for the test case of a one-dimensional H_2 autoignition flame, demonstrating its high accuracy and easy interpretability. Furthermore, the generality of the derived jump condition is shown by providing an overview of necessary assumptions to simplify the novel jump condition *a posteriori* to some established jump conditions in literature. The errors introduced by common approximations like a reduced order in Mach number, constant gas properties and the neglect of flame movement are investigated.

The proposed framework provides the basis for network model toolboxes that allow easy switching between highly accurate and highly

[5] The largest relative errors of the Mach number approximation $\mathcal{O}(\overline{M}^{1|2-3})$ appear in the coefficients $\Sigma_{sf} \leq 8\,\%$ and $\Sigma_{sg} \leq 23\,\%$. However, these relative errors are of no concern since the absolute values of Σ_{sf} and Σ_{sg} are negligible (see Fig. 5).

efficient models. Such a toolbox would be suited not only for extensive parameter studies but also for the usage in the post-processing of experimental measurements that strongly rely on the accuracy of the model [32,33]. Especially in complex network models, small modeling errors in the individual jump conditions may accumulate across the network, falsifying its transfer behavior significantly.

CRediT authorship contribution statement

Moritz Merk: Writing – review & editing, Writing – original draft, Visualization, Validation, Software, Project administration, Methodology, Investigation, Formal analysis, Conceptualization. **Felix Schily:** Writing – review & editing, Methodology, Conceptualization. **Wolfgang Polifke:** Writing – review & editing, Supervision, Conceptualization.

Declaration of competing interest

The authors declare that they have no known competing financial interests or personal relationships that could have appeared to influence the work reported in this paper.

The author Wolfgang Polifke is an Editorial Board Member and Associate Editor for the International Journal of Spray and Combustion Dynamics and was not involved in the editorial review or the decision to publish this article.

Acknowledgments

The authors thank Alexander J. Eder for the valuable discussions, his feedback and intermediate simulations that contributed to this project.

Appendix A. Supplementary data

Supplementary material related to this article can be found online at https://doi.org/10.1016/j.combustflame.2024.113958.

References

[1] T. Lieuwen, V. Yang (Eds.), Combustion Instabilities in Gas Turbine Engines: Operational Experience, Fundamental Mechanisms and Modeling, American Institute of Aeronautics and Astronautics, Reston, VA, USA, 2005.
[2] T. Poinsot, Prediction and control of combustion instabilities in real engines, Proc. Combust. Inst. 36 (2017) 1–28.
[3] H.J. Merk, Analysis of heat-driven oscillations of gas flows, Appl. Sci. Res. 6 (1956) 317–336.
[4] D. Bohn, E. Deuker, An acoustical model to predict combustion driven oscillations, in: 20th International Congress on Combustion Engines, 1993.
[5] J.J. Keller, Thermoacoustic oscillations in combustion chambers of gas turbines, AIAA J. 33 (1995) 2280–2287.
[6] C.O. Paschereit, W. Polifke, Characterization of lean premixed gas turbine burners as acoustic multi-ports, in: APS/DFD Annual Meeting, 1997.
[7] A.P. Dowling, Thermoacoustic instability, in: 6th Int. Congress on Sound and Vibration, 1999, pp. 3277–3292.
[8] J. Eckstein, T. Sattelmayer, Low-order modeling of low-frequency combustion instabilities in aeroengines, J. Propuls. Power 22 (2006) 425–432.
[9] B. Schuermans, F. Guethe, D. Pennell, D. Guyot, C.O. Paschereit, Thermoacoustic modeling of a gas turbine using transfer functions measured under full engine pressure, J. Eng. Gas Turbines Power 132 (2010) 111503.
[10] T. Emmert, M. Meindl, S. Jaensch, W. Polifke, Linear state space interconnect modeling of acoustic systems, Acta Acust. United Ac. 102 (2016) 824–833.
[11] A.P. Dowling, S.R. Stow, Acoustic analysis of gas turbine combustors, J. Propuls. Power 19 (2003) 751–764.
[12] L. Strobio Chen, S. Bomberg, W. Polifke, Propagation and generation of acoustic and entropy waves across a moving flame front, Combust. Flame 166 (2016) 170–180.
[13] J. Li, A.S. Morgans, Simplified models for the thermodynamic properties along a combustor and their effect on thermoacoustic instability prediction, Fuel 184 (2016) 735–748.
[14] F. Gant, A. Cuquel, M.R. Bothien, Autoignition flame transfer matrix: analytical model versus large eddy simulations, Int. J. Spray Combust. Dyn. 14 (2022) 72–81.
[15] B. Schuermans, W. Polifke, C.O. Paschereit, Modeling transfer matrices of premixed flames and comparison with experimental results, in: ASME 1999 International Gas Turbine and Aeroengine Congress and Exhibition, 1999.
[16] P. Durrieu, G. Hofmans, G. Ajello, R. Boot, Y. Auregan, A. Hirschberg, M.C.A.M. Peters, Quasisteady aero-acoustic response of orifices, J. Acoust. Soc. Am. 110 (2001) 1859–1872.
[17] J. Guzmán-Iñigo, D. Yang, R. Gaudron, A.S. Morgans, On the scattering of entropy waves at sudden area expansions, J. Sound Vib. 540 (2022) 117261.
[18] F.E. Marble, S.M. Candel, Acoustic disturbance from gas non-uniformities convected through a nozzle, J. Sound Vib. 55 (1977) 225–243.
[19] F. De Domenico, E.O. Rolland, S. Hochgreb, A generalised model for acoustic and entropic transfer function of nozzles with losses, J. Sound Vib. 440 (2019) 212–230.
[20] L. Magri, On indirect noise in multicomponent nozzle flows, J. Fluid Mech. 828 (2017) R2.
[21] F. De Domenico, E.O. Rolland, J. Rodrigues, L. Magri, S. Hochgreb, Compositional and entropy indirect noise generated in subsonic non-isentropic nozzles, J. Fluid Mech. 910 (2021) A5.
[22] M. Karlsson, M. Åbom, Quasi-steady model of the acoustic scattering properties of a T-junction, J. Sound Vib. 330 (2011) 5131–5137.
[23] I. Duran, S. Moreau, Solution of the quasi-one-dimensional linearized Euler equations using flow invariants and the Magnus expansion, J. Fluid Mech. 723 (2013) 190–231.
[24] F. Schaefer, W. Polifke, Low-order network modeling of a duct with non-uniform cross-section and arbitrary mean temperature gradient in the presence of mean flow, in: AIAA Propulsion and Energy 2019 Forum, 2019.
[25] S.R. Yeddula, J. Guzmán-Iñigo, A.S. Morgans, A solution for the quasi-one-dimensional linearised Euler equations with heat transfer, J. Fluid Mech. 936 (2022) R3.
[26] J.G.R. von Saldern, J.P. Moeck, A. Orchini, Nonlinear interaction between clustered unstable thermoacoustic modes in Can-Annular combustors, Proc. Combust. Inst. 38 (4) (2021) 6145–6153.
[27] G.J.J. Fournier, M. Haeringer, C.F. Silva, W. Polifke, Low-order modeling to investigate clusters of intrinsic thermoacoustic modes in annular combustors, J. Eng. Gas Turbines Power 143 (2021) 041025.
[28] J. von Saldern, A. Orchini, J. Moeck, Analysis of thermoacoustic modes in Can-Annular combustors using effective Bloch-type boundary conditions, J. Eng. Gas Turbines Power 143 (2021) 071019.
[29] G.J.J. Fournier, F. Schaefer, M. Haeringer, C.F. Silva, W. Polifke, Interplay of clusters of acoustic and intrinsic thermoacoustic modes in Can-Annular combustors, J. Eng. Gas Turbines Power 144 (2022) 121015.
[30] M. Hoeijmakers, V. Kornilov, I. Lopez Arteaga, P. de Goey, H. Nijmeijer, Intrinsic instability of flame-acoustic coupling, Combust. Flame 161 (2014) 2860–2867.
[31] T. Emmert, S. Bomberg, W. Polifke, Intrinsic thermoacoustic instability of premixed flames, Combust. Flame 162 (2015) 75–85.
[32] M. Yoko, M.P. Juniper, Data-driven modelling of thermoacoustic instability in a ducted conical flame, in: Symposium on Thermoacoustics in Combustion, 2023.
[33] A.J. Eder, M. Merk, T. Hollweck, A. Fischer, C. Lahiri, C.F. Silva, W. Polifke, Model-based inference of flame transfer matrices from acoustic measurements in an aero-engine test rig, J. Eng. Gas Turbines Power 147 (2025) 031022.
[34] B.-T. Chu, On the generation of pressure waves at a plane flame front, Symp. (Int.) Combust. 4 (1953) 603–612.
[35] B. Schuermans, Modeling and Control of Thermoacoustic Instabilities (Ph.D. thesis), École Polytechnique Fédérale de Lausanne, Lausanne, Switzerland, 2003.
[36] M. Bauerheim, F. Nicoud, T. Poinsot, Theoretical analysis of the mass balance equation through a flame at zero and non-zero mach numbers, Combust. Flame 162 (2014) 60–67.
[37] W. Polifke, Modeling and analysis of premixed flame dynamics by means of distributed time delays, Prog. Energy Combust. Sci. 79 (2020) 100845.
[38] A. Jain, L. Magri, A physical model for indirect noise in non-isentropic nozzles: Transfer functions and stability, J. Fluid Mech. 935 (2022) A33.
[39] M. Yoon, The entropy wave generation in a heated one-dimensional duct, J. Fluid Mech. 883 (2020) A44.
[40] L. Magri, J. O'Brien, M. Ihme, Effects of nozzle Helmholtz number on indirect combustion noise by compositional perturbations, J. Eng. Gas Turbines Power 140 (2018) 031501.
[41] E.O. Rolland, Sound Produced by Entropic and Compositional Inhomogeneities (Ph.D. thesis), University of Cambridge, Cambridge, UK, 2018.
[42] T.C. Lieuwen, Unsteady Combustor Physics, Cambridge University Press, New York, NY, USA, 2021.
[43] M. Merk, A.J. Eder, W. Polifke, An arbitrary Lagrangian-Eulerian framework for the consistent analysis of entropy wave generation, Combust. Flame 262 (2024) 113334.
[44] T. Poinsot, D. Veynante, Theoretical and Numerical Combustion, CNRS, Paris, France, 2012.
[45] D.A. Pennell, M.R. Bothien, A. Ciani, V. Granet, G. Singla, S. Thorpe, A. Wickstroem, K. Oumejjoud, M. Yaquinto, An introduction to the ansaldo GT36 constant pressure sequential combustor, in: ASME Turbo Expo 2017, 2017.
[46] O. Schulz, N. Noiray, Autoignition flame dynamics in sequential combustors, Combust. Flame 192 (2018) 86–100.

[47] M. Bothien, D. Lauper, Y. Yang, A. Scarpato, Reconstruction and analysis of the acoustic transfer matrix of a reheat flame from large-eddy simulations, J. Eng. Gas Turbines Power 141 (2018) 021018.
[48] F. Gant, A. Gruber, M.R. Bothien, Development and validation study of a 1D analytical model for the response of reheat flames to entropy waves, Combust. Flame 222 (2020) 305–316.
[49] H.S. Gopalakrishnan, A. Gruber, J. Moeck, Response of autoignition-stabilized flames to one-dimensional disturbances: Intrinsic response, J. Eng. Gas Turbines Power (2021).
[50] O. Schmitz, H. Klingels, P. Kufner, Aero engine concepts beyond 2030: part 1—The steam injecting and recovering aero engine, J. Eng. Gas Turbines Power 143 (2021) 021001.
[51] O. Schmitz, S. Kaiser, H. Klingels, P. Kufner, M. Obermüller, M. Henke, J. Zanger, F. Grimm, S. Schuldt, A. Marcellan, D. Cirigliano, P. Kutne, A. Heron-Himmel, S. Schneider, J. Richter, B. Weigand, A. Göhler-Stroh, A. Seitz, M. Hornung, Aero engine concepts beyond 2030: part 3—Experimental demonstration of technological feasibility, J. Eng. Gas Turbines Power 143 (2021) 021003.
[52] D.G. Crighton, A.P. Dowling, J.E. Ffowcs Williams, M. Heckl, F.G. Leppington, Modern Methods in Analytical Acoustics, Springer London, London, UK, 1992.
[53] W. Polifke, C.J. Lawn, On the low-frequency limit of flame transfer functions, Combust. Flame 151 (2007) 437–451.
[54] A. Huber, W. Polifke, Dynamics of practical premix flames, part I: Model structure and identification, 2, Int. J. Spray Combust. Dyn. 1 (2009) 199–228.
[55] H. Schwarz, L. Zimmer, D. Durox, S. Candel, Detailed measurements of equivalence ratio modulations in premixed flames using laser Rayleigh scattering and absorption spectroscopy, Exp. Fluids 49 (2010) 809–821.
[56] P.L. Blackshear, Driving standing waves by heat addition, Symp. (Int.) Combust. 4 (1953) 553–566.
[57] A.P. Dowling, G.J. Bloxsidge, Reheat buzz- an acoustically driven combustion instability, in: 9th Aeroacoustics Conference, 1984.
[58] M. Zellhuber, B. Schuermans, W. Polifke, Impact of acoustic pressure on auto-ignition and heat release, Combust. Theory Model. 18 (2014) 1–31.
[59] M. Meindl, A. Albayrak, W. Polifke, A state-space formulation of a discontinuous Galerkin method for thermoacoustic stability analysis, J. Sound Vib. 481 (2020) 115431.
[60] Mechanical and Aerospace Engineering (Combustion Research) UCSD, Chemical-kinetic mechanisms for combustion applications, 2024, https://web.eng.ucsd.edu/mae/groups/combustion/mechanism.html. (Accessed 20 June 2024).
[61] CERFACS, H2 san diego, 2024, https://www.cerfacs.fr/cantera/docs/mechanisms/hydrogen-air/UCSD. (Accessed 20 June 2024).
[62] T. Poinsot, S.K. Lele, Boundary conditions for direct simulation of compressible viscous flows, J. Comput. Phys. 101 (1992) 104–129.
[63] F. Nicoud, K. Wieczorek, About the zero mach number assumption in the calculation of thermoacoustic instabilities, Int. J. Spray Combust. Dyn. 1 (2009) 67–111.
[64] M. Meindl, C.F. Silva, W. Polifke, On the spurious entropy generation encountered in hybrid linear thermoacoustic models, Combust. Flame 223 (2021) 525–540.

D.4 PAPER-NLEVP

The Nonlinear Thermoacoustic Eigenvalue Problem and Its Rational Approximations: Assessment of Solution Strategies

Moritz Merk[1]
Department of Engineering Physics and Computation,
TUM School of Engineering and Design,
Technical University of Munich,
Garching D-85747, Germany
e-mail: moritz.merk@tfd.mw.tum.de

Philip E. Buschmann
Department of Energy and Process Engineering,
Norwegian University of Science and Technology,
Trondheim 7034, Norway

Jonas P. Moeck
Department of Energy and Process Engineering,
Norwegian University of Science and Technology,
Trondheim 7034, Norway

Wolfgang Polifke
Department of Engineering Physics and Computation,
TUM School of Engineering and Design,
Technical University of Munich,
Garching D-85747, Germany

Nonlinear eigenvalue problems (NLEVPs) arise in thermoacoustics by considering the temporal evolution of small perturbations in the relevant governing equations. In this work, two solution strategies are compared: (i) a contour-integration-based method that guarantees to provide all eigenvalues in a given domain and (ii) a method that approximates the NLEVP by a rational eigenvalue problem (REVP), which is generally easier to solve. The focus lies on numerical speed, the completeness of the computed spectrum, and the appearance of spurious modes, i.e., modes that are not part of the original spectrum but appear as a result of the approximation. To this end, two prototypical thermoacoustic systems are considered: a single-flame Rijke tube and an annular model combustor. The comparison of both methods is preceded by a detailed analysis of the user-defined input parameters in the contour-integration-based method. Our results show that both methods can resolve all types of considered eigenvalues with sufficient accuracy for applications. However, the recast linear problem is overall faster to solve and allows a priori precision estimates—unlike the contour-integration-based method. Spurious modes as a by-product of the NLEVP approximation are found to play a minor role, and recommendations are given on how to eliminate them. [DOI: 10.1115/1.4055583]

1 Introduction

Modern low-emission gas turbines are susceptible to self-excited pressure oscillations that can damage the engine, limit its operating range or increase emissions [1]. These so-called thermoacoustic instabilities originate from an unstable feedback between pressure oscillations and unsteady heat release. Designing a stable gas turbine is imperative to ensure low emissions and a stable operation. Hence, efficient and accurate numerical tools are required to aid and accelerate the design process by predicting the thermoacoustic stability of combustion chambers.

Several modeling strategies have been proposed to predict thermoacoustic stability. These strategies differ according to the number of assumptions inherent to them. In general, models with fewer assumptions predict instabilities more accurately, but demand a higher computational cost. Large eddy simulations [2,3] model the underlying physics with high accuracy, but are prohibitively expensive for parameter studies. Models based on linearization of the conservative equations represent an attractive tradeoff between costs and accuracy. A large parameter space can be explored by using them. Listed by increasing number of assumptions, these are the linearized reactive flow equations (LRF) [4], linearized Navier–Stokes equations (LNSE) [5,6], linearized Euler equations (LEE) [7], or the thermoacoustic Helmholtz equation [8]. Most simplified are low-order network models, which assume one-dimensional waves [9–11].

All of the linearized methods have in common that, after a discretization and closure with necessary input data, a so-called nonlinear eigenvalue problem (NLEVP) is obtained

$$\mathbf{L}(s)\mathbf{v} = 0, \quad \mathbf{v} \neq \mathbf{0} \tag{1}$$

The operator $\mathbf{L}$ represents the discretized problem and solutions are the eigenpairs $(s, \mathbf{v})$. The set of eigenvalues forms the spectrum $\Sigma = \{s_1, s_2, \ldots\}$. Here, $s \in \mathbb{C}$ is the Laplace variable with the growth rate $\mathrm{Re}(s)$ and angular frequency $\mathrm{Im}(s)$. Stability of a combustion chamber is given if for all eigenvalues $\mathrm{Re}(s) < 0$. The mode shape $\mathbf{v}$ is needed to determine where to effectively place acoustic dampers [12]. $\mathbf{L}$ depends nonlinearly on the eigenvalue s and linearly on $\mathbf{v}$. The number of eigenpairs is potentially infinite, and hence only a subset is sought. Eigenvalues in thermoacoustic applications can be of simple, semi-simple [13], or defective [14] type.

2 NLEVPs Include the Linear Eigenvalue Problem (LEVP)

$$\mathbf{L}(s)\mathbf{v} = (\mathbf{A} - s\mathbf{I})\mathbf{v} = 0 \iff \mathbf{A}\mathbf{v} = s\mathbf{v} \tag{2}$$

as a special case, but are significantly harder to solve since they do not exhibit a closed form solution and the dependence on s is highly problem-specific—solution methods are tailored to the problem at hand [15,16]. Three main strategies have been employed in the thermoacoustic field: iterative methods [8,17], contour integration methods [18], and methods based on approximations of $\mathbf{L}(s)$ which eliminate the nonlinear dependency on s. Thermoacoustic state-space models [6,9–11] correspond to this last approach. Related is the Nyquist criterion [19], which only assesses stability but does not provide the mode shape $\mathbf{v}$.

Any such method must—at a minimum—return all relevant eigenpairs. Since, the number of eigenpairs is (potentially) infinite not all can be computed. Moreover, only modes at low frequencies ($\lesssim$2.5 kHz) are usually considered relevant, since these are observed in experiments. For every combustor, an individual cut-off frequency has to be chosen depending on the geometrical dimensions and operating conditions.

Iterative methods require an initial guess for every eigenvalue inside the corresponding basin of attraction. However, an unknown number of eigenvalues, different sizes and shapes of basin of attractions and the lack of a general methodology on how

[1]Corresponding author.

Manuscript received July 12, 2022; final manuscript received July 28, 2022; published online December 13, 2022. Editor: Jerzy T. Sawicki.

to choose these initial guesses usually result in the computation of an incomplete spectrum [17,18]. Contour integration permits to specify an arbitrary domain in the complex plane in which all eigenpairs are found—in theory. In practice, the computation of an accurate and complete spectrum depends on user-defined parameters. The method performs well for thermoacoustic problems [18]. Finally, NLEVPs can be replaced with an NLEVP of a simpler structure, such as a rational eigenvalue problem (REVP). The REVP is still nonlinear in s but has the favorable property that it can be recast into a LEVP of higher dimension. This permits to use well-established LEVP solution methods [20]. However, the introduced approximation will alter the spectrum.

Assume that an operator $\mathbf{L}(s)$ with spectrum Σ is approximated by an operator $\tilde{\mathbf{L}}(s)$ with associated spectrum $\tilde{\Sigma}$. Formally [16], one would require that

$$\max_{s\in\tilde{\Sigma}} ||\mathbf{L}(s) - \tilde{\mathbf{L}}(s)||_2 \leq \varepsilon \tag{3}$$

needs to hold for $\tilde{\mathbf{L}}(s)$ to approximate $\mathbf{L}(s)$ well, where ε is the acceptable tolerance. The criterion is violated if $\tilde{\Sigma}$ contains eigenvalues that are not in Σ—the *spurious* eigenvalues. Conversely, $\tilde{\Sigma}$ is *incomplete* if it does not contain all eigenvalues of Σ—a potentially catastrophic case for thermoacoustic stability analysis.

This work addresses two principle points: (i) investigate the role of user-defined parameters in the contour integration method with respect to convergence and (ii) establish how and if the spectrum is polluted by spurious solutions when a thermoacoustic NLEVP is transformed into an REVP. The objective is to give recommendation if, from the point of computational cost, the nonlinear dependence in an NLEVP should be retained or if the less costly REVP strategy can be pursued without a loss in precision.

In Sec. 2, the NLEVP of the thermoacoustic Helmholtz equation is formulated. Sources of the nonlinear dependence on s are reviewed. In Sec. 3 the contour integration method is introduced from a so-called filtering perspective, which will assist in the subsequent analysis of the role of user-defined input parameters in the latter half of the section. In Sec. 4, the approximation of the NLEVP via a REVP is compared to the contour-integration-based method. Special focus is placed on the occurrence of spurious modes and the completeness of the computed spectrum. Conclusions and implications for future work are given in Sec. 5.

3 The Thermoacoustic Nonlinear Eigenvalue Problem

In this work, the NLEVP of the thermoacoustic Helmholtz equation is considered, but the findings generalize to LEE, LNSE and, in case of frequency dependent boundary conditions, to LRF models. The equation [8] reads in Laplace space

$$s^2\hat{p} - \nabla\cdot(\bar{c}^2\nabla\hat{p}) = s(\gamma-1)\hat{q} \tag{4}$$

where $\hat{p}$ and $\hat{q}$ are the Laplace-transformed pressure and heat-release rate fluctuation, respectively, and s is the Laplace variable. Physical parameters are the mean speed of sound field $\bar{c}$ and the ratio of specific heats γ. Boundary conditions are defined in terms of s-dependent impedances $\mathscr{Z}(s)$

$$\bar{c}\,\mathscr{Z}(s)\nabla\hat{p}\cdot\mathbf{n} + s\hat{p} = 0 \tag{5}$$

Equation (4) is closed by expressing $\hat{q}$ in terms of s and $\hat{p}$, by means of a flame transfer function (FTF)

$$\frac{\hat{q}}{\bar{q}} = \mathscr{F}(s)\left(\frac{\hat{\mathbf{u}}\cdot\mathbf{n}}{\bar{\mathbf{u}}\cdot\mathbf{n}}\right)_{\text{ref}} = -\frac{1}{s}\mathscr{F}(s)\left(\frac{\nabla\hat{p}\cdot\mathbf{n}}{\bar{\rho}(\bar{\mathbf{u}}\cdot\mathbf{n})}\right)_{\text{ref}} \tag{6}$$

where $\bar{\rho}$ and $\bar{\mathbf{u}}$ are the mean density and velocity, respectively. The FTF relates $\hat{q}$ to an upstream velocity fluctuation $\hat{\mathbf{u}}$ at a reference position and in a reference direction $\mathbf{n}$.

Equation (4) can be discretized using a finite element or finite volume method to account for the complex three-dimensional geometries in combustion chambers. The discrete NLEVP reads

$$\underbrace{\left[s^2\mathbf{M} + \mathbf{K} + \sum_{i=1}\frac{s}{\mathscr{Z}_i(s)}\mathbf{Z}_i + \sum_{k=1}\mathscr{F}_k(s)\mathbf{Q}_k\right]}_{\mathbf{L}(s)}\mathbf{v} = 0 \tag{7}$$

Here, $\mathbf{M}$ and $\mathbf{K}$ are the mass and stiffness matrix, respectively. Matrices $\mathbf{Z}_i$ belong to boundaries i with prescribed impedances $\mathscr{Z}_i$. Similarly, matrices $\mathbf{Q}_k$ belong to a heat-release zone k with a prescribed FTF $\mathscr{F}_k(s)$.

The quadratic coefficient of $\mathbf{M}$ only occurs in the thermoacoustic Helmholtz equation due to the second-order time-derivative in the time-domain equation. The term is linear in s for LRF, LNSE, or LEE models. Furthermore, no transfer functions $\mathscr{F}_k$ are needed for LRF models. The dimension d of $\mathbf{L}$ depends on the chosen discretization method but is approximately $10^3 - 10^6$ for industrial-sized configurations.

In Eq. (7) boundary impedances $\mathscr{Z}_i(s)$ and FTFs $\mathscr{F}_k(s)$ are the two principle sources of nonlinearity and suitable expressions need to be obtained for these. Hereby, a number of difficulties arise. Consider an FTF that is obtained from the forcing of a flame at discrete frequencies and is, hence, only known for a set of purely imaginary s. In order to describe how a complex-valued eigenvalue s responds to the forcing/attenuation effect of the flame in an NLEVP model, the FTF needs to be extrapolated into the complex plane. Several methods are available to achieve this. A distribution of time delays can describe the response of a flame to initial perturbations in a natural way [21]—yielding a transcendental function that is defined in all of $\mathbb{C}$. Without making any assumptions on the distribution of the time delays τ_j, the distributed time delay (DTD) model takes the form

$$\mathscr{F}(s) = \sum_{j=0}^{\infty} h_j\exp(-s\tau_j) \tag{8}$$

The simplest representative of this model type with a single time delay is the n–τ model [22]. Besides Eq. (8), slightly modified versions of DTD models with presumed functional forms of time delay distribution were proposed, e.g., Komarek and Polifke [23] and Æsøy et al. [24]. The unknown parameters of the DTD models are usually retrieved from numerical computations or experimental measurements [25,26]. An extensive discussion about DTD models can be found in the review of Polifke [21]. Alternatively, rational approximation procedures are applied to fit the discrete frequency response data [26]. A numerical procedure called *vector fitting* [27] will be employed later in this work.

For the boundary impedances $\mathscr{Z}_i(s)$ DTD formulations can be obtained via measurements or simulations as well. Furthermore, analytic formulations derived from first principles [28,29] are available—which might not be defined only for parts of $\mathbb{C}$. For laboratory test rigs with open/closed ends or chocked nozzles, simple, frequency independent impedances are usually sufficient [30]—as is the case in this work and FTFs are considered as the only sources of nonlinearities in the eigenvalue.

4 Shortcomings in the Contour Integration Method Explained From the Filtering Perspective

Buschmann et al. [18,31] employed Beyn's method [32] to solve thermoacoustic NLEVPs. In this section, the method is introduced from the filtering perspective [33] to aid in a later analysis. This work only focuses on Beyn's "Integral Algorithm 1" for large-scale NLEVPs originating from multidimensional spatial discretizations.

4.1 Analytical Description of Beyn's Method.

Keldysh [34] proved that a unique expansion of the resolvent $\mathbf{L}(z)^{-1}$ in terms of the left (adjoint) and right eigenvectors $\mathbf{w}$ and $\mathbf{v}$, and of the form

$$\mathbf{L}(z)^{-1} = \sum_{k=1}^{n} \mathbf{v}_k \mathbf{w}_k^H \frac{1}{(z - s_k)} + \mathbf{R}(z) \tag{9}$$

exists, if $\mathbf{L}(z)$ depends analytically on $z \in \mathbb{C}$. Here, n is the unknown number of eigenvalues, which can be infinite. $\mathbf{R}(z)$ is an unknown matrix-valued holomorphic function.

Next, Beyn utilizes Keldysh's theorem (9) and integrates $\mathbf{L}^{-1}(z)$ over a closed contour $\Gamma \subset \mathbb{C}$

$$\begin{aligned}\oint_\Gamma \mathbf{L}(z)^{-1} \mathrm{d}z = &\oint_\Gamma \sum_{k:s_k \in o(\Gamma)} \mathbf{v}_k \mathbf{w}_k^H \frac{1}{(z - s_k)} \mathrm{d}z \\ &+ \oint_\Gamma \sum_{k:s_k \notin o(\Gamma)} \mathbf{v}_k \mathbf{w}_k^H \frac{1}{(z - s_k)} \mathrm{d}z \\ &+ \oint_\Gamma \mathbf{R}(z)\, \mathrm{d}z \end{aligned} \tag{10}$$

where the sum in Eq. (9) has been split into the set of eigenvalues s_k located inside Γ, denoted as $o(\Gamma)$, and those outside of Γ. Recalling Cauchy's theorem from analytic function theory [35], the second and third term in Eq. (10) become zero. The first term can be simplified further and the integral reduces to

$$\oint_\Gamma \mathbf{L}(z)^{-1} \mathrm{d}z = 2\pi i \sum_{k=1}^{n(\Gamma)} \mathbf{v}_k \mathbf{w}_k^H \tag{11}$$

where $n(\Gamma)$ is the unknown number of eigenvalues inside of Γ. Next, we define the pth moment matrix

$$\mathbf{A}_p = \frac{1}{2\pi i} \oint_\Gamma z^p \mathbf{L}(z)^{-1} \mathrm{d}z = \mathbf{V} \mathbf{\Lambda}^p \mathbf{W}^H \in \mathbb{C}^{d \times d} \tag{12}$$

with the matrices of left and right eigenvectors $\mathbf{W} = [\mathbf{w}_1, \ldots, \mathbf{w}_{n(\Gamma)}] \in \mathbb{C}^{d \times n(\Gamma)}$ and $\mathbf{V} = [\mathbf{v}_1, \ldots, \mathbf{v}_{n(\Gamma)}] \in \mathbb{C}^{d \times n(\Gamma)}$. $\mathbf{\Lambda} \in \mathbb{C}^{n(\Gamma) \times n(\Gamma)}$ denotes the diagonal matrix of the eigenvalues s_k.

For spatially discretized problems, the number of eigenvalues inside the contour $n(\Gamma)$ will usually be much smaller than the problem dimension. Therefore, a full inversion of $\mathbf{L}$ is avoided by solving instead the smaller problem $\mathbf{L}^{-1}\tilde{\mathbf{V}}$ with a random matrix $\tilde{\mathbf{V}} \in \mathbb{C}^{d \times l}$, with the reduced rank $l \ll d$. Thus,

$$\tilde{\mathbf{A}}_p = \frac{1}{2\pi i} \oint_\Gamma z^p \mathbf{L}(z)^{-1} \tilde{\mathbf{V}} \mathrm{d}z = \mathbf{V} \mathbf{\Lambda}^p \mathbf{W}^H \tilde{\mathbf{V}} \in \mathbb{C}^{d \times l} \tag{13}$$

Note that the dimension of $\tilde{\mathbf{V}}$ has to be chosen in a way that it holds that $l > n(\Gamma)$. However, since $n(\Gamma)$ is unknown a priori, l has to be estimated. According to Beyn [32], the precise choice of $\tilde{V}$ is not relevant as long as $\mathbf{W}^H\tilde{\mathbf{V}}$ has full rank. The contour integral is discretized with a quadrature formula to yield

$$\tilde{\mathbf{A}}_p \approx \sum_{j=1}^{N} \alpha_j z_j^p \mathbf{L}(z_j)^{-1} \tilde{\mathbf{V}}, \quad p = 0, 1 \tag{14}$$

Solving Eq. (14) is the main numerical effort of Beyn's algorithm. It necessitates the computation of N LU-decompositions of the N operators $\mathbf{L}(z_j)$ and the subsequent solution of Nl linear systems. However, it is easily parallelizable due to the independence of all N operators from one another.

Once the moment matrices in Eq. (14) are assembled, a singular value decomposition (SVD) of $\tilde{\mathbf{A}}_0$ yields

$$\tilde{\mathbf{A}}_\mathbf{0} = \mathbf{V} \mathbf{W}^H \tilde{\mathbf{V}} = \mathbf{V}_\mathbf{0} \mathbf{\Sigma}_\mathbf{0} \mathbf{W}_\mathbf{0}^H \tag{15}$$

In $\mathbf{\Sigma_0}$, all singular values (and associated vectors in $\mathbf{V_0}$ and $\mathbf{W_0}$) below a threshold tol_σ are removed. This is because if the integral in Eq. (13) is evaluated analytically and $l > n(\Gamma)$, then Σ_0 contains $l - n(\Gamma)$ singular values of value zero. Since the integral is only approximated in Eq. (14) these are nonzero and need to be removed. Otherwise, $l - n(\Gamma)$ spurious modes occur in the latter computation. Consequently, each eigenpair has to be double-checked. This can be done via the residual [32] or a subsequent fixed point iteration [18].

Finally, $\tilde{\mathbf{A}}_\mathbf{1}$ and the SVD of $\tilde{\mathbf{A}}_\mathbf{0}$ in Eq. (15) are used to define a new matrix $\mathbf{D}$ as

$$\mathbf{D} := \mathbf{V}_\mathbf{0}^H \tilde{\mathbf{A}}_\mathbf{1} \mathbf{W}_\mathbf{0} \mathbf{\Sigma}_\mathbf{0}^{-1} = (\mathbf{V}_\mathbf{0}^H \mathbf{V}) \mathbf{\Lambda} (\mathbf{V}_\mathbf{0}^H \mathbf{V})^{-1} \tag{16}$$

For the specific algebraic reformulations, see Ref. [32]. The right-hand side of Eq. (16) is an eigendecomposition of $\mathbf{D}$, where $\mathbf{\Lambda}$ contains the same eigenvalues as $\mathbf{L}(z)$ in Γ. The eigenvectors $\mathbf{v}_k \in \mathbb{C}^d$ of $\mathbf{L}$ can be computed directly from the eigenvectors $\mathbf{b}_k \in \mathbb{C}^l$ of $\mathbf{D}$ via

$$\mathbf{v}_k = \mathbf{V_0} \mathbf{b}_k \tag{17}$$

Since $\mathbf{D} \in \mathbb{C}^{l \times l}$, the computation of its eigenvalues and eigenvectors is cheap. Clearly, user input is required at several points during the numerical computation, namely,

(1) dimension l of matrix $\tilde{\mathbf{V}}$ needs to be set,
(2) a contour Γ has to be prescribed,
(3) a number of sampling points N on Γ have to be specified and
(4) an SVD cutoff tol_σ needs to be defined.

Any of these parameters affects the computed eigenpairs, as will be detailed next.

4.2 Beyn's Method: Filtering a Portion of the Spectrum. Multiplying Keldysh's theorem, Eq. (9), with $\tilde{\mathbf{V}}$ from the right and inserting it into Eq. (14) gives

$$\tilde{\mathbf{A}}_p = \sum_{k=1}^{n} \mathbf{v}_k \mathbf{w}_k^H \tilde{\mathbf{V}} \sum_{j=1}^{N} \frac{\alpha_j z_j^p}{z_j - s_k} + \sum_{j=1}^{N} \alpha_j z_j^p \mathbf{R}(z_j) \tilde{\mathbf{V}}, \quad p = 0, 1 \tag{18}$$

Following van Barel and Kravanja [33], the function

$$b_p(z) = \sum_{j=0}^{N} \frac{\alpha_j z_j^p}{z_j - z} \quad p = 0, 1 \tag{19}$$

is called a filter function (of order p) and depends on the applied quadrature formula, see Eq. (14). In the limit $N \to \infty$, it becomes identical to the ideal filter

$$b_{p,\mathrm{ideal}}(z) = \begin{cases} 1, & z \text{ inside } \Gamma \\ 0, & z \text{ outside } \Gamma \end{cases} \tag{20}$$

which would be achieved by analytically solving the integral in Eq. (12). Clearly, $b_p(z)$ depends on the number of sampling points (via N) and the chosen integration method (via the integral weights α_j).

Figure 1 shows $b_0(z)$ on the imaginary axis for a circular contour $\Gamma = z_0 + R\exp(i\varphi)$ and different numbers of N. The higher N, the narrower the filter function and the better the filtering effect. If there are eigenvalues inside the tails, then these impact the computational result—they are not filtered out completely. Eigenvalues far distant from the contour have no impact.

It is important to note that $b_p(z)$ is independent of the problem size d and the parameter l. Hence, the filtering effect is solely dependent on N and the specified contour Γ. As Fig. 1 shows, the tails of the filter function can be wide and potentially include a significant number of eigenvalues outside of Γ.

4.3 Rijke Tube With Almost Defective Eigenvalue. The Rijke tube investigated in this section is two-dimensional and

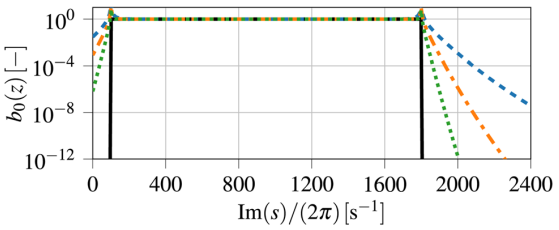

Fig. 1 Filter function $b_0(z)$ of a circular contour ($(z_0/2\pi i) = 950\,\mathrm{s}^{-1}$, $(R/2\pi) = 850\,\mathrm{s}^{-1}$) along the imaginary axis: analytic contour integration ($N\to\infty$, ——) and $N = 32$ (- - -), $N = 64$ (- - -), and $N = 128$ (·····) quadrature points

depicted in Fig. 2. The model is chosen since it exhibits several features of single-flame combustors and its parameters can be chosen such that two simple eigenvalues in close proximity almost form a defective eigenvalue. It is then of interest if contour integration has convergence difficulties for such an almost defective eigenvalue pair since it nearly violates the full rank assumption intrinsic to Eq. (13). An exactly defective eigenvalue cannot be attained numerically due to round-off errors [14]. The tube is $L = 0.5\,\mathrm{m}$ long and has a diameter of $a = 0.025\,\mathrm{m}$. A heat source of thickness $d_{\mathrm{fl}} = 0.1\,\mathrm{mm}$ is located in the middle of the tube and causes a temperature increase from $T_u = 300\,\mathrm{K}$ to $T_b = 1200\,\mathrm{K}$. The acoustic response of the heat source is modeled via an n–τ model [22]

$$\mathscr{F}(s) = n\exp(-s\tau) \tag{21}$$

The reference point lies infinitesimally upstream of the heat source in the cold zone. The gas properties are taken as those of air. At the inlet a pressure antinode ($\mathscr{Z}_{\mathrm{in}} = \infty$) and at the outlet a pressure node ($\mathscr{Z}_{\mathrm{out}} = 0$) are prescribed. The Rijke tube is discretized in FEniCS [36] with 9848 cells using a first-order continuous Galerkin finite element scheme resulting in $d = 4801$ degrees-of-freedom (DOF) of $\mathbf{L}$. The subsequent contour integration is performed with the Python script of Buschmann et al. [18] calling standard linear algebra routines from *scipy* [37] and *numpy* [38].

To investigate the convergence behavior of Beyn's method with an increasing number of quadrature points N, the algorithm is setup to find all eigenpairs inside a circle of radius $(R/2\pi) = 850\,\mathrm{s}^{-1}$ centered at $(z_0/2\pi i) = 950\,\mathrm{s}^{-1}$ (as in Buschmann et al. [18]). The flame parameters are set to $n = 0.6012354766306677$ and $\tau = 2.1769913269101874\,\mathrm{ms}$ such that two simple eigenpairs form almost a defective one inside Γ. The number of eigenvalues inside the contour was estimated to $l = 12$ and $\mathrm{tol}_\sigma = 10^{-10}$ is used. To obtain a reference solution, a highly resolved contour integration with $N = 500$ quadrature points is performed. Then, the results are refined by a fixed-point iteration with a tolerance on the residual of $\leq 10^{-12}$. The computed reference eigenvalues s_{ref} are listed in Table 1. The Rijke tube features modes of intrinsic (s_1, s_3, s_6 and s_7) and acoustic (s_2, s_4, s_5 and s_8) origin.

In the following, N is increased from 20 to 120 with an increment of 4. In Fig. 3, the accuracy of the eigenvalues of each computation are expressed in terms of the relative deviation of the eigenvalue s from the reference solution s_{ref}

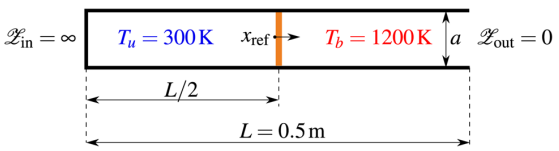

Fig. 2 Schematic depiction of the Rijke tube with chosen parameters and boundary conditions

Table 1 Reference eigenvalues s_{ref} of the Rijke tube inside a circular contour Γ of radius $(R/2\pi)=850\,\mathrm{s}^{-1}$ centered at $(z_0/2\pi i)=950\,\mathrm{s}^{-1}$

	$\frac{\mathrm{Im}(s)}{2\pi}$ [s^{-1}]	$\frac{\mathrm{Re}(s)}{2\pi}$ [s^{-1}]	Type
s_1	126.32	−102.66	Simple
s_2	295.28	50.07	Simple
s_3	692.812	−3.797	Almost defective
s_4	692.815	−3.798	
s_5	1090.63	49.23	Simple
s_6	1258.84	−97.08	Simple
s_7	1511.41	−107.88	Simple
s_8	1681.60	50.46	Simple
s_9[a]	2067.65	−3.04	Simple
s_{10}[a]	2089.74	−4.47	Simple

[a]denotes eigenvalues in the close proximity but outside of Γ.

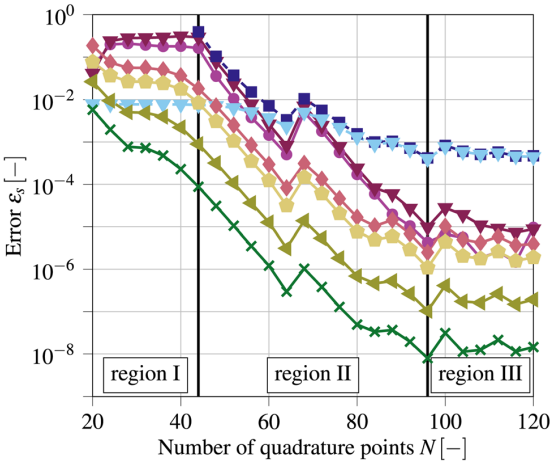

Fig. 3 Convergence of Beyn's method for the Rijke tube test case in dependence of the number of quadrature points expressed via the residual deviation of eigenvalues from the reference result with simple eigenvalues (—● s_1, —▼ s_2, —◆ s_5, —● s_6, —◀ s_7, —✕ s_8) and (almost) defective eigenvalues (- -■ s_3, - -▼ s_4)

$$\varepsilon_s = \frac{|s - s_{\mathrm{ref}}|}{|s_{\mathrm{ref}}|} \tag{22}$$

The convergence of Beyn's method can be split in three regions. In region I ($N < 44$), Beyn's method computes an incomplete spectrum with the eigenvalue s_3 missing. However, since unidentified eigenvalues inside the contour impact the accuracy of all other eigenpairs, no convergence can be observed in this region. This changes in region II starting from $N \geq 44$, when Beyn's method is able to identify all eight eigenvalues inside Γ. Increasing N from now on leads to a decrease in ε_s. In the final region III ($N \geq 96$), an increase in quadrature points no longer improves ε_s. Especially, the eigenvalues s_3 and s_4, forming the almost defective pair, show poor accuracy levels of $\varepsilon_s \approx \mathcal{O}(10^{-3} - 10^{-4})$ even for high N, whereas the simple eigenvalues achieve $\varepsilon_s \approx \mathcal{O}(10^{-5} - 10^{-8})$.

In region II ($44 \leq N \leq 96$), an interesting effect can be observed: increasing the number of quadrature points from $N = 64$ to $N = 68$ reduces the accuracy ε_s of all eigenvalues by approximately one order of magnitude and this phenomenon can be explained by the role of the filter function. Figure 4(*a*) shows the pole map for the reference solution and the cases $N = 64$ and

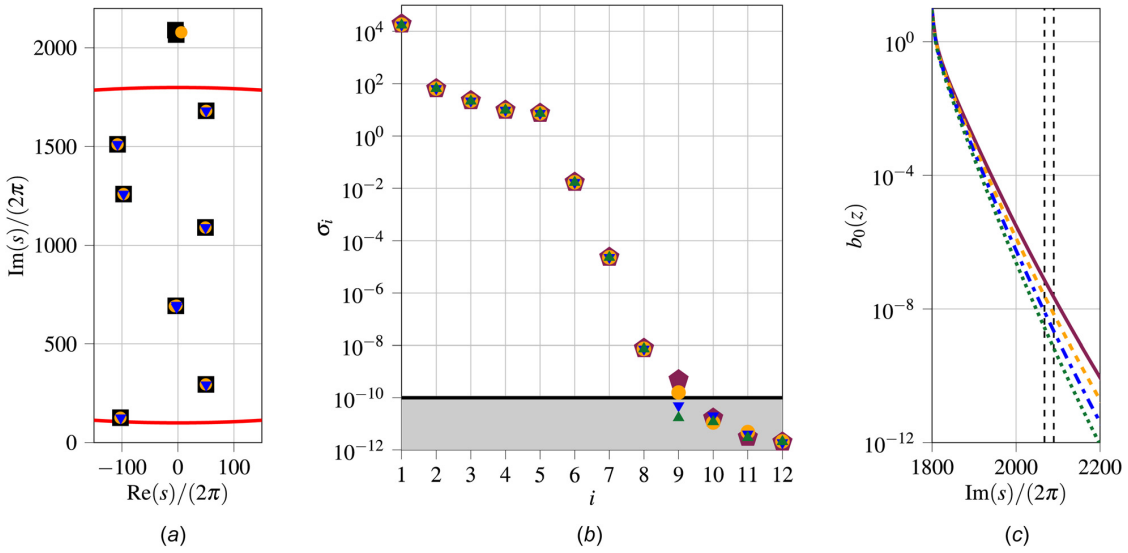

Fig. 4 (*a*) **Polemap of the Rijke tube test case inside and in close proximity to the contour — Γ. Displayed is the ■ reference solution and the eigenvalues computed with Beyn's method with ● $N = 64$ and ▼ $N = 68$. (*b*) Singular values σ_i computed for the Rijke tube test case with ⬟ $N = 60$, ● $N = 64$, ▼ $N = 68$, and ▲ $N = 72$ as well as — $\mathrm{tol}_\sigma = 10^{-10}$. (*c*) Tail of the filter function of the Rijke tube test case for — $N = 60$, - - - $N = 64$, -·- $N = 68$, and ····· $N = 72$. Eigenvalues s_9^* and s_{10}^* are located at - - -.**

$N = 68$. For $N = 64$ Beyn's method returns nine eigenvalues, where the ninth one is located outside of Γ and relates to s_9^* and s_{10}^*. The ninth eigenvalue is not obtained with $N = 68$. The reason is shown in Fig. 4(*b*). By increasing $N = 64$ to $N = 68$, the singular value σ_9 crosses the threshold of $\mathrm{tol}_\sigma = 10^{-10}$ and is therefore neglected. However, the filter function in Fig. 4(*c*) shows that s_9^* and s_{10}^* are located just inside the tails and hence not fully damped out. A decrease in accuracy is the consequence: negligence of a physical eigenvalue with a significant contribution in the applied filter decreases the accuracy of all eigenvalues.

The eigenvectors feature an analogous convergence pattern including regions I–III and a jump between $N = 64$ and $N = 68$. At $N = 72$, the maximum local deviation in absolute value is below $<0.17\%$ and the principal angle to the reference eigenspace is $<4 \times 10^{-3}$ rad. Figure 5 displays the real part of the eigenvectors of s_2, s_3, s_4, and s_8. As expected, the eigenvectors corresponding to the almost defective eigenvalue pair, s_3 and s_4, are not distinguishable by eye.

4.4 MICCA Annular Model Combustor. Annular combustion chambers exhibit a higher mode density than single-flame combustors and, in addition, clusters of intrinsic modes [18]. This increases the chances of a high number of modes in the vicinity of a contour Γ, which could adversely effect the quality of the numerical results of contour integration. To illustrate these effects, the MICCA combustor [39,40] at EM2C (CentraleSupélec) with 16 matrix burners is considered. See Fig. 6 for geometrical dimensions and boundary conditions. A rotationally symmetric mesh with 107,264 cells is discretized with FEniCS [36] using a first-order continuous Galerkin finite element method to yield 21,712DOF.

A discrete FTF is extracted from the experimental flame describing function of Laera et al. [41] (operating condition B ibid.) by taking the values with a forcing amplitude of $u'/\bar{u} = 0.1$. The data is fitted to a DTD model

$$\mathscr{F}_{\mathrm{DTD}}(s) = \sum_i^2 \mathrm{F}_i^+ + \mathrm{F}_i^-, \text{ with}$$
$$\mathrm{F}_i^\pm = \frac{g_i}{2} \exp\left(\frac{1}{2}(is \pm \beta_i)^2 \sigma_i^2 - s\tau_i\right) \tag{23}$$

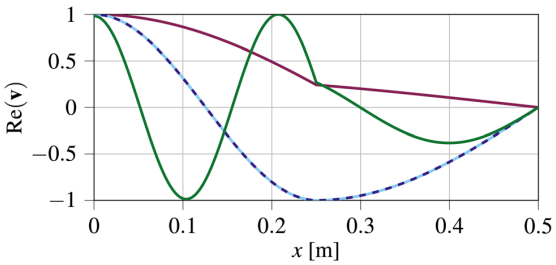

Fig. 5 Real part of reference eigenvector Re(v) along the central line of the Rijke tube for the simple eigenvalues — s_2 and — s_8 and the almost defective eigenvalues — s_3 and - - - s_4. The eigenvectors are scaled to $max|v| = 1$.

$l_{corr} = 41\,mm$
$l_{cc} = 200\,mm$
$l_{pp} = 6\,mm$
$l_b = 14\,mm$
$l_p = 70\,mm$
$l_f = 6\,mm$
$h_{cc} = 50\,mm$
$h_p = 70\,mm$
$d_f = 36\,mm$
$d_{pp} = 18.9\,mm$
$d_b = 33\,mm$
$r_p = 140\,mm$

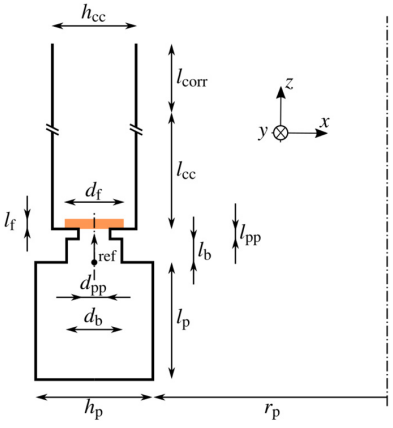

Fig. 6 Cut view of a single burner of the MICCA combustor, including the plenum (*p*), burner (*b*), perforated plate (pp), flame (*f*), combustion chamber (cc), and end correction (corr). Boundaries are set to rigid walls ($\mathscr{Z} = \infty$), except the outlet where $\mathscr{Z} = 0$ is applied.

Table 2 Parameters for the DTD model Eq. (23)

I	g_i	$\frac{\beta_i}{2\pi} \times 10^{-3}$	$\sigma_i \cdot (2\pi \times 10^4)$	τ_i (ms)
1	5.7761	4.1223	6.7446	1.6
2	1.6345	0.3094	36.00	1.2

g_i, β_i, σ_i, and τ_i are the amplitude, a modulating term of the frequency, the standard deviation, and a time delay, respectively.

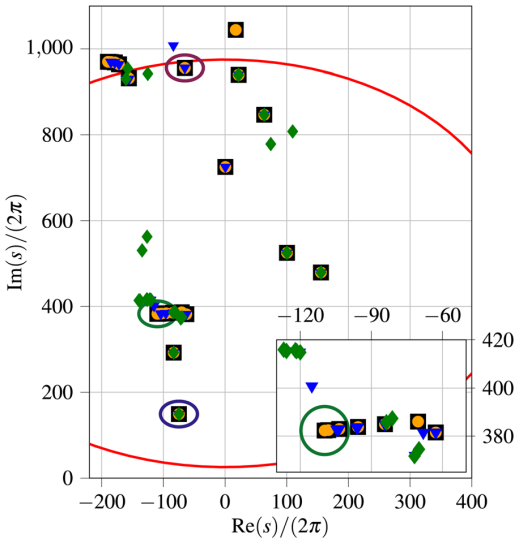

Fig. 7 Pole map of the MICCA burner inside and in close proximity to — Γ which is a circle with $(R/2\pi) = 475\,\mathrm{s}^{-1}$ and center $(z_0/2\pi i) = 500\,\mathrm{s}^{-1}$. Displayed is the ■ reference solution and the results computed with ♦ $l = 28$, ▼ $l = 35$, and ● $l = 40$ for $N = 40$. The small circles —, — and — mark the eigenvalues for which the convergence plot is displayed in Fig. 8.

as proposed by Æsøy et al. [24]. The values of the parameters g_i, β_i, σ_i, and τ_i are listed in Table 2. $\mathscr{F}_{\mathrm{DTD}}(s)$ is a transcendental, nonlinear function of s and defined in all of $\mathbb{C}$. Since the parameters can be attributed to physical mechanisms [21,42], the fit in Eq. (23) will be used as a reference analytical FTF in this work.

Figure 7 shows the reference solution inside and in the vicinity of a contour Γ. The solution is obtained in the same way as in the previous Rijke tube case. Within the depicted circle, 16 eigenvalues are located: four simple and 12 degenerate ones. The sum over all geometric multiplicities is 28; hence, none of the degenerate eigenvalues is defective. In Beyn's method, the reduced rank l has to be set larger than this sum. In the following, the number of eigenvalues is understood to be the sum over all geometric multiplicities. The contour is nearly identical to the one employed by Buschmann et al. [31]. One cluster (at approx. 400 Hz) is entirely within Γ while a second one (at approx. 970 Hz) is intersected by Γ. Including the eigenvalues just outside of Γ, the total sum over all geometric multiplicities is 39. We refer to Buschmann et al. [18] for the physical origin—intrinsic or acoustic—of the eigenvalues.

For a fixed number of sampling points $N = 40$ and with $\mathrm{tol}_\sigma = 0$, three computations with $l = 28$, $l = 35$, and $l = 40$ are performed. For $N = 40$ sampling points, the numerical filter contains all 39 eigenvalues. Hence, $l = 28$ and $l = 35$ are insufficient to account for all 39 eigenvalues and major inaccuracies in the eigenvalues are observed, as Fig. 7 shows. Only for $l = 40$ is the full spectrum inside Γ and the eigenvalues just outside returned.

Figure 7 also shows that some eigenvalues are computed accurately even with an insufficient reduced rank l. Figure 8 contains a convergence plot for three selected eigenvalues, marked in Fig. 7, for $l = 28$, 35, and 40 as N is increased. It can be seen that the eigenvalues show different behaviors: for $l = 35$ two eigenvalues (left and right in Fig. 8) converge quickly to an accuracy below 10^{-9}, but the third converges very slowly. The result is not depicted, but $N \approx 80$ ($N \approx 350$) is necessary to push the error ε_s below 10^{-2} (10^{-9}) for all eigenvalues with $l = 35$. Moreover, the convergence plot shows that the precision levels for a certain number of sampling points—no higher precision can be obtained by using contour integration alone. If $l = 28$ is employed, the number of sampling points necessary increases to $N \approx 124$ to push the error ε_s below 10^{-2}, and $N \approx 500$ for an error below 10^{-9}. The different behaviors are not connected to the mathematical type—simple or semi-simple—of the eigenvalues.

The error in terms of local absolute value of the eigenvectors are for $l = 28$, $l = 35$, and $l = 40 < \mathscr{O}(10^{-2})$ when $\varepsilon_s \leq \mathscr{O}(10^{-2})$. However, the maximal principal angle between the reference and the computed eigenspace converge even slower. If one requires a maximum angle of $\leq 0.01\pi$, $l = 35$ and $l = 28$ require $N = 120$ and $N = 184$. For $l = 40$, $N = 24$ is sufficient. Figure 9 displays one eigenvector in the reference degenerate eigenspace of the reference solution at $s/(2\pi) = (-65.2 + 955.8i)\,\mathrm{s}^{-1}$.

4.5 Interplay of the User Input Parameters. The results from Secs. 3.3 and 3.4 show that the contour cannot be understood as a sharp line, but rather as a broader strip due to the filtering effect. The presence of nonzero singular values is primarily due to eigenvalues close to the contour and an insufficient reduced rank l; the effect of a low number of quadrature points N is only secondary. Hence, rather than increasing N, it is better to keep all

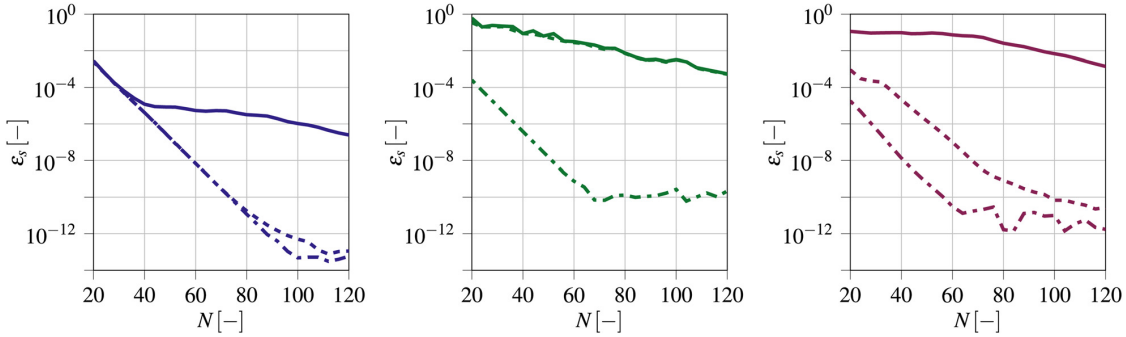

Fig. 8 Convergence of Beyn's method for the MICCA test case. Plotted are three different eigenvalues at $s/(2\pi) = (-74.6 + 148.9i)\,\mathrm{s}^{-1}$ (left), $s/(2\pi) = (-109.7 + 382.3i)\,\mathrm{s}^{-1}$ (center) and $s/(2\pi) = (-65.2 + 955.8i)\,\mathrm{s}^{-1}$ (right) and for — $l = 28$, - - - $l = 35$, and - - - $l = 40$. The corresponding eigenvalues are marked in Fig. 7.

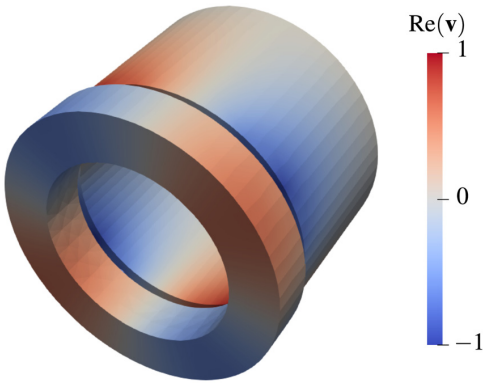

Fig. 9 Real part of an eigenvector v in the degenerate reference eigenspace at $s/(2\pi) = (-65.2+955.8i)\,\mathrm{s}^{-1}$. The eigenvector is scaled to $max|\mathbf{v}| = 1$.

Table 3 Choice of user-input parameters of Beyn's method for the Rijke tube and the MICCA cases to achieve an accuracy $\varepsilon_s \leq 10^{-2}$ for all eigenvalues and wall-clock time

Test case	l	N	tol_σ	t (s)
Rijke	12	72	10^{-10}	2.71
MICCA	28	124	0	220.97
	35	80	0	150.83
	40	20	0	39.62

singular values ($\mathrm{tol}_\sigma = 0$) and increase the reduced rank l. This is easily seen in Table 3 with $l = 35$ as with $l = 40$ where, in order to reach the same accuracy, significantly more time has to be expended. A conservatively high l combined with a comparatively small N is usually the computationally more efficient choice.

Important to note, all conclusions drawn in Sec. 3 can be generalized to arbitrary contours by analyzing the corresponding filter functions.

5 A Rational Approximation

The approximation of the NLEVP by a REVP and a subsequent reformulation into an equivalent LEVP of higher dimension is used in several previous works in thermoacoustics and usually corresponds to state-space models [4,6,9–11]. For the LEVP, well-established and diverse solution methods are readily available [20]. In this section, the error due to approximation is discussed and is compared to the results of the contour-integration based method from Secs. 3.3–3.5.

5.1 Reformulation of the Rational Eigenvalue Problem. In the NLEVP Eq. (7), the s-dependent coefficient functions $\mathscr{F}_k(s)$ and $\mathscr{Z}_i(s)^{-1}$ are approximated by the rational functions $\tilde{\mathscr{F}}_k$ and $\tilde{\mathscr{Z}}_i^{-1}$. Then the resulting REVP takes the general form

$$\tilde{\mathbf{L}}(s)\mathbf{v} = \left[\mathbf{P}(s) + \sum_{j=1} \mathscr{R}_j(s)\mathbf{R}_j\right]\mathbf{v} = 0 \tag{24}$$

where $\mathbf{P}(s) \in \mathbb{C}^{d\times d}$ is a matrix polynomial of degree m, $\mathscr{R}_i(s)$ are scalar proper rational functions, and $\mathbf{R}_i \in \mathbb{C}^{d\times d}$ are constant matrices. The domain in the complex plane, where the rational operator $\tilde{\mathbf{L}}$ approximates $\mathbf{L}$ sufficiently well is, in general, limited. Only eigenvalues inside this domain can be expected to be approximated well [16], but the completeness of the spectrum cannot be guaranteed. When using a criterion such as Eq. (3), only a region of confidence can be defined [43].

In the following, we assume for simplicity $\tilde{\mathscr{F}}_k$ and $s\tilde{\mathscr{Z}}_i^{-1}$ to be proper rational. Then, we identify

$$\tilde{\mathbf{L}}(s) = \underbrace{s^2\mathbf{M} + \sum_{t=1} \frac{s}{\mathscr{Z}_{c,t}}\mathbf{Z}_t + \mathbf{K}}_{\mathbf{P}(s)} + \underbrace{\sum_{l=1} \frac{s}{\tilde{\mathscr{Z}}_l(s)}\mathbf{Z}_l + \sum_{k=1} \tilde{\mathscr{F}}_k(s)\mathbf{Q}_k}_{\sum_{j=1} \mathscr{R}_j(s)\mathbf{R}_j} \tag{25}$$

In contrast to Eq. (7), we split the boundary term into two parts, distinguishing between constant and s-dependant boundary impedances $\mathscr{Z}_{c,t}$ and $\tilde{\mathscr{Z}}_l$. Next, an exemplary two-step reformulation of Eq. (24) into a LEVP is performed for $\tilde{\mathbf{L}}(s)$ in Eq. (25). For short notation, we restrict ourselves to a single rational term $\mathscr{R}(s)\mathbf{R}$. However, the procedure is easily generalized for multiple rational terms [9,11,44].

First, the polynomial part $\mathbf{P}(s)\mathbf{v}$ can be reformulated, e.g., via simple substitution of higher order terms

$$\left(s\begin{bmatrix}\mathbf{M} & 0\\ 0 & \mathbf{I}\end{bmatrix} + \begin{bmatrix}\mathbf{Z}_c' & \mathbf{K}\\ -\mathbf{I} & 0\end{bmatrix}\right)\begin{bmatrix}s\mathbf{v}\\ \mathbf{v}\end{bmatrix} + \begin{bmatrix}\mathbf{R}\\ 0\end{bmatrix}\mathbf{r} = 0 \tag{26}$$

where $\mathbf{I} \in \mathbb{C}^{d\times d}$ is the identity matrix of size equal to $\mathbf{M}$. $\mathbf{Z}_c' = \sum_{t=1}(1/\mathscr{Z}_{c,t})\mathbf{Z}_t$ is the combined sum of boundary terms with constant impedances and $\mathbf{r} = \mathscr{R}(s)\mathbf{v}$ is a source in volume, e.g., by heat release, or at a boundary. This reformulation step is quite expensive since it increases the DOF by a factor m. For the Helmholtz equation, $\mathbf{P}(s)$ is a quadratic matrix polynomial ($m = 2$). This results in a doubling of the DOF. For LEE, LNSE, and LRF ($m = 1$) no reformulation is necessary and the number of DOF stays the same.

Next, the proper rational source term $\mathbf{r}$ can be stated in terms of a descriptor system

$$\begin{aligned} s\mathbf{E}\mathbf{x} &= \mathbf{A}\mathbf{x} + \mathbf{B}\mathbf{v}\\ \mathbf{r} &= \mathbf{C}\mathbf{x}\end{aligned} \tag{27}$$

with the vector $\mathbf{x} \in \mathbb{C}^{r\times 1}$ of internal states of the approximated functions, the system matrix $\mathbf{A} \in \mathbb{C}^{r\times r}$, the input matrix $\mathbf{B} \in \mathbb{C}^{r\times d}$, the output matrix $\mathbf{C} \in \mathbb{C}^{d\times r}$, and the mass matrix $\mathbf{E} \in \mathbb{C}^{r\times r}$. Substitute the second equation of Eq. (27) into Eq. (26) and appending the first equation of Eq. (27) results in the generalized LEVP

$$\hat{\mathbf{L}}(s)\hat{\mathbf{v}} = \left(s\begin{bmatrix}\mathbf{M} & 0 & 0\\ 0 & \mathbf{I} & 0\\ 0 & 0 & \mathbf{E}\end{bmatrix} + \begin{bmatrix}\mathbf{Z}_c' & \mathbf{K} & \mathbf{R}\mathbf{C}\\ -\mathbf{I} & 0 & 0\\ 0 & -\mathbf{B} & -\mathbf{A}\end{bmatrix}\right)\begin{bmatrix}s\mathbf{v}\\ \mathbf{v}\\ \mathbf{x}\end{bmatrix} = 0 \tag{28}$$

The number of additional DOF introduced by this reformulation depends on the degree r of the numerator polynomial of $\mathscr{R}(s)$ [11], which is usually in the range $r \approx 10 - 100$. For multidimensional spatially discretized problems this is usually much smaller than the problem dimension ($r \ll d$) and therefore negligible, even if multiple rational approximations are used.

Importantly, the reformulation of the REVP as a LEVP can be done without introducing spurious modes or truncating the spectrum [44].

5.2 Application to the Rijke and MICCA Cases. For the Rijke case, a rational approximate of the n–τ-model, Eq. (21), is obtained by the spatial discretization of a one-dimensional advection equation [45]. The pseudospace of length τ and propagation velocity 1 m s^{-1} is resolved by 20 cells and is discretized with a third-order discontinuous Galerkin finite element scheme. The resulting linear model of $\tilde{\mathscr{F}}$ yields 80 DOF. For the MICCA combustor, vector fitting [27] is employed to compute a rational

Table 4 Wall-clock time t and range of accuracy ε_s achieved with the approximated REVP inside Γ for different test cases

Test case (DOF)	l_{req} (l_{conv})	ε_s	t (s)
Rijke (9662)	12(12)	$\mathcal{O}(10^{-10} - 10^{-6})$	0.335
MICCA-DTD (43,648)	28(28)	$\mathcal{O}(10^{-4} - 10^{-2})$	9.9
	35(40)	$\mathcal{O}(10^{-4} - 10^{-3})$	22.9
	40(58)	$\mathcal{O}(10^{-4} - 10^{-2})$	30.3
MICCA-Exp (43,568)	28(30)	$\mathcal{O}(10^{-10} - 10^{-6})$	10.8
	35(39)	$\mathcal{O}(10^{-10} - 10^{-6})$	13.2
	40(41)	$\mathcal{O}(10^{-10} - 10^{-5})$	13.2

The DOF of the LEVPs are stated.

approximation of the flame response and two cases are considered. For MICCA-DTD, the distributed time delay model in Eq. (23) is fitted (12 DOF) and is compared to the NLEVP solution of Sec. 3.4. This serves as an example for cases in which the analytical form of the FTF is known and has to be approximated. For MICCA-Exp, the experimental data [41] is fitted (6 DOF) and the NLEVP solution computed with the same rational fit is used as reference. This represents the case if only discrete data is available and has to be fitted anyway to achieve a continuous FTF.

An iterative Krylov–Schur algorithm [46,47] from SLEPc [48] is called via the python package slepc4py to solve the proxy LEVP, Eq. (28). Again, the required matrices are setup with FEniCS [36]. In addition, a shift-and-invert spectral transform [20] with the complex shift located at the center z_0 of the contour Γ is used. The eigenvalues closest to the shift, and therefore inside Γ, are then expected to be computed first. The algorithm is requested to converge at least to the same number of eigenpairs $l_{\text{req}} = l \leq l_{\text{conv}}$ as in Secs. 3.3 and 3.4 with a relative residual of $\leq 10^{-8}$. The most expensive single computational step is a LU-decomposition of the shift operator $\hat{L}(z_0)$. However, this has to be computed only once, since only a single shift is performed.

Table 4 compares the LEVP eigenvalues with the NLEVP ones. ε_s is the range of the error and t is the wall-clock time for a computation on a single core of a AMD Ryzen 5 3600 6-Core processor. Eigenvalues of the Rijke case are computed with very high accuracy. This is expected since the pseudospace discretization of the advection equation is known to approximate the n–τ-model well. All eight eigenvalues inside Γ are computed—including the pair that almost forms a defective one—and no spurious modes occur.

Figure 10 shows the two results for the MICCA case. The LEVP finds all eigenvalues in both cases. A dense cluster of spurious modes occurs only for MICCA-DTD close to the origin. It is located between a close pole-zero pair of the rational DTD fit. The LEVP with the fit of the DTD model (MICCA-DTD) shows errors not exceeding 1.32%, see Table 4, and hence the rational fit is satisfactory in the considered domain. For the direct fit of the experimental data (MICCA-Exp), the NLEVP and the LEVP yield the same eigenvalues. The computed eigenspaces show small errors in terms of maximal local absolute value ($\leq \mathcal{O}(10^{-4})$ and angular error ($\leq \mathcal{O}(10^{-2})$ rad) for all test cases and all types of eigenvalues.

The case MICCA-DTD is the only case where the proxy LEVP has an error introduced by the rational approximation, since the NLEVP can employ the DTD model directly. However, this assumes that the DTD model represents the flame response exactly. In the present work, the DTD model was obtained from the experimental flame frequency response. If such a procedure is not possible, an NLEVP formulation and a proxy LEVP would both require a fit of the experimental data, e.g., vector fitting. Then the NLEVP and the LEVP give the same result with the same error introduced by vector fitting. The use of either a DTD model or a *vectorfit* needs to be decided on a case-by-case basis and a general discussion is beyond the scope of this paper.

Spurious modes of the LEVP, like for MICCA-DTD, are in general difficult to identify since they are correct solutions of the REVP but not of the NLEVP. An identification procedure

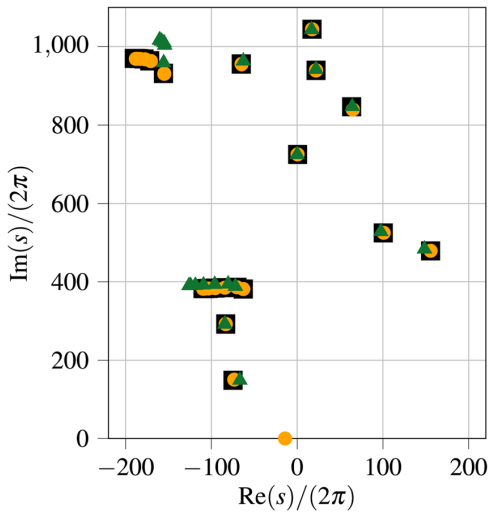

Fig. 10 Stability map for the MICCA case computed with different FTFs. (1) MICCA-DTD: ■ analytical DTD model and ● its rational approximation. (2) MICCA-Exp: ▲ rational approximation of the experimental data [41]. ▲ represents both the NLEVP and the LEVP solution since it is not distinguishable in the plot.

therefore necessitates a comparison to the original NLEVP. If this is possible, similar methods like for Beyn's method could be applied inside a region of confidence (see Sec. 4.1). However, the original NLEVP is usually unknown in practical cases and we therefore lack the comparative problem.

For single core computations, the speed-up achieved with the proxy LEVP over the NLEVP formulation is significant. The Krylov–Schur method and Beyn's method both employ an LU decomposition which is provided by the linear algebra back end UMFPACK [49] in both cases; hence, they can be compared. Even though the problem sizes are more than doubled for the LEVP models, the computations are overall faster, see Tables 3 and 4. This is expected, since Beyn's method requires N LU-decompositions, while the LEVP only requires one. The speed-up is not of factor N due to the different matrix sizes and since the employed Krylov–Schur method for the LEVP also incurs a cost. The demand in terms of memory was similar for both algorithms in the computed testcases. For the LEE, LNSE, and LRF, the relative speed-up increases further compared to the Helmholtz equation due to the similar sizes of $\mathbf{L}$ and $\hat{\mathbf{L}}$ in that case.

For parallel computations, Beyn's method has an advantage over the Krylov–Schur method in terms of scalability due to the N independent LU-decompositions. For a large numbers of cores ($\gg N$), Beyn's algorithm might outperform the Krylov–Schur algorithm in terms of run time. However, if or for which number of cores this is the case strongly depends on the problem size and type, the implementation of the algorithms, the architecture at hand, the parameters N and l of Beyn's algorithm, number of subspace iterations of the Krylov–Schur algorithm, and many other quantities. Yet, the issues of setting the user-defined input parameters for Beyn's method remain.

6 Conclusions

Two solution methods for nonlinear eigenvalue problems associated with the thermoacoustic Helmholtz equation have been assessed by solving two problems representative of systems encountered in thermoacoustic applications: a Rijke tube and the MICCA annular combustor.

In a first step, the NLEVP is solved using Beyn's contour integration method. It is established how certain user-defined parameters affect the solution. Convergence tests show that the error of the results reaches a plateau. Moreover, it is shown how the

completeness of the spectrum and the precision of the eigenvalues is primarily affected by eigenvalues close to the outside of the contour. In a second step, terms nonlinear in the eigenvalue arising from the flame response in the NLEVP are approximated with rational functions, and the ensuing problem is recast as a linear eigenvalue problem. The approximation is found to introduce only a few spurious modes, and the entire spectrum is computed. The error due to the approximation is small and found to be minor in comparison to the numerical speed-up and the avoidance of hard-to-set user inputs that is achieved by employing well-established linear solvers. Plus, the approximation error is non-existent if the flame term is only available as a rational function in the first place. For practical applications, the rational fitting of gain and phase values for real valued frequencies is standard, underscoring the use of a proxy LEVP as a sensible choice.

The findings in this work have implications for the solution strategies of linearized models that also yield discrete NLEVPs, such as LEE, LNSE, and LRF. Since these models generally result in discrete formulations of higher dimension than the NLEVPs of the thermoacoustic Helmholtz equation, an efficient solution strategy needs to be chosen. The results in this work indicate that a reformulation into an LEVP by using rational approximations of any occurring eigenvalue nonlinearities is a sensible choice due to the significant speed-up and the avoidance of hard-to-set user inputs at a cost of a small modeling error. Future work will focus on improving the approximation of the nonlinear terms via rational functions and investigate how the approximation of multiple nonlinearities—including frequency-dependent boundary conditions—affects the solutions.

Acknowledgment

The authors would like to thank Eirik Æsøy for fitting the experimental FTF to a DTD model using his numerical code.

Nomenclature

Symbols

d = degrees-of-freedom
$\mathscr{F}$ = flame transfer function
l = reduced rank
$\mathbf{L}$ = nonlinear operator
N = number of quadrature points
R = radius of contour
s = Laplace variable/eigenvalue
tol_σ = cutoff value
$\mathbf{v}, \mathbf{w}$ = right/left eigenvector
z = complex number
$\mathscr{Z}$ = impedance
z_0 = center of contour
Γ = contour
ε_s = relative deviation of s from reference
σ = singular values
Σ = spectrum of eigenpairs

Abbreviations

DOF = degrees-of-freedom
DTD = distributed time delay
FTF = flame transfer function
LEE = linearized Euler equations
LEVP = linear eigenvalue problem
LNSE = linearized Navier–Stokes equations
LRF = linearized reactive flow equations
NLEVP = nonlinear eigenvalue problem
REVP = rational eigenvalue problem

References

[1] Lieuwen, T., and Yang, V., 2005, *Combustion Instabilities in Gas Turbine Engines: Operational Experience, Fundamental Mechanisms and Modeling* (Progress in Astronautics and Aeronautics, Vol. 210), American Institute of Aeronautics and Astronautics, Reston, VA.
[2] Wolf, P., Staffelbach, G., Gicquel, L. Y. M., Müller, J.-D., and Poinsot, T., 2012, "Acoustic and Large Eddy Simulation Studies of Azimuthal Modes in Annular Combustion Chambers," Combust. Flame, **159**(11), pp. 3398–3413.
[3] Wolf, P., Balakrishnan, R., Staffelbach, G., Gicquel, L., and Poinsot, T., 2012, "Using LES to Study Reacting Flows and Instabilities in Annular Combustion Chambers," Flow, Turbul. Combust., **88**(1–2), pp. 191–206.
[4] Avdonin, A., Meindl, M., and Polifke, W., 2019, "Thermoacoustic Analysis of a Laminar Premixed Flame Using a Linearized Reacting Flow Solver," Proc. Combust. Inst., **37**(4), pp. 5307–5314.
[5] Gikadi, J., Sattelmayer, T., and Peschiulli, A., 2012, "Effects of the Mean Flow Field on the Thermo-Acoustic Stability of Aero-Engine Combustion Chambers," ASME Paper No. GT2012-69612.
[6] Meindl, M., Albayrak, A., and Polifke, W., 2020, "A State-Space Formulation of a Discontinuous Galerkin Method for Thermoacoustic Stability Analysis," J. Sound Vib., **481**, p. 115431.
[7] Hofmeister, T., Hummel, T., Berger, F., Klarmann, N., and Sattelmayer, T., 2020, "Elimination of Numerical Damping in the Stability Analysis of Non-Compact Thermoacoustic Systems With Linearized Euler Equations," ASME Paper No. GT2020-16051.
[8] Nicoud, F., Benoit, L., Sensiau, C., and Poinsot, T., 2007, "Acoustic Modes in Combustors With Complex Impedances and Multidimensional Active Flames," AIAA J., **45**(2), pp. 426–441.
[9] Schuermans, B., Bellucci, V., and Paschereit, C. O., 2003, "Thermoacoustic Modeling and Control of Multi-Burner Combustion Systems," ASME Paper No. GT2003-38688.
[10] Bothien, M., Moeck, J., Lacarelle, A., and Paschereit, C. O., 2007, "Time Domain Modelling and Stability Analysis of Complex Thermoacoustic Systems," Proc. Inst. Mech. Eng., Part A, **221**(5), pp. 657–668.
[11] Emmert, T., Meindl, M., Jaensch, S., and Polifke, W., 2016, "Linear State Space Interconnect Modeling of Acoustic Systems," Acta Acust. Acust., **102**(5), pp. 824–833.
[12] Zhao, D., and Morgans, A. S., 2009, "Tuned Passive Control of Combustion Instabilities Using Multiple Helmholtz Resonators," J. Sound Vib., **320**(4–5), pp. 744–757.
[13] Moeck, J. P., Paul, M., and Paschereit, C. O., 2010, "Thermoacoustic Instabilities in an Annular Rijke Tube," ASME Paper No. GT2010-23577.
[14] Mensah, G. A., Magri, L., Silva, C. F., Buschmann, P. E., and Moeck, J. P., 2018, "Exceptional Points in the Thermoacoustic Spectrum," J. Sound Vib., **433**, pp. 124–128.
[15] Mehrmann, V., and Voss, H., 2004, "Nonlinear Eigenvalue Problems: A Challenge for Modern Eigenvalue Methods," GAMM-Mitt., **27**(2), pp. 121–152.
[16] Güttel, S., and Tisseur, F., 2017, "The Nonlinear Eigenvalue Problem," Acta Numer., **26**, pp. 1–94.
[17] Mensah, G. A., Buschmann, P. E., and Orchini, A., 2022, "Iterative Solvers for the Thermoacoustic Nonlinear Eigenvalue Problem and Their Convergence Properties," Int. J. Spray Combust. Dyn., **14**(1–2), pp. 30–41.
[18] Buschmann, P. E., Mensah, G. A., Nicoud, F., and Moeck, J. P., 2020, "Solution of Thermoacoustic Eigenvalue Problems With a Noniterative Method," ASME J. Eng. Gas Turbines Power, **142**(3), p. 031022.
[19] Kopitz, J., and Polifke, W., 2008, "CFD-Based Application of the Nyquist Criterion to Thermo-Acoustic Instabilities," J. Comput. Phys., **227**(14), pp. 6754–6778.
[20] Saad, Y., 2011, *Numerical Methods for Large Eigenvalue Problems*, revised ed., Vol. 66, SIAM, Philadelphia, PA.
[21] Polifke, W., 2020, "Modeling and Analysis of Premixed Flame Dynamics by Means of Distributed Time Delays," Prog. Energy Combust. Sci., **79**, p. 100845.
[22] Crocco, L., and Cheng, S. I., 1956, *Theory of Combustion Instability in Liquid Propellant Rocket Motors* (AGARDograph, Vol. 8), Butterworths Scientific Publications, New York.
[23] Komarek, T., and Polifke, W., 2010, "Impact of Swirl Fluctuations on the Flame Response of a Perfectly Premixed Swirl Burner," ASME J. Eng. Gas Turbines Power, **132**(6), p. 061503.
[24] Æsøy, E., Aguilar, J. G., Wiseman, S., Bothien, M. R., Worth, N. A., and Dawson, J. R., 2020, "Scaling and Prediction of Transfer Functions in Lean Premixed H_2/CH_4-Flames," Combust. Flame, **215**, pp. 269–282.
[25] Polifke, W., 2014, "Black-Box System Identification for Reduced Order Model Construction," Ann. Nucl. Energy, **67**, pp. 109–128.
[26] Subramanian, P., Blumenthal, R. S., Sujith, R., and Polifke, W., 2015, "Distributed Time Lag Response Functions for the Modelling of Combustion Dynamics," Combust. Theory Modell., **19**(2), pp. 223–237.
[27] Gustavsen, B., and Semlyen, A., 1999, "Rational Approximation of Frequency Domain Responses by Vector Fitting," IEEE Trans. Power Delivery, **14**(3), pp. 1052–1061.
[28] Cumpsty, N. A., and Marble, F. E., 1977, "The Interaction of Entropy Fluctuations With Turbine Blade Rows; A Mechanism of Turbojet Engine Noise," Proc. R. Soc. A, **357**(1690), pp. 323–344.
[29] Candel, S., Durox, D., Schuller, T., Bourgouin, J. F., and Moeck, J. P., 2014, "Dynamics of Swirling Flames," Annu. Rev. Fluid Mech., **46**(1), pp. 147–173.
[30] Poinsot, T., 2017, "Prediction and Control of Combustion Instabilities in Real Engines," Proc. Combust. Inst., **36**(1), pp. 1–28.
[31] Buschmann, P. E., Mensah, G. A., and Moeck, J. P., 2020, "Intrinsic Thermoacoustic Modes in an Annular Combustion Chamber," Combust. Flame, **214**, pp. 251–262.
[32] Beyn, W.-J., 2012, "An Integral Method for Solving Nonlinear Eigenvalue Problems," Linear Algebra Its Appl., **436**(10), pp. 3839–3863.

[33] Van Barel, M., and Kravanja, P., 2016, "Nonlinear Eigenvalue Problems and Contour Integrals," J. Comput. Appl. Math., **292**, pp. 526–540.
[34] Keldysh, M. V., 1971, "On the Completeness of the Eigenfunctions of Some Classes of Non-Selfadjoint Linear Operators," Russ. Math. Surv., **26**(4), pp. 15–44.
[35] Prosperetti, A., 2011, *Advanced Mathematics for Applications*, Cambridge University Press, Cambridge, UK.
[36] Alnæs, M., Blechta, J., Hake, J., Johansson, A., Kehlet, B., Logg, A., Richardson, C., Ring, J., Rognes, M. E., and Wells, G. N., 2015, "The FEniCS Project Version 1.5," Arch. Numer. Software, **3**(100), pp. 9–23.
[37] Virtanen, P., Gommers, R., Oliphant, T. E., Haberland, M., Reddy, T., Cournapeau, D., Burovski, E., et al., 2020, "SciPy 1.0: Fundamental Algorithms for Scientific Computing in Python," Nat. Methods, **17**(3), pp. 261–272.
[38] Harris, C. R., Millman, K. J., van der Walt, S. J., Gommers, R., Virtanen, P., Cournapeau, D., Wieser, E., et al., 2020, "Array Programming With NumPy," Nature, **585**(7825), pp. 357–362.
[39] Bourgouin, J.-F., Durox, D., Moeck, J., Schuller, T., and Candel, S., 2015, "A New Pattern of Instability Observed in an Annular Combustor: The Slanted Mode," Proc. Combust. Inst., **35**(3), pp. 3237–3244.
[40] Laera, D., Prieur, K., Durox, D., Schuller, T., Camporeale, S., and Candel, S., 2017, "Impact of Heat Release Distribution on the Spinning Modes of an Annular Combustor With Multiple Matrix Burners," ASME J. Eng. Gas Turbines Power, **139**(5), p. 051505.
[41] Laera, D., Schuller, T., Prieur, K., Durox, D., Camporeale, S. M., and Candel, S., 2017, "Flame Describing Function Analysis of Spinning and Standing Modes in an Annular Combustor and Comparison With Experiments," Combust. Flame, **184**, pp. 136–152.
[42] Æsøy, E., Aguilar, J. G., Bothien, M. R., Worth, N. A., and Dawson, J. R., 2021, "Acoustic-Convective Interference in Transfer Functions of Methane/Hydrogen and Pure Hydrogen Flames," ASME J. Eng. Gas Turbines Power, **143**(12), p. 121017.
[43] Schmid, M., Blumenthal, R., Schulze, M., Polifke, W., and Sattelmayer, T., 2013, "Quantitative Stability Analysis Using Real Frequency Response Data," ASME Paper No. GT2013-95459.
[44] Su, Y., and Bai, Z., 2011, "Solving Rational Eigenvalue Problems Via Linearization," SIAM J. Matrix Anal. Appl., **32**(1), pp. 201–216.
[45] Meindl, M., Emmert, T., and Polifke, W., 2016, "Efficient Calculation of Thermoacoustic Modes Utilizing State-Space Models," 23rd International Congress on Sound and Vibration (ICSV23), Athens, Greece, July 10–14, pp. 3006–3013.
[46] Stewart, G. W., 2002, "A Krylov–Schur Algorithm for Large Eigenproblems," SIAM J. Matrix Anal. Appl., **23**(3), pp. 601–614.
[47] Stewart, G. W., 2002, "Addendum to 'A Krylov–Schur Algorithm for Large Eigenproblems'," SIAM J. Matrix Anal. Appl., **24**(2), pp. 599–601.
[48] Hernandez, V., Roman, J. E., and Vidal, V., 2005, "SLEPc: A Scalable and Flexible Toolkit for the Solution of Eigenvalue Problems," ACM Trans. Math. Software, **31**(3), pp. 351–362.
[49] Davis, T. A., 2004, "Algorithm 832: UMFPACK V4.3—An Unsymmetric-Pattern Multifrontal Method," ACM Trans. Math. Software, **30**(2), pp. 196–199.

List of Figures

1.1 Change in global surface temperature T_{glob} relative to 1850-1900 (Dataset from [121, 128, 237]). The red shaded area indicates temperature levels above the 1.5 °C limit agreed on in the Paris agreement [238]. 1

1.2 Burner assembly of a gas turbine combustor (left) new and (right) damaged by thermoacoustic instabilities. (Goy *et al.*. [99] (original, Copyright © 2005 by E.ON UK and republished in this work with permission) and Huang and Yang [118] (reproduction with improved quality)) 3

3.1 Illustrative network model of a ducted slit flame. The model is stacked as a sequence of two compact elements, representing a flame (**F**) and an area change (**AC**), and two non-compact elements, representing ducts (**D**). The flame transfer function $\mathscr{F}$ referenced to the reference point "ref" provides the flow-flame interaction closure (see Sec. 3.3) to the flame element. Boundary conditions (**BC**) at the in- and outlet complete the model. 15

3.2 Schematic depiction of an exemplary 2-port network element represented in terms of (left) the scattering matrix **S** with the corresponding characteristic input and output disturbances, and (right) the transfer matrix **T** with the upstream and downstream primitive variables. 16

3.3 Flame response data in the form of (left) the *unit impulse response* and (right) the bode plot of the corresponding FTF $\mathscr{F}(s)$ evaluated for zero growth rate ($\mathrm{Re}(s) = \sigma = 0$). 18

4.1 Illustrative example of the real part of eigenvectors $\mathrm{Re}(\hat{\mathbf{v}})$ in an annular combustor corresponding to (a) a simple eigenpair, and (b) a semi-simple eigenpair with $N_{\mathrm{a}} = N_{\mathrm{g}} = 2$. 23

5.1 Schematic representation of (a) a simple test rig and (b) a test rig with a realistic gas turbine combustor as test section, both under reactive ("hot") conditions. Sirens are not shown. 29

5.2 Eigenvalues of the MICCA combustor [32, 143] at EM2C (CentraleSupérlec) computed with different solution strategies. Displayed are the computed physical eigenvalues (•), the missed physical eigenvalues (◦) and computed spurious eigenvalues (•) calculated with (a) a fixed-point iteration (outer iteration method) with the passive thermoacoustic modes as initial guesses (▪) as proposed by Nicoud and Benoit [182], (b) Beyn's method [23] (contour integration) utilizing the contour displayed, and (c) the Krylov-Schur algorithm [228, 229] applied to an approximated REVP. (Results are adopted from (a) Buschmann *et al.* [40] and (b) & (c) PAPER-NLEVP [167]) 33

B.1 Schematic representation of a 1-N-junction with $N = 2$. The junction is separated in $N = 2$ flow tubes with the volumes V_1 (▪) and V_2 (▪). The flow tubes are coupled only via the pressure on the interfacing streamline (-··-). The junction is enclosed in a duct of constant cross section. 55

B.2 Schematic representation of a N-1-junction with $N = 2$ enclosed by the control volume V (– –). The junction is enclosed in a duct of constant cross-section. . 56

C.1 Schematic representation of a non-compact premixed flame (——) including a moving flame front. The infinitely thin flame front separates the control volume V (– –) into the subvolumes V_1 (▪) and V_2 (▪). 59

C.2 Schematic representation of a non-compact premixed flame sheet (▪) enclosed in the control volume V (– –). The center position of the flame sheet $x_f(t)$ displaces with time. 61

List of Tables

2.1 Impact of acoustic waves, vortical perturbations, entropic inhomogenities [50, 150] and compositional inhomogenities on various primitive flow variables. . . 11

4.1 Structure of the operator $\mathscr{N}(s)$ for different linearized models. 21

5.1 Closure models for the spatial distribution $\mathscr{Q}(s, \mathbf{x})$ 27

5.2 Established jump conditions derived for premixed flames and the assumptions used. The table marks the subset of the modelled characteristics (acoustic Π^+/Π^-, entropic $\mathfrak{s}$, compositional $\mathfrak{c}_k$), the usage of simplified gas properties (c_p), the approximation order in Mach number ($\mathscr{O}(\overline{\mathrm{M}}^x)$) and if the flame movement u'_s is accounted for. Lumped compositional perturbations, e.g., in terms of equivalence perturbations, are checked in brackets. Two exponents are detailed for $\mathscr{O}(\overline{\mathrm{M}}^x)$ if the approximation order in Mach number is chosen differently for the mean field (first exponent) and the perturbed fields (second exponent). More details are found in PAPER-JUMP [169]. (Table adopted from PAPER-JUMP [169]) 31

Bibliography

[1] M. Åbom. A note on the experimental determination of acoustical two-port matrices. *Journal of Sound and Vibration*, 155(1):185–188, 1992. doi: 10.1016/0022-460X(92)90655-H.

[2] J. Achury and W. Polifke. Modulation of Spray Droplet Number Density and Size Distribution by an Acoustic Field. *The Journal of Computational Multiphase Flows*, 9(1):32–46, 2017. doi: 10.1177/1757482X17690751.

[3] E. Æsøy. *The Effect of Hydrogen Enrichment on the Thermoacoustic Behaviour of Lean Premixed Flames*. PhD thesis, Norwegian University of Science and Technology, Trondheim, Norway, 2022.

[4] E. Æsøy, J. G. Aguilar, S. Wiseman, M. R. Bothien, N. A. Worth, and J. R. Dawson. Scaling and Prediction of Transfer Functions in Lean Premixed H2/Ch4-Flames. *Combustion and Flame*, 215:269–282, 2020. doi: 10.1016/j.combustflame.2020.01.045.

[5] E. Æsøy, J. G. Aguilar, M. R. Bothien, N. A. Worth, and J. R. Dawson. Acoustic-Convective Interference in Transfer Functions of Methane/Hydrogen and Pure Hydrogen Flames. *Journal of Engineering for Gas Turbines and Power*, 143(12):121017, 2021. doi: 10.1115/1.4051960.

[6] P. Agostinelli, D. Laera, I. Chterev, I. Boxx, L. Gicquel, and T. Poinsot. On the impact of H2-enrichment on flame structure and combustion dynamics of a lean partially-premixed turbulent swirling flame. *Combustion and Flame*, 241:112120, 2022. doi: 10.1016/j.combustflame.2022.112120.

[7] Air Transport Action Group. Waypoint 2050: An Air Transport Action Group Project. `https://aviationbenefits.org/media/167417/w2050_v2021_27sept_full.pdf`, Sept. 2021. (Last accessed: Aug. 14, 2024).

[8] A. Q. Al-Shetwi, M. Hannan, K. P. Jern, M. Mansur, and T. Mahlia. Grid-connected renewable energy sources: Review of the recent integration requirements and control methods. *Journal of Cleaner Production*, 253:119831, 2020. doi: 10.1016/j.jclepro.2019.119831.

[9] C. Alanyalıoğlu, H. Reinhardt, A. Fischer, C. Lahiri, H. Nicolai, and C. Hasse. Comparison of acoustic, optic, and heat release rate based flame transfer functions for a lean-burn injector under engine-like conditions. In *Symposium on Thermoacoustics in Combustion*, Zurich, Switzerland, Sept. 2023.

[10] A. Amsden. Kiva3v. a block-structured kiva program for engines with vertical or canted valves. Technical Report LA-13313-MS, Los Alamos National Laboratory, Los Alamos, New Mexico, USA, 1997.

[11] A. A. Amsden. Kiva3. a kiva program with block-structured mesh for complex geometries. Technical Report LA-12503-MS, Los Alamos National Laboratory, Los Alamos, New Mexico, USA, 1993.

[12] A. M. Annaswamy and A. F. Ghoniem. Active Control in Combustion Systems. *IEEE Control Systems Magazine*, 15(6):49–63, 1995. doi: 10.1109/37.476386.

[13] A. M. Annaswamy and A. F. Ghoniem. Active control of combustion instability: Theory and practice. *IEEE Control Systems Magazine*, 22(6):37–54, 2002. doi: 10.1109/MCS.2002.1077784.

[14] W. E. Arnoldi. The Principle of Minimized Iterations in the Solution of the Matrix Eigenvalue Problem. *Quarterly of Applied Mathematics*, 9(1):17–29, 1951. doi: 10.1090/qam/42792.

[15] J. Asakura, T. Sakurai, H. Tadano, T. Ikegami, and K. Kimura. A numerical method for nonlinear eigenvalue problems using contour integrals. *JSIAM Letters*, 1:52–55, 2009. doi: 10.14495/jsiaml.1.52.

[16] A. Avdonin. *Local Modeling and Uncertainty Quantification of the Linear Flame Response*. PhD thesis, Technical University of Munich, Garching, Germany, 2022.

[17] A. Avdonin, M. Meindl, and W. Polifke. Thermoacoustic analysis of a laminar premixed flame using a linearized reacting flow solver. *Proceedings of the Combustion Institute*, 37(4):5307–5314, 2019. doi: 10.1016/j.proci.2018.06.142.

[18] S. Bade, M. Wagner, C. Hirsch, T. Sattelmayer, and B. Schuermans. Influence of Fuel-Air Mixing on Flame Dynamics of Premixed Swirl Burners. In *Proceedings of the ASME Turbo Expo 2014: Turbine Technical Conference and Exposition. Volume 4A: Combustion, Fuels and Emissions*, Düsseldorf, Germany, June 2014. ASME. doi: 10.1115/GT2014-25381.

[19] R. Balachandran, B. O. Ayoola, C. F. Kaminski, A. P. Dowling, and E. Mastorakos. Experimental investigation of the nonlinear response of turbulent premixed flames to imposed inlet velocity oscillations. *Combustion and Flame*, 143(1–2):37–55, 2005. doi: 10.1016/j.combustflame.2005.04.009.

[20] G. K. Batchelor. *An Introduction to Fluid Dynamics*. Cambridge Mathematical Library. Cambridge University Press, Cambridge, UK, 14 edition, 2010. ISBN 978-0-521-66396-0.

[21] M. Bauerheim, F. Nicoud, and T. Poinsot. Theoretical Analysis of the Mass Balance Equation Through a Flame at Zero and Non-Zero Mach Numbers. *Combustion and Flame*, 162:60–67, 2014. doi: 10.1016/j.combustflame.2014.06.017.

[22] M. Bauerheim, I. Duran, T. Livebardon, G. Wang, S. Moreau, and T. Poinsot. Transmission and reflection of acoustic and entropy waves through a stator–rotor stage. *Journal of Sound and Vibration*, 374:260–278, 2016. doi: 10.1016/j.jsv.2016.03.041.

[23] W.-J. Beyn. An integral method for solving nonlinear eigenvalue problems. *Linear Algebra and its Applications*, 436(10):3839–3863, 2012. doi: 10.1016/j.laa.2011.03.030.

[24] J. Bibrzycki, T. Poinsot, and A. Zajdel. Investigation of Laminar Flame Speed of CH4/N2/O2 and CH4/CO2/O2 Mixtures Using Reduced Chemical Kinetic Mechanisms. *Archivum combustionis*, 30(4):287–296, 2010.

[25] S. Blanes, F. Casas, J. Oteo, and J. Ros. The Magnus expansion and some of its applications. *Physics Reports*, 470(5-6):151–238, 2009. doi: 10.1016/j.physrep.2008.11.001.

[26] A. Blondé, B. Schuermans, K. Pandey, and N. Noiray. Effect of Hydrogen Enrichment on Transfer Matrices of Fully and Technically Premixed Swirled Flames. *Journal of Engineering for Gas Turbines and Power*, 145(12):121009, 2023. doi: 10.1115/1.4063415.

[27] B. C. Bobusch, J. P. Moeck, C. O. Paschereit, and S. Sadig. Thermoacoustic Stability Analysis of a Kerosene-Fueled Lean Direct Injection Combustor Employing Acoustically and Optically Measured Transfer Matrices. In *Proceedings of the ASME Turbo Expo 2012: Turbine Technical Conference and Exposition. Volume 2: Combustion, Fuels and Emissions, Parts A and B*, Copenhagen, Denmark, June 2012. ASME. doi: 10.1115/GT2012-69034.

[28] D. Bohn and E. Deuker. An acoustical model to predict combustion driven oscillations. In *20th International Congress on Combustion Engines*, London, UK, Dec. 1993. CIMAC.

[29] S. Bomberg, T. Emmert, and W. Polifke. Thermal Versus Acoustic Response of Velocity Sensitive Premixed Flames. *Proceedings of the Combustion Institute*, 35(3):3185–3192, 2015. doi: 10.1016/j.proci.2014.07.032.

[30] M. Bothien, J. P. Moeck, A. Lacarelle, and C. O. Paschereit. Time Domain Modelling and Stability Analysis of Complex Thermoacoustic Systems. *Proceedings of the Institution of Mechanical Engineers, Part A: Journal of Power and Energy*, 221(5):657–668, 2007. doi: 10.1243/09576509JPE384.

[31] M. Bothien, D. Lauper, Y. Yang, and A. Scarpato. Reconstruction and Analysis of the Acoustic Transfer Matrix of a Reheat Flame From Large-Eddy Simulations. *Journal of Engineering for Gas Turbines and Power*, 141(2):021018, 2018. doi: 10.1115/1.4041151.

[32] J.-F. Bourgouin, D. Durox, J. P. Moeck, T. Schuller, and S. Candel. Self-Sustained Instabilities in an Annular Combustor Coupled by Azimuthal and Longitudinal Acoustic Modes. In *Proceedings of the ASME Turbo Expo 2013: Turbine Technical Conference and Exposition. Volume 1B: Combustion, Fuels and Emissions*, San Antonio, Texas, USA, June 2013. ASME. doi: 10.1115/GT2013-95010.

[33] G. E. Box and G. C. Tiao. *Bayesian Inference in Statistical Analysis*. John Wiley & Sons, Ltd, 1 edition, Apr. 1992. ISBN 978-0-471-57428-6 978-1-118-03319-7. doi: 10.1002/9781118033197.

[34] M. J. Brear, F. Nicoud, M. Talei, A. Giauque, and E. R. Hawkes. Disturbance energy transport and sound production in gaseous combustion. *Journal of Fluid Mechanics*, 707:53–73, 2012. doi: 10.1017/jfm.2012.264.

[35] P. Brokof, C. M. Douglas, and W. Polifke. The role of hydrodynamic shear in the thermoacoustic response of slit flames. *Proceedings of the Combustion Institute*, 40(1): 105362, 2024. doi: 10.1016/j.proci.2024.105362.

[36] T. P. Bui, W. Schröder, and M. Meinke. Acoustic Perturbation Equations for Reacting Flows to Compute Combustion Noise. *International Journal of Aeroacoustics*, 6(4):335–355, 2007. doi: 10.1260/147547207783359468.

[37] T. P. Bui, W. Schröder, and M. Meinke. Numerical analysis of the acoustic field of reacting flows via acoustic perturbation equations. *Computers & Fluids*, 37(9):1157–1169, 2008. doi: 10.1016/j.compfluid.2007.10.014.

[38] T. P. Bui, M. Ihme, W. Schröder, and H. Pitsch. Analysis of Different Sound Source Formulations to Simulate Combustion Generated Noise Using a Hybrid LES/APE-RF Method. *International Journal of Aeroacoustics*, 8(1):95–123, 2009. doi: 10.1260/147547209786235028.

[39] P. E. Buschmann, G. A. Mensah, and J. P. Moeck. Intrinsic thermoacoustic modes in an annular combustion chamber. *Combustion and Flame*, 214:251–262, 2020. doi: 10.1016/j.combustflame.2019.11.006.

[40] P. E. Buschmann, G. A. Mensah, F. Nicoud, and J. P. Moeck. Solution of Thermoacoustic Eigenvalue Problems With a Noniterative Method. *Journal of Engineering for Gas Turbines and Power*, 142(3):031022, 2020. doi: 10.1115/1.4045076.

[41] S. M. Candel. *Analytical Studies of Some Acoustic Problems of Jet Engines*. PhD thesis, California Institute of Technology, Pasadena, CA, USA, 1972.

[42] R. H. Cantrell and R. W. Hart. Interaction between Sound and Flow in Acoustic Cavities: Mass, Momentum, and Energy Considerations. *The Journal of the Acoustical Society of America*, 36(4):697–706, 1964. doi: 10.1121/1.1919047.

[43] A. Cárdenas Miranda and W. Polifke. Combustion Stability Analysis of Rocket Engines with Resonators Based on Nyquist Plots. *Journal of Propulsion and Power*, 30(4):962–977, 2014. doi: 10.2514/1.B35149.

[44] A.-L. Cauchy. *Résumé Des Leçons Données à l'Ecole Royale Polytechnique Sur Le Calcul Infinitésimal*, volume 1 of *Imperimerie Royale*. 1823.

[45] G. Cerri, M. Gazzino, F. Botta, and C. Salvini. Production Planning with Hot Section Life Prediction for Optimum Gas Turbine Management. *International Journal of Gas Turbine, Propulsion and Power Systems*, 2(1):9–16, 2008. doi: 10.38036/jgpp.2.1_9.

[46] Y. Chen, L. J. Ayton, and D. Zhao. Modelling of intrinsic thermoacoustic instability of premixed flame in combustors with changes in cross section. *Combustion Science and Technology*, 192(5):832–851, 2019. doi: 10.1080/00102202.2019.1594799.

[47] I. Chterev and I. Boxx. Effect of hydrogen enrichment on the dynamics of a lean technically premixed elevated pressure flame. *Combustion and Flame*, 225:149–159, 2021. doi: 10.1016/j.combustflame.2020.10.033.

[48] B.-T. Chu. On the generation of pressure waves at a plane flame front. *Symposium (International) on Combustion*, 4(1):603–612, 1953. doi: 10.1016/S0082-0784(53)80081-0.

[49] B. T. Chu. On the energy transfer to small disturbances in fluid flow (Part 1). *Acta Mechanica*, 1(3):215–234, 1965. doi: 10.1007/BF01387235.

[50] B. T. Chu and L. S. G. Kovasznay. Non-Linear Interactions in a Viscous Heat-Conducting Compressible Gas. *Journal of Fluid Mechanics*, 3(5):495–514, 1957. doi: 10.1017/S0022112058000148.

[51] J. Y. Chung and D. A. Blaser. Transfer function method of measuring in-duct acoustic properties. I. Theory. *Journal of the Acoustical Society of America*, 68(3):907–913, 1980. doi: 10.1121/1.384778.

[52] S. M. Correa. Power generation and aeropropulsion gas turbines: From combustion science to combustion technology. *Symposium (International) on Combustion*, 27(2):1793–1807, 1998. doi: 10.1016/S0082-0784(98)80021-0.

[53] B. Ćosić, J. P. Moeck, and C. O. Paschereit. Nonlinear Instability Analysis for Partially Premixed Swirl Flames. *Combustion Science and Technology*, 186(6):713–736, 2014. doi: 10.1080/00102202.2013.876420.

[54] B. Ćosić, S. Terhaar, J. P. Moeck, and C. O. Paschereit. Response of a swirl-stabilized flame to simultaneous perturbations in equivalence ratio and velocity at high oscillation amplitudes. *Combustion and Flame*, 162(4):1046–1062, 2015. doi: 10.1016/j.combustflame.2014.09.025.

[55] E. Cuadra. Acoustic Wave Generation by Entropy Discontinuities Flowing Past an Area Change. *The Journal of the Acoustical Society of America*, 42(4):725–732, 1967. doi: 10.1121/1.1910643.

[56] F. E. C. Culick. *Unsteady Motions in Combustion Chambers for Propulsion Systems*. Number AC/323(AVT-039)TP/103 in RTO AGARDograph. Research and Technology Organisation/North Atlantic Treaty Organisation, Neuilly-sur-Seine Cedex, France, 2006. ISBN 92-837-0059-7.

[57] N. A. Cumpsty and F. E. Marble. *The Generation of Noise by the Fluctuations in Gas Temperature into a Turbine*. Caltech Library, Pasadena, California, USA, 1974.

[58] N. A. Cumpsty and F. E. Marble. The Interaction of Entropy Fluctuations with Turbine Blade Rows; A Mechanism of Turbojet Engine Noise. *Proceedings of the Royal Society A*, 357:323–344, 1977. doi: 10.1098/rspa.1977.0171.

[59] F. De Domenico, E. O. Rolland, and S. Hochgreb. A generalised model for acoustic and entropic transfer function of nozzles with losses. *Journal of Sound and Vibration*, 440:212–230, 2019. doi: 10.1016/j.jsv.2018.09.011.

[60] F. De Domenico, E. O. Rolland, J. Rodrigues, L. Magri, and S. Hochgreb. Compositional and entropy indirect noise generated in subsonic non-isentropic nozzles. *Journal of Fluid Mechanics*, 910:A5, 2021. doi: 10.1017/jfm.2020.916.

[61] J. A. De Gouw, D. D. Parrish, G. J. Frost, and M. Trainer. Reduced emissions of CO_2, NO_X, and SO_2 from U.S. power plants owing to switch from coal to natural gas with combined cycle technology. *Earth's Future*, 2(2):75–82, 2014. doi: 10.1002/2013EF000196.

[62] J. Donéa and A. Huerta. *Finite Element Methods for Flow Problems*. Wiley, Chichester ; Hoboken, New Jersey, USA, 2003. ISBN 978-0-471-49666-3.

[63] A. P. Dowling. The Calculation of Thermoacoustic Oscillation. *Journal of Sound and Vibration*, 180(4):557–581, 1995. doi: 10.1006/jsvi.1995.0100.

[64] A. P. Dowling. Thermoacoustic Instability. In *6th International Congress on Sound and Vibration*, Copenhagen, Denmark, July 1999. International Institute of Acoustics and Vibration.

[65] A. P. Dowling and S. R. Stow. Acoustic Analysis of Gas Turbine Combustors. *Journal of Propulsion and Power*, 19(5):751–764, 2003. doi: 10.2514/2.6192.

[66] S. Ducruix, D. Durox, and S. Candel. Theoretical and experimental determinations of the transfer function of a laminar premixed flame. *Proceedings of the Combustion Institute*, 28(1):765–773, 2000. doi: 10.1016/S0082-0784(00)80279-9.

[67] I. Duran and S. Moreau. Solution of the quasi-one-dimensional linearized Euler equations using flow invariants and the Magnus expansion. *Journal of Fluid Mechanics*, 723: 190–231, 2013. doi: 10.1017/jfm.2013.118.

[68] I. Duran, S. Moreau, F. Nicoud, T. Livebardon, E. Bouty, and T. Poinsot. Combustion Noise in Modern Aero-Engines. *Journal AerospaceLab*, 7:1–11, 2014. doi: 10.12762/2014.AL07-05.

[69] P. Durrieu, G. Hofmans, G. Ajello, R. Boot, Y. Auregan, A. Hirschberg, and M. C. A. M. Peters. Quasisteady Aero-Acoustic Response of Orifices. *Journal of Acoustical Society of America*, 110(4):1859–1872, 2001. doi: 10.1121/1.1398058.

[70] J. Eckstein and T. Sattelmayer. Low-order modeling of low-frequency combustion instabilities in aeroengines. *Journal of Propulsion and Power*, 22(2):425–432, 2006. doi: 10.2514/1.15757.

[71] A. J. Eder, B. Dharmaputra, M. Désor, C. F. Silva, A. M. Garcia, B. Schuermans, N. Noiray, and W. Polifke. Generation of Entropy Waves by Fully Premixed Flames in a Non-Adiabatic Combustor with Hydrogen Enrichment. *Journal of Engineering for Gas Turbines and Power*, 145(11):111001, 2023. doi: 10.1115/1.4063283.

[72] A. J. Eder, A. Fischer, C. Lahiri, M. Merk, M. Staufer, R. Eggels, C. F. Silva, and W. Polifke. Identification of the dynamics of a turbulent spray flame at high pressure. In *Symposium on Thermoacoustics in Combustion*, Zurich, Switzerland, Sept. 2023.

[73] A. J. Eder, M. Merk, T. Hollweck, A. Fischer, C. Lahiri, C. F. Silva, and W. Polifke. Model-based inference of flame transfer matrices from acoustic measurements in an aero-engine test rig. In *Proceedings of the ASME Turbo Expo 2024: Turbomachinery Technical Conference & Exposition*, London, UK, 2024. ASME. doi: 10.1115/GT2024-124263.

[74] A. J. Eder, M. Merk, T. Hollweck, A. Fischer, C. Lahiri, C. F. Silva, and W. Polifke. Model-based inference of flame transfer matrices from acoustic measurements in an aero-engine test rig. *Journal of Engineering for Gas Turbines and Power*, 147(3):031022, 2025. doi: 10.1115/1.4066366.

[75] T. Emmert, S. Bomberg, and W. Polifke. Intrinsic Thermoacoustic Instability of Premixed Flames. *Combustion and Flame*, 162(1):75–85, 2015. doi: 10.1016/j.combustflame.2014.06.008.

[76] T. Emmert, M. Meindl, S. Jaensch, and W. Polifke. Linear State Space Interconnect Modeling of Acoustic Systems. *Acta Acustica united with Acustica*, 102(5):824–833, 2016. doi: 10.3813/AAA.918997.

[77] R. Ewert and W. Schröder. Acoustic perturbation equations based on flow decomposition via source filtering. *Journal of Computational Physics*, 188(2):365–398, 2003. doi: 10.1016/S0021-9991(03)00168-2.

[78] H. Farhat and C. Salvini. Novel Gas Turbine Challenges to Support the Clean Energy Transition. *Energies*, 15(15):5474, 2022. doi: 10.3390/en15155474.

[79] A. Fattahi, N. Karimi, and N. Hajialigol. Dynamics of entropy wave generation in a simplified model of gas turbine combustor: A theoretical investigation. *Physics of Fluids*, 32(10):106107, 2020. doi: 10.1063/5.0021729.

[80] J. E. Ffowcs Williams and M. S. Howe. The Generation of Sound by Density Inhomogeneities in Low Mach Number Nozzle Flows. *Journal of Fluid Mechanics*, 70(3):605–622, 1975. doi: 10.1017/S0022112075002224.

[81] A. Fick. On liquid diffusion. *Journal of Membrane Science*, 100(1):33–38, 1995. doi: 10.1016/0376-7388(94)00230-V.

[82] A. Fischer and C. Lahiri. Ranking of aircraft fuel-injectors regarding low frequency thermoacoustics based on an energy balance method. In *Proceedings of the ASME Turbo Expo 2021: Turbomachinery Technical Conference and Exposition. Volume 3B: Combustion, Fuels, and Emissions*, Virtual, Online, June 2021. ASME. doi: 10.1115/GT2021-59561.

[83] A. Fischer, C. Lahiri, and T. Doerr. Design, build, and commissioning of the new thermo-acoustics combustion test rig Scarlet. Technical Report DLRK2017-450116, Rolls-Royce Deutschland, 2017.

[84] G. J. J. Fournier, M. Haeringer, C. F. Silva, and W. Polifke. Low-Order Modeling to Investigate Clusters of Intrinsic Thermoacoustic Modes in Annular Combustors. *Journal of Engineering for Gas Turbines and Power*, 143(4):041025, 2021. doi: 10.1115/1.4049356.

[85] G. J. J. Fournier, F. Schaefer, M. Haeringer, C. F. Silva, and W. Polifke. Interplay of Clusters of Acoustic and Intrinsic Thermoacoustic Modes in Can-Annular Combustors. *Journal of Engineering for Gas Turbines and Power*, 144(12):121015, 2022. doi: 10.1115/1.4055381.

[86] F. Gant, A. Gruber, and M. R. Bothien. Development and validation study of a 1D analytical model for the response of reheat flames to entropy waves. *Combustion and Flame*, 222:305–316, 2020. doi: 10.1016/j.combustflame.2020.09.005.

[87] F. Gant, B. Bunkute, and M. R. Bothien. Reheat flames response to entropy waves. *Proceedings of the Combustion Institute*, 38(4):6271–6278, 2021. doi: 10.1016/j.proci.2020.05.007.

[88] F. Gant, A. Cuquel, and M. R. Bothien. Autoignition flame transfer matrix: Analytical model versus large eddy simulations. *International Journal of Spray and Combustion Dynamics*, 14(1-2):72–81, 2022. doi: 10.1177/17568277221086261.

[89] G. Geiser, H. Nawroth, A. Hosseinzadeh, F. Zhang, H. Bockhorn, P. Habisreuther, J. Janicka, C. O. Paschereit, and W. Schroeder. Thermoacoustics of a turbulent premixed flame. In *20th AIAA/CEAS Aeroacoustics Conference*, Atlanta, Georgia, USA, June 2014. American Institute of Aeronautics and Astronautics. doi: 10.2514/6.2014-2476.

[90] K. J. George and R. Sujith. Disturbance energy norms: A critical analysis. *Journal of Sound and Vibration*, 331(7):1552–1566, 2012. doi: 10.1016/j.jsv.2011.11.027.

[91] K. J. George and R. I. Sujith. On Chu's disturbance energy. *Journal of Sound and Vibration*, 330(22):5280–5291, 2011. doi: http://dx.doi.org/10.1016/j.jsv.2011.06.016.

[92] J. Gikadi. *Prediction of Acoustic Modes in Combustors Using Linearized Navier-Stokes Equations in Frequency Space*. PhD thesis, Technical University of Munich, München, Germany, 2013.

[93] J. Gikadi, T. Sattelmayer, and A. Peschiulli. Effects of the mean flow field on the thermoacoustic stability of aero-engine combustion chambers. In *Proceedings of the ASME Turbo Expo 2012: Turbine Technical Conference and Exposition. Volume 2: Combustion, Fuels and Emissions, Parts A and B*, pages 1203–1211, Copenhagen, Denmark, June 2012. ASME. doi: 10.1115/GT2012-69612.

[94] H. S. Gopalakrishnan, A. Gruber, and J. Moeck. Response of Auto-Ignition-Stabilized Flames to One-Dimensional Disturbances: Intrinsic Response. *Journal of Engineering for Gas Turbines and Power*, 143(12):121011, 2021. doi: 10.1115/1.4052058.

[95] H. S. Gopalakrishnan, A. Gruber, and J. P. Moeck. Computation and prediction of intrinsic thermoacoustic oscillations associated with autoignition fronts. *Combustion and Flame*, 254:112844, 2023. doi: 10.1016/j.combustflame.2023.112844.

[96] Government of India. India's Long-Term Low-Carbon Development Strategy. `https://unfccc.int/sites/default/files/resource/India_LTLEDS.pdf`, Nov. 2022. (Last accessed: Aug. 14, 2024).

[97] Government of the Federal Republic of Germany. Update to the long-term strategy for climate action of the Federal Republic of Germany. https://unfccc.int/sites/default/files/resource/Anlage%202_Update%20to%20the%20long-term%20strategy%20for%20climate%20action%20of%20the%20Federal%20Republic%20of%20Germany_02Nov2022_0.pdf, Nov. 2022. (Last accessed: Aug. 14, 2024).

[98] Government of the People's Republic of China. China's Mid-Century Long-Term Low Greenhouse Gas Emission Development Strategy. https://unfccc.int/sites/default/files/resource/China%E2%80%99s%20Mid-Century%20Long-Term%20Low%20Greenhouse%20Gas%20Emission%20Development%20Strategy.pdf, Oct. 2021. (Last accessed: Aug. 14, 2024).

[99] C. J. Goy, S. R. James, and S. Rea. Monitoring Combustion Instabilities: E.ON UK's Experience. In *Combustion Instabilities In Gas Turbine Engines: Operational Experience, Fundamental Mechanisms, and Modeling*, pages 163–175. American Institute of Aeronautics and Astronautics, Reston, Virginia, USA, 2006. doi: 10.2514/5.9781600866807.0163.0175.

[100] G. Guandalini, S. Campanari, and M. C. Romano. Power-to-gas plants and gas turbines for improved wind energy dispatchability: Energy and economic assessment. *Applied Energy*, 147:117–130, 2015. doi: 10.1016/j.apenergy.2015.02.055.

[101] B. Gustavsen and A. Semlyen. Rational approximation of frequency domain responses by vector fitting. *IEEE Transactions on Power Delivery*, 14(3):1052–1061, 1999. doi: 10.1109/61.772353.

[102] S. Güttel and F. Tisseur. The nonlinear eigenvalue problem. *Acta Numerica*, 26:1–94, 2017. doi: 10.1017/S0962492917000034.

[103] J. Guzmán-Iñigo, D. Yang, R. Gaudron, and A. S. Morgans. On the scattering of entropy waves at sudden area expansions. *Journal of Sound and Vibration*, 540:117261, 2022. doi: 10.1016/j.jsv.2022.117261.

[104] G. Heilmann. *A Consistent Helmholtz Framework for the Accurate Prediction of Linear and Nonlinear Thermoacoustic Stability in Gas Turbine Combustors*. PhD thesis, Technical University of Munich, Garching, Germany, 2023.

[105] G. Heilmann, T. Liu, P. Romero Vega, and T. Sattelmayer. A Novel Decomposition Approach Preventing Spurious Entropy Generation in Hybrid Thermoacoustic Stability Computations. *Journal of Engineering for Gas Turbines and Power*, 144(9):091013, 2022. doi: 10.1115/1.4055189.

[106] W. D. Heiss. The physics of exceptional points. *Journal of Physics A: Mathematical and Theoretical*, 45(44):444016, 2012. doi: 10.1088/1751-8113/45/44/444016.

[107] P. A. Hield, M. J. Brear, and S. H. Jin. Thermoacoustic Limit Cycles in a Premixed Laboratory Combustor with Open and Choked Exits. *Combustion and Flame*, 156(9):1683–1697, 2009. doi: 10.1016/j.combustflame.2009.05.011.

[108] B. Higgins, M. Q. McQuay, F. Lacas, J. C. Rolon, N. Darabiha, and S. Candel. Systematic measurements of OH chemiluminescence for fuel-lean, high-pressure, premixed, laminar Flames. *Fuel*, 80(1):67–74, 2001. doi: 10.1016/S0016-2361(00)00069-7.

[109] J. O. Hirschfelder, C. F. Cutriss, and R. B. Bird. *Molecular Theory of Gases and Liquids*. Wiley \& Sons Ltd, New York, New York, USA, 1966. ISBN 978-0-471-40065-3.

[110] M. Hoeijmakers, V. Kornilov, I. Lopez Arteaga, P. de Goey, and H. Nijmeijer. Intrinsic Instability of Flame-Acoustic Coupling. *Combustion and Flame*, 161(11):2860–2867, 2014. doi: 10.1016/j.combustflame.2014.05.009.

[111] T. Hofmeister, T. Hummel, B. Schuermans, and T. Sattelmayer. Quantification of Energy Transformation Processes Between Acoustic and Hydrodynamic Modes in Non-Compact Thermoacoustic Systems via a Helmholtz-Hodge Decomposition Approach. In *Proceedings of the ASME Turbo Expo 2019: Turbomachinery Technical Conference and Exposition. Volume 4A: Combustion, Fuels, and Emissions*, Phoenix, Arizona, USA, June 2019. ASME. doi: 10.1115/GT2019-90240.

[112] T. Hofmeister, T. Hummel, B. Schuermans, and T. Sattelmayer. Modeling and Quantification of Acoustic Damping Induced by Vortex Shedding in Noncompact Thermoacoustic Systems. *Journal of Engineering for Gas Turbines and Power*, 142(3):031016, 2020. doi: 10.1115/1.4044936.

[113] T. Hollweck. *Extended Model-Based Inference of Flame Transfer Matrices from Acoustic Measurements*. Semester Thesis, Technical University of Munich, Garching, Germany, 2024.

[114] N. Hosseini, V. Kornilov, I. Lopez Arteaga, W. Polifke, O. Teerling, and L. de Goey. Intrinsic thermoacoustic modes and their interplay with acoustic modes in a Rijke burner. *International Journal of Spray and Combustion Dynamics*, 10(4):315–325, 2018. doi: 10.1177/1756827718782884.

[115] A. S. Householder. *The Numerical Treatment of a Single Nonlinear Equation*. McGraw-Hill, London, UK, 1970. ISBN 978-0-07-030465-9.

[116] M. S. Howe. Contributions to the Theory of Aerodynamic Sound, with Application to Excess Jet Noise and the Theory of the Flute. *Journal of Fluid Mechanics*, 71(4):625–673, 1975. doi: 10.1017/S0022112075002777.

[117] M. S. Howe and J. T. C. Liu. The generation of sound by vorticity waves in swirling duct flows. *Journal of Fluid Mechanics*, 81(2):369–383, 1977. doi: 10.1017/S0022112077002109.

[118] Y. Huang and V. Yang. Dynamics and Stability of Lean-Premixed Swirl-Stabilized Combustion. *Progress in Energy and Combustion Science*, 35(4):293–364, 2009. doi: 10.1016/j.pecs.2009.01.002.

[119] M. Ihme. Combustion and Engine-Core Noise. *Annual Review of Fluid Mechanics*, 49 (1):277–310, 2017. doi: 10.1146/annurev-fluid-122414-034542.

[120] Intergovernmental Panel on Climate Change (IPCC). *Climate Change 2023: Synthesis Report. Contribution of Working Groups I, II and III to the Sixth Assessment Report of the Intergovernmental Panel on Climate Change [Core Writing Team, H. Lee and J. Romero (Eds.)]. IPCC, Geneva, Switzerland.* WMO, Geneva, Switzerland, 1 edition, 2023. doi: 10.59327/IPCC/AR6-9789291691647.

[121] Intergovernmental Panel On Climate Change (IPCC). *Climate Change 2021 – The Physical Science Basis: Working Group I Contribution to the Sixth Assessment Report of the Intergovernmental Panel on Climate Change*. Cambridge University Press, 1 edition, 2023. doi: 10.1017/9781009157896.

[122] J. P. Johnston and W. E. Schmidt. Measurement of acoustic reflection from an obstruction in a pipe with flow. *The Journal of the Acoustical Society of America*, 63(5):1455–1460, 1978. doi: 10.1121/1.381891.

[123] M. P. Juniper. Sensitivity analysis of thermoacoustic instability with adjoint Helmholtz solvers. *Physical Review Fluids*, 3(11):110509, 2018. doi: 10.1103/PhysRevFluids.3.110509.

[124] M. P. Juniper and M. Yoko. Generating a physics-based quantitatively-accurate model of an electrically-heated Rijke tube with Bayesian inference. *Journal of Sound and Vibration*, 535:117096, 2022. doi: 10.1016/j.jsv.2022.117096.

[125] S. Kaji and T. Okazaki. Propagation of Sound Waves Through a Blade Row: I. Analysis Based on the Semi-Actuator Disk Theory. *Journal of Sound and Vibration*, 11(3):339–353, 1970. doi: 10.1016/S0022-460X(70)80038-4.

[126] S. Kaji and T. Okazaki. Propagation of sound waves through a blade row. II. Analysis based on the acceleration potential method. *Journal of Sound and Vibration*, 11(3):355–375, 1970. doi: 10.1016/S0022-460X(70)80039-6.

[127] M. Karlsson and M. Åbom. Quasi-steady model of the acoustic scattering properties of a T-junction. *Journal of Sound and Vibration*, 330(21):5131–5137, 2011. doi: 10.1016/j.jsv.2011.05.012.

[128] D. Kaufman. *Chapter 2 of the Working Group I Contribution to the IPCC Sixth Assessment Report - Data for CCB 2.1, Figure 1 V20221114*. NERC EDS Centre for Environmental Data Analysis, 2023. doi: 10.5285/0F05C2FB8F814D60AC2D657A70E9A7F5.

[129] J. Kaufmann, M. Vogel, J. Papenbrock, and T. Sattelmayer. Comparison of the flame dynamics of a premixed dual fuel burner for kerosene and natural gas. *International Journal of Spray and Combustion Dynamics*, 14(1-2):176–185, 2022. doi: 10.1177/17568277221091405.

[130] M. V. Keldysh. On the Completeness of the Eigenfunctions of Some Classes of Non-Selfadjoint Linear Operators. *Russian Mathematical Surveys*, 26(4):15–44, 1971. doi: 10.1070/RM1971v026n04ABEH003985.

[131] J. J. Keller. Thermoacoustic Oscillations in Combustion Chambers of Gas Turbines. *AIAA Journal*, 33(12):2280–2287, 1995. doi: 10.2514/3.12980.

[132] J. J. Keller, W. Egli, and J. Hellat. Thermally Induced Low-Frequency Oscillations. *Zeitschrift für angewandte Mathematik und Physik (ZAMP)*, 36(2):250–274, 1985. doi: 10.1007/BF00945460.

[133] J. O. Keller and K. Saito. Measurements of the Combusting Flow in a Pulse Combustor. *Combustion Science and Technology*, 53(2-3):137–163, 1987. doi: 10.1080/00102208708947024.

[134] A. Kierkegaard, S. Boij, and G. Efraimsson. A frequency domain linearized Navier-Stokes equations approach to acoustic propagation in flow ducts with sharp edges. *The Journal of the Acoustical Society of America*, 127(2):710–719, 2010. doi: 10.1121/1.3273899.

[135] A. Kierkegaard, S. Allam, G. Efraimsson, and M. Åbom. Simulations of whistling and the whistling potentiality of an in-duct orifice with linear aeroacoustics. *Journal of Sound and Vibration*, 331(5):1084–1096, 2012. doi: 10.1016/j.jsv.2011.10.028.

[136] A. Kierkegaard, S. Boij, and G. Efraimsson. Simulations of the scattering of sound waves at a sudden area expansion. *Journal of Sound and Vibration*, 331(5):1068–1083, 2012. doi: 10.1016/j.jsv.2011.09.011.

[137] N. Kings and F. Bake. Indirect Combustion Noise: Noise Generation by Accelerated Vorticity in a Nozzle Flow. *International Journal of Spray and Combustion Dynamics*, 2 (3):253–266, 2010. doi: 10.1260/1756-8277.2.3.253.

[138] T. Kitano, K. Kaneko, R. Kurose, and S. Komori. Large-eddy simulations of gas- and liquid-fueled combustion instabilities in back-step flows. *Combustion and Flame*, 170:63–78, 2016. doi: 10.1016/j.combustflame.2016.05.005.

[139] M. Klein. Overview of Worldwide Ground-Based Regulatory Framework. In T. C. Lieuwen and V. Yang, editors, *Gas Turbine Emissions*, pages 95–120. Cambridge University Press, Cambridge, UK, 1 edition, 2013. ISBN 978-0-521-76405-6 978-1-139-01546-2. doi: 10.1017/CBO9781139015462.007.

[140] T. Komarek and W. Polifke. Impact of Swirl Fluctuations on the Flame Response of a Perfectly Premixed Swirl Burner. *Engineering for Gas Turbines and Power*, 132(6):061503, 2010. doi: 10.1115/1.4000127.

[141] B. Kroposki, B. Johnson, Y. Zhang, V. Gevorgian, P. Denholm, B.-M. Hodge, and B. Hannegan. Achieving a 100% Renewable Grid: Operating Electric Power Systems with Extremely High Levels of Variable Renewable Energy. *IEEE Power and Energy Magazine*, 15(2):61–73, 2017. doi: 10.1109/MPE.2016.2637122.

[142] S. Kulkarni, C. F. Silva, and W. Polifke. Response of Spray Number Density and Evaporation Rate to Velocity Oscillations. *Int. J. Spray Comb. Dynamics*, 14(1-2):107–117, 2022. doi: 10.1177/17568277221085957.

[143] D. Laera, K. Prieur, D. Durox, T. Schuller, S. M. Camporeale, and S. Candel. Impact of Heat Release Distribution on the Spinning Modes of an Annular Combustor With Multiple Matrix Burners. *Journal of Engineering for Gas Turbines and Power*, 139(5):051505, 2017. doi: 10.1115/1.4035207.

[144] M. Leyko, F. Nicoud, and T. Poinsot. Comparison of Direct and Indirect Combustion Noise Mechanisms in a Model Combustor. *AIAA Journal*, 47(11):2709–2716, 2009. doi: 10.2514/1.43729.

[145] M. Leyko, I. Duran, S. Moreau, F. Nicoud, and T. Poinsot. Simulation and modelling of the waves transmission and generation in a stator blade row in a combustion-noise framework. *Journal of Sound and Vibration*, 333(23):6090–6106, 2014. doi: 10.1016/j.jsv.2014.06.034.

[146] J. Li and A. S. Morgans. Simplified models for the thermodynamic properties along a combustor and their effect on thermoacoustic instability prediction. *Fuel*, 184:735–748, 2016. doi: 10.1016/j.fuel.2016.07.050.

[147] T. Lieuwen and V. Yang, editors. *Combustion Instabilities in Gas Turbine Engines: Operational Experience, Fundamental Mechanisms and Modeling*, volume 210 of *Progress in Astronautics and Aeronautics*. American Institute of Aeronautics and Astronautics, Reston, Virginia, USA, 2006. ISBN 978-1-56347-669-3.

[148] T. Lieuwen, Y. Neumeier, and B. Zinn. The Role of Unmixedness and Chemical Kinetics in Driving Combustion Instabilities in Lean Premixed Combustors. *Combustion Science and Technology*, 135(1-6):193–211, 1998. doi: 10.1080/00102209808924157.

[149] T. Lieuwen, V. McDonell, E. Petersen, and D. Santavicca. Fuel Flexibility Influences on Premixed Combustor Blowout, Flashback, Autoignition, and Stability. *Journal of Engineering for Gas Turbines and Power*, 130(1):011506, 2008. doi: 10.1115/1.2771243.

[150] T. C. Lieuwen. *Unsteady Combustor Physics*. Cambridge University Press, New York, New York, USA, 2 edition, 2021. ISBN 978-1-108-88900-1.

[151] Y. Liu, X. Sun, V. Sethi, D. Nalianda, Y.-G. Li, and L. Wang. Review of modern low emissions combustion technologies for aero gas turbine engines. *Progress in Aerospace Sciences*, 94:12–45, 2017. doi: 10.1016/j.paerosci.2017.08.001.

[152] D. J. MacKay. *Information Theory, Inference, and Learning Algorithms*. Cambridge University Press, New York, New York, USA, 2003. ISBN 978-0-521-64298-9.

[153] L. Magri. On indirect noise in multicomponent nozzle flows. *Journal of Fluid Mechanics*, 828:R2, 2017. doi: 10.1017/jfm.2017.591.

[154] L. Magri, J. O'Brien, and M. Ihme. Compositional inhomogeneities as a source of indirect combustion noise. *Journal of Fluid Mechanics*, 799:R4, 2016. doi: 10.1017/jfm.2016.397.

[155] F. E. Marble and S. M. Candel. Acoustic Disturbance from Gas Non-Uniformities Convected Through a Nozzle. *Journal of Sound and Vibration*, 55(2):225–243, 1977. doi: 10.1016/0022-460X(77)90596-X.

[156] M. March, J. Renner, and T. Sattelmayer. Acoustic and Optical Investigations of the Flame Dynamics of Rich and Lean Kerosene Flames in the Primary Zone of an Air-Staged Combustion Test-Rig. *Journal of Engineering for Gas Turbines and Power*, 146 (1):011004, 2024. doi: 10.1115/1.4063380.

[157] K. R. McManus, T. Poinsot, and S. M. Candel. A Review of Active Control of Combustion Instabilities. *Progress in Energy and Combustion Science*, 19(1):1–29, 1993. doi: 10.1016/0360-1285(93)90020-F.

[158] M. Meindl. *Linearized Modeling of Thermoacoustic Systems Utilizing a Discontinuous Galerkin Finite Element Method*. PhD thesis, Technical University of Munich, Garching, Germany, 2022.

[159] M. Meindl, M. Merk, F. Fritz, and W. Polifke. Determination of acoustic scattering matrices from linearized compressible flow equations. *Journal of Theoretical and Computational Acoustics*, 27(3):1850027, 2018. doi: 10.1142/S2591728518500275.

[160] M. Meindl, A. Albayrak, and W. Polifke. A state-space formulation of a discontinuous Galerkin method for thermoacoustic stability analysis. *Journal of Sound and Vibration*, 481:115431, 2020. doi: 10.1016/j.jsv.2020.115431.

[161] M. Meindl, C. F. Silva, and W. Polifke. On the spurious entropy generation encountered in hybrid linear thermoacoustic models. *Combustion and Flame*, 223:525–540, 2021. doi: 10.1016/j.combustflame.2020.09.018.

[162] G. A. Mensah and J. P. Moeck. Acoustic Damper Placement and Tuning for Annular Combustors: An Adjoint-Based Optimization Study. *Journal of Engineering for Gas Turbines and Power*, 139(6):061501, 2017. doi: 10.1115/1.4035201.

[163] G. A. Mensah, L. Magri, C. F. Silva, P. E. Buschmann, and J. P. Moeck. Exceptional points in the thermoacoustic spectrum. *Journal of Sound and Vibration*, 433:124–128, 2018. doi: 10.1016/j.jsv.2018.06.069.

[164] G. A. Mensah, P. E. Buschmann, and A. Orchini. Iterative solvers for the thermoacoustic nonlinear eigenvalue problem and their convergence properties. *International Journal of Spray and Combustion Dynamics*, 14(1-2):30–41, 2022. doi: 10.1177/17568277221084464.

[165] H. J. Merk. Analysis of heat-driven oscillations of gas flows. *Applied Scientific Research, Section A*, 6:317–336, 1956. doi: 10.1007/BF03184653.

[166] M. Merk, P. E. Buschmann, J. P. Moeck, and W. Polifke. The nonlinear thermoacoustic eigenvalue problem and its rational approximations: Assessment of solution strategies. In *Proceedings of the ASME Turbo Expo 2022: Turbomachinery Technical Conference and Exposition. Volume 3A: Combustion, Fuels, and Emissions*, Rotterdam, Netherlands, June 2022. ASME. doi: 10.1115/GT2022-79653.

[167] M. Merk, P. E. Buschmann, J. P. Moeck, and W. Polifke. The Nonlinear Thermoacoustic Eigenvalue Problem and Its Rational Approximations: Assessment of Solution Strategies. *Journal of Engineering for Gas Turbines and Power*, 145(2):021028, 2023. doi: 10.1115/1.4055583.

[168] M. Merk, A. J. Eder, and W. Polifke. An Arbitrary Lagrangian-Eulerian framework for the consistent analysis of entropy wave generation. *Combustion and Flame*, 262:113334, 2024. doi: 10.1016/j.combustflame.2024.113334.

[169] M. Merk, F. Schily, and W. Polifke. A Jacobian-based framework for the derivation of comprehensive thermoacoustic jump conditions. *Combustion and Flame*, 274:113958, 2025. doi: 10.1016/j.combustflame.2024.113958.

[170] Y. Méry. Impact of Heat Release Global Fluctuations and Flame Motion on Transverse Acoustic Wave Stability. *Proceedings of the Combustion Institute*, 36(3):3889–3898, 2017. doi: 10.1016/j.proci.2016.08.009.

[171] Y. Méry. Dynamical response of a perfectly premixed flame and limit behavior for high power density systems. *Combustion and Flame*, 192:410–425, 2018. doi: 10.1016/j.combustflame.2018.02.007.

[172] Y. Méry, L. Hakim, P. Scouflaire, L. Vingert, S. Ducruix, and S. Candel. Experimental investigation of cryogenic flame dynamics under transverse acoustic modulations. *Comptes Rendus Mécanique*, 341(1-2):100–109, 2013. doi: 10.1016/j.crme.2012.10.013.

[173] J. P. Moeck. *Analysis , Modeling , and Control of Thermoacoustic Instabilities*. PhD thesis, Technische Universität Berlin, Berlin, Germany, 2010.

[174] J. P. Moeck, M. Paul, and C. O. Paschereit. Thermoacoustic Instabilities in an Annular Rijke Tube. In *Proceedings of the ASME Turbo Expo 2010: Power for Land, Sea, and Air. Volume 2: Combustion, Fuels and Emissions, Parts A and B*, Glasgow, UK, June 2010. ASME. doi: 10.1115/GT2010-23577.

[175] C. L. Morfey. Acoustic energy in non-uniform flows. *Journal of Sound and Vibration*, 14(2):159–170, 1971. doi: 10.1016/0022-460X(71)90381-6.

[176] A. S. Morgans and I. Duran. Entropy Noise: A Review of Theory, Progress and Challenges. *International Journal of Spray and Combustion Dynamics*, 8(4):285–298, 2016. doi: 10.1177/1756827716651791.

[177] R. Muir. The application of a semi-actuator disk model to sound transmission calculations in turbomachinery, part I: The single blade row. *Journal of Sound and Vibration*, 54(3):393–408, 1977. doi: 10.1016/0022-460X(77)90448-5.

[178] R. Muir. The application of a semi-actuator disk model to sound transmission calculations in turbomachinery, part II: Multiple blade rows. *Journal of Sound and Vibration*, 55(3):335–349, 1977. doi: 10.1016/S0022-460X(77)80017-5.

[179] M. Myers. Transport of Energy by Disturbances in Arbitrary Steady Flows. *Journal of Fluid Mechanics*, 226:383–400, 1991. doi: 10.1017/S0022112091002434.

[180] M. Namba and K. Fukushige. Application of the equivalent surface source method to the acoustics of duct systems with non-uniform wall impedance. *Journal of Sound and Vibration*, 73(1):125–146, 1980. doi: 10.1016/0022-460X(80)90497-6.

[181] F. Nicoud and T. Poinsot. Thermoacoustic instabilities: Should the Rayleigh criterion be extended to include entropy changes? *Combust. and Flame*, 142(1-2):153–159, 2005. doi: 10.1016/j.combustflame.2005.02.013.

[182] F. Nicoud, L. Benoit, C. Sensiau, and T. Poinsot. Acoustic Modes in Combustors with Complex Impedances and Multidimensional Active Flames. *AIAA Journal*, 45(2):426–441, 2007. doi: 10.2514/1.24933.

[183] OECD. *World Energy Outlook 2023*. World Energy Outlook. OECD, Oct. 2023. ISBN 978-92-64-64773-2. doi: 10.1787/827374a6-en.

[184] A. Orchini, T. Pedergnana, P. E. Buschmann, J. P. Moeck, and N. Noiray. Reduced-order modelling of thermoacoustic instabilities in can-annular combustors. *Journal of Sound and Vibration*, 526:116808, 2022. doi: 10.1016/j.jsv.2022.116808.

[185] H. Padé. Sur la représentation approchée d'une fonction par des fractions rationnelles. *Annales scientifiques de l'École normale supérieure*, 9:3–93, 1892. doi: 10.24033/asens.378.

[186] C. O. Paschereit and W. Polifke. Characterization of Lean Premixed Gas Turbine Burners as Acoustic Multi-Ports. In *APS/DFD Annual Meeting*, San Francisco, California, USA, Nov. 1997. APS.

[187] C. O. Paschereit and W. Polifke. Investigation of the Thermo-Acoustic Characteristics of a Lean Premixed Gas Turbine Burner. In *Proceedings of the ASME 1998 International Gas Turbine and Aeroengine Congress and Exhibition. Volume 3: Coal, Biomass and Alternative Fuels; Combustion and Fuels; Oil and Gas Applications; Cycle Innovations*, Stockholm, Sweden, June 1998. ASME. doi: 10.1115/98-GT-582.

[188] C. O. Paschereit, B. Schuermans, W. Polifke, and O. Mattson. Measurement of Transfer Matrices and Source Terms of Premixed Flames. *J. Eng. Gas Turbines and Power*, 124 (2):239–247, 2002. doi: 10.1115/1.1383255.

[189] K. Pausch, S. Herff, F. Zhang, H. Bockhorn, and W. Schröder. Noise sources of lean premixed flames. *Flow, Turbulence and Combustion*, 103(3):773–796, 2019. doi: 10.1007/s10494-019-00032-0.

[190] K. Pausch, S. Herff, and W. Schröder. Noise sources of an unconfined and a confined swirl burner. *Journal of Sound and Vibration*, 475:115293, 2020. doi: 10.1016/j.jsv.2020.115293.

[191] D. A. Pennell, M. R. Bothien, A. Ciani, V. Granet, G. Singla, S. Thorpe, A. Wickstroem, K. Oumejjoud, and M. Yaquinto. An Introduction to the Ansaldo GT36 Constant Pressure Sequential Combustor. In *Proceedings of the ASME Turbo Expo 2017: Turbomachinery Technical Conference and Exposition. Volume 4B: Combustion, Fuels and Emissions*, Charlotte, North Carolina, USA, June 2017. ASME. doi: 10.1115/GT2017-64790.

[192] M. Peters. *Aeroacoustic Sources in Internal Flows*. PhD thesis, Technische Universiteit Eindhoven, Eindhoven, Netherlands, 1993.

[193] M. C. A. M. Peters, A. Hirschberg, A. J. Reijnen, and A. P. J. Wijnands. Damping and Reflection Coefficient Measurements for an Open Pipe at Low Mach and Low Helmholtz Numbers. *Journal of Fluid Mechanics*, 256:499–534, 1993. doi: 10.1017/S0022112093002861.

[194] T. Poinsot. Prediction and Control of Combustion Instabilities in Real Engines. *Proceedings of the Combustion Institute*, 36(1):1–28, 2017. doi: 10.1016/j.proci.2016.05.007.

[195] T. Poinsot and D. Veynante. *Theoretical and Numerical Combustion*. CNRS, Toulouse, France, 3 edition, 2011. ISBN 978-2-7466-3990-4.

[196] T. Poinsot, F. Bourienne, S. Candel, E. Esposito, and W. Lang. Supression of combustion instabilities by active control. *Journal of Propulsion and Power*, 5(1):14–20, 1989. doi: 10.2514/3.23108.

[197] W. Polifke. Modeling and analysis of premixed flame dynamics by means of distributed time delays. *Progress in Energy and Combustion Science*, 79:100845, 2020. doi: 10.1016/j.pecs.2020.100845.

[198] W. Polifke, A. Poncet, C. O. Paschereit, and K. Döbbeling. Determination of (thermo-) acoustic transfer matrices by time-dependent numerical simulation. In *7th International Conference on Numerical Combustion*, York, UK, 1998.

[199] W. Polifke, C. O. Paschereit, and K. Döbbeling. Constructive and Destructive Interference of Acoustic and Entropy Waves in a Premixed Combustor with a Choked Exit. *International Journal of Acoustics and Vibration*, 6(3):135–146, 2001. doi: 10.20855/IJAV.2001.6.382.

[200] W. Polifke, A. Poncet, C. O. Paschereit, and K. Döbbeling. Reconstruction of Acoustic Transfer Matrices by Instationary Computational Fluid Dynamics. *Journal of Sound and Vibration*, 245(3):483–510, 2001. doi: 10.1006/jsvi.2001.3594.

[201] R. Price, I. Hurle, and T. Sugden. Optical studies of the generation of noise in turbulent flames. *Symposium (International) on Combustion*, 12(1):1093–1102, 1969. doi: 10.1016/S0082-0784(69)80487-X.

[202] J. W. S. Rayleigh. The Explanation of Certain Acoustical Phenomena. *Nature*, 18:319–321, 1878. doi: 10.1038/018319a0.

[203] J. Renner, M. March, T. A. Do, M. Merk, C. Hirsch, and T. Sattelmayer. Flame Transfer Functions of the Lean Burnout Zone of an RQL Combustion Chamber - Dynamic Response to Primary Zone and Mixing Port Velocity Fluctuations. *International Journal of Spray and Combustion Dynamics*, 15(2):175682772311591, 2023. doi: 10.1177/17568277231159172.

[204] O. Reynolds. IV. On the dynamical theory of incompressible viscous fluids and the determination of the criterion. *Philosophical Transactions of the Royal Society of London (A)*, 186:123–164, 1895. doi: 10.1098/rsta.1895.0004.

[205] G. A. Richards, D. L. Straub, and E. H. Robey. Passive control of combustion dynamics in stationary gas turbines. *Journal of Propulsion and Power*, 19(5):795–810, 2003. doi: 10.2514/2.6195.

[206] E. O. Rolland. *Sound Produced by Entropic and Compositional Inhomogeneities*. PhD thesis, University of Cambridge, Cambridge, UK, 2018.

[207] Y. Saad. *Numerical Methods for Large Eigenvalue Problems: Revised Edition*, volume 66 of *Classics in applied Mathematics*. SIAM, 2011.

[208] T. Sakurai and H. Sugiura. A projection method for generalized eigenvalue problems using numerical integration. *Journal of Computational and Applied Mathematics*, 159 (1):119–128, 2003. doi: 10.1016/S0377-0427(03)00565-X.

[209] T. Sattelmayer. Influence of the Combustor Aerodynamics on Combustion Instabilities From Equivalence Ratio Fluctuations. *Journal of Engineering for Gas Turbines and Power*, 125(1):11–19, 2003. doi: 10.1115/1.1365159.

[210] F. Schaefer and W. Polifke. Low-order network modeling of a duct with non-uniform cross-section and arbitrary mean temperature gradient in the presence of mean flow. In *AIAA Propulsion and Energy 2019 Forum*, Indianapolis, Indiana, USA, Aug. 2019. American Institute of Aeronautics and Astronautics. doi: 10.2514/6.2019-4376.

[211] F. Schaefer, S. Guo, and W. Polifke. The Impact of Exceptional Points on the Reliability of Thermoacoustic Stability Analysis. *Journal of Engineering for Gas Turbines and Power*, 143(2):021010, 2021. doi: 10.1115/1.4049351.

[212] S. Schimek, S. Göke, C. Schrödinger, and C. O. Paschereit. Flame Transfer Function Measurements With CH4 and H2 Fuel Mixtures at Ultra Wet Conditions in a Swirl Stabilized Premixed Combustor. In *Proceedings of the ASME Turbo Expo 2012: Turbine Technical Conference and Exposition. Volume 2: Combustion, Fuels and Emissions, Parts A and B*, Copenhagen, Denmark, June 2012. ASME. doi: 10.1115/GT2012-69788.

[213] M. Schmid, R. Blumenthal, M. Schulze, W. Polifke, and T. Sattelmayer. Quantitative Stability Analysis Using Real Frequency Response Data. *Journal of Engineering for Gas Turbines and Power*, 135(12):121601, 2013. doi: 10.1115/1.4025299.

[214] B. Schuermans. *Modeling and Control of Thermoacoustic Instabilities*. PhD thesis, úndefinedcole Polytechnique Fédérale de Lausanne, Lausanne, Switzerland, 2003.

[215] B. Schuermans, V. Bellucci, and C. O. Paschereit. Thermoacoustic Modeling and Control of Multi-Burner Combustion Systems. In *Proceedings of the ASME Turbo Expo 2003, collocated with the 2003 International Joint Power Generation Conference. Volume 2: Turbo Expo 2003*, Atlanta, Georgia, USA, June 2003. ASME. doi: 10.1115/GT2003-38688.

[216] B. Schuermans, V. Bellucci, F. Guethe, F. Meili, P. Flohr, and C. O. Paschereit. A Detailed Analysis of Thermoacoustic Interaction Mechanisms in a Turbulent Premixed Flame. In *ASME Turbo Expo 2004: Power for Land, Sea, and Air. Volume 1: Turbo Expo 2004*, Vienna, Austria, June 2004. ASME. doi: 10.1115/GT2004-53831.

[217] B. Schuermans, F. Guethe, and W. Mohr. Optical transfer function measurements for technically premixed flames. *Journal of Engineering for Gas Turbines and Power*, 132 (8):081501, 2010. doi: 10.1115/1.3124663.

[218] B. Schuermans, F. Guethe, D. Pennell, D. Guyot, and C. O. Paschereit. Thermoacoustic Modeling of a Gas Turbine Using Transfer Functions Measured Under Full Engine Pressure. *Journal of Engineering for Gas Turbines and Power*, 132(11):111503, 2010. doi: 10.1115/1.4000854.

[219] B. B. Schuermans, W. Polifke, and C. O. Paschereit. Modeling Transfer Matrices of Premixed Flames and Comparison With Experimental Results. In *Proceedings of the ASME 1999 International Gas Turbine and Aeroengine Congress and Exhibition. Volume 2: Coal, Biomass and Alternative Fuels; Combustion and Fuels; Oil and Gas Applications; Cycle Innovations*, Indianapolis, Indiana, USA, June 1999. ASME. doi: 10.1115/99-GT-132.

[220] O. Schulz and N. Noiray. Autoignition flame dynamics in sequential combustors. *Combustion and Flame*, 192:86–100, 2018. doi: 10.1016/j.combustflame.2018.01.046.

[221] M. Schulze, T. Hummel, N. Klarmann, F. M. Berger, B. Schuermans, and T. Sattelmayer. Linearized Euler Equations for the Prediction of Linear High-Frequency Stability in Gas Turbine Combustors. *Journal of Engineering for Gas Turbines and Power*, 139 (3):031510, 2017. doi: 10.1115/1.4034453.

[222] J. Schwing, F. Grimm, and T. Sattelmayer. A model for the thermo-acoustic feedback of transverse acoustic modes and periodic oscillations in flame position in cylindrical flame tubes. In *Proceedings of ASME Turbo Expo 2012: Turbine Technical Conference and Exposition. Volume 2: Combustion, Fuels and Emissions, Parts A and B*, Copenhagen, Denmark, June 2012. ASME. doi: 10.1115/GT2012-68775.

[223] A. F. Seybert and D. F. Ross. Experimental determination of acoustic properties using a two-microphone random-excitation technique. *The Journal of the Acoustical Society of America*, 61(5):1362–1370, 1977. doi: 10.1121/1.381403.

[224] C. F. Silva. Intrinsic thermoacoustic instabilities. *Progress in Energy and Combustion Science*, 95:101065, 2023. doi: 10.1016/j.pecs.2022.101065.

[225] K. O. Smith and J. Blust. Combustion Instabilities In Industrial Gas Turbines: Solar Turbines' Experience. In T. C. Lieuwen and V. Yang, editors, *Combustion Instabilities In Gas Turbine Engines*, pages 29–41. American Institute of Aeronautics and Astronautics, Reston, Virginia, USA, 2006. ISBN 978-1-56347-669-3 978-1-60086-680-7. doi: 10.2514/5.9781600866807.0029.0041.

[226] Y. Song, J. Li, and L. Yang. Effect of flame motion on longitudinal combustion instabilities. *Aerospace Science and Technology*, 122:107427, 2022. doi: 10.1016/j.ast.2022.107427.

[227] Y. Song, X. Liu, J. Li, and L. Yang. Effect of the flame motion on azimuthal combustion instabilities. *Aerospace Science and Technology*, 130:107930, 2022. doi: 10.1016/j.ast.2022.107930.

[228] G. W. Stewart. A Krylov–Schur Algorithm for Large Eigenproblems. *SIAM Journal on Matrix Analysis and Applications*, 23(3):601–614, 2002. doi: 10.1137/S0895479800371529.

[229] G. W. Stewart. Addendum to "A Krylov–Schur Algorithm for Large Eigenproblems". *SIAM Journal on Matrix Analysis and Applications*, 24(2):599–601, 2002. doi: 10.1137/S0895479802403150.

[230] L. Strobio Chen, S. Bomberg, and W. Polifke. Propagation and Generation of Acoustic and Entropy Waves Across a Moving Flame Front. *Combustion and Flame*, 166:170–180, 2016. doi: 10.1016/j.combustflame.2016.01.015.

[231] Y. Su and Z. Bai. Solving Rational Eigenvalue Problems via Linearization. *SIAM Journal on Matrix Analysis and Applications*, 32(1):201–216, 2011. doi: 10.1137/090777542.

[232] X. Sun, X. Wang, L. Du, and X. Jing. A new model for the prediction of turbofan noise with the effect of locally and non-locally reacting liners. *Journal of Sound and Vibration*, 316(1-5):50–68, 2008. doi: 10.1016/j.jsv.2008.02.053.

[233] The European Union and its Member States. Long-term low greenhouse gas emission development strategy of the European Union and its Member States. `https://unfccc.int/sites/default/files/resource/HR-03-06-2020%20EU%20Submission%20on%20Long%20term%20strategy.pdf`, Mar. 2020. (Last accessed: Aug. 14, 2024).

[234] The United States Department of State and the United States Executive Office of the President. The Long-Term Strategy of the United States: Pathways to Net-Zero Greenhouse Gas Emissions by 2050. `https://unfccc.int/sites/default/files/resource/US_accessibleLTS2021.pdf`, Nov. 2021. (Last accessed: Aug. 14, 2024).

[235] D. J. Torres and M. F. Trujillo. KIVA-4: An unstructured ALE code for compressible gas flow with sprays. *Journal of Computational Physics*, 219(2):943–975, 2006. doi: 10.1016/j.jcp.2006.07.006.

[236] N. C. W. Treleaven, A. Garmory, and G. J. Page. A Numerical Study on the Effects of Acoustic Forcing on Fuel Spray Dynamics in Gas Turbines. In *Proceedings of the ASME Turbo Expo 2020: Turbomachinery Technical Conference and Exposition. Volume 4A: Combustion, Fuels, and Emissions*, Virtual, Online, Sep 2020. ASME. doi: 10.1115/GT2020-14238.

[237] B. Trewin. *Global Temperature Time Series from IPCC AR6*. Zenodo, Mar. 2022. doi: 10.5281/ZENODO.6321535.

[238] United Nations. *The Paris Agreement*. United Nations Framework Convention on Climate Change, 2016.

[239] M. Van Barel and P. Kravanja. Nonlinear eigenvalue problems and contour integrals. *Journal of Computational and Applied Mathematics*, 292:526–540, 2016. doi: 10.1016/j.cam.2015.07.012.

[240] G. Varillon, P. Brokof, and W. Polifke. Global Linear Stability Analysis of a Slit Flame Subject to Intrinsic Thermoacoustic Instability. In *Proceedings of the 29th International Congress on Sound and Vibration*, Prague, Czech Republic, July 2023. Society of Acoustics.

[241] J. von Saldern, A. Orchini, and J. Moeck. Analysis of Thermoacoustic Modes in Can-Annular Combustors Using Effective Bloch-Type Boundary Conditions. *Journal of Engineering for Gas Turbines and Power*, 143(7):071019, 2021. doi: 10.1115/1.4049162.

[242] J. G. R. von Saldern, J. P. Moeck, and A. Orchini. Nonlinear interaction between clustered unstable thermoacoustic modes in can-annular combustors. *Proceedings of the Combustion Institute*, 38(4):6145–6153, 2021. doi: 10.1016/j.proci.2020.06.236.

[243] H. Voß and V. Mehrmann. Nonlinear Eigenvalue Problems: A Challenge for Modern Eigenvalue Methods. *GAMM-Mitteilungen*, 27:121–152, 2004. doi: 10.1002/gamm.201490007.

[244] G. Wang, X. Liu, S. Wang, L. Li, and F. Qi. Experimental investigation of entropy waves generated from acoustically excited premixed swirling flame. *Combustion and Flame*, 204:85–102, 2019. doi: 10.1016/j.combustflame.2019.03.005.

[245] JM. Wicker, MW. Yoon, and V. Yang. Linear and non-linear pressure oscillations in baffled combustion chambers. *Journal of Sound and Vibration*, 184(1):141–171, 1995. doi: 10.1006/jsvi.1995.0309.

[246] L. J. Williams, J. Meadows, and A. K. Agrawal. Passive control of thermoacoustic instabilities in swirl-stabilized combustion at elevated pressures. *International Journal of Spray and Combustion Dynamics*, 8(3):173–182, 2016. doi: 10.1177/1756827716642193.

[247] P. Wolf, R. Balakrishnan, G. Staffelbach, L. Gicquel, and T. Poinsot. Using LES to study reacting flows and instabilities in annular combustion chambers. *Flow, Turbulence and Combustion*, 88:191–206, 2012. doi: 10.1007/s10494-011-9367-7.

[248] P. Wolf, G. Staffelbach, L. Y. M. Gicquel, J.-D. Müller, and T. Poinsot. Acoustic and Large Eddy Simulation studies of azimuthal modes in annular combustion chambers. *Combustion and Flame*, 159(11):3398–3413, 2012. doi: 10.1016/j.combustflame.2012.06.016.

[249] D. Yang, F. M. Sogaro, A. S. Morgans, and P. J. Schmid. Optimising the acoustic damping of multiple Helmholtz resonators attached to a thin annular duct. *Journal of Sound and Vibration*, 444:69–84, 2019. doi: 10.1016/j.jsv.2018.12.023.

[250] V. Yang. Introductions - Stability Characteristics and Control Approach. In *Active Control of Engine Dynamics*, pages 1–1–1–17. RTO, 2002. ISBN 92-837-1081-9. doi: 10.14339/RTO-EN-020.

[251] S. R. Yeddula, J. Guzmán-Iñigo, and A. S. Morgans. A solution for the quasi-one-dimensional linearised Euler equations with heat transfer. *Journal of Fluid Mechanichs*, 936:R3, 2022. doi: 10.1017/jfm.2022.101.

[252] M. Yoko and M. P. Juniper. Data-driven modelling of thermoacoustic instability in a ducted conical flame. In *Symposium on Thermoacoustics in Combustion*, Zurich, Switzerland, Sept. 2023.

[253] M. Yoko and M. P. Juniper. Inferring Flame Transfer Functions of Turbulent Conical Flames From Pressure Measurements. In *Proceedings of the ASME Turbo Expo 2024: Turbomachinery Technical Conference and Exposition*, London, UK, June 2024. ASME.

[254] M. Yoko and M. P. Juniper. Adjoint-accelerated Bayesian inference applied to the thermoacoustic behaviour of a ducted conical flame. *Journal of Fluid Mechanics*, 985:A38, 2024. doi: 10.1017/jfm.2024.276.

[255] S. Yokota and T. Sakurai. A projection method for nonlinear eigenvalue problems using contour integrals. *JSIAM Letters*, 5(0):41–44, 2013. doi: 10.14495/jsiaml.5.41.

[256] M. Yoon. The entropy wave generation in a heated one-dimensional duct. *Journal of Fluid Mechanics*, 883:A44, 2020. doi: 10.1017/jfm.2019.901.

[257] M. Zellhuber, C. Meraner, R. Kulkarni, W. Polifke, and B. Schuermans. Large Eddy Simulation of Flame Response to Transverse Acoustic Excitation in a Model Reheat Combustor. *Journal of Engineering for Gas Turbines and Power*, 135(9):091508, 2013. doi: 10.1115/1.4024940.

[258] M. Zellhuber, B. Schuermans, and W. Polifke. Impact of Acoustic Pressure on Auto-Ignition and Heat Release. *Combustion Theory and Modelling*, 18(1):1–31, 2014. doi: 10.1080/13647830.2013.817609.

[259] M. Zellhuber, J. Schwing, B. Schuermans, T. Sattelmayer, and W. Polifke. Experimental and Numerical Investigation of Thermo-Acoustic Sources Related to High-Frequency Instabilities. *International Journal of Spray and Combustion Dynamics*, 6(1):1–34, 2014. doi: 10.1260/1756-8277.6.1.1.

[260] G. Zhang, X. Wang, L. Li, X. Jing, and X. Sun. Control of thermoacoustic instability with a drum-like silencer. *Journal of Sound and Vibration*, 406:253–276, 2017. doi: 10.1016/j.jsv.2017.06.027.

[261] G. Zhang, X. Wang, L. Li, and X. Sun. Effects of Perforated Liners on Controlling Combustion Instabilities in Annular Combustors. *AIAA Journal*, 58(7):3100–3114, 2020. doi: 10.2514/1.J059099.

[262] D. Zhao and X. Y. Li. A Review of Acoustic Dampers Applied to Combustion Chambers in Aerospace Industry. *Progress in Aerospace Sciences*, 74:114–130, 2015. doi: 10.1016/j.paerosci.2014.12.003.

[263] D. Zhao, Z. Lu, H. Zhao, X. Y. Li, B. Wang, and P. Liu. A review of active control approaches in stabilizing combustion systems in aerospace industry. *Progress in Aerospace Sciences*, 97:35–60, 2018. doi: 10.1016/j.paerosci.2018.01.002.